EXPERIMENTAL STUDY ON TURBULENT FLOW FIELD, BUBBLE ENTRAINMENT, AND SCALE EFFECTS IN PLUNGING BREAKING WAVES

A Dissertation

by

BYOUNGJOON NA

Submitted to the Office of Graduate and Professional Studies of
Texas A&M University
in partial fulfillment of the requirements for the degree of

DOCTOR OF PHILOSOPHY

Chair of Committee,	Kuang-An Chang
Committee Members,	Hamn-Ching Chen
	Robert E. Randall
	Scott A. Socolofsky
	Achim Stössel
Head of Department,	Robin Autenrieth

August 2016

Major Subject: Civil Engineering

ABSTRACT

First, the kinematics and dynamics of deep-water plunging breakers of 0.2 m wave height were investigated. Flow properties were measured using modified particle image velocimetry (PIV) and bubble image velocimetry (BIV); void fraction was measured using the fiber optic reflectometer (FOR) in the aerated crest region. A similarity profile of void fraction was found in the successive impinging and splash-up rollers. In the highly foamy splashing roller, the increase of turbulent level and vorticity level were strongly correlated with the increase of void fraction when the range of void fraction was between 0 and 0.4. When including the density variation due to the air bubbles, the wave energy dissipated exponentially a short distance after breaking about 54% and 85% of the total energy dissipated within one and two wavelengths beyond the breaking wave impingement point, respectively.

Then, turbulent flow field and bubble size distributions were discussed as an extension of the first part. The most excited mode of the local intermittency measure of the turbulent flow and its corresponding length scale were obtained using a wavelet-based method and found to correlate with the swirling strength and vorticity. The number of bubbles with a chord length less than 2 mm demonstrated good correlation with the swirling strength. The power law scaling and the Hinze scale of the bubbles determined from the bubble chord length distribution compared favorably with existing measurements. The turbulent dissipation rate, accounting for void fraction, was estimated using mixture theory. A significant discrepancy of approximately 67% between the total energy dissipation rate and the turbulence dissipation rate was found. Of this uncounted

dissipation, 23% was caused by bubble-induced dissipation.

Finally, the kinematics and the bubble entrainment in a 1-m height of plunging breaking wave in a very large wave tank of 5 m in width and depth and 300 m in length were discussed. To investigate the scale effects, velocity fields, turbulence, and void fraction were compared with the study of small scale plunging breakers (of 0.2-m wave height) discussed in the first two chapters. The temporal evolutions of the maximum surface horizontal velocity in the two scales are comparable, with a maximum difference only about $0.2C$ where C is the phase velocity. The measured vertical profile of the wave-averaged turbulent kinetic energy can be fitted to an exponential curve, consistent with the previous studies in surf zone breaking waves. The temporal contours of void fraction are similar between the two scales.

DEDICATION

This dissertation is dedicated,

With love and respect,

To my wife, a daughter and a son, parents and parents-in-law.

ACKNOWLEDGEMENTS

I would like to thank my advisor, Dr. Kuang-An Chang, for his guidance, advice, support, and encouragement throughout the course of this research. Without his insight and experience, this dissertation could not have been completed.

I would like to thank my committee members, Dr. Hamn-Ching Chen, Dr. Robert E. Randall, Dr. Scott A. Socolofsky, and Dr. Achim Stössel for their guidance and advice throughout the research. I wish to thank the other professors in the department of Civil Engineering and Ocean Engineering. I would like to thank Dr. Zhi-Cheng Huang at National Central University, Taiwan for his feedbacks in completing the journal papers.

I thank to the former student of Dr. Kuang-An Chang, Dr. Ho Joon Lim for allowing me to use his data and results in this dissertation. Thanks to my research mate, Mr. Wei-Liang Chuang for the help, friendship and encouragement. Thanks also go to Mr. John Reed for his advice and help during the time working as a teaching assistant. I would like to thank all my colleagues in the department for their friendship during my study.

Lastly, I would like to express special thanks to my wife, daughter and son, parents and parents-in-law. This dissertation would not have been completed without their love, encouragement, patience and support.

TABLE OF CONTENTS

Page

CHAPTER

CHAPTER

LIST OF FIGURES

Page

LIST OF TABLES

Page

CHAPTER I

INTRODUCTION

1.1 Background of Breaking Waves

Wave breaking in the ocean is a nonlinear phenomenon that has a significant effect on air entrainment, turbulence, energy dissipation, and numerous environmental processes. During the breaking process, a complex two-phase flow is generated, the flow entrains air and consequently enhances the rate of air-sea gas exchange (Farmer et al., 1993) which has a profound effect on climate (Melville et al., 2002). Wave breaking plays an important role in the exchange of mass, momentum, and energy between the atmosphere and the ocean. A number of physical processes are influenced by the bubbles generated under breaking waves, including sea-surface sound (Deane 1997), production of aerosols (Blanchard 1963), and increase of gas and heat transfer between the ocean and the atmosphere (Sutherland and Melville, 2013). Moreover, extreme wave slamming, a potential hazard for ships and offshore structures is closely associated with violent plunging breaking waves.

Researches on breaking waves have been progressed extensively both in deep water (Bonmarin, 1989; Banner and Peregrine, 1993; Melville, 1996; Perlin et al., 2013) and in nearshore surf zones (Peregrine, 1983; Battjes, 1988; Christensen et al., 2002; Longo et al., 2002). Many excellent reviews on breaking waves has been reported using experimental and/or numerical methods as various flow measurement techniques and computer with high capacity and speed have been developed rapidly over the several

decades.

Experimental study of breaking waves were mostly conducted qualitatively until late 1970's because reliable quantitative measurement techniques were not available. Earlier quantitative measurements on breaking waves relied on flow visualization techniques that were employed to parameterize the asymmetry and steepness of the waves at the breaking moment (Bonmarin, 1989) and to observe the mixing of post breaking turbulent flow (Rapp and Melville, 1990). In the last four decades, non-intrusive optical techniques such as laser Doppler velocimetry (LDV), particle image velocimetry (PIV), and bubble image velocimetry (BIV) have been developed and employed to perform quantitative measurements on breaking waves.

The LDV technique is a point measurement with a high temporal resolution that is mainly capable of measuring velocity under the trough level (e.g. Nadaoka et al., 1989; Rapp and Melville, 1990; Ting and Kirby, 1996; Stansby and Feng, 2005; Shin and Cox, 2006; Longo, 2009). The PIV technique has been extensively employed in numerous breaking wave studies (e.g. Perlin et al, 1996; Chang and Liu, 1999; Melville et al, 2002; Govender et al., 2004; Kimmoun and Branger, 2007; Drazen and Melville, 2009; Huang et al., 2009) because the velocity measurements for the entire flow field can be measured that lead to reveal turbulent structures. The BIV technique is a relatively new technique that is capable of measuring velocity fields inside the highly aerated region under breaking waves where the traditional PIV have great difficulties due to the scatter of light from air bubbles. Recently, BIV has been successfully applied to measure the velocity fields in the study of the kinematics of bubble plumes generated under breaking waves and hydraulic

jump (e.g. Ryu et al., 2005; Rodriguez-Rodriguez et al., 2011; Lim et al., 2015; Lin et al., 2012).

Despite the great advances in the breaking wave study, few studies focused on understanding turbulent flow structures under breaking waves (Chang and Liu, 1999; Melville et al., 2002; Govender et al., 2004; Drazen and Melville, 2009; Huang et al., 2010). Besides, most results were based on the velocity measurements outside the aerated region, under the trough level, further away from the breaking point, and under weak spilling breakers where air entrainment is less intense. Recently, Kiger and Duncan (2012) reviewed the bubbly flows and air entrainment under breaking waves and concluded that a vast part of the air entrainment process under plunging breaking waves is still poorly understood mainly associated with the measurement difficulties in highly aerated region.

Coherent structures have been shown to be an important feature in turbulent flows such as the breaking waves, as they have been shown to affect small-scale turbulence (Bonnet and Delville, 2001; Camussi, 2002). Wavelet analysis has been reported to be a satisfactory tool to investigate the multiple scales of coherent structures (e.g. Camussi and Felice, 2006; Longo, 2009; Huang et al., 2010). Camussi and Felice, (2006) showed that the mean size of coherent structure is about 4% - 5% of the turbulent boundary layer thickness in a free-surface circulating flow. Longo (2009) and Huang et al., (2010) estimated the sizes of eddies that carry most turbulence energy in the pre-breaking and the active breaking region of surf-zone spilling breakers, respectively.

Since plunging breaking waves are multiphase flows that feature a highly aerated region, measuring void fraction (the ratio of gas volume to total volume) is essential for

investigating certain flow properties that involve the fluid density, such as the mean and kinetic energy budget and the potential energy of the flow. Measurement of void fraction under breaking waves has been progressing in both field and laboratory settings using acoustic, electrical, and optical methods (e.g., Lamarre and Melville, 1991; Lamarre and Melville, 1992; Vagle and Farmer, 1998; Deane and Stokes, 2002; Chang et al., 2003; Cox and Shin, 2003; Blenkinsopp and Chaplin, 2007; Rojas and Loewen, 2007; Lim et al., 2008; Ryu and Chang, 2008; Lim et al., 2015). However, the relation between void fraction and surrounding turbulent flows under breaking waves has rarely been reported except for few studies (e.g., Cox and Shin, 2003; Mori and Kakuno, 2008) mainly due to the difficulties in combined measurements of velocity fields and void fraction.

Studies of breaking-induced bubble size and population distributions have been conducted using photographic, acoustic, laser, and in situ measurements (Deane and Stokes, 2002; Deane, 1997; Mori, 2002; Chanson et al., 2002). Furthermore, the bubble population distribution has been reported to follow a power-law scaling (Baldy, 1993; Garrett et al., 2000; Deane and Stokes, 2002; Mori et al., 2007). Despite the progress on measuring bubbles in breaking waves, the relation of bubbles and turbulence has not been as well understood especially in waves with intense air entrainment and a large number of bubbles.

Few exceptions are the recent numerical study of Ma et al., (2011) and Derakhti and Kirby, (2014). Ma et al., (2011) developed a polydisperse two-fluid model to simulate bubbly flows under surf zone breaking waves. Their model captured the bubble-size spectrum at different depths and showed that as the depth increases, the spectrum became

steeper due to buoyancy. The simulated turbulent dissipation rate was found to be much higher with the presence of bubbles. The bubble-induced turbulence suppression was linearly correlated with the void fraction in the high turbulence region. Derakhti and Kirby, (2014) conducted large-eddy simulations of a single breaking event in deep water. They concluded that bubble-induced dissipation accounts for more than 50% of the total dissipation. Their results also showed that turbulent kinetic energy is damped by 20% by dispersed bubbles in plunging breaking waves. The numerical simulations were validated to a satisfactory degree with experiments, but a lack of simultaneous measurements of velocity and void fraction in the aerated region still contributes certain uncertainties, if not difficulties, in model validations.

Field measurements of breaking waves have been successfully conducted to investigate turbulence (e.g. George et al., 1994; Doron et al., 2001), void fraction (Lamarre and Melville, 1991), and bubble size distribution (Deane, 1999; Deane and Stokes, 2002). However, challenges in controlling environmental conditions and operating instruments in the field studies remain a hurdle in explaining the connection between turbulence and air entrainment. A near-prototype scale laboratory experiment, with a breaking wave height of O(1 m), is essential in providing an intermediate step to fill the gap between the small-scale laboratory measurements and the field observations for turbulence under breaking waves (Thornton et al. 2000). While a few studies focused on turbulence (Scott et al., 2005; Oh et al., 2008; Yoon and Cox, 2010; Huang and Hwang, 2015), to the author's knowledge, almost no study measured void fraction and bubbles under large scale laboratory breaking waves.

1.2 Objective and Scope of the Study

The objective of the present study is to investigate turbulent flow field, bubble entrainment, and scale effects in plunging breaking waves in deep water. The plunging breaking waves in two different scales generated by wave focusing methods (Skyner et al, 1990) are examined experimentally using a suite of measurement techniques. In the small scale breaking waves with the wave height of 0.2 m, velocity fields of the entire domain of breaking, void fraction, bubbles and wave elevations are measured using the modified PIV, BIV, and FOR. In the large scale breaking waves with the wave height of 1 m, surface velocity fields in the aerated region, void fraction, wave elevations, bubbles, and internal velocities below the aerated region are measured using BIV, FOR, and ADV.

This dissertation is composed of the six main chapters. The chapter I and chapter VI present the introduction and the conclusion as well as the future work, respectively of the entire dissertation. Each chapter in chapters II to IV follows a format of an individual journal paper. The chapters II to IV follow a structure of combining papers.

Chapter II presents the experimental results on the kinematics and dynamics of an aerated flow with void fraction properties under the small scale plunging breaking waves in deep water. Combining the measurements of the velocity and void fraction enables us to examine the relation between flow kinematics and fluid density under the breaking wave. The distinct evolving patterns of void fraction at the splash-up regions are discussed. The correlation among void fraction, vorticity, and turbulent intensity in the foamy turbulent flow under the breaking wave are discussed. The mass flux, momentum flux, kinetic energy, potential energy, and total energy fluxes are computed and compared

with and without considering void fraction.

Chapter III focuses on the relation between turbulent flow fields and bubbles generated by wave breaking which is essentially an extended discussion continued from Chapter II. The wavelet-based technique is applied to extract the vortical structures and estimate their length scales in the impinging and the splash-up rollers. The distribution of number of bubbles and their size distributions are measured using FOR. The probability density function of bubble size versus bubble number is presented to examine the power scaling and Hinze scale of bubbles. Turbulent dissipation rate based on the mixture viscosity model is discussed with and without considering void fraction.

Chapter IV presents a unique data set of the combined measurements of the surface velocity, the velocity below the region with intense air entrainment, void fraction, and free surface elevation in very large scale plunging breaking waves of 1-m wave height. The results are compared to the results of the small scale breaker as discussed in Chapter II and III to investigate possible scale effects in kinematics, dynamics, and air entrainment of the plunging breaking waves. With the wavelet-based technique employed, the plan-view turbulent length scale of the energetic eddies is estimated at the surface of the violent first splash-up process. The measured surface velocity fields are decomposed into wave induced and turbulence induced components to investigate the temporal and spatial evolution of mean and turbulent kinetic energy.

Chapter V discusses the preliminary results of the measured bubbles in the large scale plunging breaking waves as an extension of Chapter IV. The length of the bubble cloud and its evolution is investigated focusing on the comparison between the small and large

scale breaking waves. The average number of bubbles and the bubble size distribution are compared between both scales.

Chapter II has been published in Journal of Geophysical Research: Oceans (Lim et al., 2015). Chapter III has been published in Journal of Geophysical Research: Oceans (Na et al., 2016). Chapter IV is in revision for submission to Journal of Geophysical Research: Oceans

CHAPTER II

EXPERIMENTAL STUDY ON PLUNGING BREAKING WAVES IN DEEP WATER*

2.1 Introduction

Surface wave breaking plays an important role in the exchange of mass, momentum, and energy between the atmosphere and the ocean (Melville and Matusov, 2002). Wave breaking produces a complex two-phase flow, the flow entrains air and consequently enhances the rate of air-sea gas exchange (Farmer et al., 1993) which may have a profound effect on climate (Melville et al., 2002). Many ocean and coastal engineers have been interested in the wave loading generated by extreme waves and their interaction with marine structures. They investigated potential damages to these structures caused by significant impacts of breaking waves and associated overtopping greenwater (Ryu et al., 2007). The limitation has been caused by the absence of combined measurements of flow velocities and entrained air bubbles in the complex two-phase flow.

---

*Reprinted with permission from "Experimental study on plunging breaking waves in deep water" by Lim, Chang, Huang, and Na (2015). *Journal of Geophysical Research: Oceans*. DOI 10.1002/2014JC010269, Copyright (2015) John Wiley and Sons

Qualitative observations on geometrical properties of unsteady breaking waves in deep water have been reported by Bonmarin (1989) using visualization techniques. Asymmetry and steepness of the waves were parameterized at the breaking moment. The plunging jet and splash-up process were also described. Rapp and Melville (1990) used flow visualization with dye to observe the mixing of post-breaking turbulent flow under unsteady breaking waves in a laboratory. The penetration depth of dye imposed by breaking-generated turbulence was used to quantify the integral length of turbulence mixing. They also used laser Doppler velocimetry (LDV) to obtain the mean velocity field and turbulent kinetic energy (TKE) after wave breaking. A large circulation was first observed in the post-breaking velocity field and the TKE was found to decay following t^{-1} with t being the time after wave breaking. Perlin et al. (1996) used particle image velocimetry (PIV) to measure the crest-region velocity field of a near-breaking plunging breaker. The water particle velocity in the vertical crest region was found to be about 1.3C with C being the wave phase speed estimated from linear wave theory. Melville et al. (2002) used PIV to measure the post-breaking velocity field under laboratory unsteady breaking waves in deep water. A mosaic of images was used to construct a large spatial coverage of ensemble-averaged velocities and overcome the insufficient resolution of using a single field of view (FOV). A coherent vortex slowly propagating downstream was observed in the post-breaking velocity field. The decay of vorticity and Reynolds stress was found to follow t^{-1}, consistent with their previous finding of the TKE decay. Vertical profiles for terms in the TKE budget equation were also estimated. Drazen and Melville (2009) subsequently improved the resolution of PIV measurements so the turbulent

wavenumber spectra of the post-breaking turbulent cloud were resolved. The integral length scale, Taylor microscale, and eddy viscosity were successfully estimated. Terms in the TKE budget equation, including the local change of TKE, advection, production, turbulent transport, and turbulent dissipation, were also estimated.

A refined criterion and estimate of energy dissipation for wave breaking have been proposed and enhanced in recent studies. Tian et al. (2008) performed an experimental and numerical study to investigate the breaking criterion in deep water. They examined the existing breaking criterion and found that, although it is sensitive to the choice of local wavenumber, a particular wavenumber differentiates between wave groups that lead to breaking and those that do not. Tian et al. (2010) continued their study to parameterize energy dissipation rate for wave breaking. A simple eddy viscosity model was employed to simulate energy dissipation; the model was validated with experimental measurements. The estimated eddy viscosity is of the order of 10-3 m^2/s and of strong dependence on wave breaking strength.

The flow structure, vorticity, and terms in the TKE budget equation under surf-zone breaking waves have been studied experimentally using LDV (e.g., Nadaoka et al., 1989; Ting and Kirby, 1995; Stansby and Feng, 2005) and PIV (e.g., Govender et al., 2002; Govender et al., 2004; Kimmoun and Branger, 2007; Huang et al., 2009), and studied numerically using the Reynolds averaged Navier-Stokes model (Lin and Liu, 1998) and large eddy simulations (Watanabe et al., 2005). Other studies, such as gentle spilling breakers with minimum bubble entrainment reported by Qiao and Duncan (2001) and periodic breaking waves in water of intermediate depth reported by Chang and Liu (1998;

1999), may be relevant to the physical process of deep-water wave breaking. Studies for laboratory surf-zone breaking waves and gentle spilling breaking waves have also been extended from the trough level into the breaking roller region. However, few studies featuring quantitative measurements in the aerated roller region under unsteady deep-water plunging breakers have been reported.

Since plunging breaking waves are multiphase flows that feature a highly aerated region, void fraction (the ratio of gas volume to total volume) measurements are essential for investigating certain flow properties that involve the fluid density, such as the mean and turbulent kinetic energy budget and the potential energy of the flow. Void fraction measurements for breaking waves have been performed in field and laboratory using intrusive probes applying acoustic, electrical, and optical methods (e.g., Lamarre and Melville, 1991; Lamarre and Melville, 1992; Vagle and Farmer, 1998; Deane and Stokes, 2002; Chang et al., 2003; Cox and Shin, 2003; Blenkinsopp and Chaplin, 2007; Rojas and Loewen, 2007; Lim et al., 2008; Ryu and Chang, 2008). More recently, Mori et al. (2009) reviewed these various measurement techniques for the bulk of air and bubbles generated by breaking waves in the surf zone. It has been widely accepted that using intrusive probes is perhaps the most appropriate approach in measuring void fraction in highly aerated breaking waves. Deane (1997) performed acoustic and optical measurements of surf-zone breaking waves and obtained a void fraction of 0.3 – 0.4. Cox and Shin (2003) used an impedance probe to measure void fraction in three different types of breaking waves (spilling, plunging, and spilling/plunging) in the surf zone and found the maximum ensemble averaged void fraction was between 0.15 and 0.2. They also presented the

temporal variation of void fraction above and below the still water level. The averaged void fraction in each case was self-similar and was modeled with linear growth and exponential decay. Hoque and Aoki (2005) used a conductivity probe to obtain the void fraction under breaking waves in the surf zone. They reported that the void fraction distribution followed the analytical solution of a diffusion equation. The maximum void fraction at the still water level was 0.2 and 0.16 for plunging and spilling waves, respectively. Mori and Kakuno (2008) used a dual-tip resistance-type probe and ADV to measure the void fraction and flow velocity under laboratory surf-zone breaking waves. They found that the void fraction linearly correlates with the turbulence intensity and the bubble size spectra (diameter versus number per unit area) have a slope of −1 and −3.4 for small and large bubbles, respectively, which are independent of the distance from the breaking point and water depth.

Laboratory measurements of bubble cloud characteristics under mechanically generated deep-water breaking waves were carried out by Lamarre and Melville (1991; 1992) with a conductivity probe. Their results showed that the bubble clouds approximately move at $1.0C$ shortly after wave breaking, the mean void fraction within a wave period follows a power law with respect to time, and the normalized volume and potential energy of the bubble plumes decay exponentially. Loewen et al. (1996) experimentally studied the size distribution of large bubbles entrained by deep-water breaking waves in freshwater and saltwater using a photographic technique. They found that bubble size spectra and bubble depth distributions can be represented as exponential functions. Leifer and de Leeuw (2006) and Leifer et al. (2006) studied bubble plumes

under mechanically generated breaking waves with wind effects using images. Bubble size distributions for different bubble plumes were measured and the bubble population was categorized into dense and diffuse plumes. The plume formation rate reached a maximum at the fetch when the maximum intensity of wave breaking occurred.

Blenkinsopp and Chaplin (2007) measured void fraction of breaking waves in laboratory using optical fiber probes. They used a submerged reef structure to generate different types of breaking waves (strong plunging, plunging, and spilling/plunging) and found that integral properties of the void fraction have a remarkable similarity among those types. Rojas and Loewen (2010) used an optical fiber sensor to measure void fraction beneath mechanically generated deep-water spilling and plunging breakers. As the optical probe passed the first splash-up roller and the air cavity, the void fraction decreased to a local minimum of 0.1, then increased to a local maximum of about 0.97, and finally followed by a decrease to zero when the probe reencountered pure water. They found that the speed of the entrained air cavity is about $0.7C$, while the speed of the bubble cloud entrained by the splash-up is about $0.9C$ for plunging breakers and $1.0C$ for spilling breakers. Anguelova and Huq (2012) used an imaging technique to extract the length, depth, and void fraction of bubble clouds in a laboratory wind-wave flume. The bubble clouds were found to travel at $0.5C$ at the beginning of the cloud formation. The length and thickness of the bubble clouds ranged from $0.1L$ to $0.7L$ and $0.5H_s$ to $2\ H_s$, respectively, where L is wavelength an H_s is the significant wave height. The void fraction reached 0.8 – 0.99 at the wave crest phase but decreased to 0.2 – 0.3 at the trough phase.

Compared with spilling waves, plunging waves have a much higher void fraction,

especially near the first impingement and splash-up. Very recently, Kiger and Duncan (2012) reviewed the bubbly flows and air-entrainment mechanisms under breaking waves. They concluded that a vast part of the air entrainment process under plunging breaking waves is still poorly understood. Despite the importance of void fraction and velocities inside the aerated region of plunging breakers, only a small number of void fraction measurements exist; let alone measurements of both flow velocities and void fraction. Studies of wave breaking experimentally applying a multiphase approach have rarely been reported. Therefore, both spilling and plunging breakers need to be investigated using such an approach. This holds especially true for plunging breakers because of their larger air cavities and higher void fraction, posing a greater challenge in the wave breaking study. While more studies have focused on spilling breakers, especially spilling breakers with a diminishingly low void fraction, studies on plunging breakers have been nearly nonexistent due to measurement difficulties. In addition, issues related to extreme wave slamming, a potential hazard for ships and offshore structures, is more likely to associate with deep water plunging breakers. This has led to the need for combining velocity and void fraction measurements to quantify the process under deep-water plunging breaking waves.

This paper presents experimental results on the kinematics and dynamics of an aerated flow with void fraction properties under mechanically generated, unsteady plunging breakers in deep water. Wave gauges and image techniques were used to obtain the free surface elevation and identify boundaries of the aerated region during the breaking process. A modified PIV method was used to measure the entire flow field, including

velocities in the plunging jet, the aerated rollers during splashing, and the interior water flow region beneath the breaking waves. The velocities in the foamy areas were also measured by the bubble image velocimetry (BIV) technique (Ryu et al., 2005). Mosaics of images were used to cover a larger area of the ensemble-averaged results. In addition, void fraction in the aerated region was measured using the fiber optic reflectometer (FOR) technique (Chang et al., 2003; Lim et al., 2008) at three vertical cross sections coincident with three of the wave gauges and the void fraction data were used to quantify the mixture density. The velocity fields and void fraction under the breaking waves were studied and the effects of void fraction on the kinematics and dynamics of breaking waves were investigated. Discrepancies in breaking wave properties with and without the density consideration were also demonstrated. Note that nearly all existing studies, especially the experimental ones, calculated breaking wave properties based on the density of water alone due to a lack of void fraction information. When density is considered, especially for plunging breakers, most researchers focused on the void fraction distributions (Blenkinsopp and Chaplin, 2007), relation between void fraction and turbulent intensity (Cox and Shin, 2003), and relation between void fraction and turbulent kinetic energy (Mori et al., 2007). There have been few studies that used void fraction to quantitatively determine the mixture density and applied the density to compute the breaking wave properties, probably due to hurdles in measuring both void fraction and velocity in such a flow.

2.2 Experiment

2.2.1 Experimental Apparatus and Wave Generation

The experiment was performed in a two-dimensional glass-walled wave tank housed in the Department of Civil Engineering at Texas A&M University. The tank is 35 m long, 0.91 m wide, and 1.2 m deep, equipped with a flap-type wavemaker. It may be reasonable to approximate surf-zone breaking waves using a two-dimensional wave flume in depth-limited water due to their dominant propagation direction. On the contrary, wave breaking in deep water can be three dimensional. For a growing sea with a steady unidirectional wind forcing, the directional spreading of the waves is limited. In such case, the three-dimensional effect is relatively minor at the center of the breaking waves, suggesting a local two-dimensional approximation may be reasonable. Hence the present study using the two-dimensional tank is considered as a simplified approach due to limitations of the facilities and techniques. A 1:5.5 sloping beach with a horsehair layer is located at the far end of the tank to absorb wave energy and reduce reflection. The definition of the coordinate system is that x represents the horizontal direction along the wave propagation, y the cross tank direction, and z the vertical upward direction.

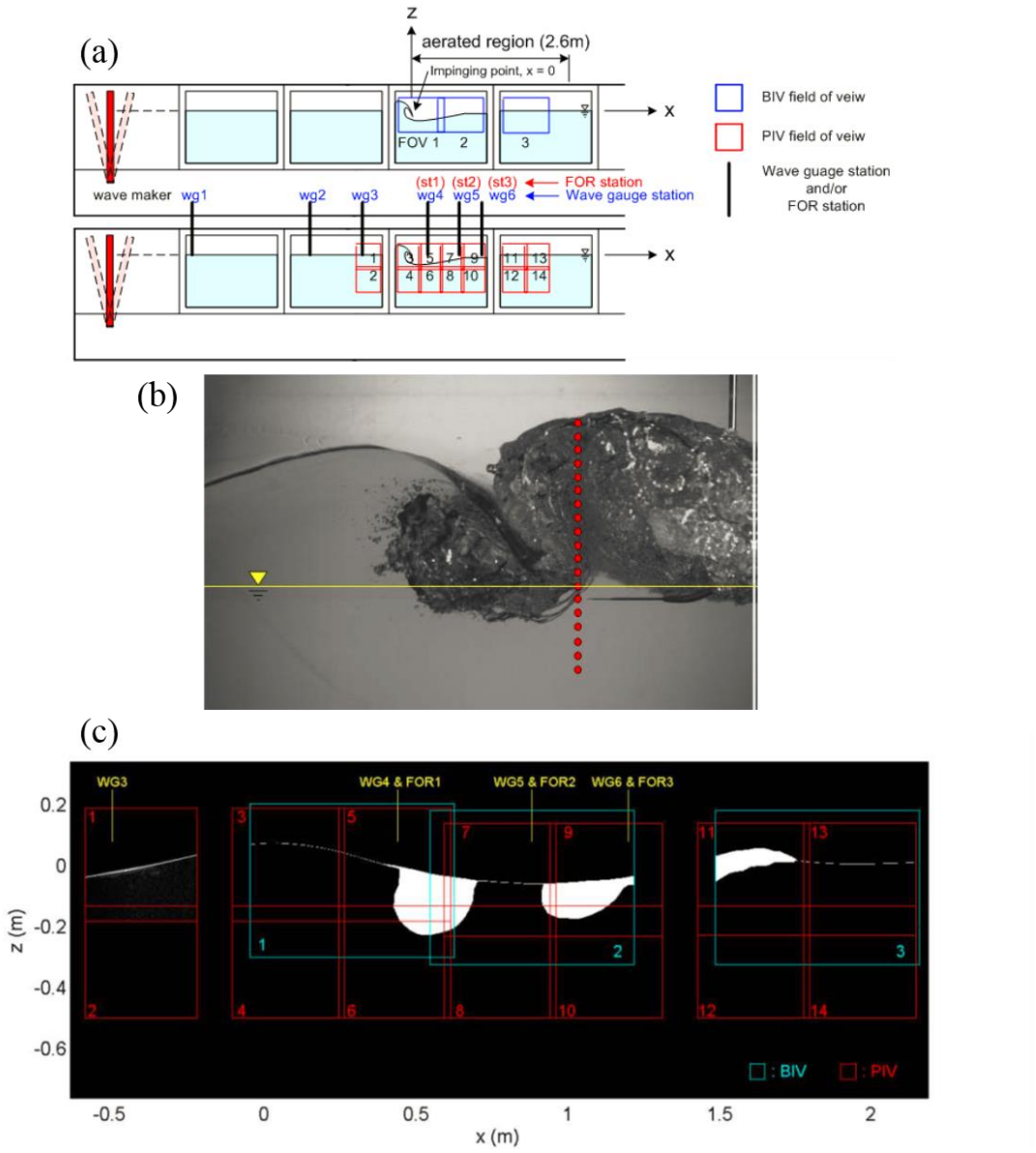

Fig. 2.1 Experimental apparatus and measurement locations: (a) Sketch of wave tank and measurement locations. (b) Measurement points at the first FOR station. (c) Measurement locations and PIV and BIV FOVs with the aerated regions masked.

The origin at $x = 0$ is defined as the breaking-wave impingement, $z = 0$ is defined as the still water level, and time $t = 0$ is defined as the moment of wave impingement. The experimental setup and measurement locations are sketched in Fig. 2.1.

Wave gauges and the BIV, PIV, and FOR techniques were used to measure the wave profiles, flow velocities, and void fraction. The BIV technique measures the velocity field of aerated region in the breaking waves. The modified PIV technique measures the entire flow field, including the pre-breaking region and the highly aerated region. The FOR technique measures the void fraction at three vertical stations located at each splash-up region coincident with three wave gauge locations. See Ryu et al. (2005; 2007) and Lin et al. (2012) for details of BIV and its applications in wave breaking measurements, Chang et al. (2003), Lim et al. (2008), and Ryu and Chang (2008) for details of FOR and its applications in wave breaking measurements.

A wave focusing technique similar to that used in Skyner et al. (1990) was applied to generate a wave packet and produce an unsteady plunging breaking wave in a constant water depth of $h = 0.80$ m. The wave packet consists of 13 waves of various wavenumbers and amplitudes with a central frequency of $f_c = 1.1$ Hz (Fig. 2.2). Only one plunging breaking wave that broke at a desired location with good repeatability was generated in each run. The breaking wave (or primary wave) has a wave height of $H = 0.204$ m and a wave period of $T = 0.83$ s. Based on linear wave theory, the wavelength is $L = 1.08$ m, the phase speed is $C = 1.30$ m/s, the wave steepness is $H/L = 0.19$, and the wave is in a deep water condition of $kh = 4.7$ with k being the wavenumber. When performing the experiment, it was found that the dominant frequency varies along the downstream

measurement stations after the waves break. The wave profiles measured at the pre-breaking location and at the splash-ups were analyzed using wavelet transform (Hwung et al., 2007) and shown in Fig. 2.2c-e. The results indicate that the local peak frequency locates in the central frequency of the wave packet before wave breaking. However, both the peak frequency and the amplitude upshift to a higher frequency. Assuming the linear dispersion relation is applicable for the breaking waves, the upshift of the peak frequency would indicate a shortening of the wavelength. In the present study, we do not believe our data are strong enough to confirm the shortening of wavelength after wave breaking. More studies are needed to clarify the observation.

The laboratory generated breaking waves were intended to mimic breaking waves in the ocean. In reality, mechanisms in the generation of breaking waves in ocean include nonlinear wave-wave interactions, wave-current interactions, wave modulations, and directional and wind effects, among others. These mechanisms are three dimensional and frequency coupled. It is therefore not amenable to the current facility we have. The breaking waves generated using the wave focusing method and presented in the present study are simplified by limiting to only frequency focusing.

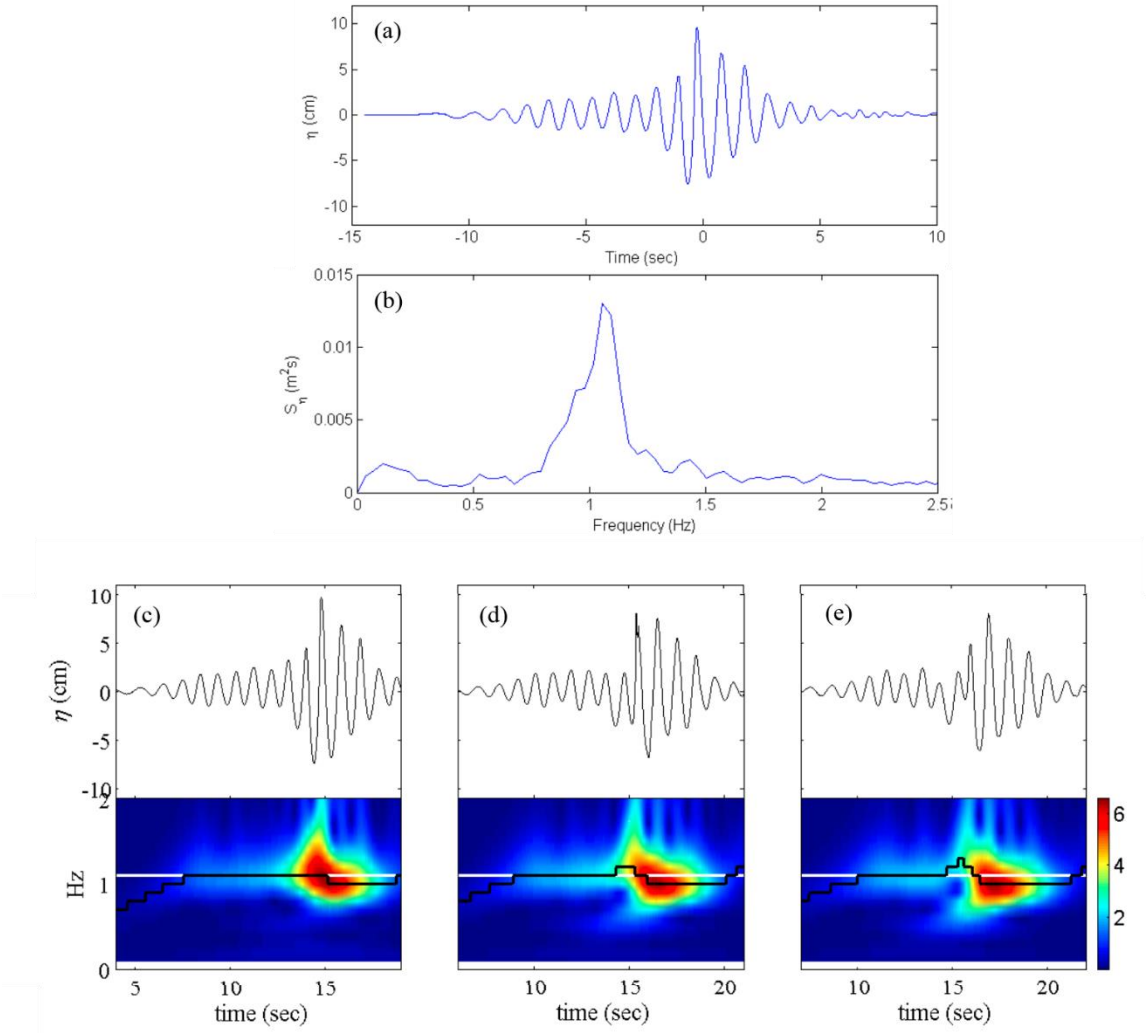

Fig. 2.2 (a) Measured mean surface elevation at WG3 and (b) corresponding power spectrum at WG3. Measured mean surface elevations with corresponding wavelet amplitude spectra shown in the lower panels at (c) WG3, (d) WG4, and (e) WG6. In the each wavelet amplitude spectrum, the white horizontal line at around 1.1 Hz is the central frequency (f_c), and the black line is the local peak frequency.

A total of 20 repeated runs were performed with the same test condition at each measurement location for all the measurements. That means a total of 1,120 repeated runs were performed, including 14 fields of view (FOVs) in the PIV measurements with 20 repeated runs for each FOV (a total of 280 runs), 3 FOVs in the BIV measurements with 20 repeated runs each (a total of 60 runs), 38 FOR measurement points with 20 repeated runs each (a total of 760 runs), and 6 wave gauge measurements with 20 repeated runs (a total of 20 runs). The time interval between the consecutive test runs was at least 15 minutes to allow the water surface to calm. That required several months to complete the repeated runs. The authors indeed spent more than one year to complete the data collection when including initial trial tests to optimize the systems and data acquisition. Repeatability of wave generation was checked based on wave gauge records and PIV velocity measurements at FOV1. It was found that the generated waves are highly repeatable before breaking (to be discussed later).

The mean and fluctuating quantities were calculated from the ensemble average of the 20 instantaneous measurements. Chang and Liu (1999) suggested that meaningful turbulence information can be obtained by ensemble-averaging more than 16 repetitions. Huang et al. (2009) reported that the relative error was less than 0.05 for the ensemble-averaged velocities with 12 repetitions, and for the ensemble-averaged gradient of turbulent fluctuations with 20 repetitions.

2.2.2 Wave Profile Measurements

Six double-wired resistant-type wave gauges (WG1 to WG6) were used to measure water surface elevations at x = -2.98 m, -1.31 m, -0.57 m, 0.43 m, 0.88 m, and 1.20 m as

shown in Fig. 2.1a. Among the gauges, WG3 was set at the location a short distance (0.17 m) upstream from where the front face of the plunging breaker becomes vertical, and WG4, WG5, and WG6 were set at the middle of the first three splash-up regions where the splash-ups were fully developed (with a maximum bubble cloud). The wave parameters discussed above for the primary wave was determined using zero up-crossing method based on the WG3 measurements (Fig. 2.2a). Note that the traditional resistant-type wave gauges used in the present experiment only measure the total "wetted length" (i.e., length in contact with water), so the free surface elevation may be underestimated when the flow is aerated. The dewetting process potentially may cause only one side of the wires wet that leads to an inaccurate measurements. Nevertheless, the distance between the two wires is 2 cm which is one order of magnitude smaller than the wave height of 20 cm therefore it is unlikely an issue for the surface measurement. Having that said, the wave gauge data were not used in the mass, momentum, and energy calculations in the subsequent analysis; images and FOR measurements were used for the elevation and density information.

Fig. 2.3a shows spatial profiles of wave envelopes and time series of wave surface elevations obtained from the BIV and PIV images and from wave gauges. The root-mean-square (RMS) variations of free surface elevations (~ 0.65 – 0.71 mm) between the 20 runs are negligibly small before wave breaking (WG1 to WG3, not shown here), indicating the generated waves are highly repeatable. Fig. 2.3b-d shows that the RMS value reaches the maximum (~ 30 mm) at the first splash-up (WG4) and then reduces to about 10 mm at the second and third splash-ups (WG5 and WG6). This reflects a highly turbulent and aerated nature of the roller at the first splash-up region and a weakly turbulent and

decaying aeration during the later splashing process.

Significant differences of the mean surface elevations measured by the resistance-type wave gauges and by images were observed at WG4 to WG6. Since the image techniques identify the upper boundary of the aerated crest region, while the wave gauge only measures the total wetted length, the differences between these two values are equivalent to the total vertical void length of the aerated region (Appendix 2C). The difference is the largest at WG4 because of the maximum void fraction in the first splash-up (to be discussed later). The difference decreases as the wave continued to break and propagate downstream and the discrepancy at WG6 is relatively small. The difference suggests that the void fraction in the aerated region should be considered in order to correctly account for dynamic properties such as the kinetic and potential energy.

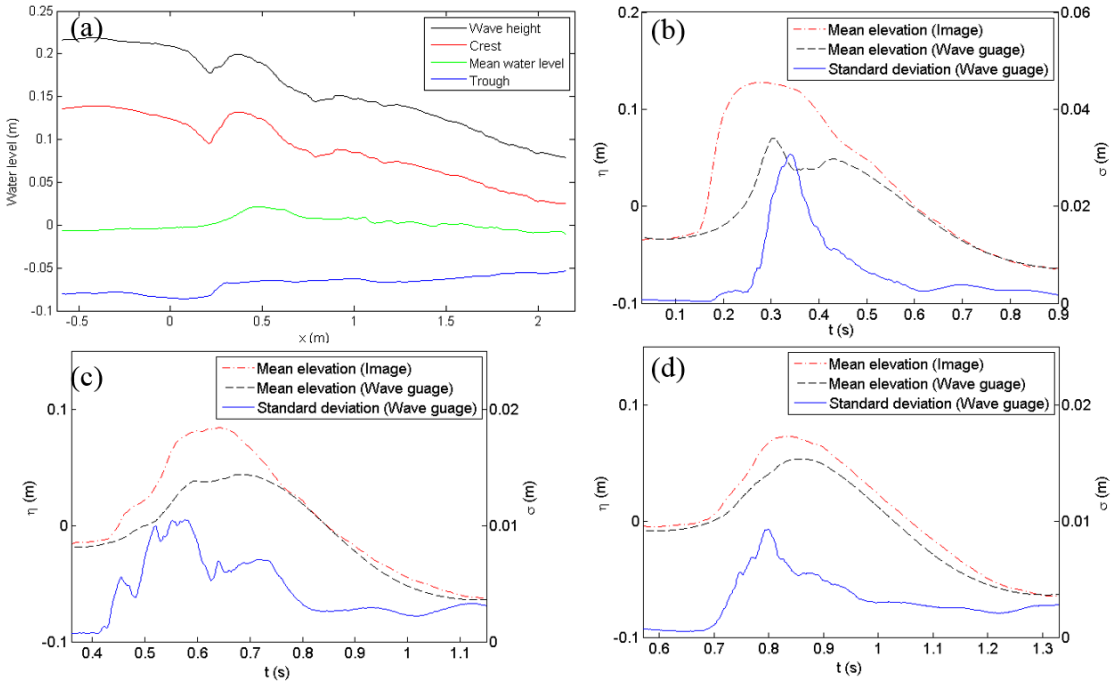

Fig. 2.3 (a) Spatial profiles of wave envelopes with indications of breaking process obtained from BIV and PIV images. (b-d) Time series of mean wave elevations and standard deviation measured by the resistance-type wave gauges and from BIV and PIV images at (b) first splash-up (WG4, x = 0.43 m), (c) second splash-up (WG5, x = 0.88 m), and (d) third splash-up (WG6, x = 1.20 m).

2.2.3 Velocity Measurements

The BIV technique was used to obtain the velocity field in the aerated region after the overturning wave impinged on its front surface. The images were captured by a high speed camera mounted with a 105-mm focal lens. The camera has a resolution of 1024×1024 pixels, a 10-bit dynamic range, and a maximum framing rate of 1200 frames per second (fps). The camera's framing rate was set at 500 fps and the aperture was set at f/1.8 throughout the experiment. The time interval between consecutive recorded images is thus 2 ms. Two regular 600 W light bulbs with reflecting mounts and a translucent flat plate were used to illuminate the flow from behind the tank. No lasers are needed in the BIV measurements. The depth of field (DOF) for the captured images is 0.21 m with its center at 0.2 m behind the tank's front wall. The camera was located at 4.7 m in front of the center of the DOF, resulting in an uncertainty of 2.2% caused by the limited DOF thickness in the acquired images for later velocity determination. In the BIV measurements, 3 fields of view (FOV) of 0.66×0.50 m^2 were used to cover the entire aerated region of the plunging breaker, as shown in Fig. 2.1a, resulting in a spatial resolution of 0.64 mm/pixel. There is a small overlap region of 84 mm between FOV1 and FOV2 and a gap of 270 mm between FOV2 and FOV3 due to a steel column of the wave tank. After acquiring the images, velocities were determined using commercial software from LaVision, Inc. An adaptive multi-pass algorithm with an initial interrogation window of 32×32 pixels and a final window of 16×16 pixels with a 50% overlap was applied in the process. Accordingly, the final resolution of the velocity vectors is 8×8 pixels, corresponding to 5.26×5.26 mm^2. A time interval, Δt, of 2 ms or 4 ms was used for image cross-correlation, depending on

the flow velocities. The BIV images were also used to obtain the free surface information and identify the aerated region by tracking points with a high-intensity gradient in the ensemble averaged images. The principle and validation of the BIV technique are detailed in Ryu et al. (2005; 2007), Chang et al. (2011), and Lin et al. (2012).

The PIV technique was originally employed to measure only the velocity field outside the aerated region and under the trough level to z = -0.51 m (or z/h = -0.64) after obtaining the air-water mixture velocities in the aerated region by using BIV. However, it was found that the air-water mixture velocity field inside the aerated region could also be obtained by using a weak continuous laser and a high dynamic range camera with a short camera exposure time. A 5-W continuous Argon-Ion laser was used as the light source and two cylindrical concave lenses were used to generate the wide light sheet. The same camera and framing rate as in the BIV measurements were used in the PIV measurements. The camera exposure time was set at 100 μs. This exposure time is short enough to prevent particle images from streaking and bubbles becoming saturated, yet long enough for the particles to be visible with a decent intensity. The seeding particles have a mean diameter of 56 μm and a specific weight of 1.02. In the PIV measurements, fourteen FOVs centered at 0.2 m behind the front tank wall were used to cover the entire flow field of breaking waves, including the aerated region. Note that the bottom located at z = -0.80 m and the light sheet was redirected upward by a mirror mounted on the bottom.

The sizes of the 14 FOVs (see Fig. 2.1) are fixed as 0.37×0.37 m^2. Similar to image processing in BIV, the velocity maps were obtained using the adaptive multi-pass algorithm with an initial interrogation window of 64×64 pixels and a final window of

32×32 pixels with a 50% overlap. The resolution of the velocity vectors is 16×16 pixels, corresponding to 5.78×5.78 mm^2. There is an overlap of 20 mm between adjacent FOVs. Using the mosaic concept the 14 FOVs cover the entire flow field of the plunging breaker with sufficient spatial and temporal resolutions. The PIV velocity measurements were validated by comparing the measurements with Stokes wave theory for the water velocities, and measurements from the BIV method for the air-water mixture velocities. Fig. 2.4 shows examples of the instantaneous velocity fields measured by PIV at FOVs 1, 3, 5, and 7. No interpolations were performed in the instantaneous velocity fields; empty velocity vectors in the instantaneous velocity fields are rarely found even in the highly aerated region. Note that the seeding particles were not clearly visible in the aerated crest. The PIV correlation algorithm was not really based on particle displacements but more on micro-foam structures and bubble displacements, as explained in Govender et al. (2002) and Kimmoun and Branger (2007). The algorithm of the modified PIV is similar to that of BIV.

The BIV technique correlates the texture created by bubble-water interfaces in the images thus more bubbles with smaller diameters (in comparison with the interrogation window size of about 10 mm in both BIV and PIV measurements) are preferred for a better accuracy in the correlation. Based on preliminary data for the bubble chord length distribution at FOR station 1, approximately 88% of the bubbles have a chord length less than 5 mm. The results indicate that even in the most violent region most bubbles are small enough to obtain adequate image correlation. In addition, the present PIV and BIV images were taken by a high speed camera with a framing rate of 500 Hz, equivalent to a temporal

resolution of 0.002 s for the velocity measurements. The typical turbulent dissipation rate induced by wave breaking is in the range of $10^{-4} – 10^{-2}$ m^2/s^3, resulting in a Kolmogorov time scale of about 0.01 – 0.1 s which is greater than the 0.002 s temporal resolution. Accordingly, the spatial and temporal resolutions of the present PIV and BIV measurements are high enough to minimize possible bubble distortion between two successive images. In addition, possible displacement of the light sheet plane, if occurred, would be much shorter than the distance between the camera and the light sheet plane (and therefore insignificant error it would cause in the measurements), especially with the light sheet coming from a mirror mounted on the bottom of the tank.

Since a direct validation for the aerated flow measurements is not available, Ryu et al. (2005) validated BIV velocity measurements using a bubble plume. They showed that the performance of BIV is comparable to that of typical PIV. Validations were also performed in Ryu and Chang (2008) (by indirectly comparing the overtopped mass of an overtopping flow by integrating BIV velocity measurements with FOR void fraction measurements), in Chang et al. (2011) (by comparing BIV velocity measurements taken from two orthogonal planes in the same overtopping flow), and in Lin et al. (2012) (by comparing BIV measurements with trajectories of bubbles released into a submerged hydraulic jump). However, none of the validations were performed by directly comparing velocities in violent free surface flows, such as the flow in the present study, due to a lack of available laboratory data.

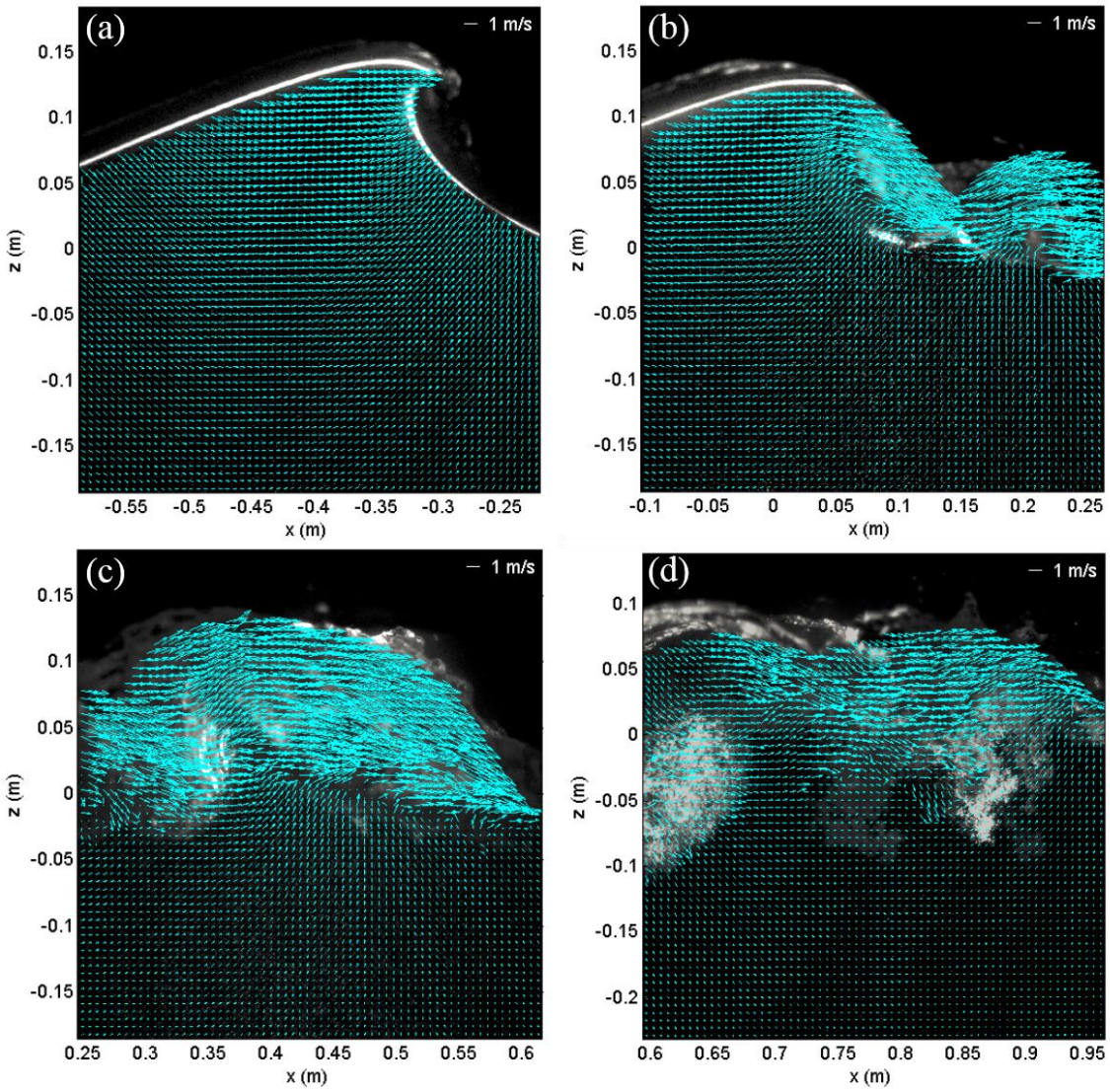

Fig. 2.4 Examples of instantaneous velocity field measured by PIV at t = (a) -0.14 s (FOV1, overturning moment), (b) 0.09 s (FOV3, first impingement and splash-up), (c) 0.25 s (FOV5, first splash-up), (d) 0.56 s (FOV7, second impingement and splash-up).

2.2.4 Void Fraction Measurements

The FOR technique was used to obtain the void fraction in the aerated region of breaking waves. Based on the coherent mixing of scattered signals with Fresnel reflection from the tip of an optical fiber, FOR is capable of measuring the velocity and void fraction of both phases at a given point in the gas-liquid flow. The technique is nearly noninvasive because of its small dimension of the optical fiber (typical diameter 125 μm), high spatial resolution (typically less than 50 μm), and high temporal resolution (typically less than 10 μs). The principle, validation, and applications of the FOR technique are described in detail in Chang et al. (2002; 2003), Lim et al. (2008), and (Ryu and Chang, 2008). The FOR measurements were sampled at 100 kHz throughout the experiment. There are three FOR measurement stations located at the middle of the three splash-ups as shown in Fig. 2.1a. Fig. 2.1b shows the first FOR measurement station (FOR1) corresponding to the location of the first splash-up and WG4. The dots in the figure, with an interval of 10 mm, represent the FOR measurement locations. The total numbers of measurement points at stations 1, 2, and 3 are 19, 12 and 7, respectively. These numbers were determined by the vertical spreading of the bubble cloud at each station, from z = -0.06 m to 0.12 m, -0.04 m to 0.07 m, and 0 to 0.06 m for stations 1, 2, and 3. Measurements at the location below the lowest point for each station were also performed (but not shown here) to verify that the void fraction was negligibly small.

Validations for FOR void fraction measurements were performed using bubble plumes in a narrow pipe with a void fraction up to 14% (Chang et al. 2003; Lim et al. 2008). For a higher void fraction validation, using the same method did not work well due

to the high uncertainty in identifying the "water surface" with a large amount of bubbles bursting on the free surface of the pipe. However, void fraction measurements, along with velocity measurements, were validated in a greenwater flow that has a similar void fraction and velocity scale to the plunging breakers in the present study by indirectly comparing overtopping mass collected using a container (Ryu and Chang, 2008). Appendix 2C also provides a simple evidence to validate the void fraction measurements based on the differences between images and wave gauge data.

For later use, we define the wave-averaged quantity f_{wa} (wet-period averaged) and period-averaged quantity f_{pa} (averaged over one-wave period) for a variable f at a given point as follows:

$$f_{wa}(x,z) = \frac{\int_{t_{tr}(x,z)}^{t_{tr}(x,z)+T} \delta(x,z,t) f(x,z,t) dt}{\int_{t_{tr}(x,z)}^{t_{tr}(x,z)+T} \delta(x,z,t) dt} \tag{2.1}$$

$$f_{pa}(x,z) = \frac{\int_{t_{tr}(x,z)}^{t_{tr}(x,z)+T} \delta(x,z,t) f(x,z,t) dt}{\int_{t_{tr}(x,z)}^{t_{tr}(x,z)+T} dt} \tag{2.2}$$

where $t_{tr}(x,z)$ is the time when the front trough reaches a specific measurement cross section and T is the wave period. $\delta(x,z,t)=1$ when the point at time t is in water and $\delta(x,z,t)=0$ otherwise. The time resolution dt is 0.01 s in the present study. We further

define the depth-averaged time-mean quantity f_{da} for the variable f at a given cross section x by "depth" averaging the corresponding period-averaged quantity f_{pa} as follows:

$$f_{da}(x) = \frac{\int_{z=-L/2}^{\eta(x)} f_{pa}(x,z)dz}{\int_{z=-L/2}^{\eta(x)} dz} \tag{2.3}$$

where η is the free water surface. Note that the vertical integral accounts for only one-half wavelength instead of the entire water depth due to the deep water wave condition ($h/L > 0.5$). The observed quantity and the cumulative integrals of f_{pa}, integrated from η, reach constant when z approaches $-L/2$. In the experiment, the PIV measurements cover from $z = -0.64h$ (equivalent to $0.474L$) to above the maximum free surface.

2.3 Velocity Fields of Breaking Waves

2.3.1 Qualitative Description of Breaking Process

Fig. 2.5 demonstrates the plunging breaking process using images taken by the high speed camera at 500 fps. A total of three impingements and three splash-ups of air-water mixture were observed during the process. In the formation of the breaking wave, the overturning water jet falls and impacts on the water surface ahead to form the first clockwise (positive) roller and generates the first bubble cloud. Immediately after the jet hits the frontal water surface with large momentum, the water surface is broken and pushed upward, forming the first foamy splash-up and generating the second clockwise rolling bubble cloud (Fig. 2.5a, b). Earlier works like that of Miller (1976) provided most

qualitative description but the present study contains some new information such as the description of the penetration/pushing-up of the overturning impinging wave and the backward impingement between the first and second clockwise rollers. The breaking process is generally in accordance with the results reported by Bonmarin (1989) and Perlin et al. (1996).

Note that there have yet been definite answers to the formation of the splash up followed by the jet impingement. Peregrine (1983) proposed three schemes (rebounding, penetrating and intermediate between the two). Bonmarin (1989) and Perlin et al. (1996) later reported that the impinging jets in their experiments seemed to penetrate the surface based on slow motion of film videos. Based on the high-speed BIV video images and obtained velocity field, the present study also observed the same – penetration of the impinging jet.

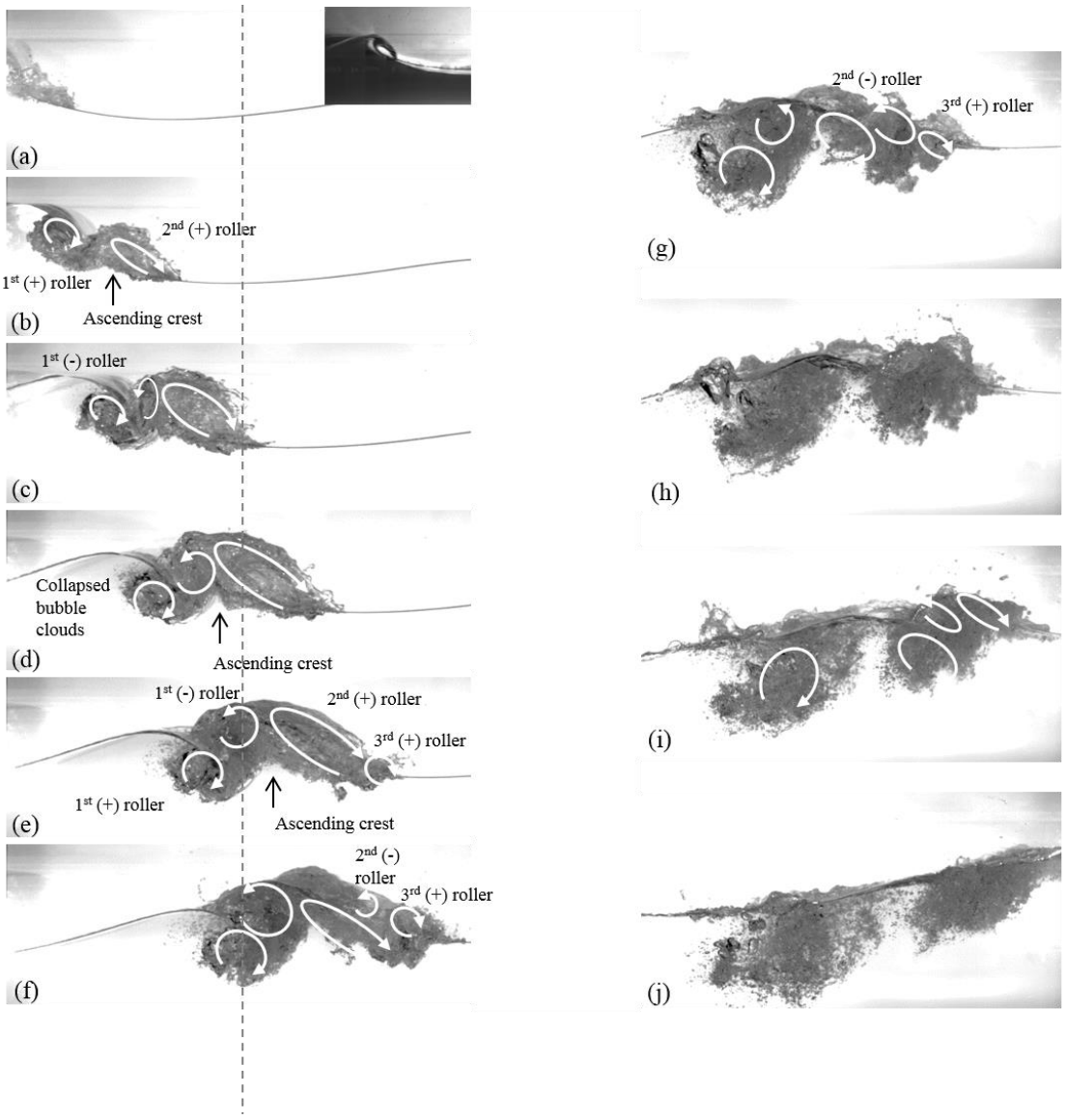

Fig. 2.5 Images illustrating the plunging breaking process from the first impingement to the second splash-up in one wave period at *t* = (a) 0.03 s, (b) 0.11 s, (c) 0.19 s, (d) 0.27 s, (e) 0.35 s, (f) 0.43 s, (g) 0.51 s, (h) 0.59 s, (i) 0.67 s, (j) 0.83 s. The overturning jet formation is also shown in the subfigure in (a). The arrows sketch the rotation directions of the bubble clouds (+: clockwise; - : counterclockwise) based on high-speed video images. The vertical dashed line indicates the location of the first FOR measurement station.

When the first rolling cloud continues to move downward and penetrates into the deeper water, a new counterclockwise (negative) rolling cloud is generated to form a "backward impingement" between the first and the second clockwise rolling clouds (Fig. 2.5c, d). We called the new rolling cloud a backward impingement since its rotational direction is counterclockwise and it impacts and accumulates air-water mixture over the first downward penetrating clockwise rolling cloud. From the images, we can observe that there exists an undisturbed water region of a triangular shape between the two clockwise rolling clouds. We called the crest of this region a newly formed ascending crest, which is similar to the structure of surf-zone breaking waves reported by Nadaoka et al. (1989).

The fully developed first splash-up continues to impinge on the surface of the wave trough in front of it and forms the second splash-up, which in turn generates the third clockwise rolling cloud (Fig. 2.5e). Note that the first splash-up follows the first impingement immediately due to the large momentum of water jet and reaches an elevation higher than the initial overturning jet (Fig. 2.5c). However, the air-water mixture and spray impingement from the second splash-up roller does not cause the subsequent splash-up immediately. Although the mixture velocity of the first splash is high (to be discussed in Section 5), the fluid density is very low (i.e., very high void fraction, to be discussed in Section 4) so the second impingement does not have as much momentum to generate a strong splash-up as the first one generated by the overturning jet. When the second splash-up roller further penetrates and propagates downstream (indicated as the third positive roller), a new second counterclockwise rolling cloud is found between the second and third clockwise rolling clouds (Fig. 2.5f, g). The second splash-up also

impinges further to produce a weak third splash-up, which generates the fourth clockwise and widely distributed rolling cloud (not covered in the figure). Eventually the wave momentum weakens and the degassing stage starts. Large bubbles in the air cavity of the first clockwise roller start to reach the free surface and burst, while the two main bubble clouds, generated by the first impingement and subsequent splash-ups, almost completely separate (Fig. 2.5h-j).

The first overturning jet penetrates into the free surface without noticeable rebound during the process of the first impingement and splash-up, bringing the entrained air cavity with it which later returns to the free surface and bursts. The generation of one counterclockwise and the two clockwise bubble clouds during the first splash-up (Fig. 2.5c, d) is similar to that sketched by Rojas and Loewen (2010). The first and second clouds penetrate into water, reaching about 1.25H and 0.86H in depth, respectively. Larger air bubbles in the air cavity, entrained in the first impingement, begin to float then burst on the free surface from t = 0.51 to t = 1.00 s (Fig. 2.5g-j). Small sized bubbles, which do not have enough buoyancy, follow the mean flow motion and float toward the free surface gradually. All the bubbles of visible sizes, equivalent to 2 pixels or 0.72 mm in the PIV images based on the Nyquist frequency, disappear around t = 3.0 s (3.6T).

2.3.2 Mean Velocity and Vorticity

After two-dimensional instantaneous velocities were measured by PIV and BIV, the horizontal and vertical mean velocities (U and W) were obtained by ensemble averaging the instantaneous velocities from the 20 repeated runs:

$$U(x,z,t) = \frac{1}{N}\sum_{i=1}^{N} u_i(x,z,t) \tag{2.4}$$

$$W(x,z,t) = \frac{1}{N}\sum_{i=1}^{N} w_i(x,z,t) \tag{2.5}$$

where u_i and w_i are the instantaneous horizontal and vertical velocities, the subscript i represents the ith measurement, and N is the total number of repeated runs. Fig. 2.6 shows the evolution of the mean velocity field during the wave breaking process. The normalized maximum mean horizontal velocities at all the 475 cross sections from the 14 PIV FOVs are shown in Fig. 2.6a. Local maximum velocities occur at each splash-up. In the entire wave breaking process, the maximum horizontal velocity occurs at t = 0.05 s at the beginning the first splash-up with a magnitude of 2.14C, corresponding to the moment in Fig. 2.6d. The maximum velocity then decreases gradually and becomes lower than the wave phase speed after one wave period (slightly over x/L = 1).

The wave front face becomes vertical at x = -0.42 m and t = -0.20 s with a maximum horizontal velocity of about 1.4C (C=1.30 m/s) occurred at the crest (Fig. 2.6b). This velocity is comparable to 1.3C found by Perlin et al. (1996). The measured maximum horizontal and downward velocities increase to 1.68C and 0.71C at the overturning jet just before the first impingement (Fig. 2.6c). The value is similar to that of a overturning jet for periodic breaking waves in water of intermediate depth found by Chang and Liu (1998). The maximum horizontal velocity then increases to 2.14C at the beginning of the first

splash-up (Fig. 2.6d).

It is difficult to observe the rolling motion inside the bubble clouds since the horizontal velocities in the flow are very high. We computed the relative velocities by subtracting the phase speed from the horizontal velocities, equivalent to an observer moving at the phase speed C. The relative mean velocity field during the first splash-up process is shown in Fig. 2.7a, b. Two clockwise rolling clouds are observed in the first impinging roller and first splash-up. Remarkably, a new counterclockwise rolling cloud is also observed between the first and second clockwise rolling clouds during the splash-up (Fig. 2.7b). We further computed the vorticity Ω of the mean flow (defined as $\Omega = \partial U / \partial z - \partial W / \partial x$, Fig. 2.7c, d). Clearly, two positive vortical structures (clockwise rolling clouds) and one negative vortical structure (counterclockwise rolling cloud) are found in the first splash-up process, consistent with the observation of the relative mean velocities and the visualization images.

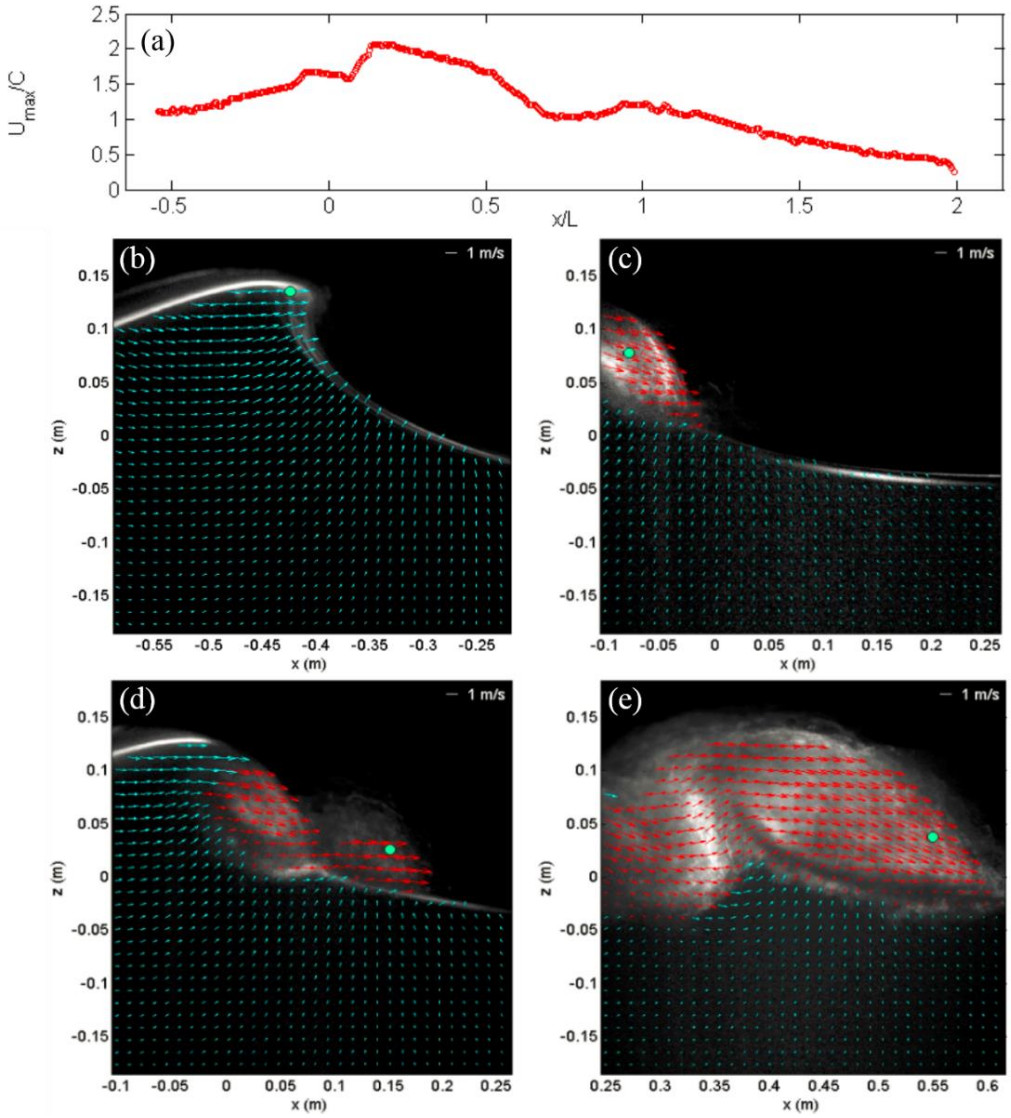

Fig. 2.6 (a) Nondimensionalized maximum mean horizontal velocity (by *C*) under the plunging breaking wave along the wave tank. Mean velocity field in the breaking process at (b) *t* = -0.2 s (FOV1, pre-breaking), (c) *t* = -0.02 s (FOV3), (d) *t* = 0.05 s (FOV3, the first splash-up), (e) *t* = 0.25 s (FOV5), (f) *t* = 0.41 s (FOV7, the second splash-up), (g) *t* = 0.56 s (FOV7), (h) *t* = 0.68 s (FOV9), (i) *t* = 0.80 s (FOV9). Note that a green dot in each velocity map represents the location of the maximum speed, and only one quarter of total velocity vectors (in every other row and every other column) are plotted.

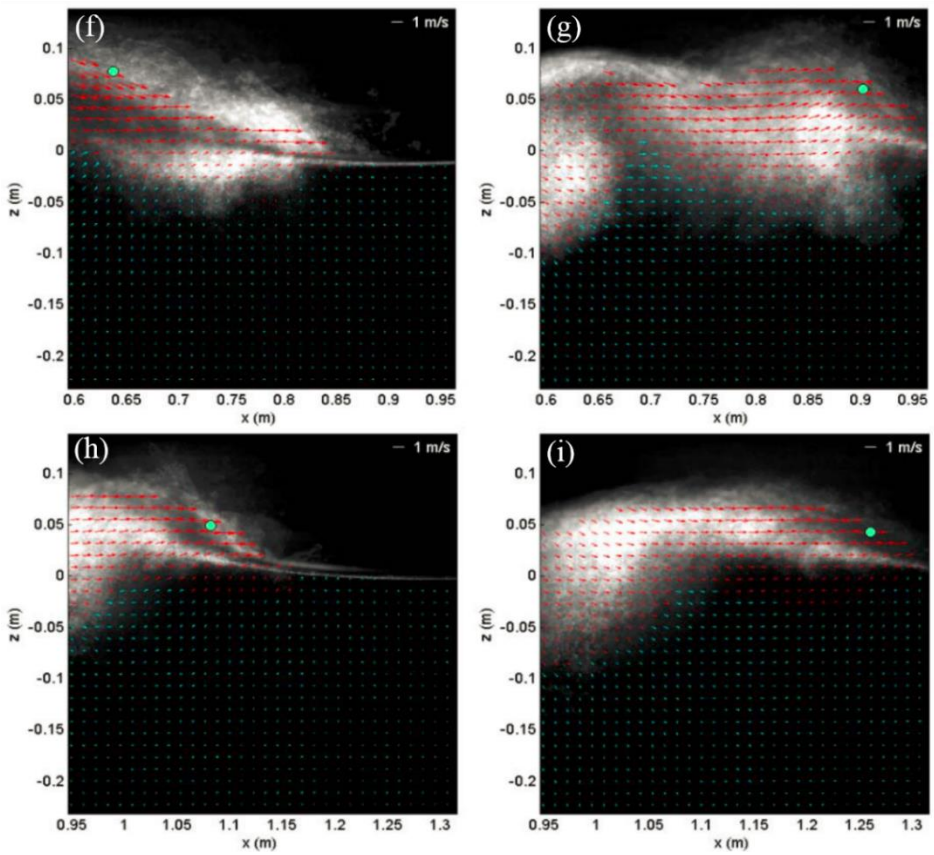

Fig. 2.6 (Continued).

The subsequent evolution of mean-flow vorticity is shown in Fig. 2.8. Multiple concentrated vortical structures (two positive and one negative) are apparent in the aerated rolling crest region after the initiation of impingement and splash-up (Fig. 2.8a, b). The second splash-up starts to generate the third clockwise rolling cloud (positive vorticity) as shown in Fig. 2.8c, d. A second concentrated negative vertical structure (counterclockwise) is found between the second and third positive vortical structures (Fig. 2.8e, f). Except for the rolling plunging jet, concentrated vortices are found near the lower boundary of the aerated region rather than in the center of the rolling splashing clouds. The results are obtained from ensemble-averaging repetitive runs, showing these eddies are coherent and repetitively generated in the bubble clouds. These vortical structures spread along the free surface and propagate with the bubble clouds during the second and third impingements.

In the breaking process, the maximum positive vorticity (~ 100 s^{-1}) occurs around t = 0.05 s, accompanying the occurrence of the maximum horizontal velocity. For breaking waves of a comparable scale but in shallow water, the maximum vorticity generated by a weak surf-zone plunging jet and first splash-up is about 35 – 65 s^{-1} (Stansby and Feng, 2005; Kimmoun and Branger, 2007), which is similar to the measured vorticity of the unsteady breaking waves in deep water. The normalized maximum vorticity in the shallow breaking waves is about one order of magnitude higher than C/h (Chang and Liu, 1999; Stansby and Feng, 2005; Kimmoun and Branger, 2007; Huang et al., 2009), which is however not the case in the present deep-water breaking waves.

The measured maximum vorticity were normalized with the scaling parameter C/H and shown in Fig. 2.9a, b. The normalized maximum positive vorticity reaches about 16

around t/T = 0.06 (caused by the first impinging roller), then decreases to less than 4 in one wave period, occurring near the mean water level. All the measured values of normalized maximum negative vorticity are much lower than that of the positive vorticity. The normalized maximum negative vorticity occurs in the crest regions with a magnitude of about -6 (caused by the first counterclockwise eddy during the first splash-up). Fig. 2.9c, d shows the wave-averaged and period-averaged normalized vorticity (by C/H). The maximum magnitude is close to unity. Remarkably, a group of concentrated vorticity, generated by the impingements and splash-ups, can be observed near the mean water level. The averaged vorticity structures slanted downstream with an asymmetrical distribution in the vertical direction, indicating the ejection of rolling impingements into the water.

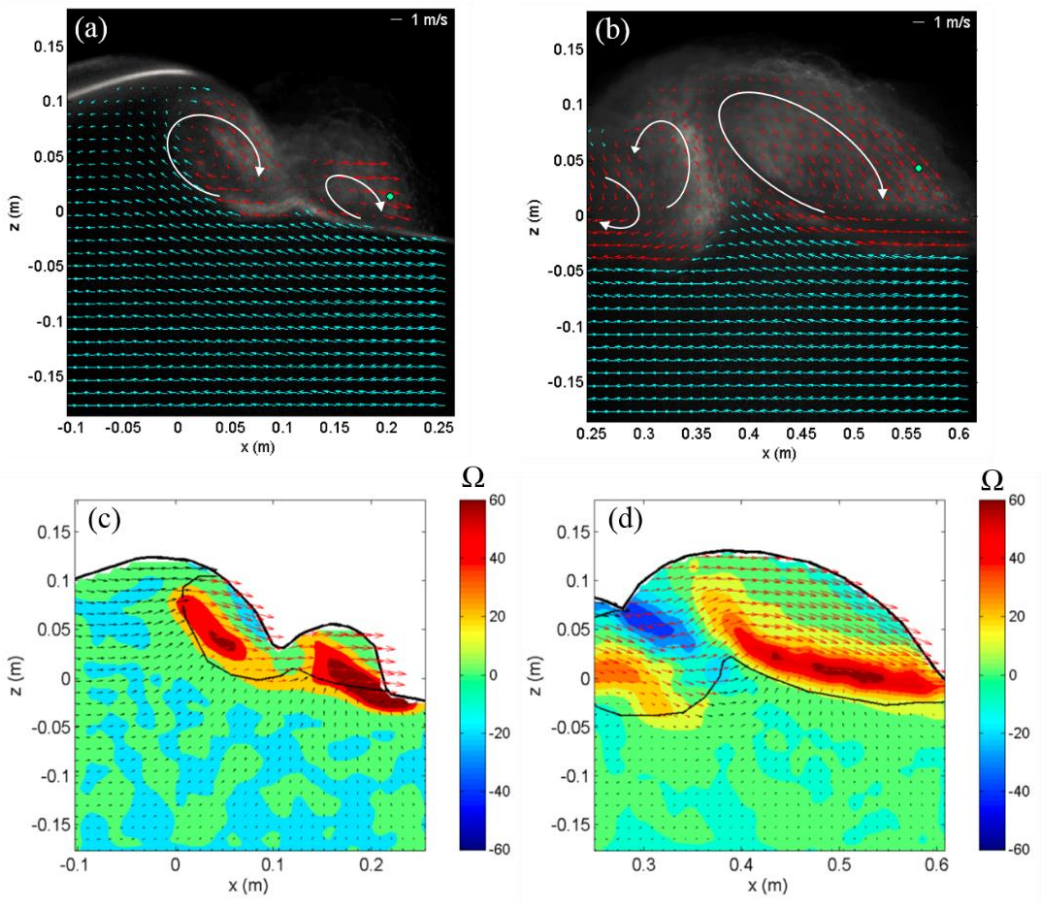

Fig. 2.7 Generation of vortical structures in the rolling bubble clouds during the first splash-up process. (a, b) Relative mean velocities with a moving frame at speed *C* (i.e., *U*-*C*). (c, d) The corresponding vorticity (unit: s^{-1}) of the mean flow. Note that (a, c) are at the beginning of the first splash-up (*t* = 0.07s, FOV3) and (b, d) demonstrate the developed first splash-up (*t* = 0.26s, FOV5). Multiple vortical structures can be observed in the aerated region, which are marked as red vectors in (a, b) and by solid lines in (c, d). The white arrows sketch the rotation direction. While only two clockwise rolling clouds (positive vorticity) are initially generated by the overturning jet and the first splash-up as shown in (a, c), a counterclockwise rolling cloud appears in between them after the splash-up developed as shown in (b, d).

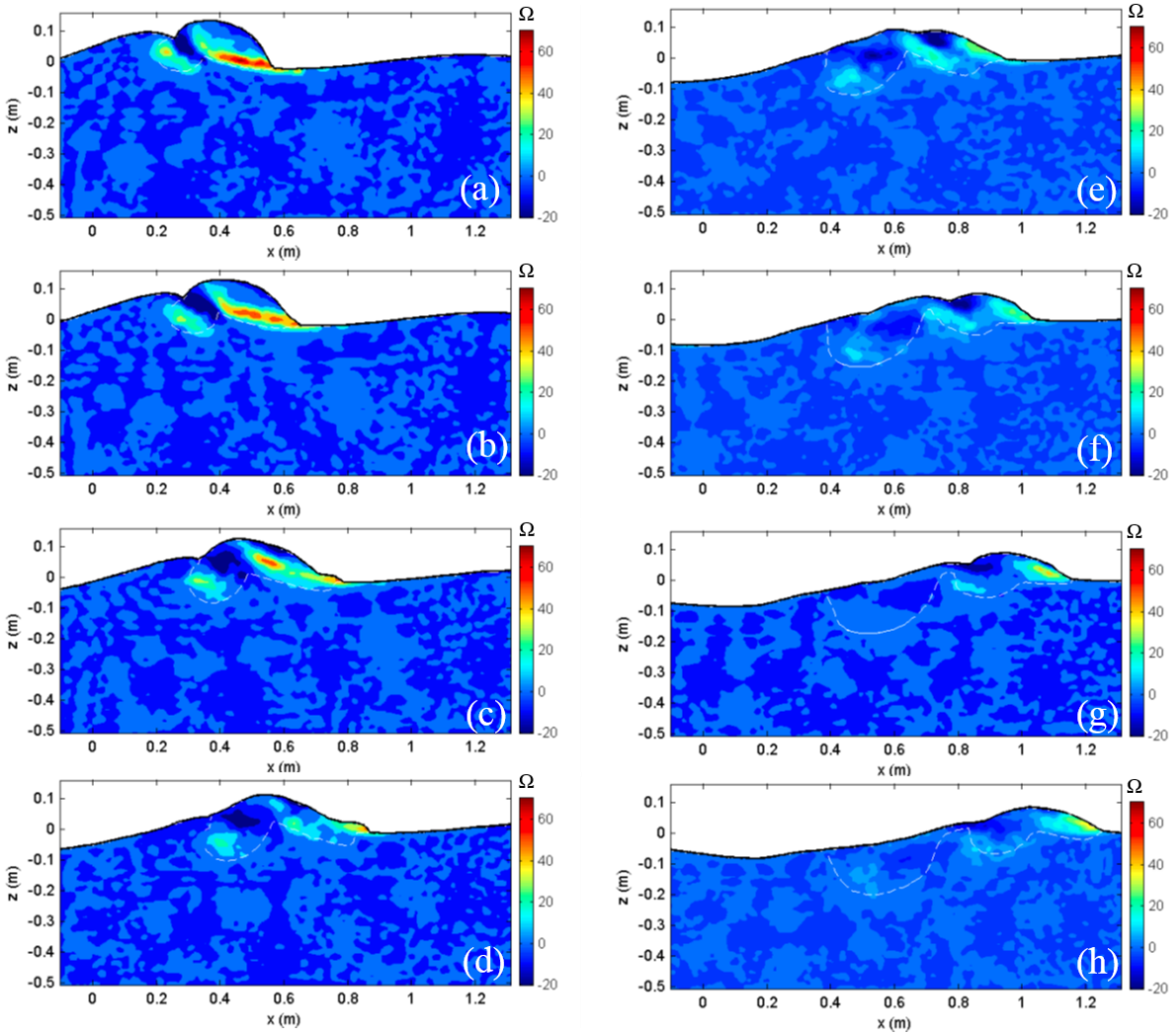

Fig. 2.8 Evolution of vorticity of the mean flow (unit: s^{-1}). The frames are at *t* = (a) 0.23 s, (b) 0.27 s, (c) 0.35 s, (d) 0.43 s, (e) 0.51 s, (f) 0.59 s, (g) 0.67 s, (h) 0.75 s. The white dash-lines are boundaries of the aerated region.

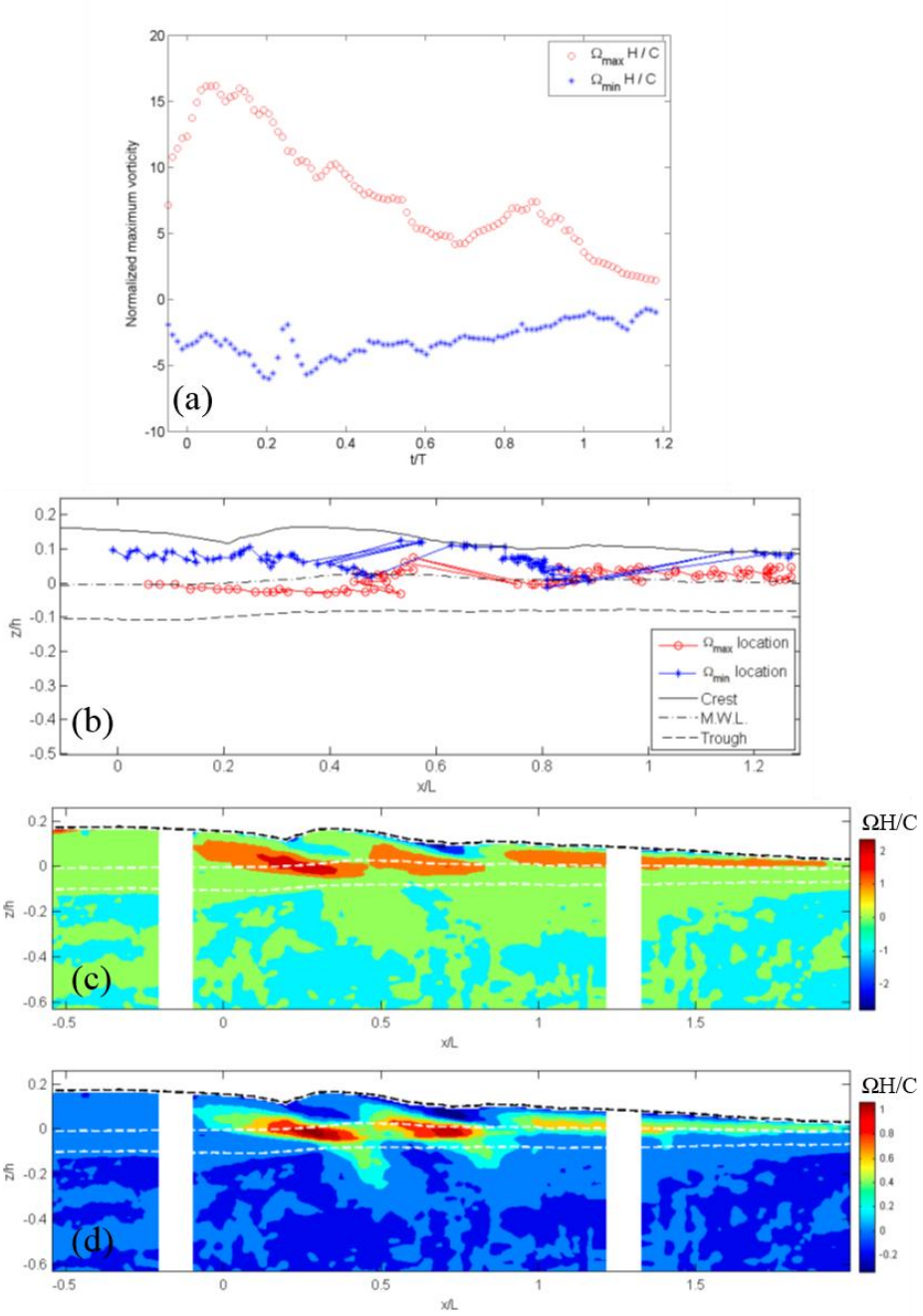

Fig. 2.9 (a) Temporal variation, and (b) spatial variation of normalized maximum vorticity (by *C/H*) over all FOVs, covering all three impingements and splash-ups during the wave breaking process. (c) Wave-averaged normalized vorticity; (d) period-averaged normalized vorticity.

2.3.3 Turbulent Intensity

As the mean velocities were obtained from ensemble average, the instantaneous horizontal and vertical fluctuating velocities, u' and w', are computed as:

$$u'(x,z,t) = u(x,z,t) - U(x,z,t) \tag{2.6}$$

$$w'(x,z,t) = w(x,z,t) - W(x,z,t) \tag{2.7}$$

Since the cross-tank velocity component was not measured, we define turbulent intensity I as:

$$I = \sqrt{\langle u'^2 \rangle + \langle w'^2 \rangle}, \quad I_x = \sqrt{\langle u'^2 \rangle}, \quad I_z = \sqrt{\langle w'^2 \rangle} \tag{2.8}$$

where $\langle\ \rangle$ denotes the ensemble-average operator. Fig. 2.10 shows the turbulent intensity in the rolling bubble clouds during the first splash-up of the plunging breaking wave. The fluctuating horizontal intensity I_x mainly occurs at the lower boundary of the aerated region where high shear stresses occur between the high-speed rotation in the roller region and the relative low-speed wave motion under the trough region as evidenced in Fig. 2.7a and 2.7c. On the contrary, the high fluctuating vertical intensity I_z occurs near the juncture of the impinging roller and the splash-up roller due to the vertical shear caused by the downward and upward motion of the rollers. Pseudo turbulence is unlikely to play a noticeable role here due to the relative large displacements in pixel (about 5 to 10 pixels) in the measurements, while the pseudo turbulence scale is no greater 0.25 pixels (Chang

and Liu, 2000).

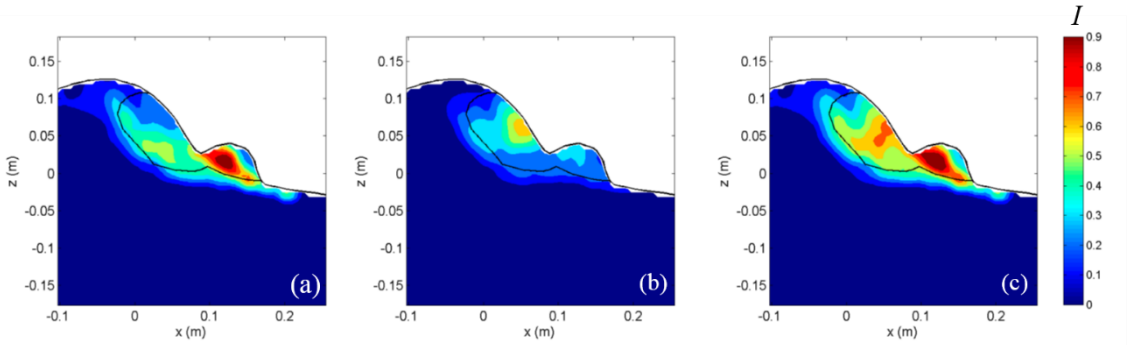

Fig. 2.10 Turbulent intensity (units: m/s) in the rolling bubble clouds during the first splash-up of plunging breaking wave (t = 0.07 s, FOV3). (a) I_x (b) I_z (c) I.

Fig. 2.11 shows the evolution of turbulent intensity within one wave period after wave breaking. Multiple concentrated structures of high turbulent intensity are found during the impingements and splash-ups. In the beginning of the breaking process (Fig. 2.11a-e), concentrated high values of I is only found near the front or lower boundary of the first impinging roller and the first splash-up roller, indicating that the plunging process occurs locally in the crest region and little turbulence is generated in the interior water region below the foamy breaking rollers. Subsequently, high I values are generated in the following second and third relatively small splash-ups (Fig. 2.11f-j). Turbulence continues to generate and diffuse, and the high I region elongates and eventually fills the entire wave crest in the wave breaking process. Coherent motion of the turbulent intensity induced by the wave breaking rollers is also moving downstream and penetrating into the interior flow region outside the rollers.

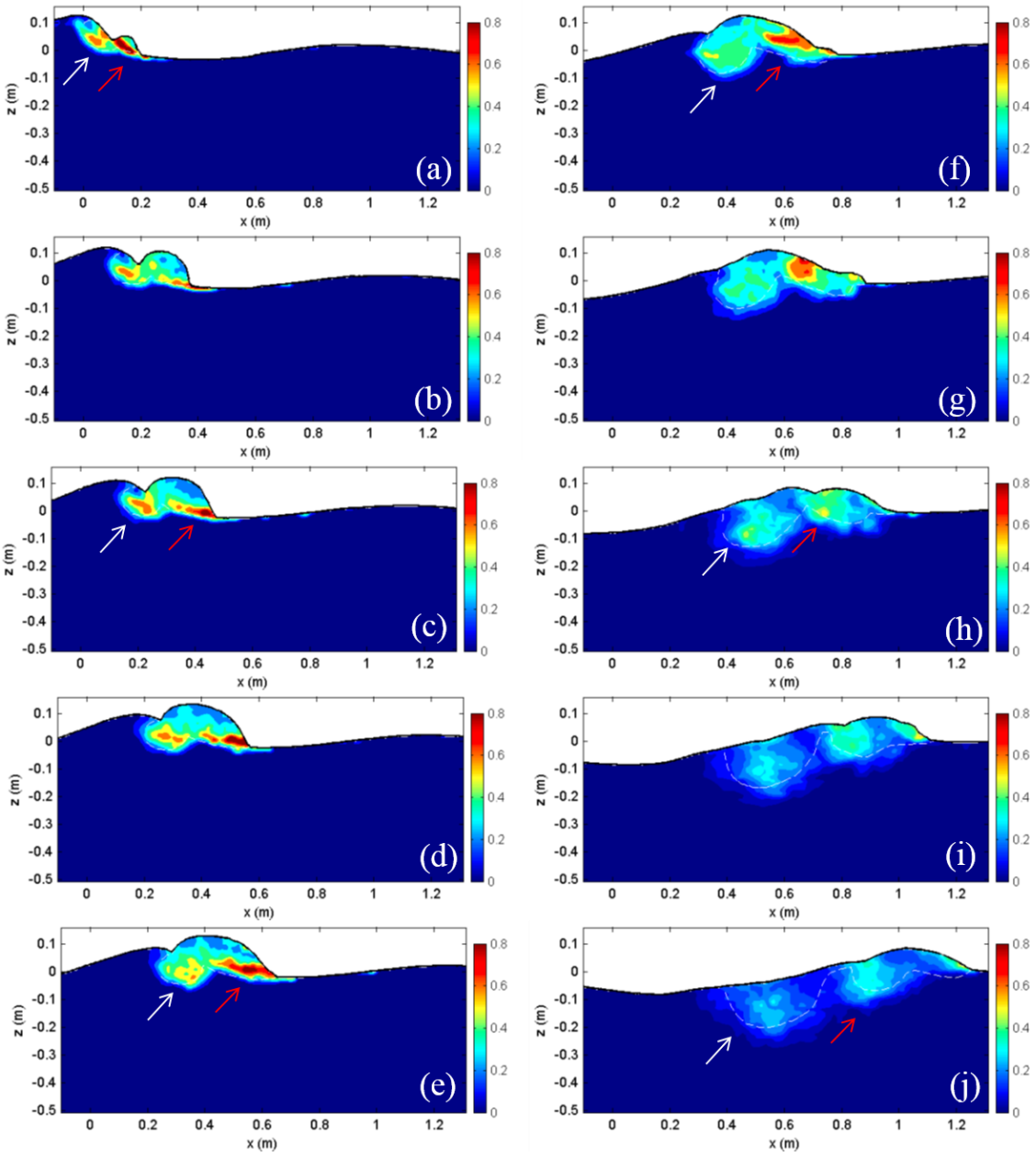

Fig. 2.11 Evolution of turbulence intensity in one wave period (units: m/s) at *t* = (a) 0.06 s, (b) 0.14 s, (c) 0.18 s, (d) 0.23 s, (e) 0.27 s, (f) 0.35 s, (g) 0.44 s, (h) 0.54 s, (i) 0.64 s, (j) 0.75 s. The white and red arrows mark the structures induced by the first impinging roller and the first splash-up roller, respectively.

Advection and diffusive transports are important mechanisms for the movement and spread of the structure to the trough level (Chang and Liu, 1999; Kimmoun and Branger, 2007; Drazen and Melville, 2009). The maximum turbulent intensity is approximately 0.3 to $0.4V_{max}$ over the entire breaking process in the plunging breaker with V_{max} being the maximum speed of the flow. The distribution of the turbulent intensity is similar to that of the vorticity field and the images of the rolling bubble clouds mentioned above, indicating these large eddies may play a significant role in turbulence generation.

2.4 Void Fraction of Breaking Waves

With the help from images recorded by the high speed camera, we are able to relate the FOR signals to the wave breaking process. The probe at the measurement point encounters several stages of the breaking process, including the first splash-up roller, the ascending crest region, the first backward impingement, and the first impinging roller. A voltage value of around 0.08 V indicates that the fiber sensor tip is in water, whereas a value around 1.0 V indicates that the tip is in air. However, the higher voltage signals that represent the gas phase do not always remain at 1.0 V because the fiber tip does not dry immediately. The signals fluctuate with a value higher than 0.08 V during the drying process. The voltage difference between the liquid phase and gas phase is highly distinguishable, even though the gas-phase signals fluctuate due to the rapid response of phase change when the probe is leaving water. A threshold value to separate the two phases and obtain void fraction was set close to the gas phase (0.11 V in the present study). The value is to account for the maximum noise level of the liquid-phase signals. The FOR technique has been validated in Chang et al. (2002; 2003) and Lim et al. (2008). The time-

series of mean void fraction, $\langle \alpha \rangle$, at each measurement point is computed by ensemble-averaging over 20 repeated runs:

$$\langle \alpha(x,z,t) \rangle = \frac{\sum_{i=1}^{N} \alpha_i(x,z,t)}{N} \tag{2.9}$$

where $\alpha_i(x,z,t)$ is the ith local instantaneous void fraction and $N = 20$ is the number of the total repeat runs in the experiment. To match the temporal resolution of the PIV velocity measurements, the original α_i measured at 100 kHz was running averaged with a size of 1000 points, resulting in an α_i of 100 Hz for computing the mean void fraction $\langle \alpha \rangle$.

Contours of $\langle \alpha \rangle$ at the three FOR stations are shown in Fig. 2.12. The contours are obtained with a temporal resolution of 0.01 s and a vertical spatial resolution of 10 mm. At t = 0.2 - 0.3 s, a very high and concentrated $\langle \alpha \rangle$ with a value up to 0.9 is observed in the first splash-up (i.e., the second clockwise rolling clouds in Fig. 2.5) as shown in Fig. 2.12a; the value of $\langle \alpha \rangle$ decreases rapidly below the trough level. It should be pointed out that the void fraction in the present deep water plunging breaking waves is significantly different from that in the surf zone breakers. Cox and Shin (2003) showed that the maximum ensemble averaged void fraction in surf zone breaking waves is 0.15 – 0.20. Furthermore, the maximum ensemble averaged void fraction at the still water level ($z = 0$) is about 0.94 in the present study which is more than 4 times greater than that

measured in the surf-zone plunging breakers reported by Hoque and Aoki (2005). The $\langle\alpha\rangle$ value drops to zero in the ascending crest region (the triangular zone around z = 0 mm at t = 0.3 s) between the first splash-up roller and the first impinging roller. Behind the highly aerated region of the first splash-up, there exist several smaller concentrated structures with $\langle\alpha\rangle$ varying between 0.3 and 0.5 in the crest region at t = 0.3 – 0.45 s. These structures correspond to the collapsed bubble cloud of the first impinging roller. This distribution of void fraction time history is similar to those found by Rojas and Loewen (2010) as well as Lamarre and Melville (1991) and Blenkinsopp and Chaplin (2007). The maximum void fraction, occurred approximately at the middle of the first splash-up roller ($z \sim 0.05$ and $t \sim 0.22$), is about 0.98 in the current study. This value agrees well with the value of 0.98 taken at an equivalent location reported in Blenkinsopp and Chaplin (2007) (in their figure 4c). Compared to the first splash-up, the overall $\langle\alpha\rangle$ value is lower in the second and third splash-ups as shown in Fig. 2.12b, c. However, the front of these splash-ups still maintains a very high $\langle\alpha\rangle$ value (up to 0.8) but the high $\langle\alpha\rangle$ region becomes significantly smaller. The region with very high and concentrated $\langle\alpha\rangle$ evolves during the sequence of the splash-ups. These results are similar to that observed by Blenkinsopp and Chaplin (2007). Note that the maximum $\langle\alpha\rangle$ measured by Rojas and Loewen (2010) is about 0.6, occurring in the third cloud, and the maximum $\langle\alpha\rangle$ in the second cloud is only 0.17, indicating $\langle\alpha\rangle$ is strongly temporal and spatial dependence in the unsteady breaking waves.

The vertical profiles of wave-averaged and period-averaged void fraction, $\langle \alpha \rangle_{wa}$ and $\langle \alpha \rangle_{pa}$ computed using Eq. 1 and Eq. 2, respectively, are shown in Fig. 2.13a, b. For the wave-averaged void fraction, the maximum values occur at the top of the wave crest, reaching 0.57, 0.49, and 0.32 at the first, second, and third splash-ups, respectively. The wave-averaged void fraction is about 0.37 at z/L = 0.03 at FOR station 1. This value is close to the time-averaged void fraction of 0.29 to 0.37 reported by Rojas and Loewen (2010) in their table 3 (the air cavity cases). The minor deviations may be caused by the different locations (x/L) the measurements were taken and time intervals used in the averaging process in the two experiments. The void fraction at the third splash-up decreases significantly when compared with that at the first two splash-ups. The maximum values of the period-averaged void fraction are also located near the top of the wave crest, equal to 0.18, 0.12, and 0.07 for the first, second, and third splash-ups. The ratio between the wave-averaged void fraction and period-averaged void fraction is about 4 to 1. The time series of the depth-averaged void fraction $\langle \alpha \rangle_{da}$ computed using Eq. 3 at each FOR station is plotted in Fig. 2.13c. The depth average was calculated from z = -0.20 m (i.e., z = -H) to the free surface rather than from z = -L/2. This is because the maximum penetration depth of the bubble clouds is only slightly greater than -0.20 m. The averaged void fraction essentially approaches zero at this depth for all the stations, as seen in Fig. 2.13a, b. The maximum depth-averaged void fraction occurs at t = 0.21 s at the first splash-up, t = 0.54 s near the toe of the second splash-up, and t = 0.78 s at the toe of the third splash-up with a magnitude of 0.38, 0.15, and 0.10, respectively.

The wave-averaged and period-averaged void fractions at each FOR station in Fig. 2.13a, b are normalized by its corresponding maximum void fraction and the maximum penetration depth of the bubble cloud, d_b, as shown in Fig. 2.14a, b. The maximum penetration depth in the plot is defined as the location of z in Fig. 2.13a, b where the averaged void fraction approaches zero. The results show that the normalized period-averaged void fraction exhibits a good similarity among the three impingements, indicating a possible similar behavior among the impingements of different intensities. Blenkinsopp and Chaplin (2007) found that the integral properties of void fraction have a remarkable similarity among different types of breaking waves when evolving over time. Fig. 2.14c shows the normalized depth-averaged void fraction; the void fraction at each station is normalized by its corresponding maximum value while measurements at station 2 and 3 are shifted to the left so the locations of the maxima are matched. The distributions of the depth-averaged void fractions are similar to each other and are similar to what Cox and Shin (2003) found. The distributions seem to increase rapidly and linearly and then decay slowly and exponentially. Following Cox and Shin (2003), the data were fitted with a linear-growth, exponential decay formula $\langle\alpha\rangle/\langle\alpha\rangle_{\max} = a(t/T-b)\exp[-c(t/T-b)]$ using the least squares method with the coefficients found as a = 25, b = 0.15, and c = 11. The coefficients found in the present study are quite different from those of the surf-zone spilling waves reported by Cox and Shin (2003).

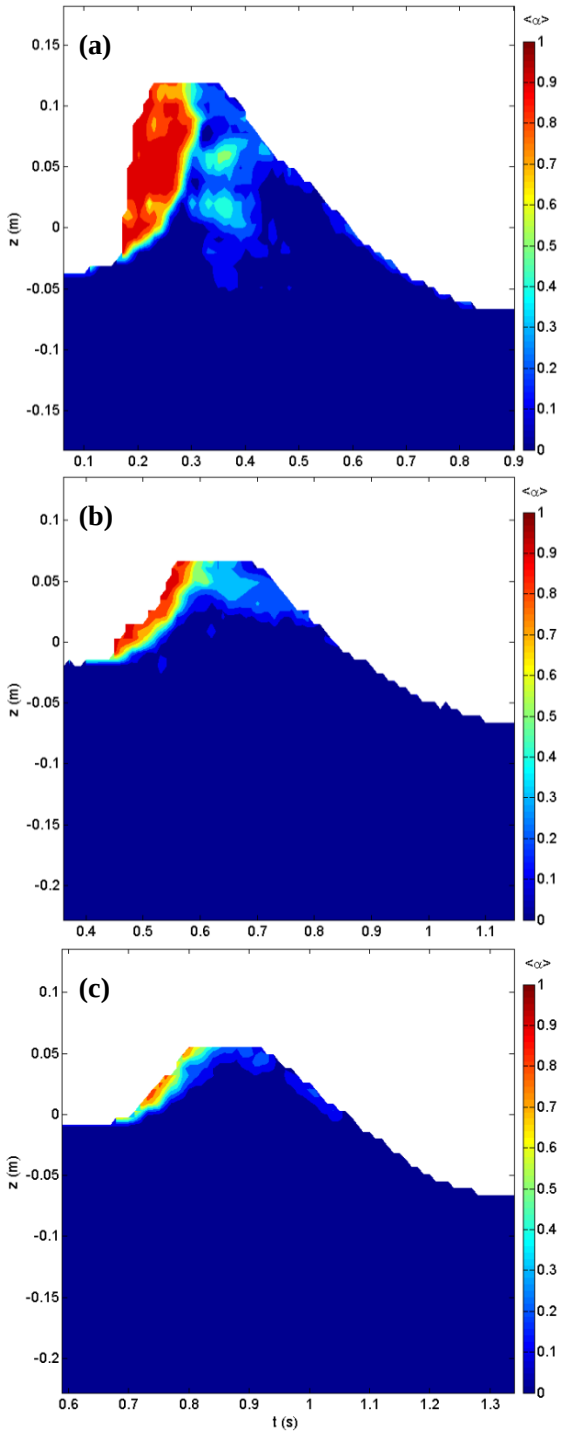

Fig. 2.12 Contours of the FOR measured void fraction <α> at (a) station 1 (first splash-up), (b) station 2 (second splash-up), and (c) station 3 (third splash-up).

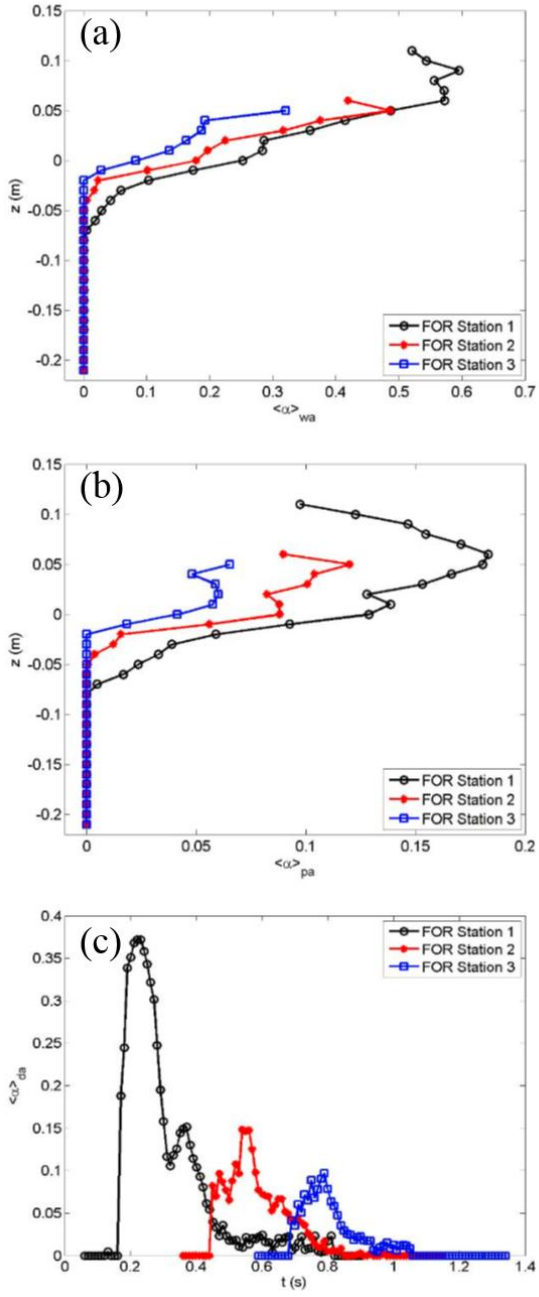

Fig. 2.13 (a) Vertical profiles of wave-averaged void fraction $\langle\alpha\rangle_{wa}$, (b) vertical profiles of period-averaged void fraction $\langle\alpha\rangle_{pa}$, and (c) time series of depth-averaged void fraction at the three FOR stations $\langle\alpha\rangle_{da}$.

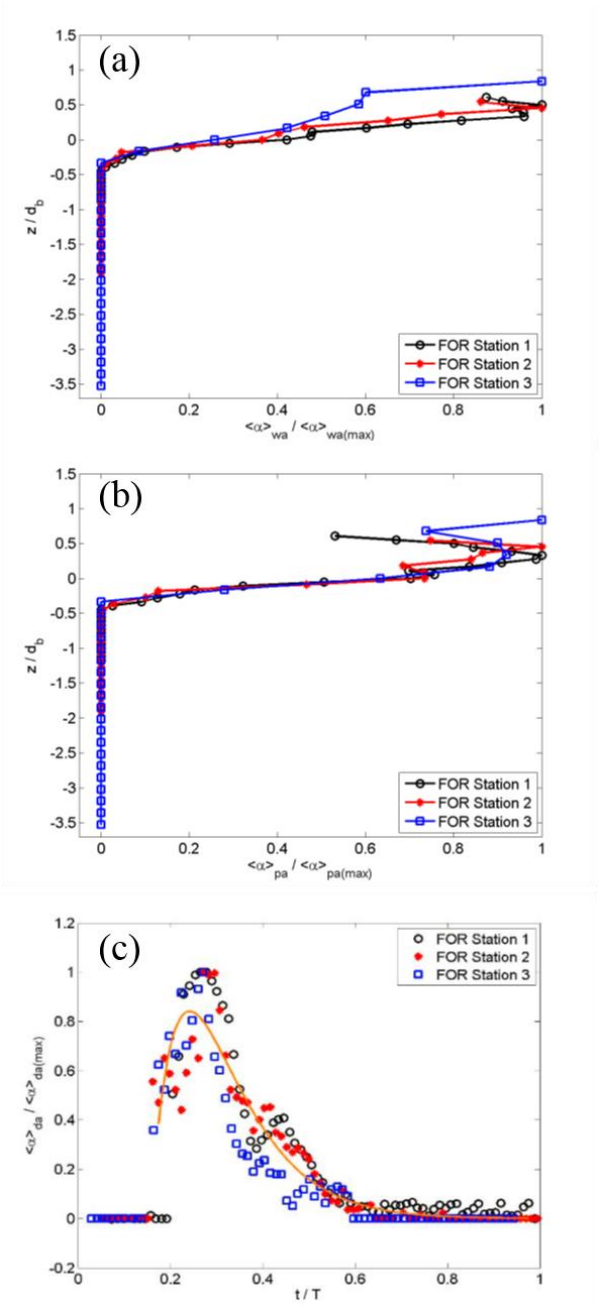

Fig. 2.14 (a) Normalized wave-averaged void fraction $\langle\alpha\rangle_{wa}$, (b) normalized period-averaged void fraction $\langle\alpha\rangle_{pa}$, and (c) normalized depth-averaged void fraction $\langle\alpha\rangle_{da}$. The solid line in (c) is the fitted curve.

The difference may be contributed from the distinct evolution process and intensity of void fraction between the deep-water plunging waves in the present study and the shallow water spilling waves in Cox and Shin's study. Note that Lamarre and Melville (1991) and Rojas and Loewen (2010) found that the decay of void fraction in deep water breakers may be modeled by a power law following $(t/T)^{-2.3}$ and $(t/T)^{-2.6}$, respectively. The decay rate in the present study is slower between $t/T = 0.3$ and 0.35 but otherwise similar if compared with these two power law profiles.

2.5 Effect of Void Fraction

2.5.1 Relation among Void fraction, Vorticity, and Turbulent Intensity

To better understand the violent two-phase turbulent plunging breaker, it may be useful to examine relations among void fraction and some other representations of the flow. Fig. 2.15a shows the temporal evolution of the ensemble-averaged void fraction at FOR station 1 (the first splash-up). The void fraction signatures reveal distinct evolving patterns of entrained bubbles under the plunging breaker. Based on the signatures as well as the high-speed video images, the breaking process that the FOR probe experienced at the first splash-up station can be divided into three stages as denoted in the figure: Stage 1 corresponds to the period when the FOR sensor encounters a high concentration of air bubbles generated by the first splash-up (t < 0.25 s) and the air cavity of the first impinging roller (0.25 s < t < 0.32 s). The value of $\langle \alpha \rangle$ in the first splash-up and in the air cavity of the impinging roller is very high, reaching an overall value of about 0.8 – 1.0. The ensemble-averaged void fraction fluctuates as the front of the first splash-up passes

through and exhibits a concentrated elliptical structure of high void fraction in the splash-up roller. The maximum void fraction is located at the center of the roller and decreases outward. The triangular-shaped ascending crest region beneath the roller shows very low void fraction.

Stage 2 covers the period when the FOR sensor experiences the collapsed bubble cloud of the impinging roller (0.32 s < t < 0.43 s). The maximum void fraction is about 0.3 – 0.5.

Stage 3 represents the wake region as the bubble cloud propagating away from the FOR sensor (0.43 s < t). The maximum void fraction is less than 0.2.

The foamy splashing and impinging rollers in stage 1 and stage 2 are considered as a strong turbulence source while stage 3 resembles a wake region since the turbulent flow underneath the backward face of the breaking rollers has been described as a turbulent wake (e.g., Svendsen, 1987). Fig. 2.15b, c shows the corresponding plots for root-squared vorticity of the mean flow $\left(\Omega^2\right)^{1/2}$ and turbulent intensity I, respectively. The patterns among the three plots are quite similar except in stage 2 where the high value of void fraction is closer to the free surface due to buoyancy.

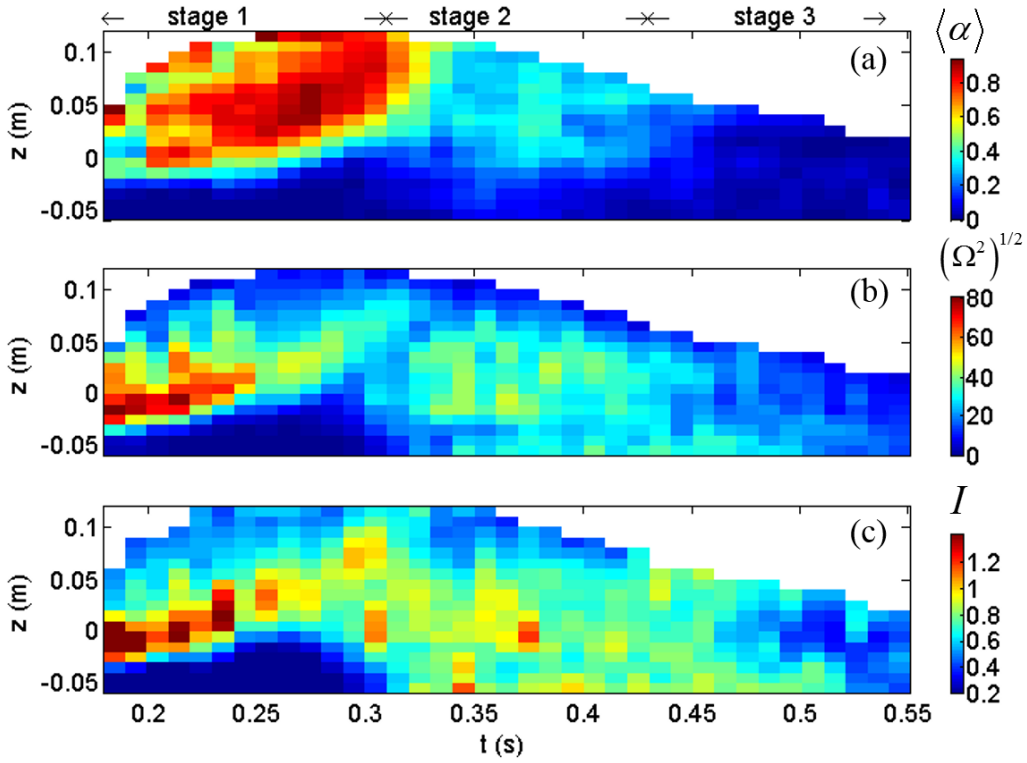

Fig. 2.15 Contour map of temporal evolution of (a) ensemble-averaged void fraction, (b) corresponding root-squared vorticity $(\Omega^2)^{1/2}$ (unit: s^{-1}), and (c) turbulent intensity *I* (units: m/s) at FOR station 1. Three stages are distinguished based on the signatures of the measured void fraction: Stage 1 corresponds to the period when the FOR sensor encounters high concentration air bubbles generated by the first splash-up (*t* < 0.25 s) and the air cavity of the first impinging roller (0.25 < *t* < 0.32 s). Stage 2 covers the period of the collapsed bubble cloud of the impinging roller (0.32 < *t* < 0.43 s). Stage 3 represents the wake region as the bubble cloud propagating away from the FOR sensor (0.43 < *t*).

The vertical profiles of time-averaged void fraction, root-squared vorticity, and turbulent intensity in stage 1 to stage 3 are shown in Fig. 2.16 to Fig. 2.18, respectively. Scatter plots of void fraction versus vorticity and turbulent intensity are shown as well. We can see that the profiles of vorticity and turbulent intensity both show depending trends with that of void fraction but the trends are quite different among the three stages, indicating the two-phase flow mixture under the breaking waves is an unsteady process and the three quantities are somewhat related.

In stage 1 featuring the violent foamy splashing, the vorticity and turbulent intensity in Fig. 2.16a-c are both positively correlated with void fraction. We can see that void fraction increases from zero upward to about 0.7 – 0.8 from the undisturbed flow region (z < -0.03 m) to the center of the bubble cloud of splashing (z ~ 0.05-0.06 m), whereas similar increasing trends are also observed in the vertical profiles of the vorticity and turbulent intensity. In particular, clear evidences of the positive correlations between void fraction and vorticity and between void fraction and turbulent intensity can be seen in the scatter plots in Fig. 2.16d, e. In the relatively low void fraction region (void fraction ~ 0 to 0.6), vorticity and turbulent intensity significantly increases from zero to a maximum value of about 50 s^{-1} and 1 ms^{-1}, respectively, against void fraction, indicating that turbulent properties are strongly correlated by void fraction in the relatively low void fraction region. After void fraction reaches the maximum at z = 0.04 m, void fraction only varies in a narrow range. Even though vorticity and turbulent intensity reach maximum values at about the same elevation, their values, unlike the nearly constant void fraction, decrease. The profiles of vorticity and turbulence intensity are indeed very similar.

In stages 2 and 3, the profiles of void fraction, vorticity, and turbulent intensity in Fig. 2.17 and Fig. 2.18 all exhibit minor variations along the water column from the trough level to the free surface. The magnitude of turbulent intensity in the collapsed impinging roller (Fig. 2.17c) is comparable to that in the splashing roller (Fig. 2.16c) even though void fraction in the collapsed impinging roller is much lower than that in the splashing roller. This implies that the passing air bubbles may inject and transfer energy into the flow which in turn causes the residue turbulence to remain energetic and the flow to maintain a similar level of fluctuations. In stages 2 and 3 the void fraction level is higher near the free surface but not the magnitude of vorticity and turbulence intensity. The bubbles seem to be less effective in energizing the flow when near the free surface, evidenced in all the three stages. Lin et al. (2012) reported that the integral length scale of a similar violent two-phase flow decreases significantly near the free surface in the entire roller region of a steady breaker generated by a hydraulic jump in a constant-depth channel. Although reason is unclear, the results imply that bubble fluctuations weaken as they move closer to the free surface. The bubbles are thus less effective on energizing the flow turbulence near the free surface.

Deane and Stokes (2002) suggested that the following two mechanisms are sources of air entrainment in plunging waves: firstly, smaller bubbles less than 1-2 mm in diameter are formed by the impact and subsequent splashing of the overturning jet and in the shear layer between the jet and the water in the trough region in front of the breaking wave; secondly, larger bubbles with a diameter greater than 2 mm are formed by the fragmentation of the air “tube” or “vortex” trapped between the overturning jet and the

wave front face as the wave breaks. Our preliminary analysis of chord length of air bubbles, calculated based on the resident time of each air bubble encounter multiplied by the corresponding mean velocity, shows that the chord length of 65% entrained bubbles in the first splash-up roller is less than 2 mm. The result implies that there exists a large portion of small bubbles during the most violent phase of wave breaking (i.e., stage 1 in Fig. 2.16) and these small bubbles are generated by the strong impingement and subsequent splashing on the water surface. This means that the first mechanism reported by Deane and Stokes (2002) is likely the main mechanism for the creation of the small bubbles in the splashing roller. However, the other 35% of larger bubbles may still inject energy to the flow and thus enhance turbulence.

The positive correlation between void fraction and turbulent intensity in Fig. 2.16 is also similar to the previous finding by Lance and Bataille (1991). They reported that turbulent kinetic energy increases strongly with the increase of void fraction, although the maximum void fraction is less than 0.03 in their study. According to Deane and Stokes (2002) the coincidence of high void fraction with high turbulence in the breaking waves may not indicate the turbulent properties are strongly enhanced by void fraction. The question whether a high concentration of bubbles will enhance the turbulence is somewhat inconclusive.

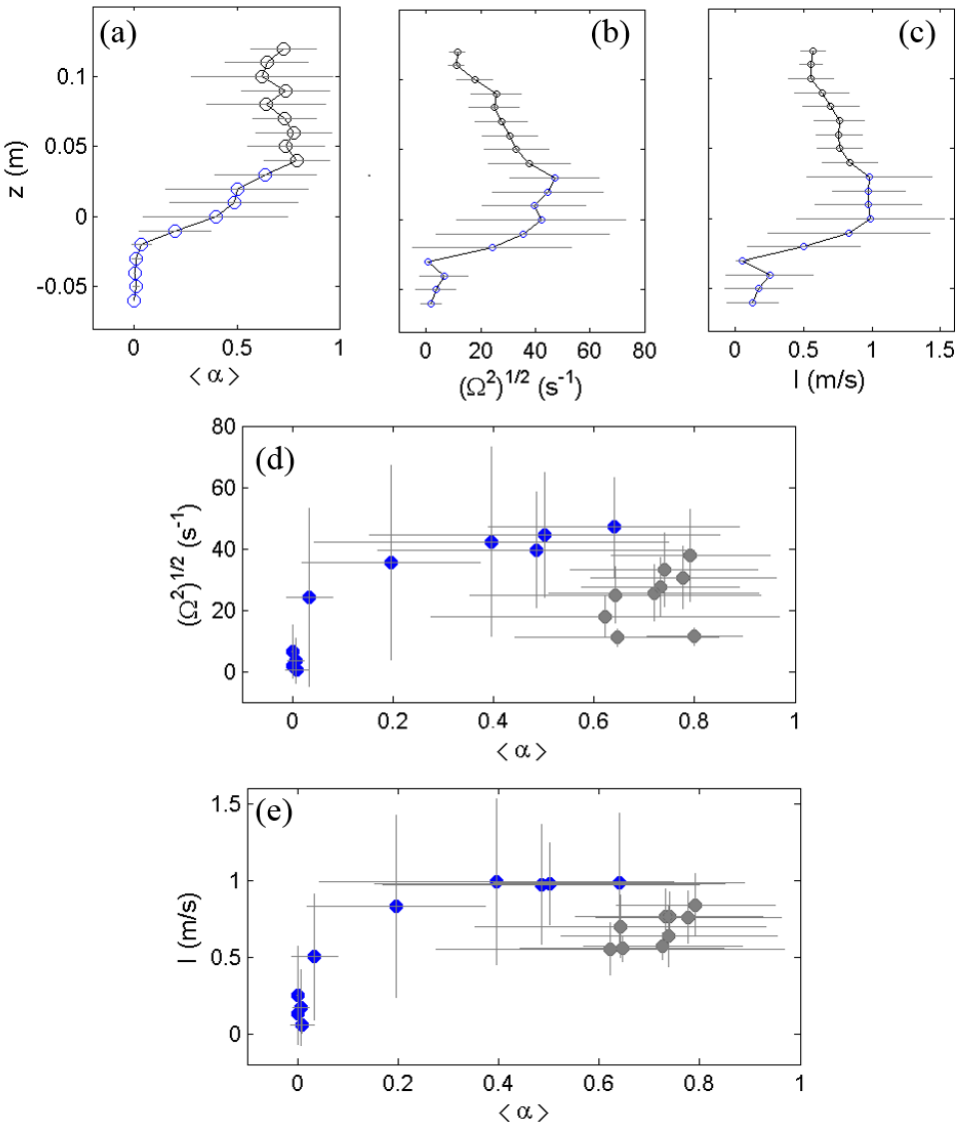

Fig. 2.16 Mean void fraction $\langle\alpha\rangle$, root-squared vorticity of mean flow $\left(\Omega^2\right)^{1/2}$, and turbulent intensity *I* in the foamy splashing roller (stage 1 in Fig. 2.15). (a-c) Vertical profiles of wet average over stage 1 for $\langle\alpha\rangle$, $\left(\Omega^2\right)^{1/2}$, and *I*. (d-e) Scatter plots of $\langle\alpha\rangle$ against $\left(\Omega^2\right)^{1/2}$ and *I*. The horizontal and vertical gray lines are standard deviations of the wet-averaged quantities.

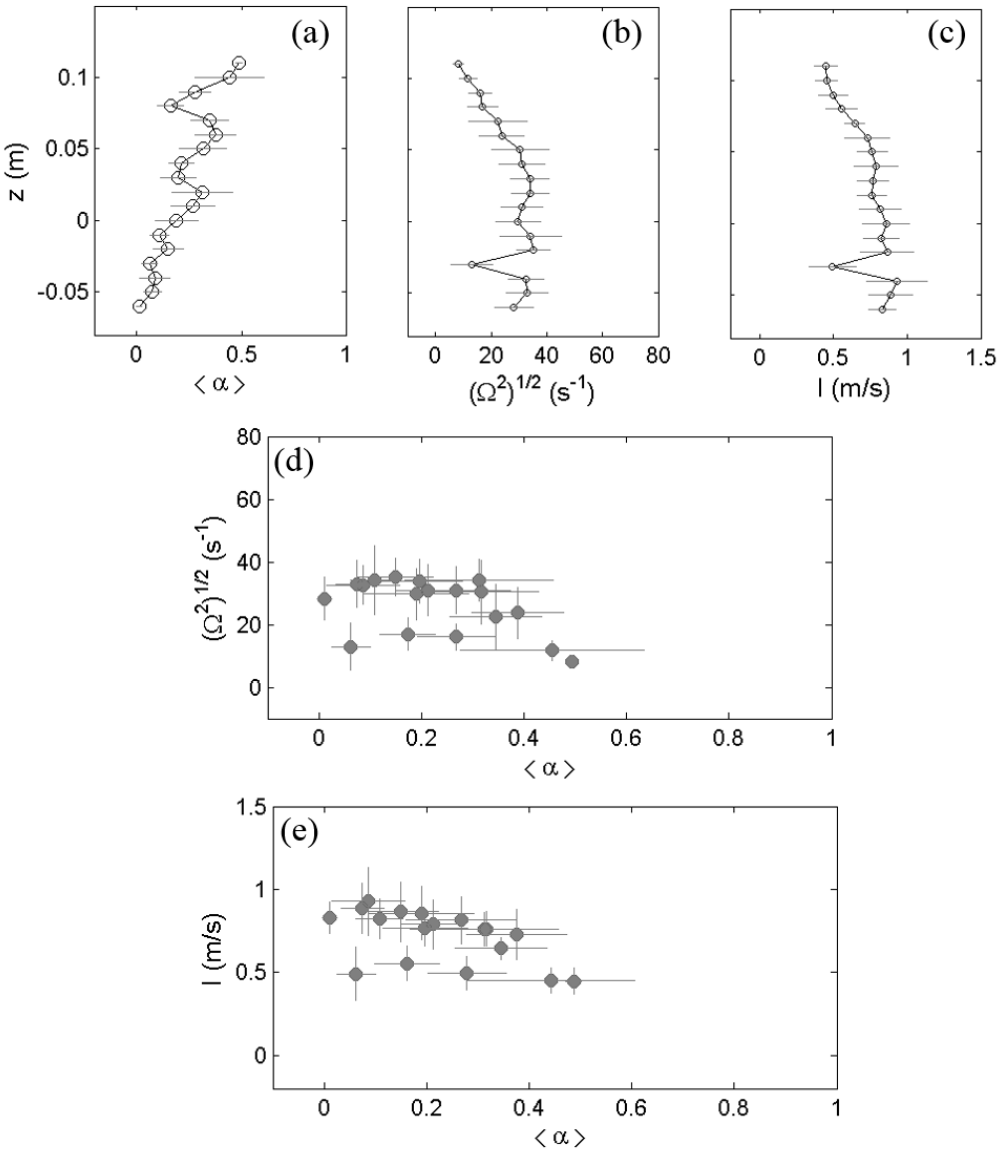

Fig. 2.17 Mean void fraction $\langle \alpha \rangle$, root-squared vorticity of mean flow $\left(\Omega^2\right)^{1/2}$, and turbulent intensity *I* in the collapsed bubbles of impinging roller (stage 2 in Fig. 2.15) corresponding to Fig. 2.16.

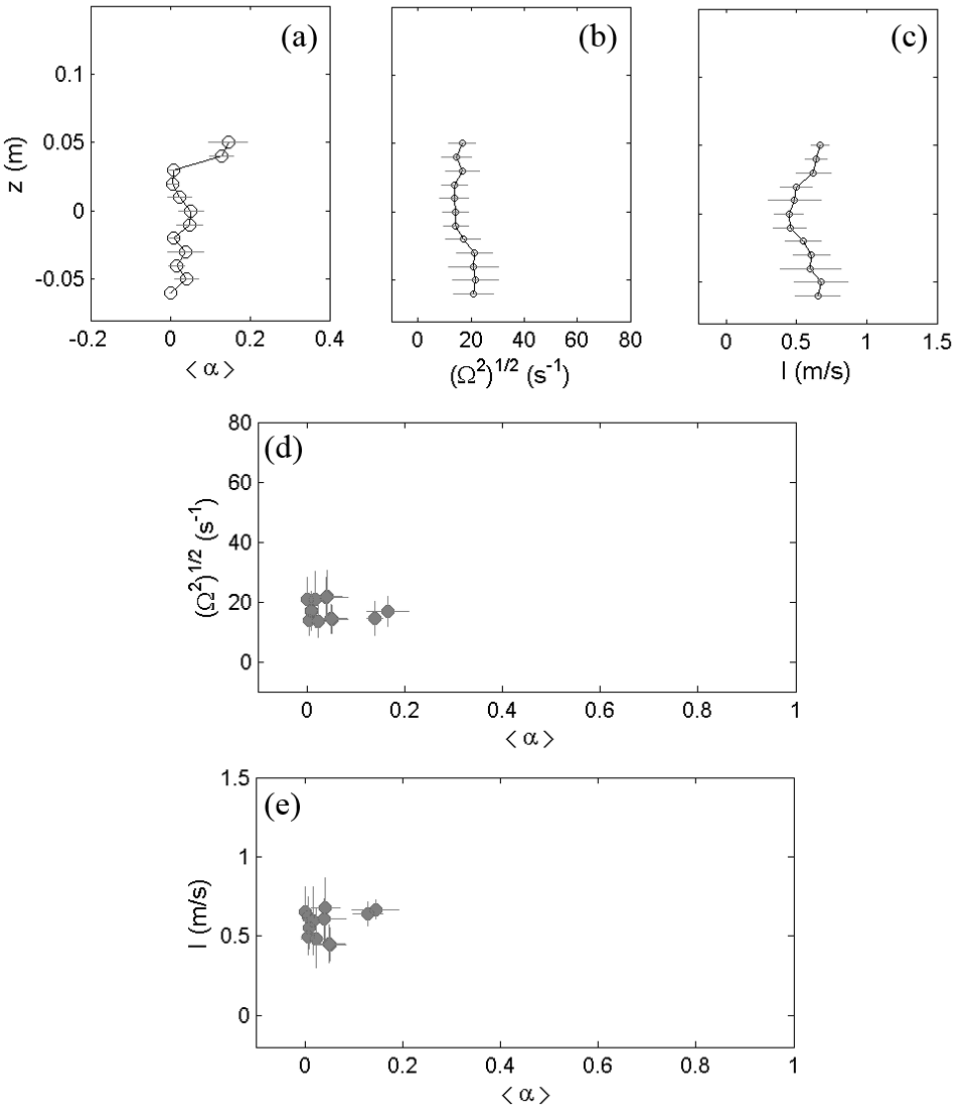

Fig. 2.18 Mean void fraction $\langle \alpha \rangle$, root-squared vorticity of mean flow $\left(\Omega^2\right)^{1/2}$, and turbulent intensity *I* in the wake region (stage 3 in Fig. 2.15) corresponding to Fig. 2.16.

2.5.2 Density Variation and Wave Energy

The density variation in the plunging breaker was considered based on the void fraction measurements. The mass, momentum, mean kinetic energy, turbulent kinetic energy, and potential energy over one wave period at each FOR measurement station were calculated based on the void fraction, free surface, and velocity measurements. In addition, energy dissipation was also calculated by accounting for the density variation. In a two-phase turbulent flow, the mean gas-liquid mixture density can be written as follows:

$$\rho_m = \rho_a \langle \alpha \rangle + \rho_w \left(1 - \langle \alpha \rangle\right) \approx \rho_w \left(1 - \langle \alpha \rangle\right) \tag{2.10}$$

where the subscripts *a*, *w*, and *m* represent air, water, and air-water mixture, respectively, and α is the local void fraction.

By considering the mixture density ρ_m, the net mass ($M_{x(\alpha)}$ and M_x), and momentum ($S_{xx(\alpha)}$ and S_{xx}) per unit width in the *y* direction passing each cross section (at the three FOR stations) over one wave period with and without considering the void fraction can be written as follows:

$$\begin{aligned} M_x &= \rho_w \int_{-h}^{\eta(x)} U_{pa}(x,z)dz \\ M_{x(\alpha)} &= \frac{\int_{-h}^{\eta(x)} \int_{t_{tr}(x)}^{t_{tr}(x)+T} \rho_m(x,z,t) U(x,z,t) dt dz}{\int_{t_{tr}(x)}^{t_{tr}(x)+T} dt} \end{aligned} \tag{2.11}$$

$$S_{xx} = \rho_w \int_{-h}^{\eta(x)} U_{pa}{}^2(x,z)dz$$
$$S_{xx(\alpha)} = \frac{\int_{-h}^{\eta(x)} \int_{t_{tr}(x)}^{t_{tr}(x)+T} \rho_m(x,z,t) U^2(x,z,t) dt dz}{\int_{t_{tr}(x)}^{t_{tr}(x)+T} dt} \tag{2.12}$$

where the subscript α indicates void fraction being included. Similarly, the period-averaged (K_{pa} and k_{pa}), depth-integrated (K_{di} and k_{di}), and depth-averaged (K_{da} and k_{da}) mean kinetic energy and turbulent kinetic energy can be written as follows:

$$K_{pa}(x,z) = \frac{\int_{t_{tr}(x)}^{t_{tr}(x)+T} \delta(x,z,t)\left(1-\langle\alpha\rangle\right) K(x,z,t) dt}{\int_{t_{tr}(x)}^{t_{tr}(x)+T} dt}$$
$$k_{pa}(x,z) = \frac{\int_{t_{tr}(x)}^{t_{tr}(x)+T} \delta(x,z,t)\left(1-\langle\alpha\rangle\right) k(x,z,t) dt}{\int_{t_{tr}(x)}^{t_{tr}(x)+T} dt} \tag{2.13}$$

$$K_{di}(x) = \int_{-h}^{\eta(x)} K_{pa}(x,z)dz$$
$$k_{di}(x) = \int_{-h}^{\eta(x)} k_{pa}(x,z)dz \tag{2.14}$$

$$K_{da}(x) = \frac{K_{di}(x)}{\int_{-L/2}^{\eta(x)} dz}$$
$$k_{da}(x) = \frac{k_{di}(x)}{\int_{-L/2}^{\eta(x)} dz} \tag{2.15}$$

where K and k in the integral are the mean and turbulent kinetic energy per unit water mass,

respectively, and the subscripts di and da represent the depth-integrated and the depth-averaged quantities, respectively. Note that K was obtained from the mean horizontal velocity (U) and mean vertical velocity (W) with a presumption that the mean cross-tank velocity (V) is zero, i.e.

$$K = \frac{1}{2}\left(U^2 + W^2\right) \tag{2.16}$$

Similarly, the turbulent kinetic energy was approximated as:

$$k = \frac{1.33}{2}\left(\left\langle u'^2 \right\rangle + \left\langle w'^2 \right\rangle\right) = \frac{1.33}{2} I^2 \tag{2.17}$$

where the constant 1.33 accounts for the missing y-direction velocity (e.g., Chang and Liu, 1999). The factor of 1.33, suggested by Svendsen (1987) and used in many wave breaking studies, has been verified for progressive plunging surf-zone breaking waves (Christensen, 2006).

Fig. 2.19 shows contours of the mean horizontal momentum per unit water mass, $\left(1-\langle\alpha\rangle\right)U$, at each FOR station with and without considering the density variation caused by bubbles. As shown in Fig. 2.19a-1, high values of U occur at the front of the splash-up roller (second clockwise roller). However, when multiplied by $\left(1-\langle\alpha\rangle\right)$, the high values of $\left(1-\langle\alpha\rangle\right)U$ shift to the impinging roller (first clockwise roller) rather than the splash-up roller as shown in Fig. 2.19b-1. This means that the mean momentum at the splash-up will be significantly overestimated if void fraction is not considered. The same

conclusion also applies to the second and third splash-ups, as shown in the remaining panels in Fig. 2.19. Likewise, Fig. 2.20 shows the mean kinetic energy per unit water mass $\left(1-\langle\alpha\rangle\right)K$, at each FOR station with and without considering the void fraction. As expected, similar patterns are observed between the mean horizontal momentum and mean kinetic energy. Again, the results indicate that the mean momentum and mean kinetic energy at the splash-ups will be significantly overestimated if the fluid density is assumed constant without accounting for the void fraction caused density variation.

Fig. 2.21a shows a comparison of the net mass flux (per unit width in *y*) integrated over one wave period (i.e., the net mass transport) with and without considering the void fraction (i.e., $M_{x(\alpha)}$ and M_x in Eq. 2.11). The net mass, without accounting for void fraction, was obtained based on the 475 velocity columns in the PIV measurements. For mass flux accounting for density variation, the three FOR stations at $x/L > 0$ provide the needed void fraction information, whereas a fourth addition station at $x/L < -0.41$ was also added (in front of the breaking point so $\langle\alpha\rangle = 0$) as a reference. As seen in Fig. 2.21a, there exists a huge discrepancy between the mass fluxes at FOR station 1 (at the first splash-up); the discrepancy reduces significantly at the second and third splash-ups at FOR stations 2 and 3. When considering the void fraction, the net mass flux at the first, second, and third splash-ups decreases by about 70%, 50%, and 170%, respectively. If compared with the positive net mass flux at $x/L = -0.41$ before wave breaking, the net mass flux drops from close to the pre-breaking level at the first splash-up to nearly zero at the third splash-up at x/L slightly greater than unity. The results are consistent with the setup of the mean water level as shown in Fig. 2.3a (the mean water level increases between $x = 0.3$ m and $x =$

0.7m). A comparison of the net momentum flux integrated over one wave period (i.e., $S_{xx(\alpha)}$ and S_{xx} in Eq. 12) is shown in Fig. 2.3b. Similarly, the net momentum flux decreases by about 60%, 22%, and 22% at FOR stations 1 to 3, respectively, when void fraction is accounted for. When compared with the pre-breaking momentum flux at x/L = -0.41, the net flux increases about 51% at the first FOR station. After that, the flux continues to decrease, dropping to 11% and 45% below the pre-breaking level at FOR stations 2 and 3, respectively.

Fig. 2.21c shows the comparison of period averaged and depth integrated mean kinetic energy (K_{da}) and turbulent kinetic energy (k_{da}) computed using Eq. 2.15 and normalized by C^2. When considering the void fraction, the mean kinetic energy at the first splash-up drops 55%; it also drops 19% and 14% at the second and third splash-ups, respectively. When compared with the mean kinetic energy at the pre-breaking level at x/L = -0.41, the mean kinetic energy at the three FOR stations reduces about 6%, 42%, and 55%, respectively. This is a huge difference to that the mean kinetic energy increases more than twice at FOR station 1 if the void fraction is not accounted for. For turbulent kinetic energy, the value reduces about 31%, 11% and 24% at FOR stations 1, 2, and 3, respectively, when void fraction is considered. The differences are not as pronounced as that in the mean kinetic energy comparison.

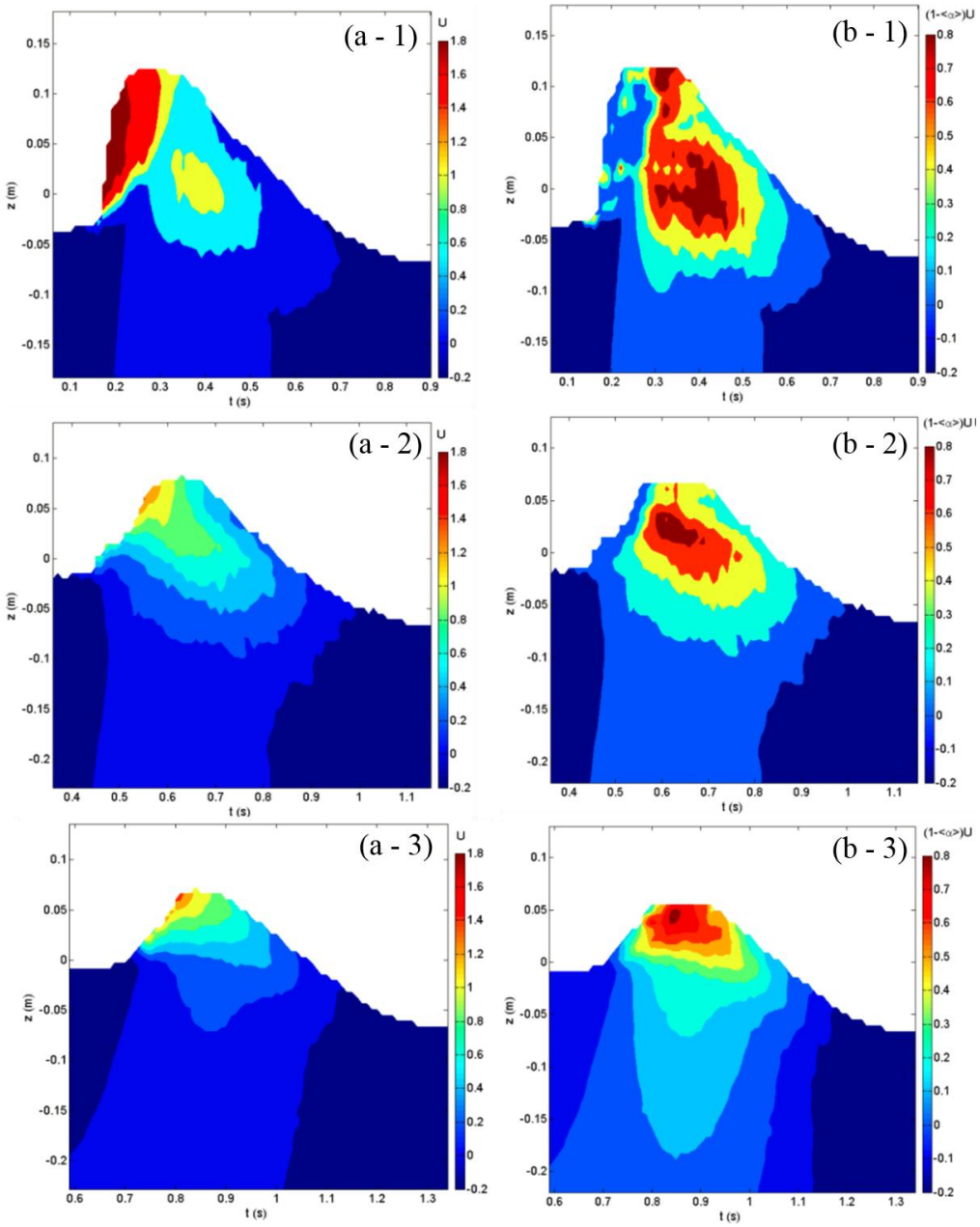

Fig. 2.19 Contours of mean horizontal momentum per unit water mass (units: m/s) at the three FOR stations: (a1) *U* at station 1, (b1) $\left(1-\langle\alpha\rangle\right)U$ at station 1, (a2) *U* at station 2, (b2) $\left(1-\langle\alpha\rangle\right)U$ at station 2, (a3) *U* at station 3, (b3) $\left(1-\langle\alpha\rangle\right)U$ at station 3.

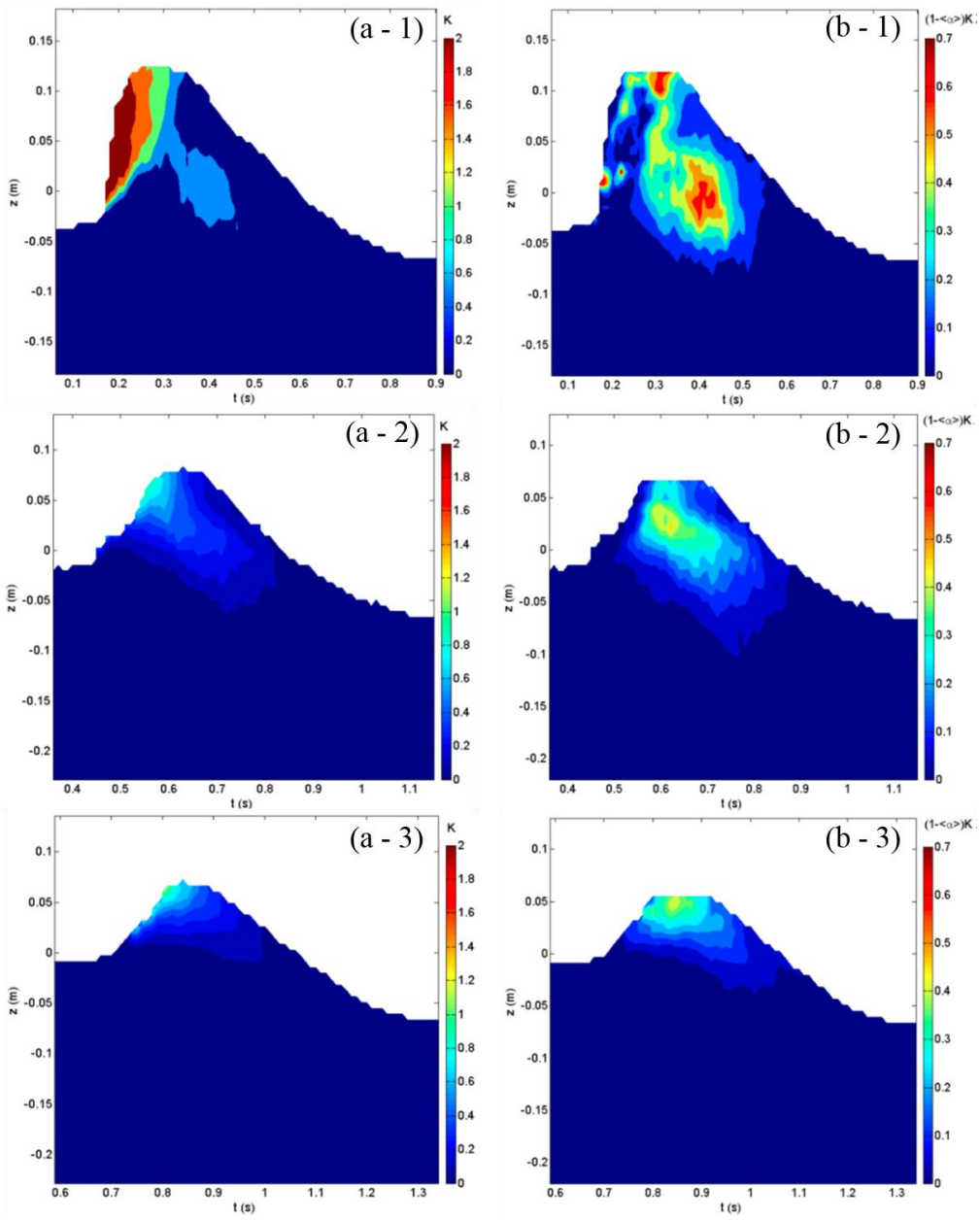

Fig. 2.20 Contours of mean kinetic energy per unit water mass (units: m^2/s^2) at the three FOR stations: (a1) *K* at station 1, (b1) $\left(1-\langle\alpha\rangle\right)K$ at station 1, (a2) *K* at station 2, (b2) $\left(1-\langle\alpha\rangle\right)K$ at station 2, (a3) *K* at station 3, (b3) $\left(1-\langle\alpha\rangle\right)K$ at station 3.

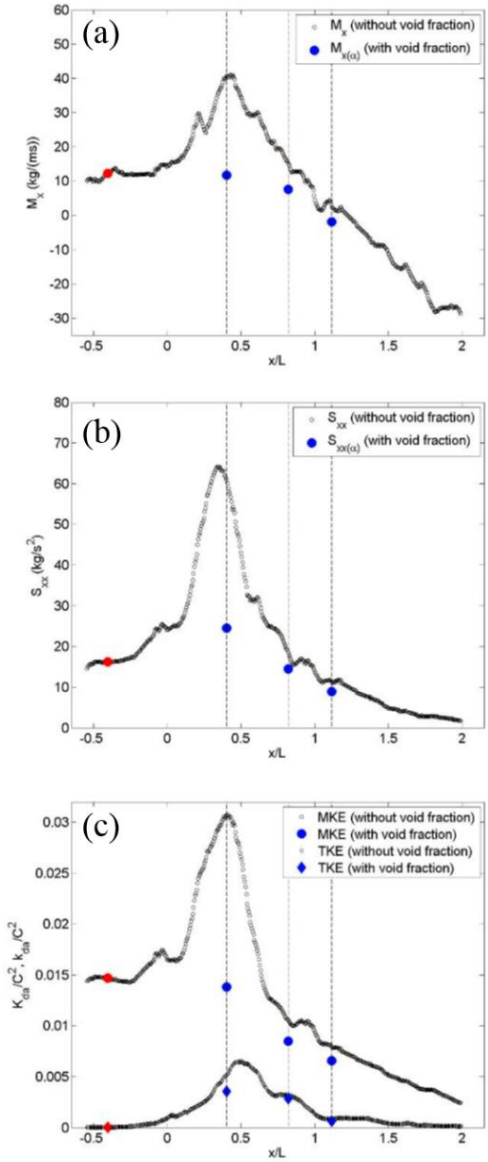

Fig. 2.21 (a) Mass (M_x), (b) momentum (S_{xx}), and (c) normalized (by C^2) mean kinetic energy (K_{da}) and turbulent kinetic energy (k_{da}) with and without considering void fraction. Open circles, without considering void fraction; filled circles and diamonds, considering void fraction. The three vertical dashed lines represent the three FOR stations. The filled red circles and diamonds at x/L = -0.41 represent the reference magnitude with $\langle \alpha \rangle = 0$ prior to breaking.

According to Fig. 2.21c with the void fraction being considered, the ratio for k_{da}/K_{da} is about 1/4 during the first impingement and splash-up process at FOR station 1. The value of k varies only slightly during the second impingement and splash-up process at FOR station 2. It is then followed by a significant reduction at FOR station 3. The normalized turbulent kinetic energy, as expected, is close to zero (4.1×10^{-5}) at x/L = -0.41 before breaking. The magnitude increases during the first impinging and splash-up process to 3.6×10^{-3} at FOR station 1 (x/L = 0.4). The magnitude then drops about 20% and 83% at FOR stations 2 and 3, respectively. The ratios of k_{da}/K_{da} at the four stations, starting from the pre-breaking location, without considering void fraction (i.e., assuming $\langle\alpha\rangle = 0$) are approximately 0.3%, 17%, 31%, and 10% when the void fraction is not considered. When void fraction is accounted for, the ratios become 0.3%, 26%, 34%, and 9%. Interestingly, even though the magnitude of k_{da} and K_{da} would be significantly overestimated (by more than 100% for K_{da}) at FOR station 1 during the first impinging and splash-up process if void fraction is not accounted for, these two sets of ratios are not too different.

Fig. 2.22a shows the variation of the depth integrated total kinetic energy, (k_{di}+ K_{di}), with and without considering void fraction (Eq. 14). Discrepancies in total kinetic energy are about 52%, 17%, and 15% at FOR stations 1 to 3, respectively, with and without considering the void fraction. Compared with the total kinetic energy at pre-breaking at x/L = -0.41, the total kinetic energy increases 18% due to the significant increase of the turbulent kinetic energy during the first impingement and splash-up process, although the mean kinetic energy decreases slightly (Fig. 2.21c). The total kinetic energy at the second

and third FOR stations reduces by 23% and 49%, respectively, when compared with that at x/L = -0.41. Based on the figure, about 85% of the total kinetic energy is dissipated at x/L = 2 without considering void fraction – a reasonable estimate since the effect of void fraction continues to reduce due to the decrease of void fraction downstream. Similarly, the mean kinetic energy is also reduced by approximately 85% at x/L = 2 (Fig. 2.21c).

Fig. 2.22b shows the variation of the depth integrated potential energy with and without considering void fraction. The potential energy using the free surface elevation determined from the images (PE), wave gauges (PE), and FOR (PE_α), was computed as follows.

$$PE = \int_{-h}^{\eta} gzdz - \frac{1}{2}gh^2$$
$$PE_\alpha = \int_{-h}^{\eta} (1-\alpha)gzdz - \frac{1}{2}gh^2 \qquad (2.18)$$

The measured free surface elevation from the images results in an overestimated potential energy while the free surface elevation from the wave gauges causes an underestimated potential energy due to the existence of the aerated region. Discrepancies in potential energy are about 39%, 28%, and 19% at FOR stations 1 to 3, respectively, with (FOR) and without (image) considering the void fraction. Compared with the pre-breaking potential energy at x/L = -0.41, the potential energy at the three FOR stations decreases about 33%, 65% and 67%. Furthermore, it is estimated that about 86% of the potential energy is reduced at x/L= 2, similar to the reduction of the total kinetic energy in Fig. 2.22a.

Finally, the variation of total energy (and therefore dissipation) accounting for the fluid density variation is plotted in Fig. 2.22c. Compared with the total energy at pre-breaking at x/L = -0.41, approximately 54% and 85% of the total energy are dissipated at x/L = 1 and x/L = 2, respectively. The data indicate that the total energy decreases relatively slowly before x/L = 0.33, then decreases rapidly beyond that point, roughly following the inverse trend with respect to the distance, i.e., $E \propto 1/x$. This is in consistence with $E \propto 1/t$ reported by other researchers (Rapp and Melville, 1990; Melville et al., 2002; Drazen and Melville, 2009). The inverse-decay trend also occurs in the total kinetic energy, after a moderate increase (about 20%) at the first impingement and splash-up process at FOR station 1. However, the potential energy seems to decay linearly with respect to the distance x. Based on the data, the total energy may be formulated as

$$\frac{E_\alpha}{E_L} = 1.47e^{-1.17x/L} \qquad \text{for} \quad \frac{x}{L} > 0.33 \tag{2.19}$$

where E_α is the breaking wave energy with void fraction considered and E_L is the pre-breaking wave energy. For $x/L \le 0.33$, E_α/E_L=1.0 is assumed. The data fit better using the exponential decay than the inverse decay with respect to x.

Results in Fig. 2.22c were calculated as depth integrated and period averaged wave energy per unit mass (units: m^3/s^2) using Eq. 2.14. To calculate the total energy loss per unit width (units: J/m), they need to be multiplied by $\rho_w C_g T$ so they are comparable to the loss calculated applying Eq. 2.20 below. Based on the figure, the energy loss ratio from the pre-breaking point at WG3 to the last wave gauge measurement at WG6 is

approximately 60%, equivalent to ΔE = 16 J/m. The energy loss ΔE can also be estimated using free surface measurements at two wave gauges as

$$\Delta E = \rho_w g C_g \int_{t_1}^{t_2} (\eta_2^{\,2} - \eta_1^{\,2})\,\mathrm{d}t \tag{2.20}$$

where ρ_w is the density of water, g the gravitational acceleration, C_g the group velocity, t_1 and t_2 are the beginning and ending times, and η_1 and η_2 are free surface elevations. By integrating energy flux at WG3 (pre-breaking) and WG6 (FOR station 3, middle of third splash-up roller) from the quiescent condition until the return of the quiescent condition, the estimated energy loss is ΔE = 16 J/m which is identical to the loss calculated from figure 22c.

The estimated ΔE is in good agreement with that reported by Drazen et al. (2008). For the comparison, the proportionality factor or "breaking parameter" in the present study was calculated as $b = 0.042$ which is comparable to the value reported by Drazen et al. (2008) ($b \approx 0.04$ based on data points of the highest input wave steepness $S \approx 0.46$). Note that in the present study f_p = 1.1 Hz and the local wave steepness ka = 0.59 is very steep, whereas the local ka in Drazen et al. (2008) is not available so we used the value at the highest S. Using Figures 10 and 11 in Drazen et al. (2008) (with $b \approx 0.04$ in Figure 11 and the duration of active breaking $\tau_b \approx 0.6T$ for $S \approx 0.46$ in Figure 10), energy loss was estimated as ΔE = 13 J/m which is similar to that in the current study. The energy loss in the present study was also compared with that in Tian et al. (2008). The loss in the present study is nearly twice the value of $\Delta E \approx$ 9 J/m in Tian et al.'s "gain 2020" case based on their Table 1. Since the ka value in the present study is higher than that in Tian et

al., the twice energy loss may be due to the difference in the wave height (H = 0.20 m in the present study versus H ~ 0.1 m in Tian et al. (2008)).

Fig. 2.22b shows that the air entrainment contributed potential energy at the first splash-up (FOR 1) is about 48% of the total potential energy, estimated from the difference between the FOR and wave gauge measured potential energies in the figure. Based on Fig. 22c, the potential energy is about 33% of the total energy at that location. The air entrainment contributed potential energy is thus equivalent to 16% of the total energy. Since 85% of the total energy dissipated in the study, that means the air entrainment contributed potential energy is 18% of the total energy. This value is in close agreement with the value of 19% reported by Hoque (2002). Blenkinsopp and Chaplin (2007) reported that the peak potential energy of the entrained bubble plume reaches about 6% to 9% of the dissipated energy in the plunging breaking waves. Their finding is indeed comparable to what was found in the present study because the data in the present study includes potential energy from both the entrained bubble plume and the splash-up roller, roughly twice of that covered by Blenkinsopp and Chaplin.

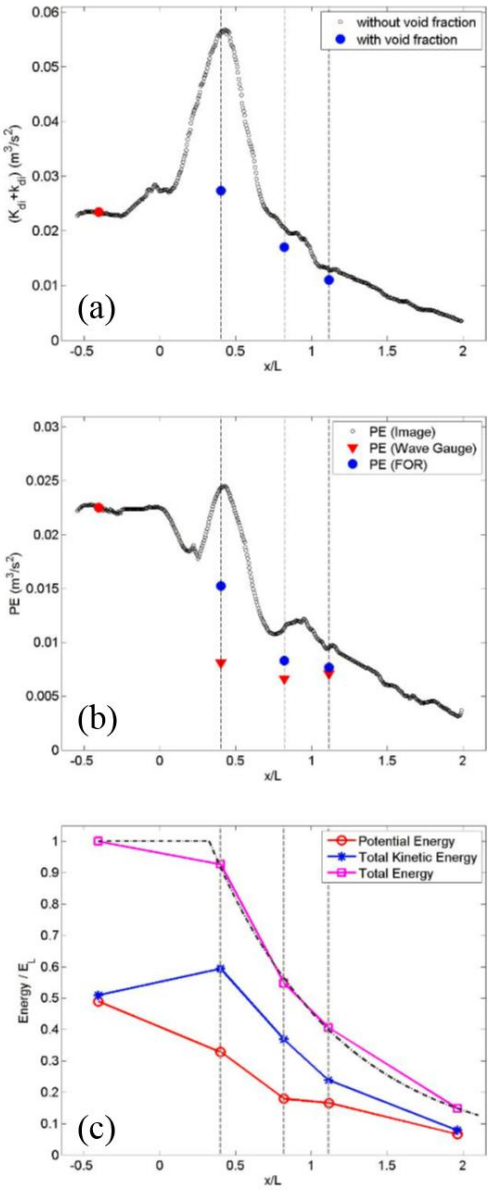

Fig. 2.22 (a) Depth integrated total kinetic energy k_{di}+ K_{di} and (b) potential energy (*PE*) with and without considering void fraction. (c) Total wave energy (E_α) accounting for void fraction normalized by the corresponding pre-breaking wave energy (E_L). The dashed line for E_α/E_L is from the empirical formula $E_\alpha/E_L = 1.47e^{-1.17x/L}$ for $x/L > 0.33$ and $E_\alpha/E_L = 1.0$ for $x/L \le 0.33$.

Based on Fig. 2.22c, the equipartition assumption between the total kinetic energy and the potential energy holds through the pre-breaking location at x/L = -0.41 where the front face of the wave becomes vertical. The assumption becomes inapplicable from the first wave impingement until about x/L = 2. The total kinetic energy is 56% higher than the potential energy at the first splash-up. Since the turbulent kinetic energy is about 26% of the mean kinetic energy (Fig. 2.21c), that means the mean kinetic energy is still 30% higher than the potential energy. Drazen et al. (2008) assumed equipartition between the depth-integrated kinetic energy and potential energy, and the total wave energy density was computed as twice the potential energy density far upstream and downstream from the breaking point. Huang et al. (2012a; 2012b) also applied equipartition in computing the total wave energy density for field measurements. The present results indicate the assumption may work fine in plunging breakers only after x/L = 2 or after the third impingement where the air bubble entrainment is less intense. However, Huang et al. (2009) showed that the depth-integrated kinetic energy approximates the potential energy for small-scale spilling breaking waves in a laboratory surf zone, indicating the equipartition assumption may work in spilling breakers with a low aeration level.

The horizontal axis in Fig. 2.22 spans over 2.5 wavelengths from $x = -0.6$ m to $x = 2.2$ m (or $x / L \approx [-0.5,\ 2]$). It covers one wavelength further downstream from WG6, located at the middle of the third fully developed splash-up. The section between FOR station 3 and the farthest downstream measurement point covers mostly "low-violent" region with relatively low aeration. The measurements and corresponding energy profiles cover only up to that section. The measurements were not continued further downstream

because great efforts have been made to cover velocity, void fraction, and free surface measurements over the large section, while there were no visible bubbles beyond the coverage section. Even though measurements beyond $x > 2L$ were not performed and the plot in Fig. 2.22 does not cover the entire breaking zone, the plot covers the most essential zone over the aerated region within which 85% of wave energy is dissipated.

At FOR station 1 where the first splash-up occurs, the increase of total kinetic energy, even though the mean kinetic energy is relatively flat (Fig. 2.21c), and decrease of density (or increase of void fraction, shown in Fig.2.13a) may explain the surprisingly high maximum velocity in the first splash-up process (reaching $2.14C$ versus the maximum velocity of $1.68C$ right before the first impinging, shown in Fig. 2.6a, d). A simple control volume analysis for mass conservation was performed (no shown here) using mean velocity maps at t = -0.01 s, 0.06 s, and 0.13 s (similar to that in Fig. 2.6) and applying central differences for time derivative. It was found that the calculated mean void fraction in the aerated region of the velocity maps (assuming a uniform void fraction for the velocity vectors in the aerated region) matches the mean void fraction measured at FOR station 1. That indicates the high velocity generated by the first splash-up is likely correct based on mass conservation. Note that if void fraction is not considered, the total energy would have increased at FOR station 1, based on Fig. 2.22a and 2.22b, which violates the energy conservation principle. The simple control volumn analysis applied here is described in Appendix D in more detail.

2.6 Discussion on Repeatability and Measurement Uncertainties

The repeatability of breaking wave generation was examined by comparing the 20 repeated free surface measurements at WG1 to WG3 and PIV velocity measurements at FOV1. These measurements were taken in front of the breaking point so the flow was essentially turbulence free. The free surface data show the averaged root-mean-square (RMS) values of $\eta_{rms} \sim 0.65$ to 0.71 mm for the 3 gauge measurements. The PIV data show the averaged RMS velocity fluctuations of $u_{rms} \sim 0.012$ m/s and $w_{rms} \sim 0.008$ m/s at FOV1. These fluctuations are considered as errors resulting from the slightly unrepeatable nature of the wavemaker and the inherent uncertainty of the PIV measurements, including the pseudo turbulence (Chang and Liu, 2000). Since η_{rms}, u_{rms}, and w_{rms} are at least two orders of magnitude lower than the wave height and phase speed, we conclude that the generated waves are highly repeatable.

The mean and fluctuating quantities were calculated from ensemble averaging the 20 instantaneous measurements. The repetition number of $N = 20$ is supported by a simple theory stating that the error can be estimated by the sample estimate of the population standard deviation divided by the square root of the size of independent samples. In the present study, the standard deviation, equivalent to the turbulent fluctuations, is about 20% of the mean so the error in the mean velocity measurements is 4.5%. The uncertainty is proportional to $\sqrt{N}$ so the error would reduce to 2.8% if N is further increased to 50.

Error analyses for mean velocities, void fraction, and turbulent intensity were also conducted using bootstrapping based on the 20 repeated runs for each quantity. For the mean velocities, the estimated error is 4.6% (normalized by C) which is consistent with

the 4.5% error estimated based on the simple theory. For void fraction, the estimated error is 0.17 (about 20% of the maximum void fraction in Fig. 2.16a) over the highly active phase between t = 0.22 s and 0.37 s at FOR station 1 in Fig. 2.15a. Similarly, the estimated error is 22% (normalized by 0.2*C*) for turbulent intensity and the error for turbulent kinetic energy is 44% (twice of that of turbulent intensity).

We further analyzed the errors for turbulence intensity with respect to the number of repetitions using the bootstrap method. The result shows that, as the number of repetitions increases, the error decreases but in a slow rate. When the number of repetitions is increased from $N = 5$ to $N = 20$, the error δ_{XN} (m/s) decreases from 0.079 m/s (or 0.061*C*) for $N = 5$ to 0.056 m/s (or 0.044C) for $N = 20$. Following the trend, the error would further reduce to 0.029 m/s (or 0.022*C*) for $N = 50$. Fig. 2.23 shows the reduction of errors of the measured mean velocity relative to the number of repetitions. Note that the turbulence level is about 0.2*C*. Additionally, the bootstrap analysis was also applied to obtain the vertical profile of errors for turbulent intensity (based on $N = 20$). The result indicates that errors outside the aerated region are relatively small (< 0.01 m/s) compared to that inside the aerated region. The maximum error occurred at the center of the roller with a magnitude about 0.077 m/s (or 0.059*C*).

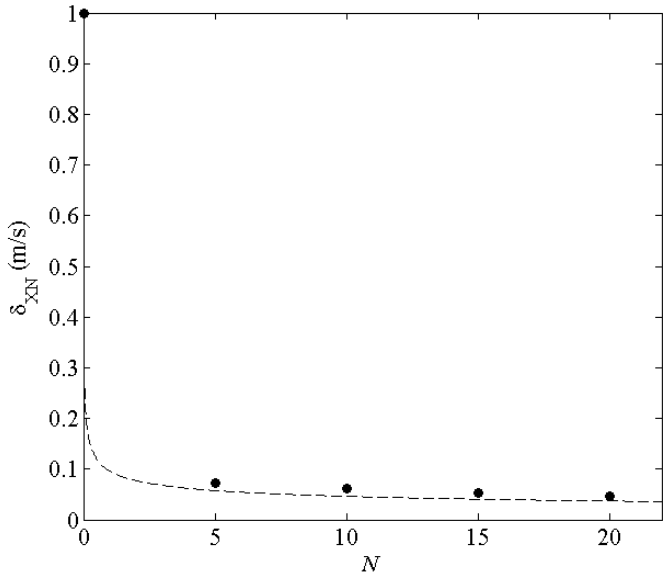

Fig. 2.23 Reduction of the errors (δ_{XN}) in the measured mean velocity with respect to the number of repetitions (*N*) using the bootstrap method.

2.7 Conclusions

We have presented combined measurements of velocities and void fraction as well as free surface under an unsteady deep-water plunging breaking wave in a laboratory. The plunging breaker was generated mechanically using a wave focusing technique. The flow velocities were measured by the modified PIV technique in the entire flow region, the void fraction at the three splash-up regions were measured using the FOR technique, and the free surface was measured using both images and wave gauges. Combining these techniques, we were able to study the flow structure in the aerated rollers and splash-ups and investigate the effect of void fraction on kinematic and dynamic properties of the flow. Not only do the data provide insight into the complex two-phase nature of the plunging wave, the data can also be used as a reference for numerical models. Some important findings are summarized below.

The maximum velocity in the plunging breaker reaches 1.68C at the first impingement, which is comparable to the speed of an overturning jet for periodic breaking waves in water of intermediate depth reported by Chang and Liu (1998). After the plunging jet penetrates into the water surface, it pushes the water in front of it to splash upward and causes the splash-up to reach a much higher maximum velocity of 2.14C at the beginning of the process (at t = 0.06T). Multiple coherent vortical structures were found in the rolling foamy clouds of impingements and splash-ups. Clockwise vortices were observed at each impinging and splash-up roller, while counterclockwise backward impingement occurs in between the impinging and splash-up roller pair. These large eddies may have a significant role in turbulent production due to their large velocity gradient and contribution to shear in the mean flow and fluctuations.

The measured void fraction under the unsteady plunging breaker is comparable to recent findings reported by Blenkinsopp and Chaplin (2007) and Rojas and Loewen (2010). Combining the void fraction measurements with the velocity measurements allows us to examine the relation between flow kinematics and fluid density under the breaking wave. Time contours of void fraction signatures reveal distinct evolving patterns of entrained bubbles under the plunging breaker, such as the splash-up and the impinging roller. The maximum void fraction at the middle of the first splash-up roller is about 0.98 which is in good agreement with that reported in Blenkinsopp and Chaplin (2007). The averaged void fraction can be modeled as a linear growth followed by an exponential decay, consistent with that reported by Cox and Shin (2003). In addition, the root-squared vorticity of the mean flow and turbulent intensity in the foamy turbulent flow are strongly correlated to

the entrained bubbles and void fraction level. In the violent foamy splashing stage, the vorticity and turbulent intensity are strongly correlated to and possibly enhanced by the void fraction in the relatively low void fraction region (void fraction ~ 0 to 0.6 in the lower part of the roller); these quantities then start to decrease as the void fraction varying within a narrow range after reaching the maximum (void fraction ~ 0.6 to 0.8 in the upper part of the roller). The turbulent intensity in the collapsed bubble cloud of impinging roller and wake region is comparable to that in the splashing stage even though the void fraction in the this stage is much lower. The possible cause could be that the passing air bubbles inject and transfer energy into the flow and cause the residue turbulence to remain energetic and maintain a similar level of flow fluctuations, although other mechanisms such as turbulent production and advection may also play a role in the process.

The mass flux, momentum flux, kinetic energy, potential energy, and total energy fluxes were computed and compared with and without void fraction being accounted for. The results show that all the mean and turbulence properties in the highly aerated breaker are significantly overestimated if the void fraction is not considered – the total kinetic energy shows a 100% overestimation and the image-based potential energy shows a 50% overestimation in the first splash-up region. The potential energy associated with air entrainment at the first splash-up roller is about 18% of the total dissipated energy which is comparable to that reported by Hoque (2002) and Blenkinsopp and Chaplin (2007). The overestimation is less significant at the second and third splash-ups, reducing to about 20% to 30%. When accounting for the density variation, about 54% and 85% of the total energy are dissipated within one and two wavelengths beyond the wave impingement point,

respectively. It is evident that accounting for void fraction is essential in studying energy distribution and dissipation in breaking waves, especially in plunging breakers.

For future study, decomposing the mean motion into rotational and irrotational flows (Nadaoka et al. 1989) would be useful to extract desired turbulent eddies from the background wave-induced flow. Bubble concentrations and size distributions under breaking waves and their effects to turbulent kinetic energy budget also need to be explored to expand the void fraction based two-phase approach in the present wave-breaking study.

CHAPTER III

TURBULENT FLOW FIELD AND AIR ENTRAINMENT IN LABORATORY PLUNGING BREAKING WAVES**

3.1 Introduction

Due to their highly turbulent and multiphase nature, investigating the physics, kinematics, and dynamics of breaking waves has been a challenging task to researchers for several decades. It has received attention due to its role in air-sea interactions and climate change (Melville et al., 2002). In the plunging breaking process, a two-phase flow region forms followed by air entrainment, which occurs immediately after an overturning jet impinges onto the undisturbed frontal water surface (and then this entrainment evolves over space and time). The air entrainment has been known to develop in several stages: the entrapment of air (i.e. an air cavity) caused by the plunging jet impinging the undisturbed water surface, air entrainment around the jet impinging point, additional air entrainment near the air water interface caused by subsequent splash-ups, air entrainment between the backside of the splash-up roller and the impinging roller, and entrainment all over the splash-up region in the later breaking stages (Kiger and Duncan, 2012).

** Reprinted with permission from "Turbulent flow field and air entrainment in laboratory plunging breaking waves" by Na, Chang, Huang, and Lim (2016). *Journal of Geophysical Research: Oceans*. 10.1002/2015JC011377, Copyright (2016) John Wiley and Sons

A few measurement techniques have been developed to quantify bubble sizes and populations using a conductivity probe (Chanson, 2002; Mori et al., 2007), an optical fiber probe (Lim et al., 2008), and imaging and acoustics based methods (Deane and Stokes, 2002).

However, few measurements on the formation and evolution of bubbles under breaking waves have been reported due to the insufficient temporal and spatial resolution of exiting methods (Deane and Stokes, 2002). Moreover, the effect of bubbles on the surrounding turbulence is still an enigma because of difficulties in conducting simultaneous measurements of void fraction and velocity in the presence of active air entrainment.

Studies of turbulent flow fields in breaking waves have shown great progress over the last two decades with advanced measurement techniques. Rapp and Melville (1990) applied flow visualization with a dye to observe turbulent mixing under unsteady laboratory based breaking waves. They found that the penetration depth of the bubble cloud grows linearly over one to two wave periods, and then follows a power law of $t^{1/4}$ (with t being time). The bubble cloud evolves and reaches a depth of two to three wave heights and a horizontal length of one wavelength. Drazen and Melville (2009) used particle image velocimetry (PIV) to measure the large scale turbulent structure in post-breaking velocity fields. The penetration depth (i.e., the vertical turbulent mixing length) was observed to follow an $x^{1/2}$ dependence, with x being the streamwise direction. The integral length scale of the energetic eddies was found to increase over time as the post-breaking process continued. Huang et al. (2010) measured turbulent flow fields of surf-

zone spilling breaking waves using PIV. They reported that the length scale of vortical structures was about 0.1 to 0.2 times the local water depth, and that the structures stretched downward as the waves propagated. The higher values of the local intermittency measure (*LIM*) – calculated through a wavelet transform – also spread downward, indicating that the vortical structures may significantly contribute to turbulence.

Coherent structures have been shown to be an important feature in turbulent flows, as they affect small scale turbulence (Bonnet and Delville, 2001; Camussi, 2002). Wavelet analysis has been shown to be a satisfactory tool to study the multiple scales of coherent structures (e.g., Camussi and Felice, 2006; Longo, 2009; Ruppert-Felsot et al., 2009; Huang et al., 2010). Camussi and Felice (2006) used wavelet analysis to extract coherent structures in turbulent boundary layers. Their results showed that the mean size of coherent structures is about 4% – 5% of the boundary layer thickness. Longo (2009) applied wavelet analysis to educe the length scale of energetic eddies in the pre-breaking region of surf-zone spilling breaking waves. He reported that the sizes of eddies that carry the most turbulence energy range from ten times the Kolmogorov microscale to one wavelength. Similarly, Huang et al. (2010) revealed the existence of intermittent vortical structures under small-scale spilling breaking waves. It is, however, not clear how these swirling eddies would behave under the high foamy rollers and bubble clouds of plunging breaking waves.

Void fraction in the aerated region of breaking waves may affect the determination of certain physical quantities that involve fluid density. Without accounting for the void fraction, the kinetic energy and potential energy could be overestimated by approximately

50% and 40%, respectively, during the breaking process of a plunging breaker (Lim et al., 2015). Measurement of void fraction in breaking waves has been progressing in both field and laboratory settings using acoustic, electrical, and optical methods (e.g., Lamarre and Melville, 1991; Lamarre and Melville, 1992; Vagle and Farmer, 1998; Deane and Stokes, 2002; Chang et al., 2003; Cox and Shin, 2003; Blenkinsopp and Chaplin, 2007; Rojas and Loewen, 2007; Lim et al., 2008; Ryu and Chang, 2008; Lim et al., 2015). However, only a small number of studies focused on the relation between void fraction and surrounding turbulent flows have been performed (e.g., Cox and Shin, 2003; Mori and Kakuno, 2008). Cox and Shin (2003) used laser-Doppler velocimetry (LDV) and an impedance void fraction probe to measure the instantaneous velocity and void fraction above the trough level in the aerated region of surf-zone breaking waves. Their results showed that turbulent intensity and void fraction are positively correlated, following a linear relationship. Mori and Kakuno (2008) used a dual-tip resistance-type probe and acoustic Doppler velocimetry (ADV) to measure void fraction and flow velocities, respectively. They also found that the void fraction linearly correlates with the turbulence intensity. More recently, Lim et al. (2015) found a strong correlation among vorticity, turbulent intensity, and void fraction in the relatively lower void fraction region (void fraction between 0 and 0.6) at the initial impinging and the splashing stage of a deep-water plunging breaker.

Despite the advances made in these recent void fraction and turbulence studies, the relation between bubbles and turbulence in breaking waves has not been as well understood – especially in waves with high air entrainment and a large number of bubbles. Baldy (1993) reported that the bubble population distribution follows a power law scaling

value of -2 in wind generated breaking waves. Garret et al. (2000) proposed that the bubble size spectrum is proportional to a power-law scaling of -10/3 and that the rate at which larger bubbles fragment into smaller bubbles depends on the turbulent dissipation rate. They further modified the -10/3 power scaling and argued that the bubble size spectrum became flatter at smaller scales (or steeper at larger scales) under the influence of dissolution and buoyancy forces. Deane and Stokes (2002) employed photographical, optical, and acoustical methods to measure void fraction and bubble size distributions in both laboratory and open-ocean plunging breakers. They suggested that air entrainment in plunging breaking waves occurs due to two main mechanisms: smaller bubbles are formed by the impact, and subsequent splashing, of the overturning jet; while larger bubbles are formed by the fragmentation of the air "tube" or "vortex" trapped between the overturning jet and the wave face as the wave breaks. They showed two distinct power-law scaling relationships in bubble size distributions: for bubbles with a diameter larger than about 1 mm the bubble density spectrum was proportional to the bubble radius to the power of -10/3, while for smaller bubbles the spectrum showed a flatter -1.5 power-law scaling. Mori et al. (2007) simultaneously measured flow velocities and bubble size distributions for breaking waves on a plane slope. They found a power-law scaling of -1.5 to -1.7, independent of the experimental scale. The relationship among void fraction, turbulent intensity, and kinetic energy showed a linear dependence.

Recently, numerical simulations for the aerated wave-breaking flow were performed and validated with results from earlier laboratory experiments. Shi et al. (2010) proposed a two-fluid numerical model to simulate the evolution of air bubble plumes induced by

deep-water breaking waves. Bubbles with a radius greater than *O* (1 mm) were found to have a major contribution on the void fraction, while smaller bubbles contribute significantly to the cross-sectional area of the bubble cloud (but not to the total volume of air). A strong, degassing effect on larger bubbles was found, caused by the fast decay of air patches consisting of higher void fraction (compared with those with lower void fraction). Ma et al. (2011) developed a polydisperse two-fluid model to simulate bubbly flows under surf zone breaking waves. The bubble size spectrum was captured at different depths by the proposed model. They showed that, as the depth increases, the spectrum became steeper because of buoyancy. The simulated turbulent dissipation rate was also found to be much higher with the presence of bubbles. The bubble induced turbulence suppression was linearly correlated with the void fraction in the high turbulence region. More recently, Derakhti and Kirby (2014) performed large-eddy simulations of a single breaking event in deep water. They found that bubble induced dissipation accounts for more than 50% of the total dissipation. Their results also showed that the turbulent kinetic energy is damped by 20% by the dispersed bubbles in the plunging breaking wave. The numerical simulations were validated to a satisfactory degree with experiments, but a lack of simultaneous measurements of velocity and void fraction in the aerated region still contributes certain uncertainties, if not difficulties, in model validations.

The present study performed a laboratory experiment to quantify the highly aerated flow and bubbles under mechanically generated, unsteady plunging breaking waves in deep water. To measure velocities in the highly aerated region of breaking waves, a modified PIV technique and the bubble image velocimetry (BIV) technique were

successfully used to obtain velocities inside and outside the aerated region (Ryu et al., 2005; Lim et al., 2015). Moreover, void fraction in the aerated region was also measured using the fiber optic reflectometry (FOR) technique (Chang et al., 2003, 2008). Using the measured velocity and corresponding residence time for each bubble encounter, bubble chord lengths were obtained at three vertical cross sections. The present study is an extension of Lim et al. (2015), with a special focus on the relation between turbulence flow fields and bubbles generated by wave breaking. In section 2, the wave generation and experimental setup is described. In section 3, the distribution of local maximum of the local intermittency measure is presented using a wavelet-based technique. The local energy content is then compared with the vorticity and swirling strength. Subsequently, the length scales of vortical structures are estimated. In section 4, void fraction and bubble chord length distributions are determined and their relation with turbulence properties is discussed. Correlations between void fraction, bubble size distribution, and certain flow characteristics are also presented. Finally in section 5, turbulence dissipation rates – considering void fraction – are obtained based on the measurement data using a mixture theory of two-phase flows. The role of bubbles in the energy budget is also investigated.

3.2 Experimental Setup

The experiment was carried out in a two-dimensional wave tank located in the Department of Civil Engineering at Texas A&M University. The tank was 35 m long, 0.91 m wide and 1.2 m deep, and is equipped with a flap–type wavemaker at one end. A 1:5.5 sloping beach with a layer of horsehair was located at the opposite end to absorb wave energy and reduce reflection. A constant water depth of h = 0.80 m was maintained

throughout the experiment.

A plunging breaking wave was generated using a wave focusing technique similar to Skyner (1996). The wave packet consists of 13 waves of various wavenumbers and amplitudes with a central frequency of f_c = 1.1 Hz. Only one plunging breaking wave that broke at the desired location, with good repeatability, was generated in each run. The primary breaking wave has a wave height of H = 0.204 m and a wave period of T = 0.83 s. Based on linear wave theory, the wavelength is L = 1.08 m, the phase speed is C = 1.30 m/s, the wave steepness H/L is 0.19, and the wave is in a deep water condition of kh = 4.7 (with k being the wavenumber). The coordinate system is defined such that x represents the horizontal direction (along the wave propagation), y the cross tank direction, and z the vertical upward direction. The origin $x = 0$ and $z = 0$ is defined as the impinging point of the breaking wave and the still water level, and time t = 0 is defined as the moment of wave impingement. More details of the experiment can be found in Lim et al. (2015).

A brief description of the measurement methods employed in the study is provided below, and more details can be found in Lim et al. (2015). In the experiment, wave gauges, along with BIV, modified PIV, and FOR techniques were used to measure surface elevation, flow velocities, and void fraction of breaking waves. The BIV technique measures the velocity field of the aerated region in the breaking waves and the free surface. The modified PIV technique measures the entire flow field, including the pre-breaking region and the highly aerated region. The FOR technique detects phase changes and obtains the bubble residence time (and therefore the void fraction) at three vertical stations located at the three splash-up regions coincident with the three wave gauge locations. A

total of 20 repeated runs were performed with the same test conditions at each measurement location for all the measurements. The measured data obtained includes 14 field of views (FOVs) in the PIV measurements with 20 repeated runs for each FOV (a total of 280 runs), 3 FOVs in the BIV measurements with 20 repeated runs each (a total of 60 runs), 38 FOR measurement points with 20 repeated runs each (a total of 760 runs), and 6 wave gauge measurements with 20 repeated runs (a total of 20 runs). The mean and fluctuating quantities were calculated from ensemble averaging the 20 instantaneous measurements. Lim et al. (2015) showed that the averaged root-mean-square values of the measured free surface data before breaking range from 0.32% to 0.35% of the primary breaking wave height H, indicating high repeatability of the generated waves. They also estimated the measurement uncertainties on velocity and void fraction and concluded that the estimated errors are 4.6% and 0.17 at most, respectively.

The free surface profiles were measured using six double-wired resistance-type wave gauges (termed WG1 to WG6) at x = -2.98 m, -1.31 m, -0.57 m, 0.43 m, 0.88 m, and 1.20 m as shown in Fig. 3.1a and 3.1b. The location of WG3 was set a short distance (0.17 m) upstream from where the front face of the plunging breaker becomes vertical. WG4, WG5, and WG6 were set in the middle of the first three splash-up regions where the splash-ups were fully developed. These three wave gauges are coincident with the three FOV measurement stations (termed FOV1 to FOV3).

The BIV technique (Ryu et al., 2005) was used to measure the velocity field in the aerated region after the primary breaking wave impinges onto its front surface. The images were captured by a high speed camera that has a resolution of 1024×1024 pixels and a 10-

bit dynamic range. The framing rate was set at 500 frames per second throughout the experiment. Two regular 600 W light bulbs with reflecting mounts and a translucent flat plate were used to illuminate the flow from behind the tank. The depth of field for the captured images is 0.21 m with its center at 0.2 m behind the tank's front wall. Three FOVs of 0.66×0.50 m^2 were used to cover the entire aerated region of the plunging breaker as shown in Fig. 3.1b. There was a small overlap region of 84 mm between FOV1 and FOV2, and a gap of 270 mm between FOV2 and FOV3 due to a steel column supporting the wave tank. After acquiring the images, velocities were determined using commercial software from LaVision Inc. An adaptive multi-pass algorithm – which has an initial interrogation window of 32×32 pixels and a final window of 16×16 pixels, with a 50% overlap –was applied in the process. Accordingly, the final resolution of the velocity vectors was 8×8 pixels, corresponding to 5.26×5.26 mm^2. The BIV images were also used to obtain the free surface information and to identify the aerated region. Both the principle and the validation of the BIV technique are detailed in Ryu et al. (2005), Ryu and Chang (2008), and Lin et al. (2012).

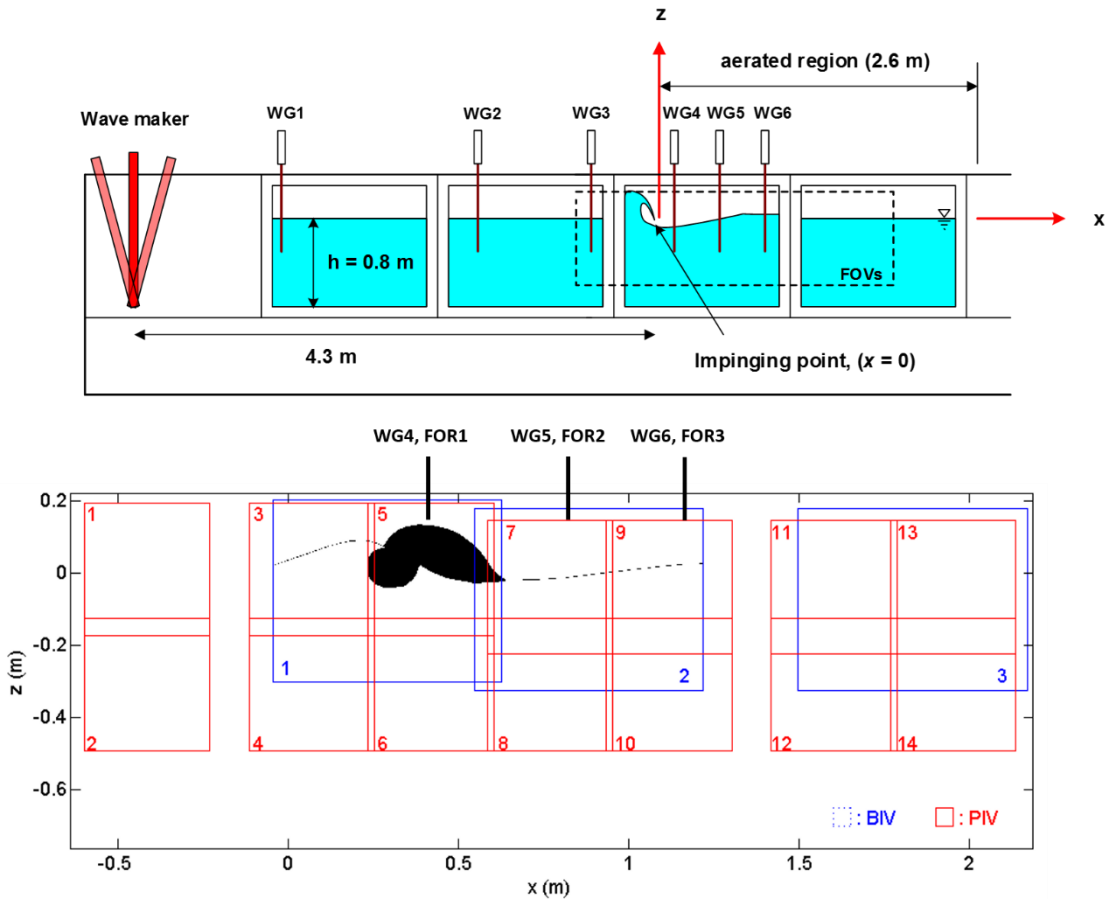

Fig. 3.1 (a) Sketch of the wave tank and locations of the wave gauges. (b) Detailed locations of the PIV and BIV fields of view with the aerated region masked as black (at t = 0.25 s).

The modified PIV technique was used to measure the velocity fields in the entire breaking region using a weak, continuous laser and a high dynamic range camera with a short exposure time (*Lim et al.*, 2015). A 5-W continuous Argon-Ion laser was used as the light source, and two cylindrical concave lenses were used to generate the wide light sheet. The same camera and framing rate as in the BIV measurements were used in the PIV measurements. In the PIV measurements, 14 FOVs centered at 0.2 m behind the tank's front wall were used to cover the entire flow field of breaking waves. The sizes of the 14 FOVs (see Fig. 3.1b) were fixed as 0.37×0.37 m^2. Similar to the image processing in BIV, the velocity maps were obtained using the adaptive multi-pass algorithm with an initial interrogation window of 64×64 pixels and a final window of 32×32 pixels, with a 50% overlap. The resolution of the velocity vectors is 16×16 pixels, corresponding to 5.78×5.78 mm^2. There is an overlap of 20 mm between adjacent FOVs. Using the mosaic concept, the 14 FOVs cover the entire flow field of the plunging breaker with sufficient spatial and temporal resolutions.

The FOR technique was used to obtain the bubble residence time and the void fraction in the aerated region of the breaking wave. FOR is capable of distinguishing air and water based on the coherent mixing of scattered signals with the Fresnel reflection from the tip of an optical fiber. FOR is a point measurement tool and nearly noninvasive due to the small diameter of the fiber (~125 μm). More details on the principle, validation, and applications of FOR can be found in Chang et al. (2002; 2003), Lim et al. (2008), Ryu and Chang (2008), and Lim et al. (2015). The sampling rate of the FOR measurements was set at 100 kHz throughout the experiment. The measurements were taken at three FOR

measurement stations located at the middle of the three splash-ups of the breaking wave. The total number of measurement points at FOR stations 1, 2, and 3 were 19, 12 and 7, respectively, with a constant interval of 10 mm. These numbers were determined by the vertical spreading of the bubble cloud at each station.

3.3 Evolution of Turbulent Flow Fields

3.3.1 Extracting Vortical Structures Using Wavelet Analysis

During the formation of the plunging breaking wave, the overturning water jet falls and impacts on the water surface ahead of it, generating the first impinging roller. This impact produces a large upward momentum, leading to the first splash-up roller. Fig. 3.2 shows a sample of the instantaneous velocities measured by PIV on a moving frame of the phase speed, C, for easy identification of the rollers. Evidently, the first impinging roller and the first splash-up roller are visible in Fig. 3.2c and Fig. 3.2d. More details about the breaking process of the plunging breaker have been presented in Lim et al. (2015), so they are not repeated here.

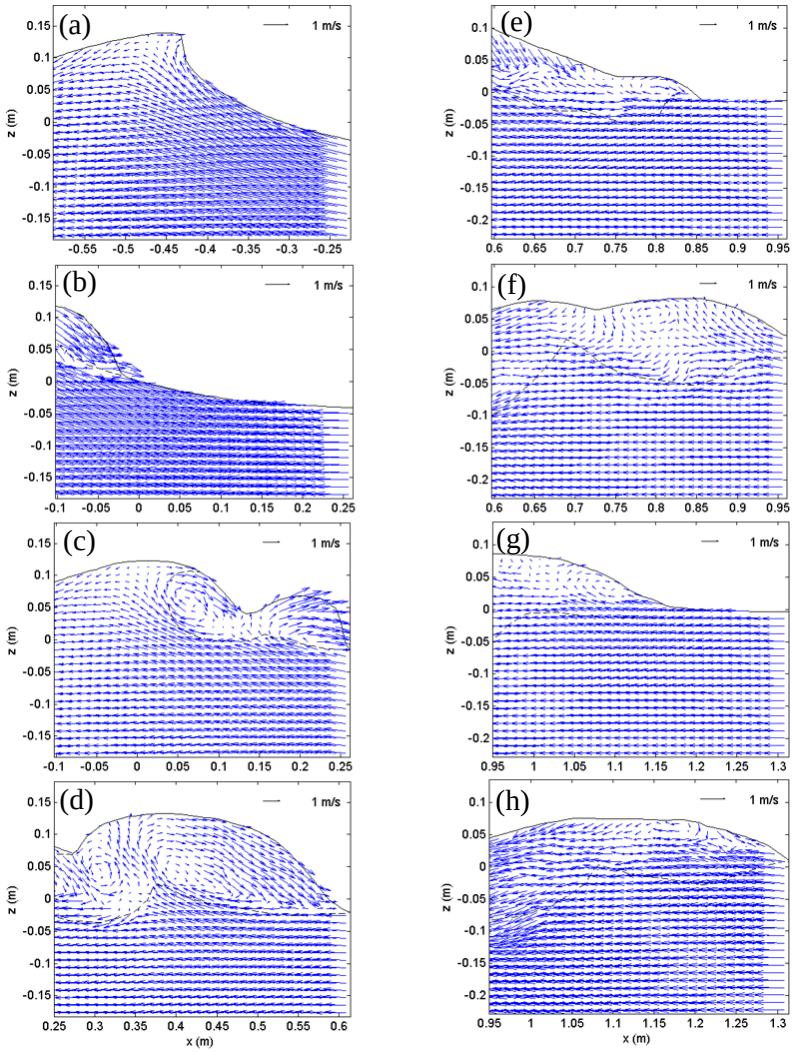

Fig. 3.2 Sample instantaneous velocity fields on a moving frame of the phase speed, *C*, during the breaking process: (a) *t* = –0.2 s (FOV1, pre-breaking), (b) *t* = –0.02 s (FOV3), (c) *t* = 0.09 s (FOV3, beginning of the first splash-up), (d) *t* = 0.25 s (FOV5, fully developed first splash-up), (e) *t* = 0.41 s (FOV7, beginning of the second splash-up), (f) *t* = 0.56 s (FOV7, fully developed second splash-up), (g) *t* = 0.68 s (FOV9, beginning of the third splash-up), (h) *t* = 0.80 s (FOV9, fully developed third splash-up). Only one quarter (in every other row and every other column) of the measured velocity vectors are plotted. The dashed lines represent the boundary of the aerated region determined using the BIV images.

Identifying vortex-like coherent structures is essential in studying the dynamics of turbulent flows. In the present study, vortical structures under the deep water breaking waves were educed using a wavelet transform with a Morlet wavelet $\varphi(z)$ defined as follows:

$$\varphi(z) = e^{iw_0 z} e^{-z^2/2} \tag{3.1}$$

where z is the position of the signal for the (different) window of the mother wavelet, and $w_0 = 6$ is suggested to satisfy the admissibility condition (Farge, 1992). It has been verified that the physical results do not depend on the choice of the mother wavelet (Farge, 1992; Camussi and Felice, 2006). The wavelet coefficient of a velocity signal is then defined as the following using the continuous wavelet transform (Farge, 1992):

$$W_f(s,z) = \frac{1}{\sqrt{s}} \int_{-\infty}^{\infty} u(\tau) \varphi^* \left(\frac{\tau - z}{s} \right) d\tau \tag{3.2}$$

Where $u(\tau)$ is the horizontal velocity, s is the scale dilation parameter, τ is the translation parameter, $\sqrt{s}$ is for energy normalization across the different scales, * denotes the complex conjugate, and the integrand represents a convolution product between the dilated and translated counterpart of the complex conjugate of the mother wavelet. In calculating the wavelet coefficients, the boundary values were extended and kept at the same values

to minimize boundary effects.

Wavelet transform in signal analysis is capable of splitting the flow into dynamically coherent vortices and incoherent background flow. A quantitative local intermittency measure (*LIM*) introduced by Farge (1992) is defined as follows:

$$LIM(s,z) = \frac{[W_f(s,z)]^2}{\left\langle [W_f(s,z)]^2 \right\rangle_z} \tag{3.3}$$

where $\left\langle [W_f(s,z)]^2 \right\rangle_z$ is the average of the square of a wavelet coefficient along the z direction. *LIM* has been successfully adopted in analyzing turbulent flows for eddy detection (e.g., Camussi, 2002; Camussi and Felice, 2006; Longo, 2009). In the present study, this method is modified to make it applicable to flows that feature both turbulent and laminar regions – such as the combined aerated turbulent region, and the unaerated laminar region below and behind it, in the present deep-water breaking waves. The inherent normalization process would otherwise contaminate the values of *LIM* in the region where most wavelet coefficients are small (e.g., the laminar flow region behind and below the highly turbulent impinging roller).

Fig. 3.3a shows sample instantaneous velocities (*u*, *w*) and vorticity (ω), and Fig. 3.3b shows the corresponding *LIM* at a vertical column located approximately in the middle of the fully developed first splash-up in FOV5. The figures indicate that the high *LIM* values coincide with the presence of vortical structures in the turbulent flow region. Camussi and Felice (2006) showed that the location of a *LIM* peak matches the location of the corresponding coherent structure by comparing the *LIM* field and the vorticity field.

Accordingly, the corresponding turbulent length scale may be determined directly from the wavelet transform results.

The distribution of $\left\langle [W_f(s,z)]^2 \right\rangle_z$ is shown in Fig. 3.3c as a histogram. It is worth pointing out that the level of *LIM* in the pre-breaking region, such as the velocity field show in FOV1, was found comparable to that in the splash-up region. This is caused by the inherent normalization process (i.e., a small value normalized by another small value) in Equation 3.3. The normalization process forces the *LIM* values in the laminar region to have a similar magnitude as those in the turbulent region, which in turn leads to the failure of the *LIM* approach in the laminar region. Nevertheless, it was found that the distribution of $\left\langle [W_f(s,z)]^2 \right\rangle_z$ in the turbulent flow region is distinct to that in the presumably laminar region. To counter the problem, setting a threshold value may be needed to distinguish the laminar and turbulent regions. It was found that the distributions are noticeably different in the vicinity of $\left\langle [W_f(s,z)]^2 \right\rangle_z = 0.01$. Therefore, velocity vectors in a water column with $\left\langle [W_f(s,z)]^2 \right\rangle_z$ less than 0.01 were identified as the laminar flow region, and a constant value of *LIM* = 0.01 was assigned to them. This conditional threshold is necessary to separate the laminar flow region where the *LIM* approach is not applicable.

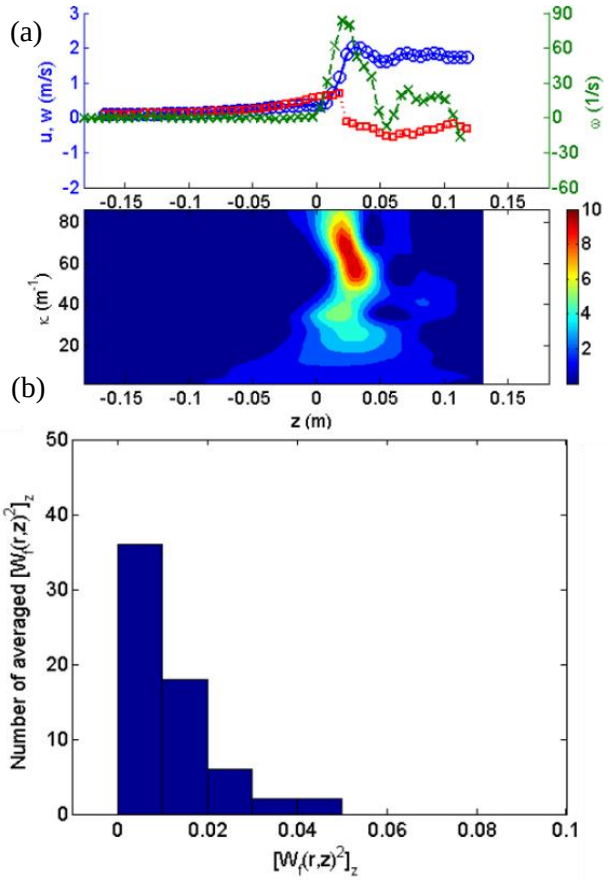

Fig. 3.3 (a) Sample vertical distributions of velocities at x = 0.41 m in FOV5 (fully developed first splash–up with a time instant corresponding to Figure 2d). In the plot, *u* (circle), *w* (square), and ω (cross) denote the streamwise velocity, vertical velocity, and vorticity, respectively. (b) Corresponding contour map of *LIM* against wavenumber κ and vertical location *z*. (c) Histogram of $\left\langle [w(s,z)]^2 \right\rangle_z$.

3.3.2 Evolution of Vortical Structures

Camussi (2002) reported that the peak of *LIM* matches the vortex core, and that the location of the vortical structure can be identified by locating the *LIM* peak. The *LIM* peak among different scales can be formulated as

$$LIMM(z) = \max\left\{LIM(s,z)\right\} \tag{3.4}$$

The value of *LIMM* represents the energy level of the most excited mode among the scale bands. Camussi and Felice (2006) reported that inversing the scale dilation parameter of *LIMM* directly gives the length scale of the identified vortex. It has been previously suggested that a conditional threshold technique could be applied to remove the 'background noise' induced by the mean shear caused by waves, so as to extract the vortical structures induced by turbulence (Cox and Kobayashi, 2000; Huang et al., 2010). Cox and Kobayashi found that the instantaneous turbulent kinetic energy and the instantaneous Reynolds stresses are several times greater than the phase-averaged background values. In the present study, high mean shear stresses were observed along the lower boundary of the aerated region due to the differential motion between the high-speed rotation in the first splash-up roller region and the relative low-speed wave motion under the trough level. Thus, the conditional threshold technique was applied to extract the turbulence-induced vortical structures.

Fig. 3.4 shows the evolution of instantaneous *LIMM* fields with the conditional threshold technique being applied. A condensed region with high values of intermittency is observed within the aerated region. At the initial stages of wave breaking (Fig. 3.4b-c), high values of *LIMM* were observed near the lower boundary of the aerated region, consistent with the distribution of turbulent intensity (Lim et al., 2015). As the wave propagates, the high values of *LIMM* spread across the aerated region at the later stages (Fig. 3.4d-f). Note that the level of *LIMM* remains high at the second splash-up roller (Fig. 3.4f) and at the third splash-up roller (Fig. 3.4h), as compared to that of the first splash-up roller (Fig. 3.4d). This result is consistent with the similar level of turbulence maintained

even at the weak third splash-up roller, as reported in Lim et al. (2015). They also reported a very low void fraction observed at the third splash-up roller, but the passage of bubbles may contribute to the high level of turbulence in the later stages of breaking.

Fig. 3.5 shows the distributions of the corresponding instantaneous length scales (*LS*) of the vortical structures. The length scales were directly calculated by inversing the wavenumber κ (i.e., the reciprocal of the scale dilation parameter) at which the *LIMM* was sought. The length scales in the highly aerated region are mostly lower than one half of the wave height of the breaking wave. In comparison, the length scales in surf-zone breakers were found to vary from between the breaker height and the wavelength in Longo (2009) to less than one half of the water depth in Huang et al. (2010).

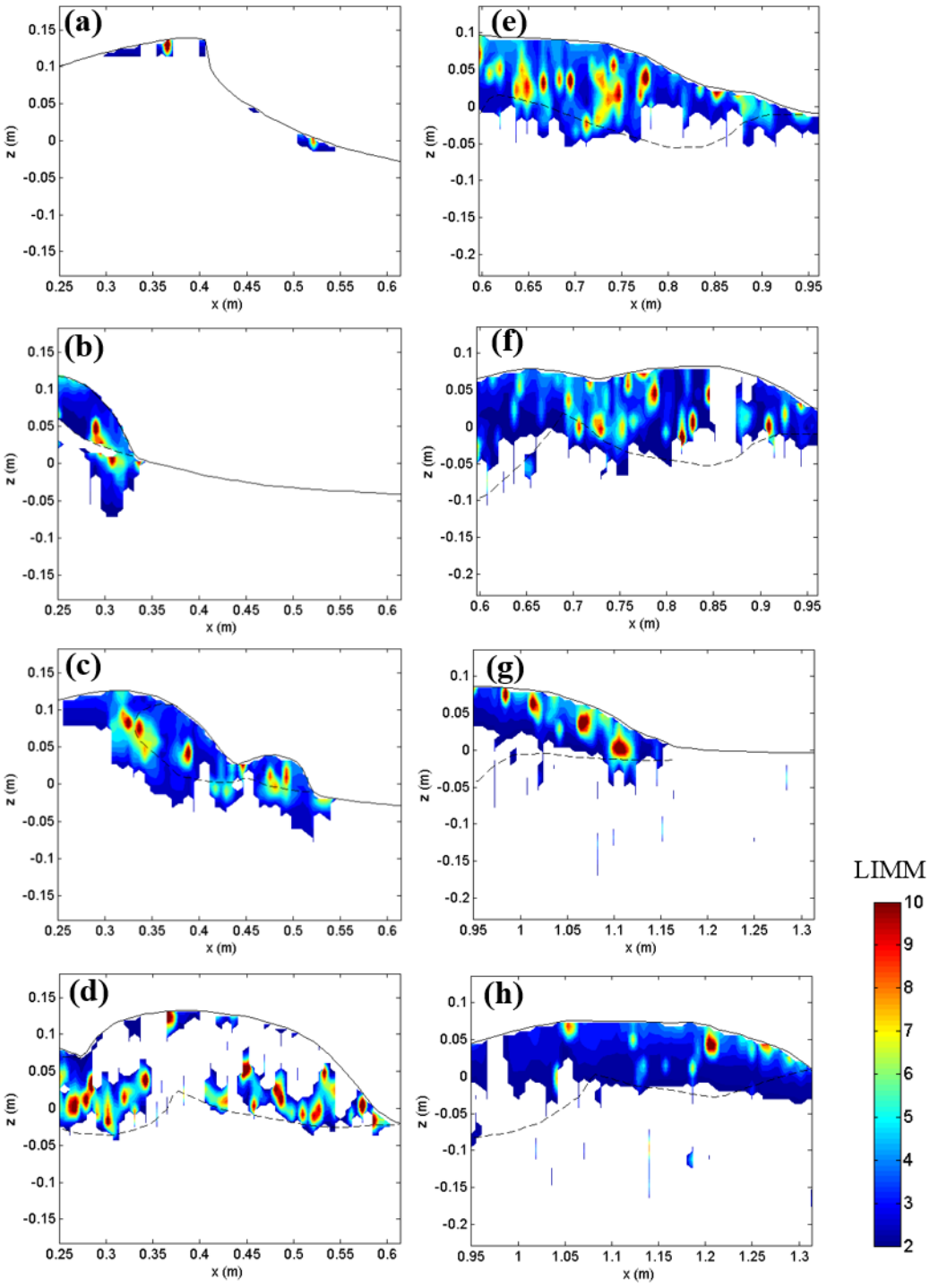

Fig. 3.4 Instantaneous *LIMM* fields corresponding to Fig. 3.2.

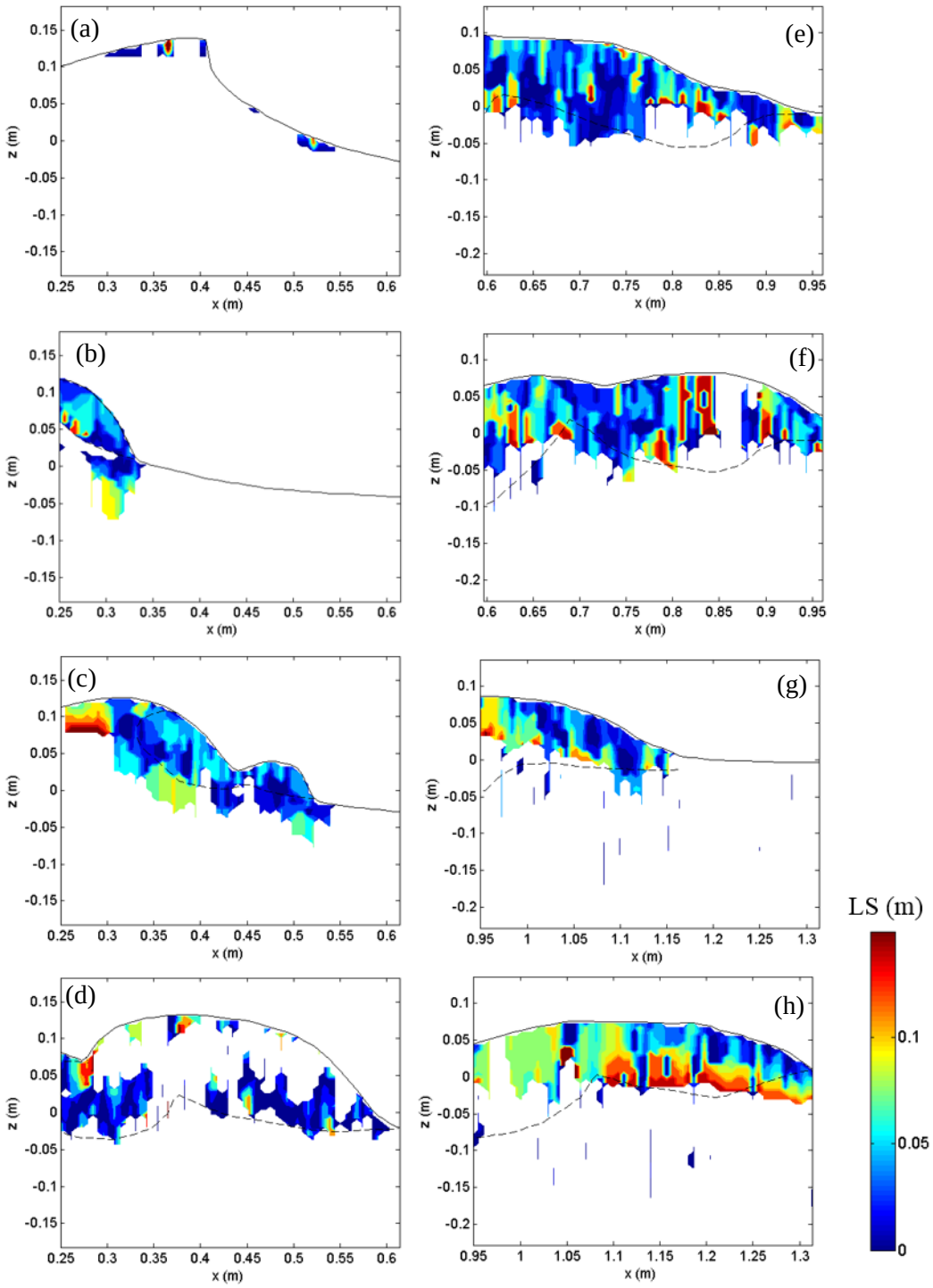

Fig. 3.5 Instantaneous length scale (*LS*) fields corresponding to Fig. 3.2 and 3.4.

3.3.3 Comparison of *LIMM*, *LS*, Swirling strength, and Vorticity

The LIMM fields were compared and validated with the corresponding swirling strength and vorticity fields. Swirling strength can be computed based on the local velocity gradient tensor. It has been applied in 2D as well as 3D flow fields (Zhou et al., 1999; Adrian et al., 2000; Camussi et al., 2002). The swirling strength, ψ, is defined as the imaginary eigenvalue of the local deformation matrix (DM) as follows:

$$DM = \begin{bmatrix} \frac{\partial u}{\partial x} & \frac{\partial u}{\partial z} \\ \frac{\partial w}{\partial x} & \frac{\partial w}{\partial z} \end{bmatrix} \tag{3.5}$$

Vorticity fields were also computed for the identification of vortical structures. Root-squared vorticity, $\omega^* = \sqrt{\omega^2}$, was used for the comparison because *LIMM* is always positive (so we are unable to distinguish the rotation direction for a vortical structure). Central differences were used to compute the spatial velocity gradients. To be consistent with the dimensionless *LIMM*, swirling strength and root-squared vorticity were also nondimensionalized over its corresponding column averaged value as follows:

$$\begin{aligned} \Psi &= \frac{\psi}{\langle \psi \rangle_z} \\ \Omega &= \frac{\omega^*}{\langle \omega^* \rangle_z} \end{aligned} \tag{3.6}$$

where $\langle \ \rangle_z$ denote the average along the z direction.

Fig. 3.6 shows the evolution of the ensemble averaged *LIMM*, 1/*LS*, Ψ and Ω over the 20 measured instantaneous fields. Note that the spatial resolution corresponding to the wavelet analysis is one half the Nyquist wavenumber (~86.5 m^{-1}), corresponding to about 0.01 m in the present study. This implies that the size of the vortices needs to be greater than 0.01 m for a reliable comparison. Overall, good agreement was found among the four variables at most stages of the breaking process. At the earlier stages of breaking shown in Fig. 3.6b-d, the condensed region with high values of *LIMM*, 1/*LS*, Ψ and Ω is consistently observed at the lower boundary of the aerated region. The concentrated region, with high values of *LIMM*, is found close to the centers of the first splash-up and the first impinging rollers when the splash-up roller is fully developed. Despite the similar patterns among *LIMM*, 1/*LS*, Ψ and Ω, the evolution of *LIMM* is more similar to that of turbulent intensity as reported in Lim et al. (2015). This is consistent with the results showing that eddies carry most of their turbulence energy under the wave crest phase (Longo, 2009). The condensed region elongates and spreads across the aerated region as turbulence continues to generate and diffuse at the later stages of breaking (Fig. 3.6e-h). For the condensed spots within the aerated rollers, those with higher values of *LIMM* seem to be more widely spread in comparison to those with high Ψ and Ω. This is probably because eddies with different scales all contribute to the determination of *LIMM*, whereas only the local velocity gradients are used in calculating Ψ and Ω.

It is practical to calculate *LIMM* using wavelet analysis to determine length scales of eddies. For example, the length scale of the eddies corresponding to the condensed high

values of *LIMM* at the center of the impinging roller marked by the left circle in the top left panel of Fig. 3.6d is about 0.05 m ($1/LS$ = 20 m^{-1}), as shown in the left circle of the top right panel of Fig. 3.6d. That length is roughly the size of the condensed region, which itself has high *LIMM* values. On the other hand, the length scale of the eddies near the lower boundary of the splash-up roller ranges from 0.03 m to 0.05 m, as shown in the right circle of the top right panel of Fig. 3.6d, which implies that the region contains a number of smaller eddies. One may also infer from the good correlation between $1/LS$ and the swirling strength that these smaller eddies feature more intense swirling motions. The similar patterns among *LIMM*, $1/LS$, Ψ and Ω indicate that the wavelet-based technique can be successfully applied to identify vortical structures and their length scales in deep water plunging breakers in the presence of an intense air entrainment.

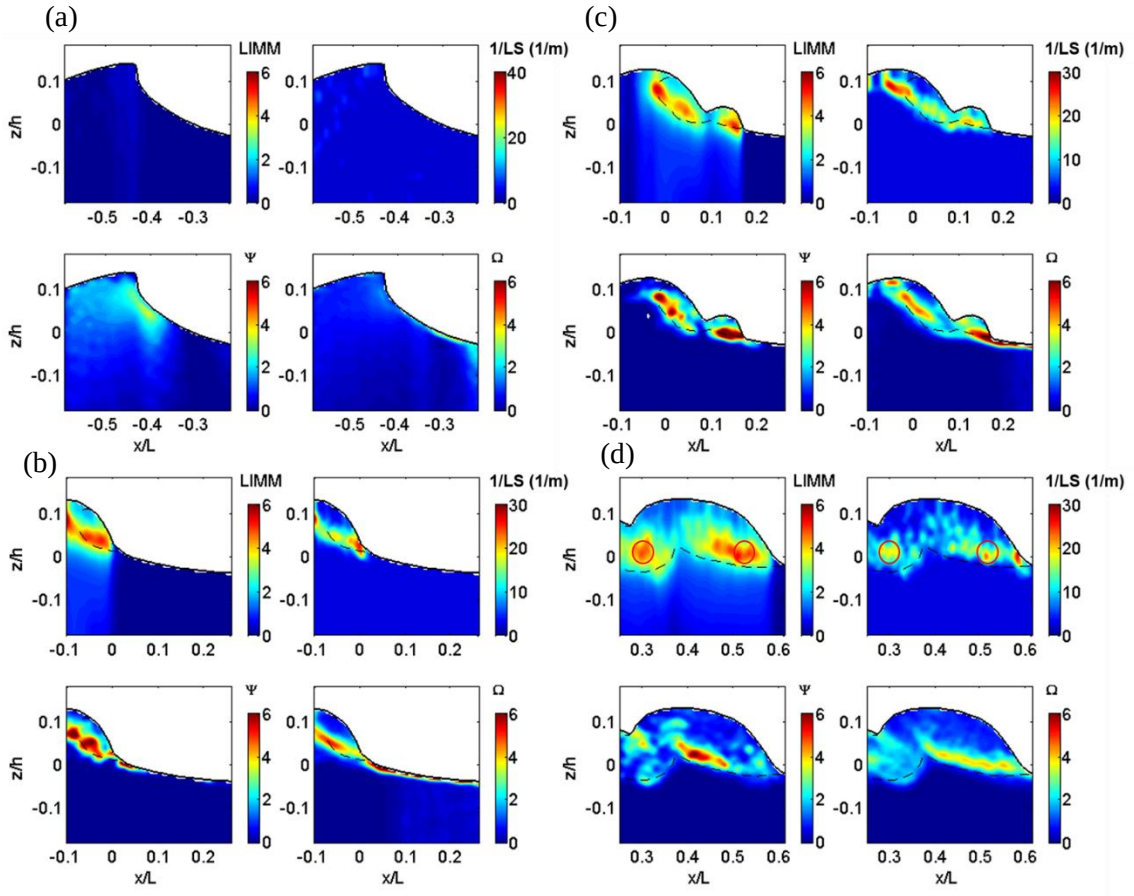

Fig. 3.6 Evolution of ensemble averaged LIMM, 1/LS (m^{-1}), nondimensionalized swirling strength (Ψ), and nondimensionalized vorticity (Ω) corresponding to the instants and locations in Fig. 3.2.

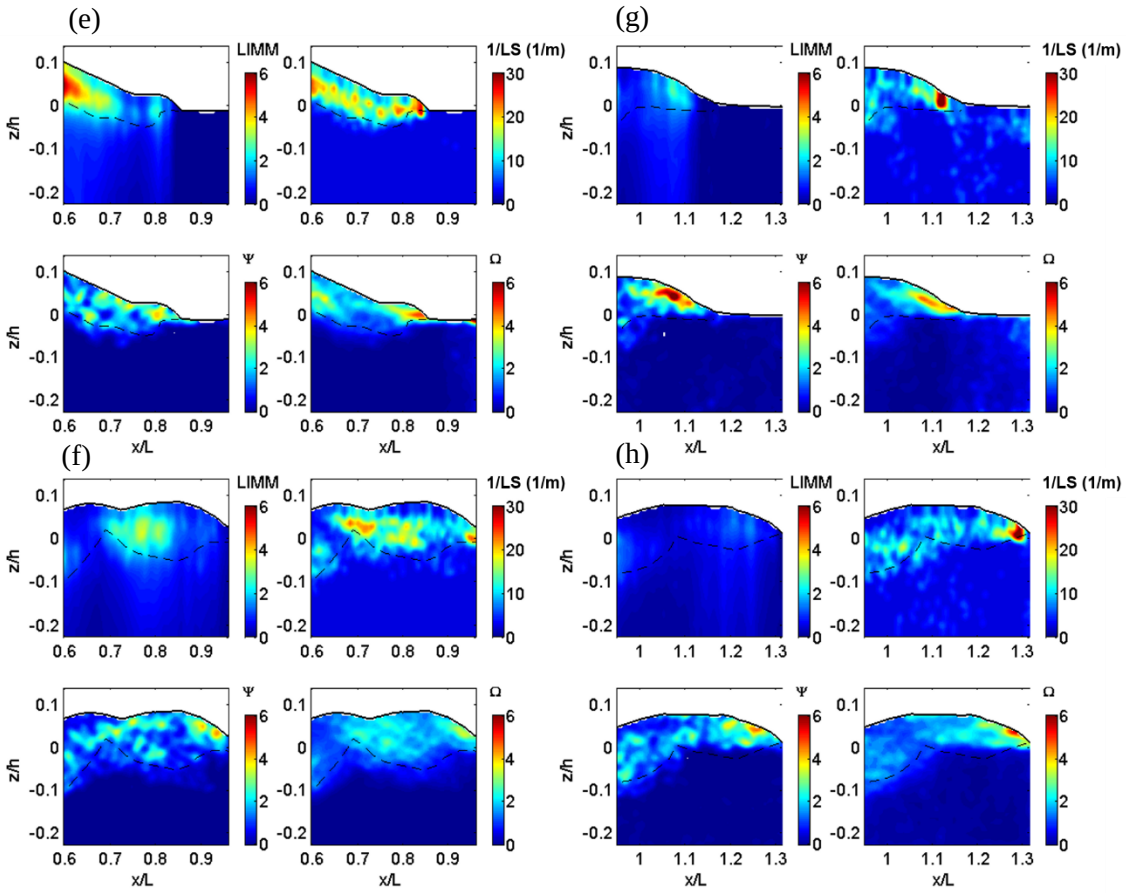

Fig. 3.6 Continued.

Fig. 3.7 shows the evolution of wave height normalized by ensemble-averaged length scales. In the region near the lower boundary of the aerated roller during the initial impinging and the first splash-up stages (Fig. 3.7b-c), the value of H / LS ranges from about 7 to 20, which corresponds to the length scales of eddies from about 0.05H to 0.15H (or 1 to 3 cm). As the breaking wave propagates, the splash-up roller and the impinging roller both begin to stretch horizontally and their length scales increase. While the most energetic eddies are able to retain their length scales at close to H for about one wave period (Fig. 3.7a-e), the length scales eventually increase after that (i.e., after Fig. 3.7f).

The value of H/LS outside the aerated region is mostly less than 1.7 (i.e., the length scales outside the aerated region are mostly greater than 0.6H or 12 cm). Note that the *LIM* approach is not applicable to the presumably laminar region outside the aerated region, so a constant value of *LIM* was assigned in the present study. This implies that the approach applying *LIMM* fails to estimate a meaningful length scale outside the aerated region. Govender et al. (2004) found that eddies in the surf-zone spilling breakers show a general increase of length scale, from wave crest downward, ranging from about 0.1h to 0.4h. With similar physical dimensions, their eddy length scale near the surface is around 2 cm – which is comparable to the physical dimensions of the eddy length scale of 1 cm to 3 cm in the aerated region in the present study. It suggests that the confining effect of the bed on eddy sizes in the breaking waves is likely insignificant. Moreover, Huang et al. (2010) showed that the length scale of eddies near the crest region in surf-zone breaking waves is close to – but about one half of – that in the present study.

The wavelet-resolved length scale inside the highly aerated region of the plunging breaking waves was compared with a classical turbulent length scale estimate based on autocorrelation. The integral length scale is a measure of the characteristic length of the energetic eddies in the flow. The integral time scale was first computed, and then was converted to the corresponding length scale by multiplying the phase speed C because the horizontal domain covered by each FOV is insufficient for the correlation computation. The integral time scale can be computed as

$$I_t = \int_0^{\infty} \frac{\langle u'(t+\tau)u'(t)\rangle}{\left\langle \left(u'(t)\right)^2 \right\rangle}\, d\tau \tag{3.7}$$

where $u'(t)$ is the horizontal component of turbulent velocity at a given point. Fig. 3.8 shows the comparisons of the wavelet-resolved length scale and the integral length at three different *z* locations at FOR station 1. Note that all the measurement locations are below the free surface over the period chosen, covering the first splash-up roller and the first impinging roller. The length scales do not vary significantly in time and space, except at 0.23 s < *t* < 0.3 s when the ascending crest (see Lim et al., 2015) with few bubbles reaches the measurement station. However, the discrepancy between the integral length scale and *LS* becomes larger at the lower measurement points. Since the wavelet-resolved length scale estimate is based on analyzing the horizontal velocity along a vertical column different from the integral length scale estimate, which is based on the autocorrelation of the horizontal velocity along an equivalent horizontal row, the discrepancy may indicate that the eddies become more elliptical at the lower part of the rollers where shear is greater.

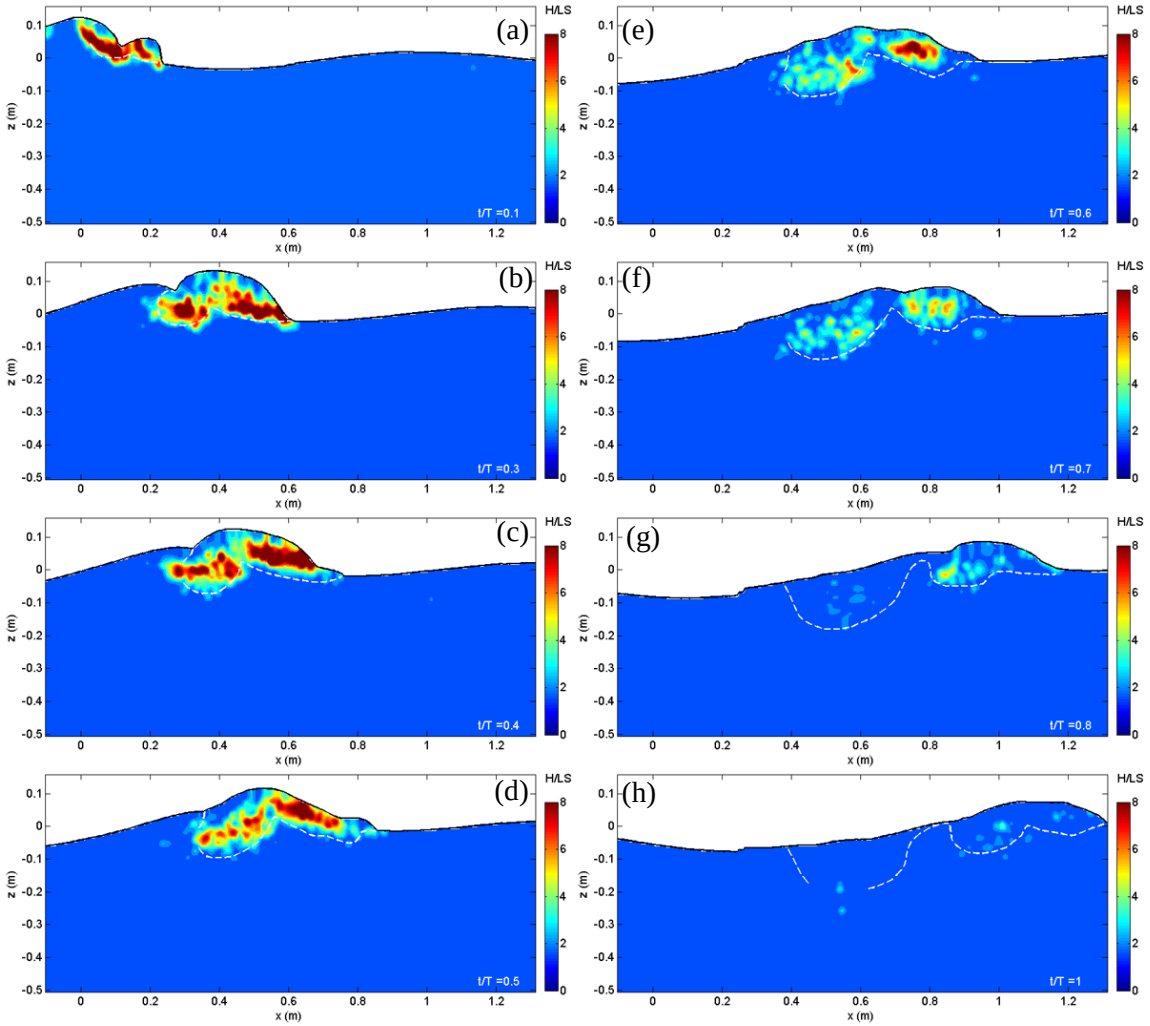

Fig. 3.7 Evolution of the normalized length scale (*H*/*LS*) at *t*/*T* = (a) 0.1, (b) 0.3, (c) 0.4 s, (d) 0.5, (e) 0.6, (f) 0.7, (g) 0.8, (h) 1.0. The dashed lines are boundaries of the aerated region identified from the BIV images.

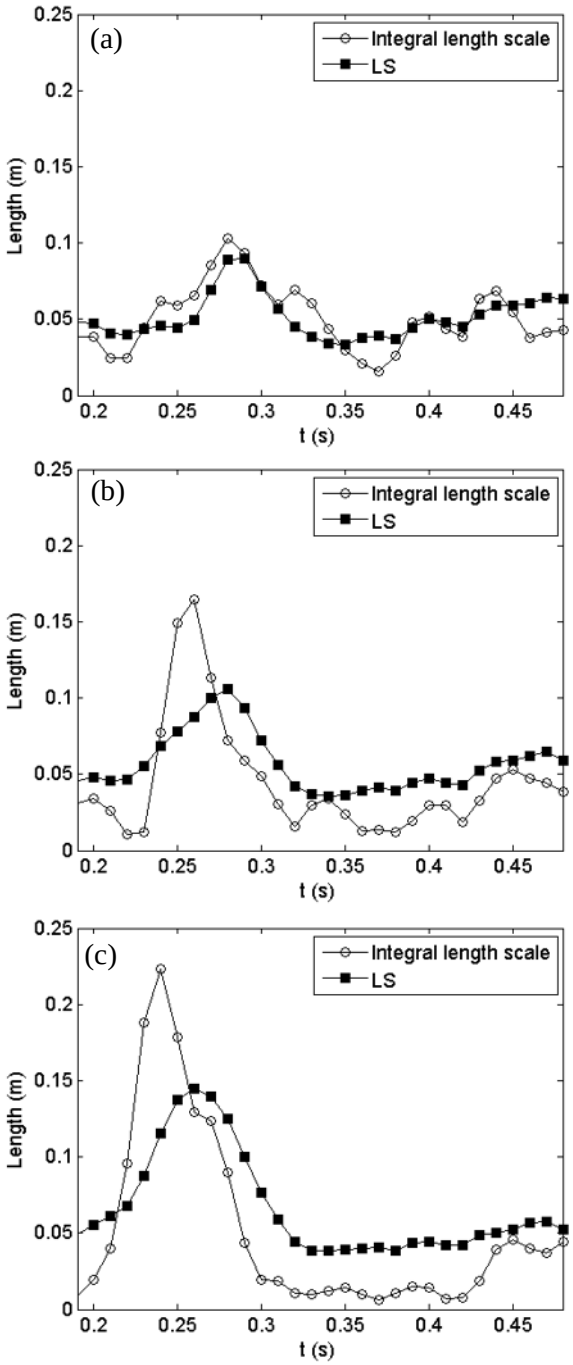

Fig. 3.8 . Comparisons between the integral length scale and the wavelet resolved length scale *LS* at *z* = (a) 0.01 m, (b) 0 m, (c) -0.01 m at FOR station 1 (*x* = 0.43 m).

3.4 Bubble Size Distribution

The FOR technique was employed to measure the void fraction and bubble size distribution within the aerated region. Fig. 3.9 shows sample FOR signals taken at station 1 (x = 0.43 m). With help from the images recorded by the high speed camera, we are able to relate the FOR signals to the wave breaking process. The probe at the measurement point encounters several stages of the breaking process, including the first splash-up roller, the ascending crest region, the first backward impingement, and the first impinging roller, as described in Lim et al. (2015). A voltage value of around 0.08 V indicates that the fiber sensor tip is in water, whereas a value around 1.0 V indicates that the tip is in air. However, the higher voltage signals that represent the gas phase do not always remain at 1.0 V because the fiber tip does not dry immediately after it leaves water. The signals fluctuate with a value higher than 0.08 V during the drying process. The voltage difference between the liquid phase and gas phase is highly distinguishable, even though the gas-phase signals fluctuate due to the rapid response of phase change when the probe is leaving water. A threshold value to separate the two phases and determine gas residence time and void fraction was set close to the gas phase (0.11 V in the present study), accounting for the maximum noise level of the liquid-phase signals. The FOR technique has been validated in Chang et al. (2003) and Lim et al. (2008). Details on void fraction measurements of the present breaking waves using FOR have been reported in Lim et al. (2015).

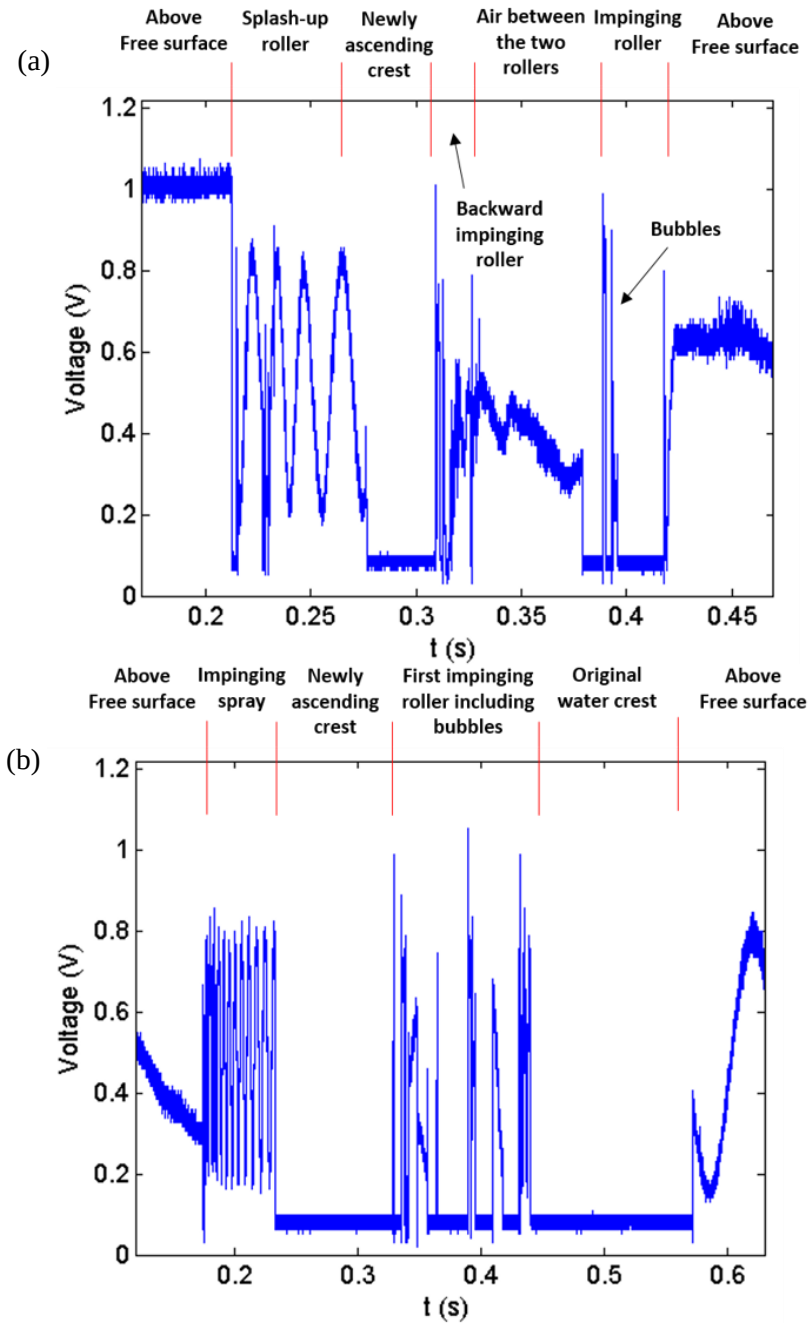

Fig. 3.9 Sample instantaneous FOR signals at station 1 (x = 0.43 m) at (a) z = 0.07 m (roughly the middle of the first splash-up roller) and (b) z = 0 m, with V > 0.11 indicating the presence of air.

The FOR signals were analyzed to detect bubbles. A total of 760 sets of FOR measurements (20 repeated runs at each of the 19, 12, and 7 vertical locations at FOR stations 1, 2 and 3, respectively) were performed to obtain the bubble chord length distributions. In the analysis, the phases that corresponded to the passage of the three splash-up rollers at each FOR station were first identified by synchronizing the BIV images and the corresponding FOR signals. The bubble signals detected only within these phases were considered as bubbles that led to the bubble size distributions in Fig. 3.12 and 3.13. Occasionally "wet" signals were detected at a relative distance ahead of the arrival of the splash-up rollers. Such signals were removed due to their likelihood of resembling droplets. However, droplets in close proximity to the splash-up rollers (or inside the rollers) could not be distinguished. Fortunately – for such small scale breakers – the BIV images showed that few droplets were observed in front of the splash-up rollers, and that a relatively small number of droplets was observed inside the splash-ups when compared to the number of bubbles. This suggests that the influence of droplets may be insignificant, at least for the small scale laboratory breakers.

The interval when the fiber tip is inside a bubble is measured and defined as the bubble residence time, T_b. Since the PIV and BIV velocity measurements in the highly aerated region are essentially based on bubble displacements, a bubble chord length, s, can be estimated as

$$s = T_b V \tag{3.8}$$

where V is the mean speed measured using PIV and BIV. To obtain the bubble chord length, both the bubble velocity and residence time must be known. Note that the FOR, BIV, and PIV measurements were not performed simultaneously. This means the FOR signals are instantaneous while the velocities are ensemble-averaged mean values – which indicates that the calculated bubble sizes would have an uncertainty of about 20% due to turbulence fluctuations. Furthermore, the above equation is for chord length estimation rather than the actual bubble size (i.e., diameter) distribution (because the probe does not always intersect a bubble at its center). To convert from a chord length distribution to the equivalent size distribution, a statistical correction is needed. Although Clark and Turton (1988), Liu and Clark (1995), and Liu et al. (1996) provided methods to convert the bubble diameter distribution from a chord length distribution based on probabilistic analysis, applying their methods was not successful in the present study (especially at the upper and lower extremes of the size distribution) because of the complex flow condition. Alternatively, Serdula and Loewen (1998) and Rojas and Loewen (2007) suggested a simple average correction factor of 3/4 to convert the measured chord length to bubble radius following the analysis of Saberi et al. (1995). The uncertainty due to the use of the average correction factor may be estimated as the standard deviation of the measured chord lengths from the averaged chord length, $\sigma^2 = \int_0^r (s-\bar{s})^2 P(x)dx$, where r is the radius of bubble, $s = \sqrt{r^2 - x^2}$ is the measured chord length, $\bar{s} = 4r/3$ is the average chord length, and $P(x)$ is the probability density function. The calculated standard deviation is about $0.47r$ or 24% of the bubble diameter.

In the present study, the total number of bubbles (s > 0.125 mm) detected is 2569, 1111, and 656 at FOR station 1, 2, and 3, respectively. Clark and Turton (1988) suggested that bubbles with a diameter smaller than the probe diameter would resist piercing unless the bubble velocity is very high. Since the chord length is always less than the diameter of a bubble, the measured chord lengths shorter than the diameter of the FOR probe of 125 μm were not included in the bubble size distribution. The results show that bubbles with a chord length s < 2 mm (defined as "smaller bubbles" hereafter) account for 42% of all the bubbles detected during the first splash-up process at FOR station 1. A similar percentage of smaller bubbles was found during the second and the third splash-ups at FOR stations 2 and 3 (although the total numbers of bubbles detected was significantly lower). Using s = 2 mm to separate bubbles into two groups is justified by the Hinze scale (Deane and Stokes, 2002) that is discussed in the following sections.

Fig. 3.10 shows the spatial distributions of the bubble chord lengths at the three FOR stations plotted as histograms. At FOR station 1, more than 85% of the smaller bubbles (i.e. $s < 2$ mm) were found above the still water level (SWL) as shown in Fig. 3.10a, indicating that the majority of the smaller bubbles were created by the impact and the subsequent splashing up in the wave breaking process. On the other hand, larger bubbles are more uniformly distributed over the vertical water column. Deane and Stokes (2002) suggested two distinct flow features that drive bubble creation in breaking waves: smaller bubbles are created by the impact and subsequent splashing, while larger bubbles are created by the collapsing air cavity. This is because bubble break-up, or fragmentation, occurs when the differential pressure force associated with turbulence exceeds the

restoring force of surface tension (Hinze, 1955). Deane and Stokes' bubble creation mechanism is consistent with the observation in the present study. At FOR station 2, the number of larger bubbles decreases to about one half of that at FOR station 1. At FOR station 3, the number of larger bubbles continues to decrease to about one fifth of that in the first splash-up, and they (i.e. these larger bubbles) were observed to burst on the free surface (based on the BIV images).

Fig. 3.11 shows the vertical distributions of the number of smaller and larger bubbles measured during the passage of the splash-up roller (Fig. 3.11a-b) and the impinging roller (Fig. 3.11c-d) at FOR station 1. The swirling strength, averaged over the corresponding "bubble generation" stage, was also plotted for comparison. By identifying the phases that correspond to the passage of different rollers at FOR station 1, bubbles generated by the first splash-up roller were distinguished from those generated by the first impinging roller (i.e. bubbles generated from the fragmentation of the air cavity). During the passage of the impinging roller, the distribution of smaller bubbles shows good correlation (correlation coefficient r = 0.72) with the swirling strength (Fig. 3.11c), whereas the correlation is weaker (r = 0.56) for the larger bubbles (Fig. 3.11d). The results imply that the local swirling motion of the energetic eddies, and the associated differential pressures acting on the bubbles, enhance the breakup of the larger bubbles into smaller bubbles. Thus, the distribution of swirling strength and the number of smaller bubbles are clearly correlated. On the other hand, during the passage of the first splash-up roller (Fig. 3.11a-b), the swirling strength shows much weaker correlation with the number of bubbles generated during the process. The results suggest that the local swirling motion that causes bubble

break-up, as shown in Fig. 3.11c-d, is not the dominant mechanism for bubble creation in the first splash-up roller. Note that the number of bubbles generated in the first splash-up roller is not significantly different from that generated in the first impinging roller, except for with the smaller bubbles ($s < 2$ mm) at $z = 0.01$ m and $z = 0.02$ m (as shown in Fig. 3.11a). In these elevations, high shear occurred due to the differential motion between the high-speed rotation in the first splash-up roller and the low-speed wave motion under the trough level.

Fig. 3.12 shows the probability density function (PDF) of bubble size measured at FOR station 1 during the passage of the first impinging roller (Fig. 3.12a) and the splash-up roller (Fig. 3.12b). Bubbles in these two rollers are analyzed separately because of their distinct behavior. The PDF is defined as

$$P(x,s)\,\mathrm{d}s = \frac{1}{N}\sum_{z} N_s(x,z,s)\Delta s \tag{3.9}$$

where P is the PDF, N is the total number of measured bubbles within one wave period, N_s is the number of bubbles per wave period at a particular measurement location (x, z) (i.e., the 19, 12, and 7 points at FOR stations 1, 2 and 3, respectively) with a particular bubble size (s), and Δs is the bin size. The bubble size distribution is, in general, represented as the bubble count per unit volume. Since the measurement volume is not well defined in the present study, it is simply plotted as a PDF. Fig. 3.12a shows two distinct power law scaling relationships during the passage of the first impinging roller. On the contrary, Fig. 3.12b does not clearly show distinct slopes during the passage of the

first splash-up roller. For the bubbles associated with the impinging roller (Fig. 3.12a), the two slopes are Φ_{1f} = -0.9 and Φ_{2f} = -2.9 with a slope change occurring at about s = 3.0 mm for both. Deane and Stokes (2002) used video recordings to obtain the bubble size distribution in breaking waves in seawater. They found that the distinct change of the two slopes (Φ_1 = -1.5 and Φ_2 = -3.3 in their study) occurred for bubble radii larger than approximately 1 ~ 2 mm, and they defined that scale as the "Hinze scale" (Hinze, 1955). Since our data is based on the chord length distribution, if the average conversion factor of 3/4 (between the chord length and the radius) is applied, the Hinze scale (in radius) becomes a_H = 2.3 mm which is close to what Dean and Stokes found. The reason for the discrepancy between the power law scaling and the Hinze scale may be attributed to the fact that the use of seawater in Deane and Stokes leads to an increase of the surface tension. Moreover, the difference may also be attributed to calculating the bubble size/frequency between images and FOR. The FOR system determines the chord lengths of bubbles that penetrate through the miniature tip of the probe ($125\mu m$ in diameter) – so only bubbles that encountered the probe tip were recorded. It is possible that smaller bubbles, which might not be accounted for in the current study, were included in Deane and Stokes (2002) – and thus explain the decreased steepness of the slope Φ_1 (in the present study).

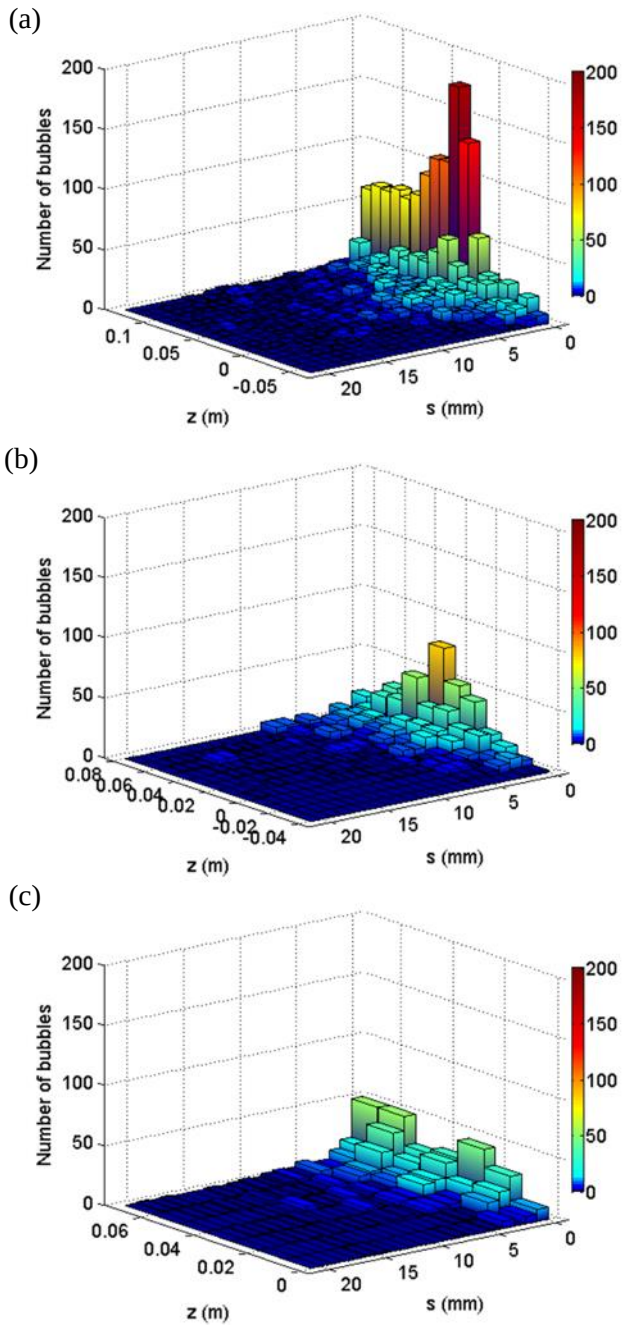

Fig. 3.10 Histograms of chord length distributions at (a) FOR station 1, (b) FOR station 2, and (c) FOR station 3.

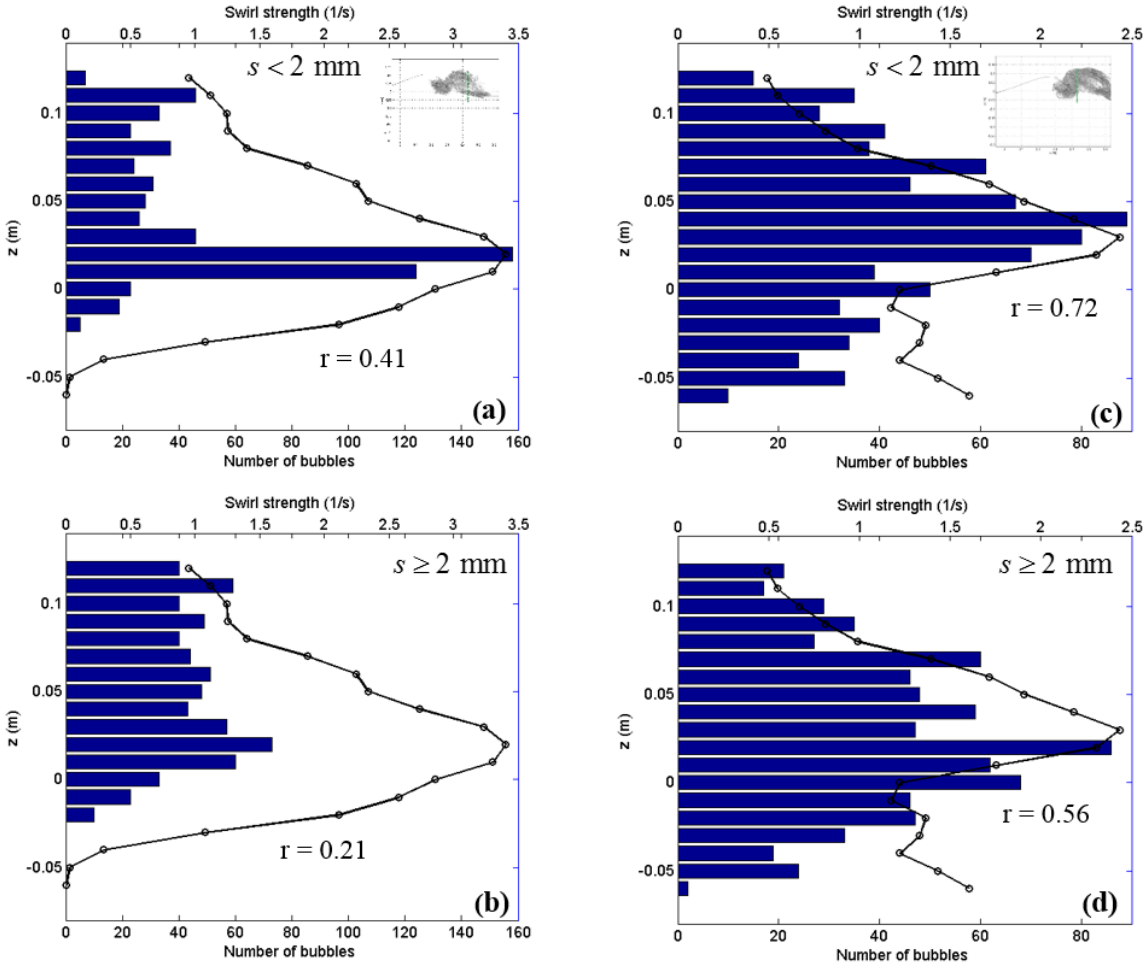

Fig. 3.11 Vertical distributions of the number of bubbles with a chord length of $s < 2$ mm (a, c) and $s \geq 2$ mm (b, d) measured during the passage of the splash-up roller (a, b) and the impinging roller (c, d) at FOR station 1. The insets illustrate the measurement locations at the two rollers. The lines indicate the vertical distribution of stage-averaged swirling strength. No bubbles were detected below $z < -0.02$ m in the splash-up roller. The r value denotes the correlation coefficient between the number of bubbles and the corresponding swirling strength.

Despite the results showing that the slope for smaller bubbles is flatter, the slope for larger bubbles and the Hinze scale in the present study are consistent with the values previously reported by Deane and Stokes (2002), Rojas and Lowen (2007), and Mori and Kakuno (2008). Using a dual-tip fiber probe in plunging breaking waves, Rojas and Lowen (2007) suggested a radius of 1.5 mm for the Hinze scale and power law scaling of Φ_1 = -1.5 and Φ_2 = -3.0. They measured bubble sizes at 1.5 cm below the SWL with repeated breaking waves. Mori et al. (2007) found a Hinze scale of 2.0 mm and 4.3 mm in their small-scale and large-scale experiments, respectively, and power law scaling of Φ_1 = -1.5 and Φ_2 = -1.7. Mori and Kakuno (2008) used an imaging technique to measure the bubble sizes and found a Hinze scale of 3.0 mm and power law scaling of Φ_1 = -1.0 and Φ_2 = -3.4 for surf zone breaking waves.

The distribution of bubbles within the splash-up roller does not show a distinct change of slope throughout the entire range of bubble sizes (Fig. 3.12b). It was observed from the images, and the corresponding FOR signals, that the splash-up roller consists of water droplets and air bubbles induced by the upward momentum due to the impact and splash up of the overturning jet. Few measurements of bubble size in the first splash-up roller were reported since most of the previous studies were mainly concentrated on bubbles located close to, or below, the SWL (e.g., Serdula and Loewen, 1998; Rojas and Loewen, 2007; Mori et al., 2007; Blenkinsopp and Chaplin, 2010). As far as the authors know, this is the first estimate of the bubble size distribution in the splash-up roller in plunging breaking waves. This makes direct comparisons infeasible. In Fig. 3.12b, the slope of the larger bubbles in the splash-up roller is not steep compared with that in the

case of the impinging roller in Fig. 3.12a. This may indicate that larger bubbles initially entrained in the splash-up roller remained close to the surface in the roller, leading to a relative large number of larger bubbles. These larger bubbles may move upward and burst out of the free surface, or may move downward and break up due to the strong swirling motion (as they move deeper). In either case the result is a smaller number of larger bubbles at depth. Similarly, Baldy (1988), Rojas and Loewen (2007), and Blenkinsopp and Chaplin (2010) observed that the slope of the larger bubbles becomes steeper with depth in the impinging roller. Direct comparisons between their observations and the present study are not possible due to an insufficient number of bubbles at each depth in the present study. However, their observations are consistent with the bubble size distribution in the splash-up roller in the present study. Even though the turbulence intensity is very high in the splash-up roller (Lim et al., 2015), bubble break-up does not occur as frequently as it does in the impinging roller (in Fig. 3.12a), leading to a flatter slope in Fig. 3.12b. The cause is not clear, but the very high void fraction in the first splash-up roller (Lim et al., 2015) is likely involved.

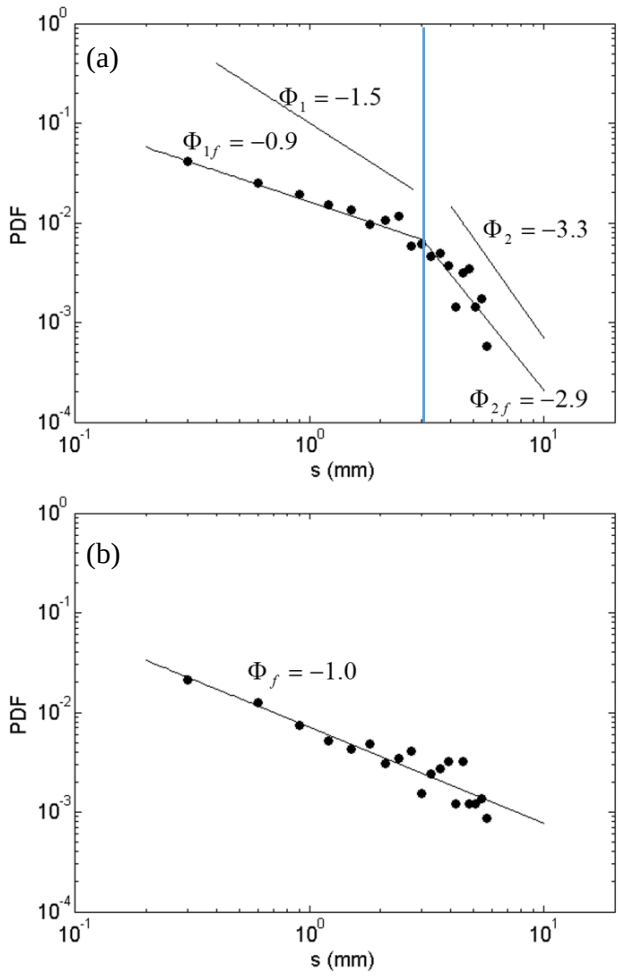

Fig. 3.12 The bubble size distributions at FOR station 1 during the passage of (a) the impinging roller (t = 0.3 – 0.7 s), and (b) the splash-up roller (t = 0 – 0.3 s). The lines in (a) are least-square fits (with exponents of Φ_{1f} and Φ_{2f}), and power-law scaling lines from Deane and Stokes (2002) (with exponents of Φ_1 and Φ_2) are shown for comparison. The vertical line at the slope change denotes the Hinze scale. The line in (b) is the least-square fit of the measurement data.

Fig. 3.13 shows the PDF of bubble sizes at FOR stations 2 and 3. In Fig. 3.13a, the two power law scaling relationships (Φ_{1f} = -1.4, Φ_{2f} = -3.2) and the Hinze scale (a_H ~ 2.8 mm) at FOR station 2 are shown. These values are similar to those found at FOR station 1 for the impinging roller (Φ_{1f} = -0.9, Φ_{2f} = -2.9, and a_H ~ 2.3 mm), as shown in Fig. 3.12a. This similarity of bubble size distribution implies that the bubble formation process is similar between the first impinging roller and the second impinging and splash-up rollers, in which the splash-up is rather weak. The same power law scaling at FOR station 2 was directly applied to the bubble size distribution at FOR station 3, as shown in Figure 13b, due to an insufficient number of bubbles for a reasonable regression fit. The weak turbulence level (less than one half of that at FOR station 2) may lead to less bubble break-up events, in addition to bubbles bursting at the free surface during that breaking stage.

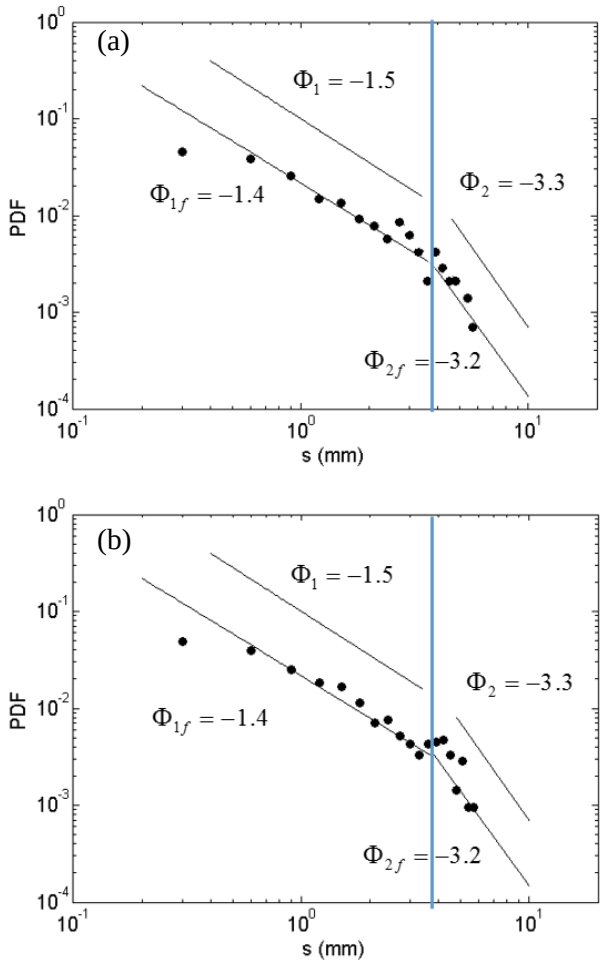

Fig. 3.13 The bubble size distributions at (a) FOR station 2 and (b) FOR station 3. The lines are least-square fits (with exponents of Φ_{1f} and Φ_{2f}) and power-law scaling lines from Deane and Stokes (2002) (with exponents of Φ_1 and Φ_2) are shown for comparison. The fitted lines for (a) are used in (b) due to an insufficient number of bubbles. The vertical line at the slope change denotes the Hinze scale.

Blenkinsopp & Chaplin (2007) presented void fraction estimates in breaking waves using an optical fiber system, and they used between 200 and 400 waves at each measurement location to ensure stable void fraction estimates. In comparison, only 20 repeats at each FOR measurement point were performed for ensemble averaging in the present study. The number of repeats is obviously insufficient to result in converged void fraction estimates, and is insufficient for bubble counting and sizing. However, this is a unique study that measured both void fraction and velocity fields. Repeating more than 20 times for each of the 38 FOR measurement points is impractical considering that a total number of 1,120 repeated measurements (760 for FOR, 340 for PIV and BIV combined, and 20 for wave gauges) have already been performed in the present study. As mentioned in Lim et al. (2015), the authors spent more than one year to complete the data collection (when including initial trial tests used to optimize the instrumentation and data acquisition), and then a few more years for data analysis and summarizing the findings. Even though the number of bubbles detected in the present study is insufficient to result in a spatial distribution of bubble sizing, the reasonably large numbers of total detected bubbles (2569, 1111, and 656 at FOR station 1, 2, and 3, respectively) seem to be enough for the depth-integrated analysis. The number of bubbles detected at FOR station 1 is indeed comparable to that used for calibration under plunging breaking waves by Rojas and Loewen (2008). The findings presented in the figures – even though not as smooth as one would expect to see for converged results – seem to be sufficient to interpret the underlying physics.

3.5 Effects of Void Fraction to Energy Dissipation

Energy dissipation in the active breaking zone of a breaking induced two-phase flow is one of the least understood parts in the study of wave breaking. Great efforts and progress have been made in the study of bubble entrainment and evolution under breaking waves both numerically (e.g. Ma et al. 2011; Derakhti and Kirby, 2014) and experimentally (e.g. Cox and Shin, 2003; Mori et al., 2007; Blenkinsopp and Chaplin, 2010). However, experimental results are mostly based on void fraction or turbulence measurements. The relation between the two – probably due to the difficulties in measuring both void fraction and velocity in the highly aerated flow – has rarely been reported. Void fraction can be used to quantify the mixture density, which in turn can be applied to estimate both the liquid phase wave energy and dissipation in plunging breaking waves (Lim et al., 2015). In this section, we expanded Lim et al.'s study to quantify the turbulent dissipation rate – both with and without considering the void fraction – and relate the turbulent dissipation rate to the total energy dissipation rate. Turbulence dissipation featuring the dispersed phase in breaking waves has rarely been reported in experimental studies. Here we also discussed the turbulence dissipation rate by dispersed bubbles, and the role it plays in energy balance in the wave breaking process.

3.5.1 Estimation and Comparison of Turbulent Dissipation Rate

For a flow with a balanced turbulence kinetic energy production and dissipation, the turbulence dissipation rate can be estimated from the Kolmogorov -5/3 spectral slope in the inertial subrange of the velocity spectrum. Using the isotropic assumption, the spectra

E and the turbulent dissipation rate ε in the inertial subrange have the following relationship (Tennekes and Lumley, 1972):

$$E(\kappa) = \frac{18}{55}\beta\varepsilon^{2/3}\kappa^{-5/3} \tag{3.10}$$

where $\beta = 1.5$ is the universal Kolmogorov constant and κ is the wavenumber along the horizontal (streamwise) direction. In the present study, the wavenumber spectra of each row of the measured velocity field was ensemble-averaged and then wave-averaged to estimate the time averaged turbulence dissipation rate. The wave-averaged quantity f_{wa} (wet-period averaged) and the period-averaged quantity $\overline{f}$ (averaged over one-wave period) for a variable f at a given point are defined as

$$f_{wa}(x,z) = \frac{\int_{t_{tr}(x,z)}^{t_{tr}(x,z)+T} \delta(x,z,t) f(x,z,t) dt}{\int_{t_{tr}(x,z)}^{t_{tr}(x,z)+T} \delta(x,z,t) dt} \tag{3.11}$$

$$\overline{f}(x,z) = \frac{\int_{t_{tr}(x,z)}^{t_{tr}(x,z)+T} \delta(x,z,t) f(x,z,t) dt}{\int_{t_{tr}(x,z)}^{t_{tr}(x,z)+T} dt} \tag{3.12}$$

where $t_{tr}(x\ ,\ z)$ is the time when the front trough reaches a specific measurement point. $\delta(x,z,t) = 1$ when the point (at time t) is in the water, and $\delta(x,z,t) = 0$ otherwise. Only

the wetted region is considered in the calculation of wave-averaged quantities, while the period-averaged values are obtained from the summation of quantities divided by the corresponding local wave period.

Fig. 3.14 shows the wave-averaged wavenumber spectra of horizontal velocity fluctuations at various depths. Based on measurements in FOV5 that feature the initial impinging and the first splash-up roller, the spectra decay less rapidly when ($\kappa < 70$ rad/m), more rapidly when close to ($70 < \kappa < 170$ rad/m), and again less rapidly when ($\kappa > 170$ rad/m). The ranges of the estimated inertial subrange, and the three stages, are similar to those reported by Drazen and Melville (2009) and Govender et al. (2004) for the post breaking velocity field and surf-zone spilling breakers, respectively. The inertial subrange typically extends from the size of large eddies, which can be determined by the physical dimensions of the flow (e.g., the wave height) relative to the Kolmogorov microscale. The vertical size of the first splash-up roller yields $\kappa \sim 42$ rad/m (or 0.15 m) for the lower limit of the inertial subrange, and our estimation of $\kappa < 70$ rad/m is in reasonable agreement. The dissipation rate in the current study roughly ranges from 10^{-4} ~ 10^{-3} m^2/s^3, resulting in a Kolmogorov microscale $\eta = \left(\nu^3 / \varepsilon\right)^{1/4}$ of about 0.1 mm – which is about one order of magnitude smaller than the spatial resolution of the current velocity measurements.

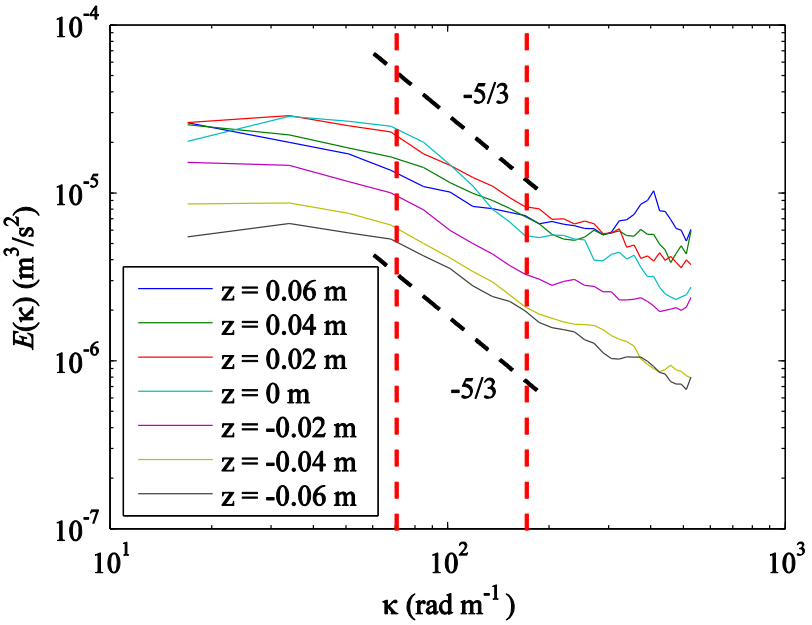

Fig. 3.14 Wave-averaged wavenumber spectra at different vertical locations. The region between the two dotted lines ($70 < \kappa < 170$ rad/m) is referred to as the inertial subrange for comparison with the Kolmogorov -5/3 scaling. All the slopes are flatter than -5/3 except the one for z = 0 m.

The less rapid decay of the spectrum in the larger wave number region in the present study was also observed in previous wave breaking studies (Govender et al., 2004; Drazen and Melville, 2009). Doron et al. (2001) and Nimmo Smith et al. (2005) reported that this less rapid decay rate is due to the build-up of energy near the border between the inertial subrange and the dissipation range. Another interesting feature in Fig. 3.14 is that the number of bubbles and the steepness of the slope seem to be related. The slopes near the inertial subrange are less steep above the SWL compared to that below the SWL, whereas the numbers of bubbles detected above the SWL are greater than that below the SWL, as shown in Fig. 3.10. Similarly, Rensen et al. (2005) observed a milder slope for a two-phase bubbly flow, in comparison to that for a grid generated single-phase turbulent flow. That

implies the energy increase at the smaller length scale is caused by the direct forcing through the bubbles, while the reduction of the energy at the larger length scales is caused by bubble accumulation.

The turbulent energy dissipation rate is estimated using several approaches, including that based on the spectrum analysis and that from the measured velocity fields (as stated in Doron et al. (2001) and detailed in the Appendix 3A). The turbulent dissipation rate ε_{LF} was computed from the wavenumber spectrum based on Equation 3.10 using least-square fits over the inertial range ($70 < \kappa < 170$ rad/m) where the -5/3 slope was found. Fig. 3.15 shows the vertical profiles of the estimated wave-averaged turbulent energy dissipation rate using five different methods at FOR stations 1 to 3. All the estimates are of the same order-of-magnitude and do not differ significantly. The ε_D values obtained from the "direct" estimate (Doron et al., 2001) are greater than those of the other four estimates. This is likely caused by the assumption that the lateral fluctuations are of similar magnitude as the streamwise fluctuations. In Fig. 3.15a, the high dissipation rate is concentrated within the aerated region above the trough level, indicating that strong turbulence is generated in the impinging and splash-up roller region at FOR station 1 (see Fig. 3.6d for comparison). The dissipation rate follows an exponential decay below the lower boundary of the splash-up roller (z ~ -0.03 m). The peak dissipation rate occurs near the SWL, and coincides with the condensed high intermittency and vorticity (as shown in Fig. 3.6d). At FOR station 3, ε_D shows a similar level of magnitude in estimating ε as compared with using other methods. This implies that the isotropic assumption may not be much of an issue when the maximum wave-averaged void fraction is small (~ 0.32) compared to the value of 0.6 at

FOR station 1 (see Figure 13a in Lim et al., 2015). The dissipation rate at FOR station 3 is reduced to about only 10% of that at FOR station 1. The turbulence dissipation rates below the lowest limit of the aerated region at FOR stations 2 (z ~ -0.04 m) and 3 (z ~ 0 m) follow an exponential decay pattern, similar to that in the spilling breakers reported by Ting and Kirby, (1996), Govender et al. (2004), and Huang et al. (2009).

In the later analysis, ε_D was chosen to present ε because it may be the most straightforward method that involves the least number of assumptions. It features all the measured gradients (which is not the case for ε_A), less empirical assumptions for the empirical relation (as in estimating ε_C and ε_E), and no assumptions about isotropic turbulence in the inertial range (as in estimation ε_{LF}). Another reason of choosing ε_D was that it led to the lowest excess energy dissipation (i.e., energy dissipation due to sources other than continuous-phase turbulence) and the least discrepancy for the estimated bubble-induced dissipation in the present study (to be discussed later).

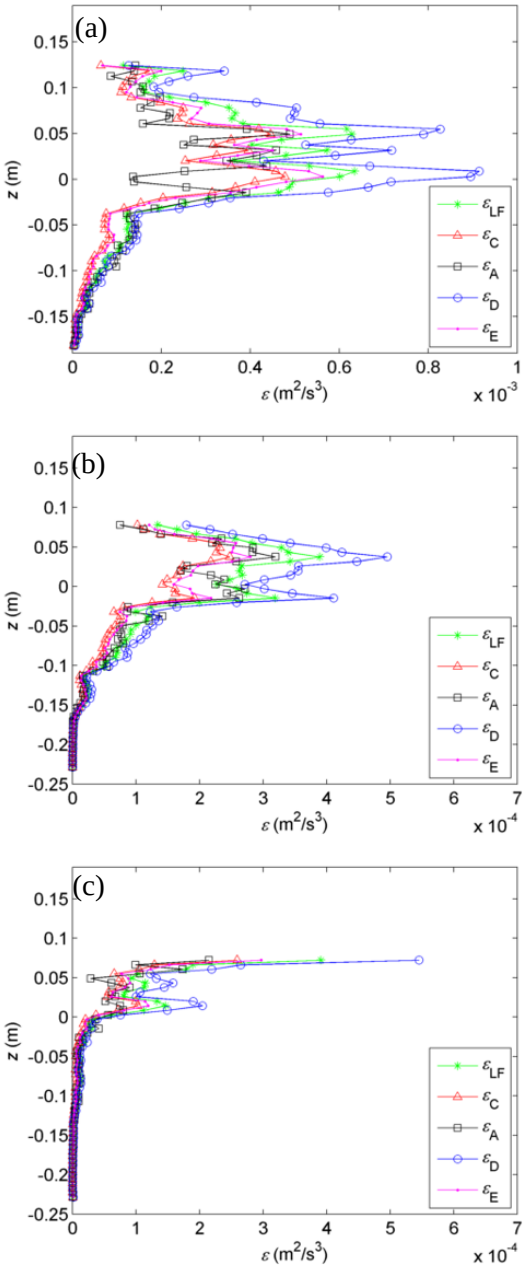

Fig. 3.15 The wave-averaged turbulence dissipation rate, ε, estimated using five different methods at (a) FOR station 1, (b) FOR station 2, and (c) FOR station 3. Details of the Methods are stated in the Appendix E.

3.5.2 Turbulent Dissipation Rate Considering Void Fraction

Implementing a two-phase (gas-liquid) model in breaking wave studies has not been practical, nor has it been widely reported. However, the multiphase nature is essential in determining energy dissipation in the active breaking region, especially in plunging breaking waves featuring high air entrainment. The dispersed bubbles entrained by waves breaking have intense interactions with the mean flow and turbulence, and produce complex two-phase bubbly flows. For example, it is well known that the presence of bubbles can suppress liquid phase turbulence (Wang et al., 1987; Serizawa and Kataoka, 1990; Ma et al., 2011) while the turbulent coherent structures generated by breaking can enhance the bubble entrainment (Baldy, 1993; Ma et al., 2012). To calculate the liquid phase turbulent dissipation rate, void fraction measurements were used to modulate the mixture viscosity based on mixture theory (Ishii and Mishima, 1984; Manninen et al., 1996). In a two-phase bubbly flow, the mixture density can be written as

$$\rho_m = \rho_a \langle \alpha \rangle + \rho_w \left(1 - \langle \alpha \rangle\right) \approx \rho_w \left(1 - \langle \alpha \rangle\right) \tag{3.13}$$

where the subscripts *a*, *w*, and *m* represent air, water, and air-water mixture, respectively, and α is the local void fraction. The mixture viscosity model (Ishii and Zuber, 1979) can be employed to estimate the dynamic viscosity of bubbly flows. It extends the linear relationship between the mixture viscosity and the continuous phase fluid viscosity to an empirical power relation as follows

$$\frac{\mu_m}{\mu_c} = \left(1 - \langle \alpha_d \rangle\right)^{-2.5\frac{\mu_d + 0.4\mu_c}{\mu_d + \mu_c}} \tag{3.14}$$

where the subscripts *c* and *d* denote continuous phase (water) and dispersed phase (air). Since, $\mu_d << \mu_c$, the power term $-2.5\left(\mu_d + 0.4\mu_c\right)/\left(\mu_d + \mu_c\right) \approx -1$. Therefore the turbulent dissipation rate in a bubbly flow can be formulated as

$$\varepsilon_m = \varepsilon_w \left(1 - \langle \alpha \rangle\right)^{-1} \tag{3.15}$$

where ε_m and ε_w denote the turbulent dissipation rate of the air-water mixture (two-phase) flow and the water (single-phase) flow, respectively.

Fig. 3.16 shows the vertical distributions of the wave-averaged turbulent dissipation rate ε_D with (denoted as ε_m) and without (denoted as ε_w) considering void fraction at the three FOR stations. Among the three FOR stations, a somewhat similar trend is observed even though the magnitudes are quite different. Evidently, the high values of ε_m occur near the lower boundary of the splash-up rollers. The distributions reflect the fact that the fluctuation level is higher with the presence of a high velocity gradient or shear, as shown in Lim et al. (2015), and becomes lower below the aerated region. To examine the effects of void fraction, the figure shows that ε_w is only 30%, 66%, and 88% of ε_m when

integrated with respect to *z* at FOR stations 1, 2 and 3, respectively, due to the difference in the void fraction level. The maximum values of wave-averaged void fraction occur at the top of the wave crest, reaching 0.57, 0.49, and 0.32 at FOR stations 1, 2, and 3, respectively (Lim et al., 2015). The discrepancy is significantly smaller at the third splash-up (FOR station 3) when compared with that at the first two splash-ups. The results indicate that the presence of bubbles plays a prominent role in enhancing the turbulent dissipation rate, especially with a void fraction over 0.5. Similarly, the presence of bubbles can suppress liquid phase turbulence (Wang et al., 1987; Serizawa and Kataoka, 1990; Ma et al., 2011), change the local vorticity, and eventually deform or displace vortex structures (Watanabe et al., 2005). Ma et al. (2011) simulated turbulence dissipation rates and showed in their Figure 6 (at $t/T = 0.1$) that the maximum turbulent dissipation rate accounting for void fraction is about 3 times of that without considering void fraction. This is consistent with our observation at FOR station 1 (Fig. 3.16a).

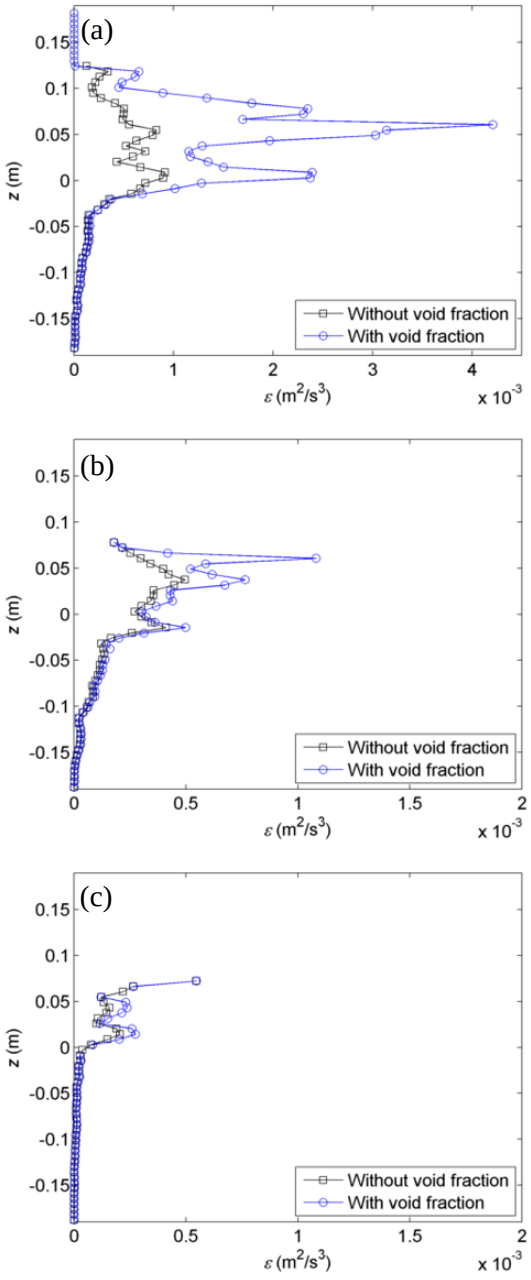

Fig. 3.16 Vertical profiles of the wave-averaged turbulent dissipation rate, ε_D, with and without considering void fraction at (a) FOR station 1, (b) FOR station 2, and (c) FOR station 3.

3.5.3 Turbulence Dissipation Rate Versus Total Energy Dissipation Rate

Following *Lim et al.* (2015), the total energy E (and therefore its dissipation) – considering the effects of void fraction – was computed as the sum of the period-averaged, depth-integrated mean kinetic energy K_{di}, the turbulent kinetic energy k_{di}, and the potential energy PE per unit mass as follows.

$$\begin{aligned} K_{di} &= \int_{-h}^{\eta} \overline{\left(1-\langle\alpha\rangle\right)\frac{1}{2}\left(U^2+W^2\right)}dz \\ k_{di} &= \int_{-h}^{\eta} \overline{\left(1-\langle\alpha\rangle\right)\frac{1.33}{2}\left(\left\langle u'^2\right\rangle+\left\langle w'^2\right\rangle\right)}\,dz \\ PE &= \int_{-h}^{\eta} \overline{(1-\langle\alpha\rangle)gz}dz-\frac{1}{2}gh^2 \\ E &= K_{di}+k_{di}+PE \end{aligned} \tag{3.16}$$

where η is the free surface elevation measured using images, and U and W are the mean horizontal and vertical velocities. The variation of total energy decreases relatively slowly before x/L = 0.33, then decreases rapidly beyond that point. This roughly follows the inverse trend with respect to the distance, as shown in Lim et al. (2015), and can be formulated as

$$\frac{E_\alpha}{E_L}=1.47\exp(-1.17x/L) \qquad \text{for } \frac{x}{L}>0.33 \tag{3.17}$$

where E_α is the breaking wave energy with void fraction considered, and E_L is the pre-breaking wave energy. For $x/L \le 0.33$, E_α/E_L = 1.0 is assumed due to the small energy variation and the lack of void fraction data. The total energy dissipation rate dE/dt is calculated by differentiating Equation 3.17 with respect to x and multiplying in the group velocity C_g as follows.

$$\frac{dE}{dt} = 1.72 \frac{C_g}{L} \exp(-1.17 x / L) \qquad \text{for} \quad \frac{x}{L} > 0.33 \tag{3.18}$$

Eq. 3.18 indicates that the maximum total energy dissipation rate occurs at $x/L \le 0.33$. For $x/L \le 0.33$, a linear increase of the dissipation from zero to dE/dt is assumed. This assumption of linear increment is based on the observation of the turbulence dissipation rate without considering the void fraction, as shown in Fig. 3.17.

To investigate the ratio of the turbulence energy dissipation rate to the total energy dissipation rate, the depth-integrated, period averaged turbulent energy dissipation rate with (ε^*_α) and without (ε^*) considering void fraction is computed as:

$$\varepsilon^* = \int_{-h}^{\eta} \overline{\varepsilon_w} \, dz \tag{3.19}$$

$$\varepsilon^*_\alpha = \int_{-h}^{\eta} \overline{\varepsilon_m} \, dz \tag{3.20}$$

Fig. 3.17 shows the normalized total energy dissipation rate dE/dt versus ε^* and ε^*_α. As expected, in the figure the discrepancies between ε^* and ε^*_α are large – equivalent to 70%,

23%, and 23% of ε^*_α at the first, second, and third splash-ups, respectively. This indicates that the turbulent dissipation rate is significantly underestimated at the first splash-up roller region where the void fraction is high, while only moderately underestimated at the second and third splash-ups. On the other hand, the figure also shows a significant discrepancy between dE/dt and ε^*_α. The ratios of the turbulent dissipation rate to the total energy dissipation rate are about 57%, 19%, and 6% at FOR stations 1 to 3, indicating that a large portion of energy dissipation contributed to mechanisms other than the continuous phase turbulent dissipation. The average ratio of ε^*_α to the total dissipation rate, integrated from the breaking point to $x = 2L$, is only 33%. Similar observations were also reported by other researchers for surf zone breaking waves. Govender et al. (2004) reported that the dissipation rate due to turbulence is much lower (less than 1%) than the total energy dissipation rate estimated using the bore approximation. Huang et al. (2009) found that the turbulent dissipation rate at its maximum is only about 10% of the total energy dissipation rate. In these two studies, other mechanisms – such as the sloping-bottom shallow-water effects that involve energy reflection from the beach, energy transmission in the swash zone, and energy dissipation by bottom friction – may be responsible for the significant discrepancy in the energy dissipation rates. However, those effects do not exist in the present constant-depth deep-water case. The unaccounted for, or the excess, energy dissipation rate increased from 43% at the first splash-up roller to 81% and 94% at the second and third splash-ups – although the gap between the total energy dissipation rate and ε^*_α is more or less constant throughout the breaking process, as shown in the figure. For energy conservation, such excess energy dissipation must be accounted for elsewhere.

Such a discrepancy was not reported in single phase flows, making bubbles the primary cause.

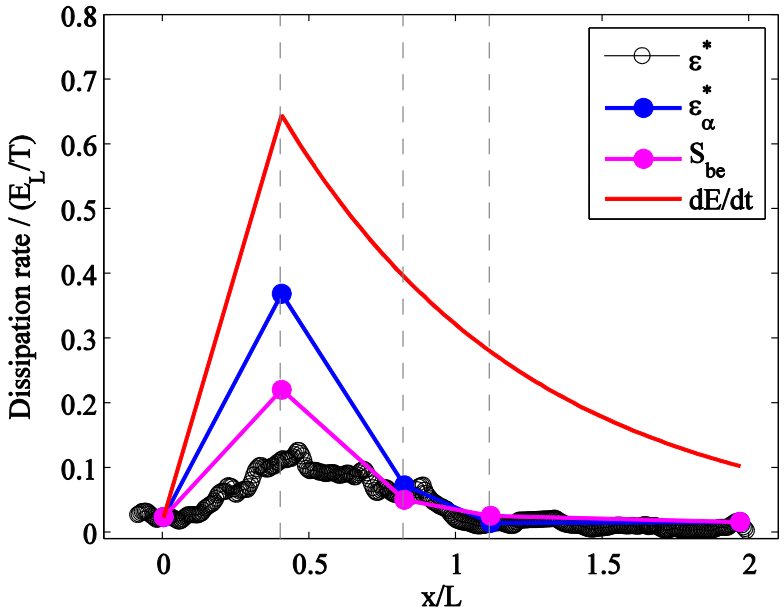

Fig. 3.17 Normalized (by E_L/T) total energy dissipation rate dE/dt, turbulent dissipation rate with and without considering void fraction ε^*_α and ε^*, and bubble induced energy dissipation rate $S_{b\varepsilon}$. The vertical dashed lines indicate the locations of the three FOR stations.

3.5.4 Estimation of Bubble Energy Dissipation Rate

The present study uses void fraction and air-water mixture velocity to quantify the contribution of the liquid phase turbulent dissipation, and its ratio, to the total energy dissipation under breaking waves with intense air entrainment. It is well known that bubbles induce significant turbulence modulation in aerated flows. The bubble effects on the turbulence energy budget are modeled through the additional source term S_{bk} in the $k-\varepsilon$ equations (Troshko and Hassan, 2001; Ma et al., 2011) as follows.

$$S_{bk} = \frac{3}{4d} C_D \bar{\alpha} |v_r|^3 \tag{3.21}$$

where C_D is the drag coefficients, $\bar{\alpha}$ is the period-averaged void fraction, d is the mean bubble diameter, and v_r is the relative velocity between bubbles and water in the present study. For bubbles within the range of $r_p < r < 4$ mm – with r being the bubble radius, and r_p being the bubble radius above which the bubbles begin to oscillate as they rise through the bubble column ($r_p \sim 0.67$ mm at 20°C) – Leifer et al. (2000) developed the following approach to estimate v_r.

$$v_r = \left[v_{rm} + j_1 (r - r_c)^{m_1} \right] \exp\left[j_2 \Gamma (r - r_c)^{m_2} \right] \tag{3.22}$$

where $v_{rm} = 222$ mm/s is the minimum velocity of an oscillating bubble, $r_c = 0.584$ mm is the critical radius below which bubbles do not oscillate, and Γ is the water temperature in Celsius. j and m are constants assigned the follo wing values: $j_1 = 0.733$, $j_2 = 4.79 \times 10^{-4}$, $m_1 = -0.849$, and $m_2 = -0.815$. Accordingly, the relative velocities based on the bubble mean radii are 0.28 m/s, 0.29 m/s, and 0.34 m/s at FOR stations 1, 2, and 3, respectively. Troshko and Hassan (2001) further discussed that the bubble-induced production is related to the bubble-induced dissipation by the single empirical coefficient, $C_\varepsilon = 0.45$ and it is universal for adiabatic bubbly flows. Following the relation, the depth-integrated bubble-induced dissipation rate can be estimated as

$$S_{b\varepsilon} = \int_{-h}^{\eta} S_{bk} C_{\varepsilon} dz \tag{3.23}$$

The normalized bubble-induced dissipation rate, $S_{b\varepsilon}/(E_L/T)$, is plotted in Fig. 3.17. The values are 0.24, 0.06, and 0.03 at FOR stations 1, 2, and 3, respectively. As shown in Fig. 3.17, the contribution of $S_{b\varepsilon}$ is significant at the first splash-up where a large volume of air is entrained. This value of 24% is significant, and accounts for about one-half of the excess energy dissipation of 47% at FOR station 1. At the subsequent second and the third splash-ups, the contributions of bubble-induced dissipation to the total energy dissipation are less significant. The low $S_{b\varepsilon}$ (and low S_{bk}) is expected because of the low turbulent kinetic energy at these two FOR stations (Lim et al., 2015). By integrating the dissipation rates from the breaking point at $x = 0$ to $x = 2L$, the total bubble-induced dissipation ($S_{b\varepsilon}$) is found as 23% of the total energy dissipation, while the excess energy dissipation is 67% (or total turbulent dissipation rate (ε^*_{α}) is 33%). Note that the energy dissipation rate contributed from the bubble break-up process is not considered in the current analysis; but it may be responsible (at least to a certain degree) for this discrepancy. Based on numerical simulations of plunging breaking waves, Derakhti and Kirby (2014) reported a 53% ratio of $S_{b\varepsilon}$ to the total energy dissipation; which is about twice the 23% ratio estimated in the present study.

Martinez-Bazan et al. (1999) reported that the frequency of bubble break-up depends on the dissipation rate of fluid turbulent kinetic energy as well as the mother-bubble diameter. Their statistical model, developed based on experimental data, showed that the bubble break-up frequency increased as a power function of the turbulent dissipation rate,

with the exponent being approximately constant and equal to 0.3. However, their model may not be directly applicable to the present study because they assumed very low void fraction ($\alpha < 10^{-5}$), and that the presence of air bubbles does not affect the evolution of turbulence. Although it is not our scope here, we believe that new wave breaking experiments – using different surfactants to produce different numbers of bubbles (and thus different void fractions) – may be needed to prove the observations made here and to quantify the bubble break-up energy.

3.6 Conclusion

In this paper, we have presented quantitative measurements of turbulent flow fields and bubble size distributions under deep-water plunging breaking waves using PIV, BIV and FOR. The wavelet-based technique was applied to extract the vortical structures and estimate their length scales in the impinging and the splash-up rollers. Evolution of bubble sizes and numbers at the three splash-up rollers were investigated in conjunction with the swirling strength of the highly aerated flow fields. The turbulent dissipation rates were estimated based on mixture theory considering void fraction, and then compared with the total energy dissipation rates.

The vortical structures, and the corresponding length scales, were successfully extracted using the wavelet-based technique by identifying the local maximum intermittency measure. The distributions of *LIMM* coincide well with classical measures of turbulence, such as swirling strength and vorticity. The estimated length scales of the vortical structures range from 0.05*H* to 0.15*H* during the initial impinging and the splash-up roller stages. The length scales estimated using the wavelet-based technique are

comparable to the integral length determined from auto-correlation.

The distributions of number of bubbles, separated as small and large bubbles by an estimated Hinze scale of approximately 2 mm in chord length (or 3 mm in diameter), were correlated with the swirling strength. During the passage of the first impinging roller, the results show that the number of smaller bubbles (s < 2 mm) is well correlated with the swirling strength of the flow, but poor correlation was found for the larger bubbles. The results imply that the local swirling motion of the energetic eddies enhances the breakup of larger bubbles into smaller bubbles in the impinging roller. On the contrary, during the passage of the first splash-up roller the swirling strength does not show clear correlation with the number of bubbles generated. This indicates that the mechanism of shearing the larger bubbles off, and splitting them into smaller bubbles, is relatively infrequent in the splash-up roller.

The PDF of bubble size versus bubble number was presented to examine the power scaling and Hinze scale of bubbles. The results show that two distinct slopes were observed in the first impinging roller, the second impinging/splash-up roller, and the third impinging/splash-up roller. The Hinze scale and slopes of power-law scaling in these rollers compare well with previously reported values. On the contrary, in the first splash-up roller the power law scaling for the larger bubble is flatter, implying that the bubble break-up events were not as frequent as those in the other rollers. The Hinze scale is also not evident in the first splash-up roller. The cause is not clear, but the very high void fraction in the roller is likely involved.

The turbulent dissipation rate was estimated based on the mixture viscosity model

with and without considering void fraction. The results show that the turbulent dissipation rate is significantly underestimated if void fraction is not accounted for. The underestimation becomes greater for higher void fraction, reaching 70% in the initial impinging and the splash-up roller region. This implies that bubbles play a prominent role in enhancing the turbulent dissipation rate. With void fraction accounted for, the turbulent dissipation rate was found to be significantly lower than the rate of total energy dissipation. The ratio of the turbulent dissipation rate to the total energy dissipation rate is 57%, 19%, and 6% at FOR stations 1, 2 and 3, respectively, with an average ratio of 33% integrated from the breaking point to two wavelengths. This imbalance is consistent with observations previously reported on surf zone breakers. The 67% excess energy dissipation is likely caused by the presence of bubbles. The integrated bubble-induced dissipation is found to be 23%. Note that the bubble break-up process is not considered in the current analysis, but it may be responsible for the remaining imbalance.

CHAPTER IV

LARGE-SCALE OBSERVATION OF FLOW PROPERTIES IN PLUNGING BREAKING WAVES

4.1 Introduction

Surface wave breaking is one of the naturally occurring multiphase flows at the air-sea interface which entrains air during the process. The bubbles and aerosols produced by wave breaking enhance gas and heat transfer between the ocean and the atmosphere (Sutherland and Melville, 2013). An accurate prediction of the amount of air entrainment is important in estimating the oxygen transfer across the air-sea interface in marine biology, and the CO_2 transfer in relation to climate change. Many excellent studies on the air entrainment mechanism, typically focusing on bubble size distribution and void fraction under breaking waves, have been reported (Lamare and Melville, 1991; Deane and Stokes, 2002; Cox and Shin, 2003; Blenkinsopp and Chaplin, 2007; Rojas and Loewen, 2007; Mori et al, 2007). Moreover, the amount of air entrainment under breaking waves influences the maximum impact pressures at the impact point of marine structures (Bullock et al., 2001). Lim et al. (2015) (hereafter referred as L15) concluded that the total energy is significantly overestimated if void fraction is not considered in laboratory generated plunging breaking waves. More recently, advances in numerical modeling connecting air entrainment with the turbulent dissipation rate have been demonstrated (Ma et al, 2011; Dekhrati and Kirby, 2014; Shi et al., 2010).

With great efforts in (mostly) experimental studies on wave breaking, there are still

some aspects of laboratory breaking waves that are not fully understood. These include the scale effects of void fraction and bubble size distribution; the evolution of turbulence with the presence of intense air bubbles; and the relation among turbulence, void fraction, and entrained bubbles during energy transfer and dissipation. To resolve these issues, measuring velocity and void fraction is essential in laboratory breaking wave studies.

The study of turbulence under breaking wave has been typically conducted in small-scale laboratory experiments using Laser Doppler Velocimetry (LDV) (e.g., Nadaoka et al., 1989; Ting and Kirby, 1994, 1996; Longo, 2003; Stansby and Feng, 2005), and Particle Image Velocimetry (PIV) and its derivatives (e.g., Perlin et al., 1996; Chang and Liu, 1998; Melville et al., 2002; Govender et al., 2004; Ryu et al., 2005, 2008; Rodriguez-Rodriguez et al., 2011; Lin et al., 2012). This is because of the well-controlled experimental conditions, and the developments in state-of-the-art measurement techniques. Laboratory measurements of void fraction and bubble size distribution under breaking waves have also been carried out by intrusive techniques using acoustic, electric, and optical methods (e.g., Loewen et al., 1996; Lamarre and Melville, 1991; Blenkinsopp et al., 2007). It is widely accepted that intrusive probes are the most appropriate tools for measuring the high concentration of air bubbles generated under breaking waves. However, small-scale studies, those with a breaking wave height of $O(0.1\text{ m})$ or less, may suffer from scale effects, especially in the gas phase. On the other hand, field measurements of turbulence in breaking waves (e.g., George et al., 1994; Doron et al., 2001), and void fraction and bubble size distribution in breaking waves (Lamarre and Melville, 1991; Deane, 1999; Deane and Stokes, 2002), have also been successfully reported. However, challenges in

controlling environmental conditions (and in operating instruments) remain as a hurdle in explaining the connection between turbulence and air entrainment.

A large-scale (or near-prototype scale) laboratory experiment, with a breaking wave height of O(1 m), is essential for providing an intermediate step to fill in the gap between the small-scale laboratory measurements and field observations for turbulence under breaking waves (Thornton et al. 2000). Scott et al. (2005) observed turbulence on a fixed barred beach (i.e., without sediments) under large scale laboratory breaking waves. They found that the turbulence level was the greatest at the bar crest, and showed that the associated turbulent kinetic energy (TKE) was transported to the bed. Subsequently, Yoon and Cox (2010) performed observations of turbulence over an evolving beach at a large scale laboratory. They found that both the time-averaged TKE and the turbulent dissipation rate showed a large increase near the bottom. Oh et al (2008) studied the evolution of turbulent coherent structures under large scale wind-generated breaking waves. They showed that the overall evolving characteristics of coherent structures in large scale and microscale breakers are qualitatively the same. Huang and Hwang (2015) investigated the evolution of surface turbulence on large-scale solitary breaking waves using an infrared imaging technique. They observed that concentrated thermal structures occurred in the moving wave crest during the uprush phase and during the late stages of the backwash phase. They also found that the TKE increased shoreward from the surf to the swash zones.

The scale effects of the mean and turbulent properties of breaking waves are often studied using the Froude similarity law (e.g., Mori et al., 2007; Huang and Hwang, 2015).

Deane and Stokes (2002) showed that the bubble size distribution measured in three breaking waves in the open ocean exhibited two distinct power-law scales, with the slope change occurring at a bubble radius of about 1 mm which is similar to that found in laboratory scale experiments. Their results provided evidence that the rate of bubble fragmentation, and its dependence on the bubble size, remains similar between large scale oceanic breakers (which are predominantly of the spilling type) and small scale laboratory plunging breakers. This suggests that the same bubble formation mechanism occurs between the two different scales of breaking waves. Mori et al. (2007) investigated void fractions, bubble distributions, and turbulent properties of surf zone breaking waves using acoustic Doppler velocimetry (ADV) and a dual-tip resistivity void probe. They observed that the void fraction of the larger scale breakers is 2 – 4 times greater than that of the smaller scale ones (following the Froude scaling law). Furthermore, Mori et al. found that the mean chord lengths and the power-law scales are similar at both scales of breaking waves, indicating that the bubble size distribution, and the rate of bubble break-up during wave breaking, may be universally independent of the breaker scale.

The objective of this study is to experimentally investigate large scale plunging breaking waves by measuring velocity fields and void fraction using bubble image velocimetry (BIV), ADV, and fiber optic reflectometers (FOR). It also focuses on providing an overview of the wave breaking process, through quantitative comparisons of the measured velocities (and the void fractions) between the small scale plunging breaking waves studied in L15 and the large scale ones analyzed in the present study. Section 2 describes the detailed experimental setup and the procedures used for BIV, FOR, and ADV.

Sections 3 to 5 discuss the results for kinematics, turbulence, and air entrainment, respectively, under large scale breaking waves (and their comparisons with the small scale results). Finally, the main conclusions are summarized in section 6.

4.2 Experimental Setup

The experiment was conducted in a large two-dimensional wave tank located in the Tainan Hydraulics Laboratory at National Cheng Kung University in Taiwan. The tank is 300 m long, 5.0 m wide, and 5.2 m deep, equipped with a piston-type wave maker at one end and a 1/20 sloping beach at the other end. The tank side walls and bottom are made of smooth concrete with an estimated roughness approximately 0.1 – 0.2 mm. A constant water depth of h = 3.0 m was maintained throughout the experiment.

Plunging breaking waves were generated using a wave focusing technique following L15. Each wave train consisted of 13 waves of different amplitudes and frequencies with a central frequency of 0.44 Hz. There was only one breaking wave generated in each wave train, whereas three identical wave trains were generated consecutively with an interval of 18 s between two consecutive wave trains. The coordinate system is defined such that x represents the horizontal direction along the wave propagation, y the cross tank direction, and z the vertical upward direction. The origin $x = 0$, y = 0, and $z = 0$ is defined at the impinging point of the breaking wave, a side wall, and the still water level, respectively, and time t = 0 is defined as the moment of wave impingement. The free surface profiles were measured using 14 capacitance-type wave gauges (termed WG01 to WG14) that were mounted 0.40 m from the side wall at the locations detailed in Fig. 4.1a and Table 4.1. A sampling rate of 25 Hz was used for wave gauges throughout the experiment. The

generated breaking wave has a wave height of H = 1.04 m, a wave period of T = 2.28 s, and a phase speed of C = 3.33 m/s calculated using linear dispersion relationship based on the reading of WG06 with the use of the zero up-crossing method. Accordingly, the wavelength is L = 7.59 m and the wave steepness is H/L = 0.14.

Fig. 4.2 shows the time series of the mean free surface elevations measured using the wave gauges. The mean elevations were obtained by averaging 35 repeated measurements. The averaged root-mean-square (RMS) values for the six wave gauges (WG01–06) before waves break was η_{rms} = 2.3 cm (or 0.02H), indicating the breaking wave generation was highly repeatable. Note that three plunging breaking waves were generated per each run in which 3 identical breaking wave generation signals were employed continuously. The test runs were repeated 40 times so a total of 120 plunging breaking waves were generated. In the figure, only the elevation data of the first breaking wave in each run was used for averaging. The water was allowed to calm for at least 40 minutes before running the consecutive test. The interval between consecutive breaking waves in each wave train is approximately 35 s which is long enough for turbulence to dissipate and bubbles to rise and disperse.

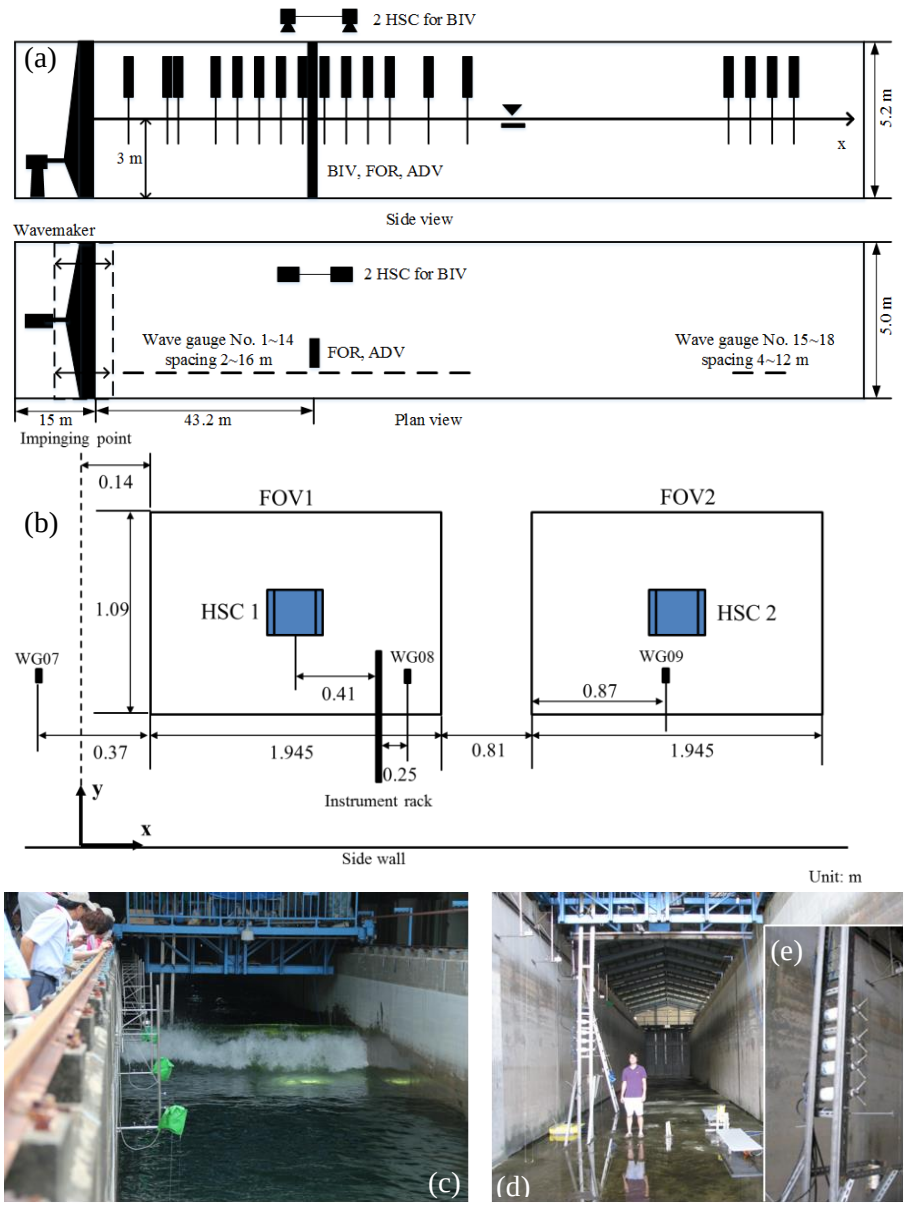

Fig. 4.1 (a) Schematic diagram of the tank and instrument configuration. (b) Plan view of the high-speed camera (HSC) FOVs. Photographs of (c) the first splash-up of the large scale breaking wave, (d) the very large tank and the instrument rack fixed at the bottom, and (e) close view of the instrument rack with the FOR and ADV probes mounted on it.

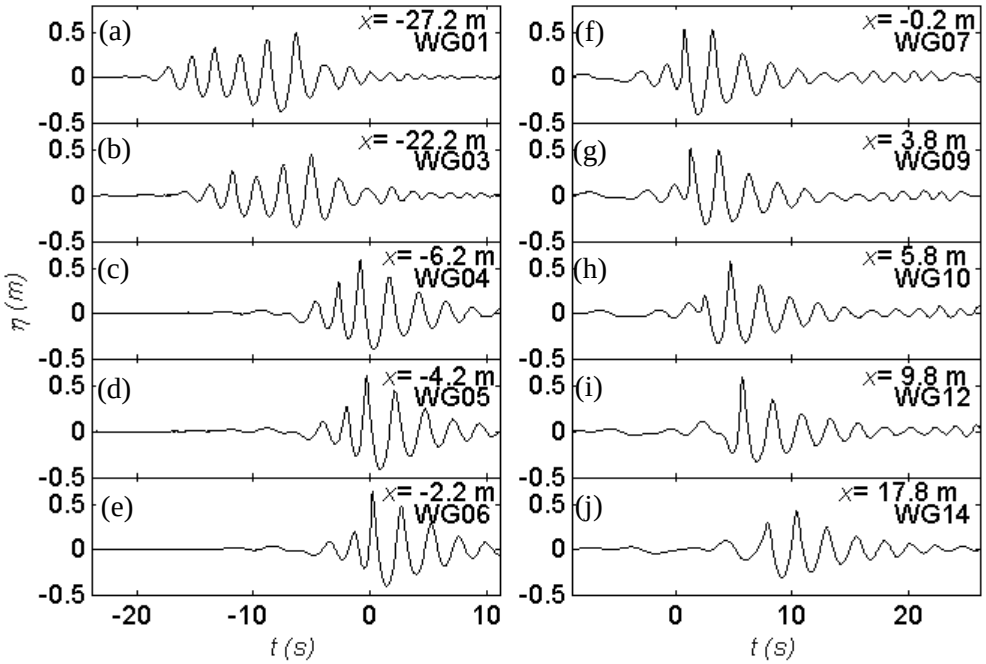

Fig. 4.2 Time series of measured free surface elevations in the tank. Note that the wave impinging point at x = 0 is very close to (f).

Surface velocity fields of the plunging breaking waves were measured using the BIV technique after each breaking wave impinged onto its front surface. The BIV technique is capable of measuring velocities in the aerated region of a gas-liquid flow, such as the breaking waves in the present study, with a high precision. The images were captured by two identical high speed cameras (M340, Vision Research) each mounted with a 50-mm focal lens. The cameras have a resolution of 2560×1600 pixels, a 12-bit dynamic range, and a maximum framing rate of 800 frames per second (fps) at the full resolution. The cameras' framing rate was set at 500 fps and the aperture was set at f/2.8 throughout the experiment. The time interval between two consecutive images is thus 2 ms. In the experiment, no lights or lasers were used for illumination. The cameras were mounted on an instrument bridge, facing 90 degree downward perpendicular to the still water surface.

The cameras were located at 4.02 m above the still water level. The depth of field (DOF) for the captured images was 0.28 m, centered at 0.20 m above the still water level. The field of view (FOV) was fixed as 1.94×1.09 m^2 so the spatial resolution is 0.76 mm/pixel. Note that the length of each FOV in the direction the wave propagation is about one quarter of the breaking wavelength. The two cameras were employed simultaneously to measure the surface velocity fields during the splash up process of the large-scale plunging breakers. The two FOVs were separated by 0.81 m as shown in Fig. 4.1b. After acquiring the images, instantaneous velocity fields were determined using commercial software from LaVision, Inc. An adaptive multi-pass algorithm with an initial interrogation window of 32×32 pixels and a final window of 16×16 pixels with a 50% overlap was applied in the process. Accordingly, the final resolution of the velocity vectors is 8×8 pixels, corresponding to 6.1×6.1 mm^2. Due to the limitation of the camera memory, only the first breaking wave in the wave trains of each run was recorded while 19 repeated measurements of BIV instantaneous velocity fields were ensemble-averaged to extract the mean velocities and turbulent fluctuations. The principle and validation of the BIV technique are detailed in Ryu et al. (2005; 2007), Ryu and Chang (2008), Lin et al. (2012), and L15.

The FOR technique (Chang et al., 2002; 2003; Lim et al., 2008; Ryu and Chang, 2008; L15) was used to obtain void fraction in the aerated region of the breaking waves. FOR is capable of measuring void fraction at a given point in a gas-liquid flow based on the coherent mixing of scattered signals with Fresnel reflection from the tip of an optical fiber. The FOR signals were recorded for 200 seconds with a sampling rate of 100 kHz for all three breaking waves per each test run. The measurements were taken at 8 selected vertical

locations mounted at the rack fixed approximately in the middle of the first splash-up of the breaking waves. The location of each FOR probe is shown in Table 1. The principles and validation of FOR technique are detailed in Chang et al. (2002; 2003), Lim et al. (2008), and L15.

The output signals received from the FOR probes are about 1.0 V and 0.08 V, indicating that the probe tip is in air and in water, respectively. The voltage difference between the gas and liquid phases is highly distinguishable. A threshold voltage that accounts for the maximum noise level (2 times the standard deviation of the water signals) of the liquid phase was set for all the FOR probes. To compute instantaneous void fraction α at each measurement point, the output signals were converted to binary first (0 for water and 1 for air), then an instantaneous void fraction was calculated using every 1000 data points. As a result, the final temporal resolution for instantaneous void fraction is 100 Hz. FOR measurements were taken for each of the 12 repeated run with three repeated breaking waves in each run. The time axis of the void fraction measured at the second and third waves in each run were shifted to match the measurements of the first wave based on the time the probe first experiences a phase change. Accordingly, the total number of repeats for calculating ensemble-averaged void fraction is 36.

The time series of flow velocities were measured by ADV at 6 vertical locations, as shown in Table 1, located at $x = 1.75\,\mathrm{m}$ which is identical to the location of the FOR probes. The sampling frequency was set at 25 Hz throughout the experiment. The raw ADV data included spike noises that are frequently experienced in the studies of wave breaking due to intense air entrainment (e.g., Elgar et al., 2001; Mori et al., 2007b; Yoon

and Cox, 2011). When a wave breaks, air bubbles penetrate into the water column and generate spike noises when they interfered with the ADV sampling volume. The spikes do not represent real velocities so need to be removed before performing turbulence statistics. To identify spike noises, a 3D phase-space threshold method (Wahl, 2003; Mori et al., 2007a) was employed to identified and remove the noises from the raw velocity measurements replace them using a cubic-spline interpolation. Since the penetration depth in the present large scale breaking wave experiment was not measured due to the concrete tank walls, the highest ADV measurement point was decided based on the penetration depth in the small scale experiment in L15.

The present experimental setup was designed such that the plunging breaking waves used in the small scale facility in L15 are reproduced in a near prototype scale. The small scale experiment in L15 was conducted in a two dimensional glass-walled wave tank that is 35 m long, 0.91 m wide, and 1.2 m deep with a constant water depth of h = 0.80 m. The comparisons of the wave properties are presented in table 2. To examine the scale effects, the ratios for the wave height and the phase speed for the breaking waves in the two scales are $\left(H_{\text{large}}/H_{\text{small}}\right)=5.1$ and $\left(C_{\text{large}}/C_{\text{small}}\right)=2.5\sim\sqrt{H_{\text{large}}/H_{\text{small}}}$, respectively, following the Froude scaling.

Table 4.1 Instrument measurement locations

The FOR and ADV probes were fixed at x = 1.75 m.

Gauge No.	WG01	WG02	WG03	WG04	WG05	WG06	WG07	WG08	WG09
x (m)	-27.2	-23.2	-22.2	-6.2	-4.2	-2.2	-0.2	1.8	3.8
Gauge No.	WG10	WG11	WG12	WG13	WG14				
x (m)	5.8	7.8	9.8	13.8	17.8				
FOR No.	FOR1	FOR2	FOR3	FOR4	FOR5	FOR6	FOR7	FOR8	
z (m)	-0.22	-0.06	0.06	0.1	0.13	0.14	0.19	0.23	
ADV No.	ADV1	ADV2	ADV3	ADV4	ADV5	ADV6			
z (m)	-0.19	-0.34	-0.55	-0.72	-0.92	-1.04			

Table 4.2 Characteristic of the plunging breaking

	H (m)	T (s)	L (m)	C (m/s)	h (m)
This study	1.04	2.28	7.59	3.33	3.0
L15	0.204	0.83	1.08	1.30	0.8

4.3 Surface Velocity Measurements Using the BIV Technique

The breaking wave impinging mechanisms also affect the subsequent flow behavior and air entrainment. Peregrine (1983) suggested three possible impinging mechanisms: (1) the impinging jet rebounds at the surface, (2) the impinging jet penetrates into the surface and pushes up the undisturbed fluid in front of it, and (3) a mix of the two. In the small scale wave tank with glassed walls (and a high-speed camera), L15 concluded that the impinging jet penetrated into the free surface without noticeable rebound. However, it is difficult to replicate the approach in the present study because of the concrete walls of the

large wave tank. Alternatively, a high speed camera was mounted on the top of a side wall to record wave impingement by looking downward (at approximately 45 degrees) with a framing rate of 1000 fps. Fig. 4.3 shows close-ups of the impinging process. In the figure, a dark streak along the cross-tank direction (indicated by the yellow arrows) can be seen immediately after the impingement. The darker region in the images represents un-aerated water. Accordingly, the streak represents a divider in between the impinging jet (that penetrated into the water surface) and the splash-up (that was pushed up by the impingement). The penetration can be better seen by examining the recorded movie which clearly shows that air bubbles inside the overturning jet were carried downward into the water, right in front of this divider. This means that the impinging jet moved downward into the water surface after the impingement, instead of the direct rebound of the impinging jet. The movement of the water jet behaved very similarly to that observed in the small scale experiment by L15. In summary, the impinging process in the large scale plunging breakers is penetration dominated, similar to the breakers in the small scale experiment.

To examine the spatial consistency of the impinging point of the plunging breakers, a second high speed camera (set at 500 fps) was used to capture the impinging points of the repeated tests. The camera was positioned at (x, y, z) = (4.8, 1.8, 2.3) m, and was placed looking downward at an angle of 20 degrees to the x-y plane. The corresponding x coordinate in these images was determined by referencing to the known location of the wave gauges from WG05 to WG08. The horizontal locations of the impinging point for 18 repeated runs were compared, and are shown in Fig. 4.4. These locations were averaged to determine the mean impinging point (39.1 m from the wavemaker), which is defined as

$x = 0$ (while the time of impingement was defined as $t = 0$). It was found that the standard deviation of the impinging location is about 1.7 m (~ 0.2L).

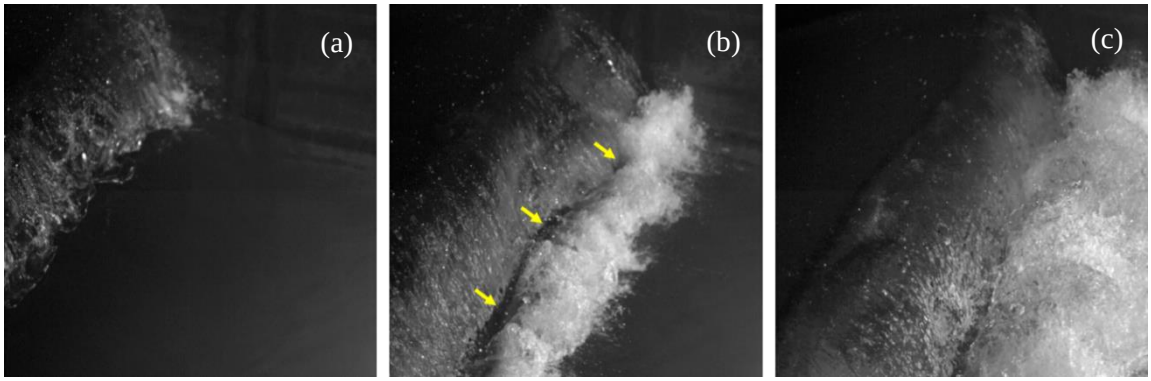

Fig. 4.3 The close-up views of the breaking wave impingement captured using a high speed camera mounted on the side of the tank looking approximately 45 degrees downward. The time interval between the adjacent images is 0.1 s. (a) is right before the wave impingement, and the wave propagates from left to right. A darker streak is seen between the two brighter regions (impinging roller and splash-up roller) in (b) immediately after wave impingement.

Two high speed cameras were used to capture the top view images of the breaking wave. The FOV sizes, and thus the spatial resolutions, vary depending on the distance between the given camera and the water surface elevation. Accordingly, the image resolution was calibrated based on the measured free surface elevation values from wave gauges WG04 – WG11, which are close to the FOVs. Fig. 4.5 shows a sample instantaneous velocity field taken at FOV1 during the first impingement and splash-up process. No significant variations in the direction of the velocity vectors are observed, because the *x*-direction velocity component is much larger than the *y*-direction components (due to the dominant wave propagation direction). Note that BIV only

measures velocities of the aerated region by tracking the bubbles, so velocity fields outside the aerated region cannot be obtained.

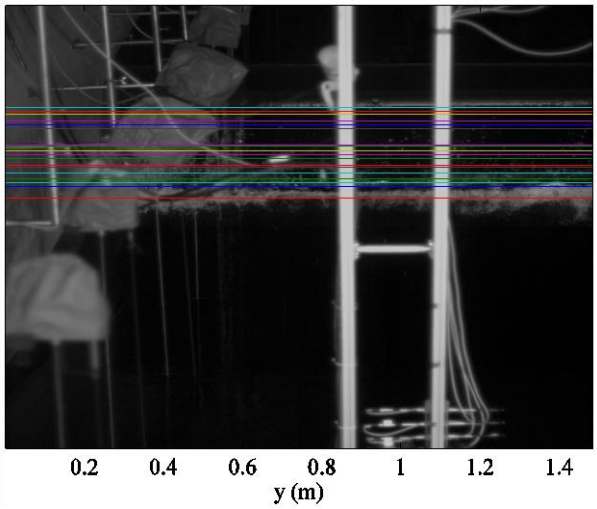

Fig. 4.4 The impingement points (in the *x* direction) of 18 repeated runs are illustrated as the horizontal lines. The wave propagates from top to bottom.

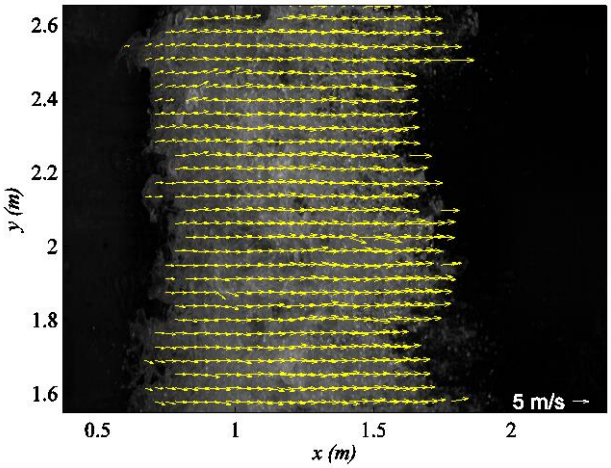

Fig. 4.5 A sample BIV measured instantaneous surface velocity field at *t*/*T* =0.3.

Measurements from repeated runs, including surface elevations, velocities, and void fraction, were ensemble-averaged to determine the mean quantities and turbulent fluctuations. In addition to ensemble-average, the wave-averaged quantity is also calculated so that only wetted region is considered. The ensemble-averaged quantity Q and the wave-averaged quantity Q_{wa} are defined as follows:

$$Q(x,y,t) = \langle q(x,y,t) \rangle = \frac{1}{N} \sum_{i=1}^{N} q(x,y,t)_i \tag{4.1}$$

$$Q_{wa}(x,y) = \frac{\int_0^T \delta(x,y,t) Q(x,y,t) dt}{\int_0^T \delta(x,y,t) dt} \tag{4.2}$$

where $\langle\ \rangle$ denotes ensemble-average. $\delta(x,z,t) = 1$ represents residence in water, and $\delta(x,z,t) = 0$ otherwise. During the ensemble-averaging process, a masking technique was performed by specifying a threshold image intensity to filter out spurious velocity vectors outside the aerated region.

The instantaneous flow velocity $\mathbf{u}$ can be decomposed into the wave induced mean velocity ($\mathbf{U}$) and turbulence fluctuations ($\mathbf{u}'$) as

$$\mathbf{u} = \mathbf{U} + \mathbf{u}' \tag{4.3}$$

where $\mathbf{u} = (u, v, w)$ denotes the instantaneous velocities along the wave propagation

direction (u) , the cross-tank direction (v), and the vertical direction (w). The vertical velocity component w could not be measured from the current top view images. The mean velocity $\mathbf{U} = (U, V, W)$ is the ensemble-averaged velocity, and $\mathbf{u}' = (u', v', w')$ is the turbulent velocity. The measured ensemble-averaged cross-tank velocity (V), as expected, is negligibly small at all phases, so it is set as zero.

Fig. 4.6 shows the ensemble-averaged velocity fields, and the corresponding contours of mean kinetic energy, on the x-y plane ($0.5\left(U^2 + V^2\right) \approx 0.5U^2$) at the first splash up region (FOV1). The ensemble-averaged velocity fields shown in Fig. 4.6a-d are on a moving frame (with phase speed C) so that the separation, and the rotating direction, of the splash-up rollers can be identified more easily. At $t/T = 0.24$ in Fig. 4.6a,e, when the splash-up process is fully developed, the horizontal velocity reached its maximum value of $U_{\max} = 1.68C$ (for the entire wave breaking process). This magnitude is close to the value of $1.84C$, which was observed on the surface in L15, at the same normalized distance (x/H). Note that the maximum mean kinetic energy on the surface in the large scale plunging breaker (during the entire breaking process) was $1.92C^2$ at $t/T = 0.24$. This is nearly identical to value obtained in the small scale experiment (L15), which was $1.90C^2$. The splash-up then became less aerated and the mean kinetic energy continued to dissipate (Fig. 4.6b-d and 4.6f-h). It is interesting to see in the images (see Fig. 4.6c-d and 4.6g-h) that the front of the first splash-up began to detach from the impinging region behind it. The raw images also show a low concentration of bubbles near the detachment (as shown in Fig. 4.6d and 4.6f) with some missing velocity vectors.

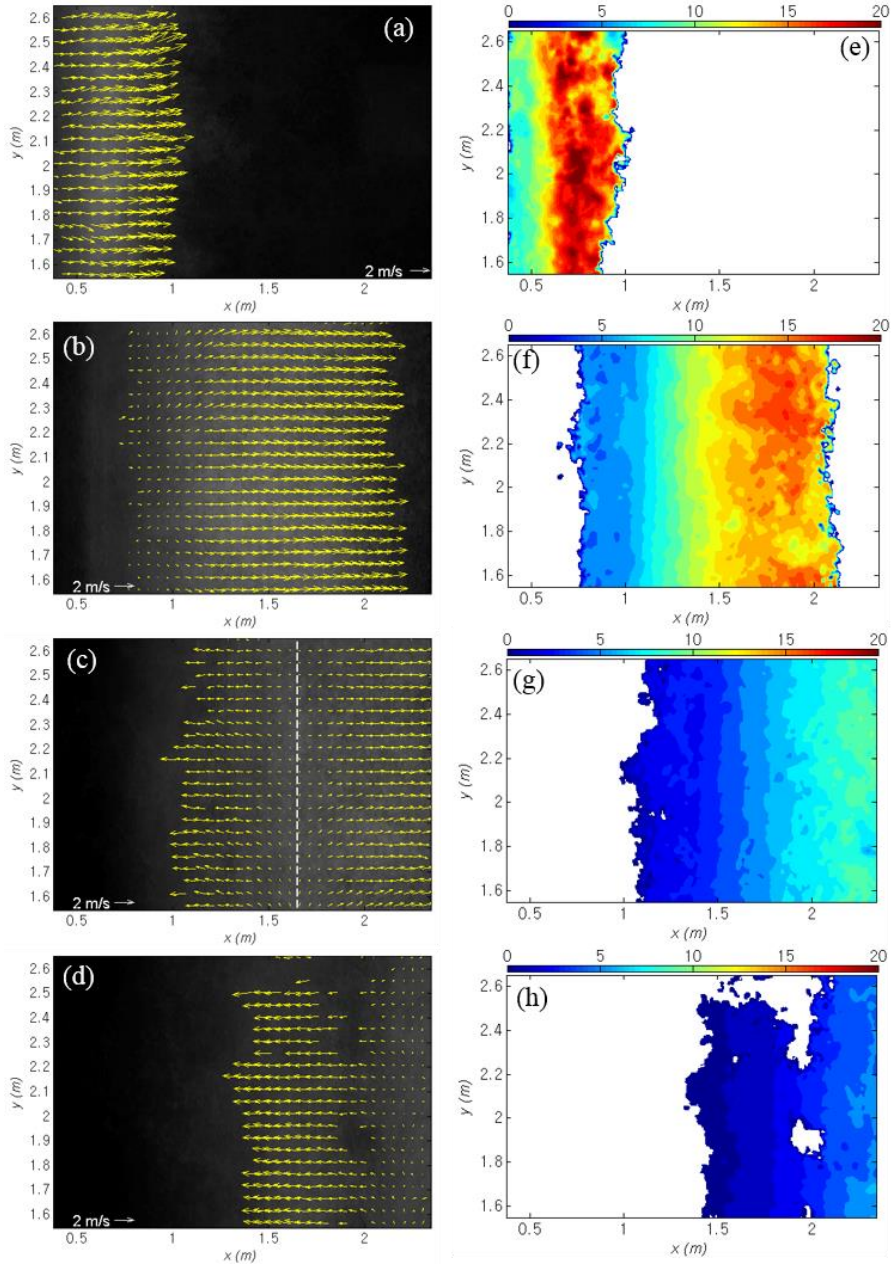

Fig. 4.6 Ensemble averaged velocity fields on a moving frame of the phase speed C (left panels) and corresponding mean kinetic energy $0.5U^2$ (right panels) at $t/T =$ (a, e) 0.24, (b, f) 0.34, (c, g) 0.45, and (d, h) 0.55. The dotted line in (c) indicates the detachment of the advancing front of the splash up and the backward impinging roller.

It is difficult to directly observe the source of this separation because of the lack of glass side walls for camera access. This low aerated flow is likely from the moving up of the triangular, un-aerated region between the first splash-up roller and the impinging roller observed by many researchers (e.g., Basco, 1985; Nadaoka et al., 1989; L15). This region moved up to the surface and caused the separation of the two rollers (as well as had very few bubbles for BIV to track). L15 observed this un-aerated region and called it the *ascending crest*, but the region reached only to about $z = 0$, and did not extend to the free surface in their study, causing the two rollers not completely separated. Although the reason for this discrepancy is unclear, a likely possibility is the shallower penetration depth of the bubble plume (in a dimensionless sense, normalized by H) after the initial impingement. This in turn gives the ascending crest a need for a shorter time to reach the free surface. A comparison of the vertical profiles of wave-averaged void fraction shows that the void fraction in the current study is lower below the still water level, but higher above the still water level, when compared with that in L15 (to be discussed later). This indeed supports the assumption of a shallower penetration depth, or a lower aeration below the still water level, in the large scale breaking waves. It is further noted that the directions of the rollers separated by the presumably ascending crest are in the opposite direction (relative to the moving frame) of C, as shown in Fig. 4.6c (with the approximate boundary indicated by the dotted line of U-C = 0). This may indicate that a backward impingement occurred in the large scale plunging breaker, which is consistent with the observation in the small laboratory scale plunging breaker in L15. L15 found that the fully developed first splash-up roller continues to impinge on the surface of the wave trough in front of it,

and generates the second impingement and the second splash-up. This process was also observed in the present study.

Fig. 4.7 shows a comparison of the temporal variation of the normalized maximum ensemble-averaged horizontal velocity U_{max}, at x = 1.75 m (which is located near the center of the fully developed first splash-up roller) between the L15 study and the present study. The present large scale velocity was spatially averaged over the cross-tank direction, and then compared with the corresponding mean surface velocity from L15. The maximum surface velocity increased rapidly after the frontal region of the fully developed splash-up approached FOV1 (at approximately $t/T = 0.2$). It reached U_{max} = 1.68C in the present study, which is close to the magnitude of 1.84C in the small scale study. U_{max} then decreased gradually as the splash-up lost its horizontal momentum, which was converted from the downward momentum of the overturning jet (that led to the breaking event). The temporal evolution of the maximum horizontal mean velocities at the surface agrees well between these two different scales.

To identify the vortical structures of the breaking waves, a wavelet-based technique (Huang et al., 2010; Na et al., 2016) was employed. We chose the Morlet wavelet as the mother wavelet, as it is frequently used in the study of fluids (Farge, 1992). Following the approach in Na et al. (2016), the continuous wavelet transform of u in the x direction is formulated as

$$W_f(s,x) = \frac{1}{\sqrt{s}} \int_{-\infty}^{\infty} u(\tau) \varphi^* \left(\frac{\tau - x}{s} \right) d\tau \qquad (4.4)$$

where u is the horizontal velocity; s is the scale parameter; τ is the translation parameter; $\varphi(x) = e^{iw_0 x} e^{-x^2/2}$ is the mother wavelet, with $w_o = 6$ as suggested by Farge (1992); * denotes the complex conjugate; and $\sqrt{s}$ is for energy normalization across the different scales. The Local Intermittency Measure (*LIM*) is a normalized local energy that reaches a relative maximum corresponding to the passage of a vortical structure. *LIM* is defined as

$$LIM(s,x) = \frac{[W_f(s,x)]^2}{\left\langle [W_f(s,x)]^2 \right\rangle_x} \tag{4.5}$$

where the denominator is the average of the square of a wavelet coefficient along the x direction. By defining the peak of *LIM* as $LIMM(x) = \max\{LIM(s,x)\}$, Camussi (2002) found that *LIMM* spatially matches with the location of the vortex core, and that the length scale of the vortex can be estimated directly from inversing the scale parameter s at the point where the peak is present.

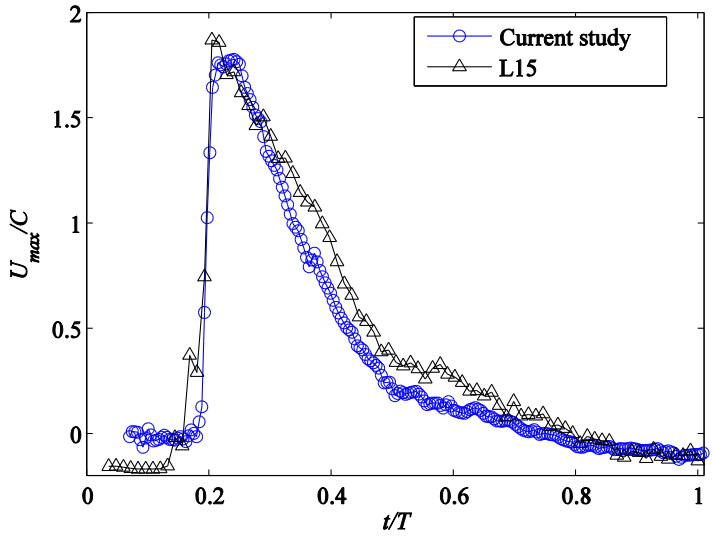

Fig. 4.7 Temporal variation of the maximum ensemble-averaged horizontal velocity U_{max} measured at x = 1.75 m near the center of the fully developed first splash-up roller in comparison to the small scale results of L15.

Fig. 4.8 shows the plan view of the evolution of the ensemble-averaged *LIMM*, and the corresponding length scales of the energetic eddies at the free surface. The condensed region with high values of *LIMM* in Fig. 4.8a, at t/T = 0.3, is at the impinging roller (approximately the upstream half at x < 1 m), and not at the splash-up roller (approximately the downstream half). The corresponding length scale *LS*, normalized by *H*, ranges approximately from H/LS = 3-6. As the breaking wave propagates, the condensed region advances (Fig. 4.8b) and spreads across the aerated region (Fig. 4.8c). Fig. 4.8b and 4.8c highlight that the patches of eddies with the smaller length scales are mostly observed at the second impingement region (approximately at $x > 2$ m), and are diffuse with time. At this second impingement region, H/LS ranges between 3 and 20, implying that energy transfer from the larger eddies to the smaller eddies is more significant in this region (Fig. 4.8b and 4.8c).

The insets in Fig. 4.8 show a side-view (the *x*-*z* plane) of the evolution of *LIMM* and H / LS in the small scale experiments from Na et al. (2016). While the large scale results demonstrate *LIMM* and H / LS in the *x*-*y* plane, the length scale represents vertical eddies with lengths in the *x* direction at the free surface. On the other hand, the small scale results in *Na et al.* are in the *x*-*z* plane, representing the horizontal eddies with their lengths in the *z* direction. By examining Fig. 4.8a and 4.8d, the H / LS plots are similar between the present large scale breaker and the surface of the small scale breaker. The energetic eddies spread to the free surface at the first impinging roller, but not at the first splash-up roller. At the free surface of the impinging roller, the length scale $H / LS \sim 7$ in the small scale measurements is consistent with that in the present large scale results. This may suggest that eddies under breaker waves may be comparable (in the dimensionless aspect) if scaled appropriately (i.e., by the wave height). The length scale is mostly between $H / LS \sim 5$ and 10, meaning the energetic eddy sizes are about 0.1 - 0.2*H* near the breaking wave surface (regardless its physical scale).

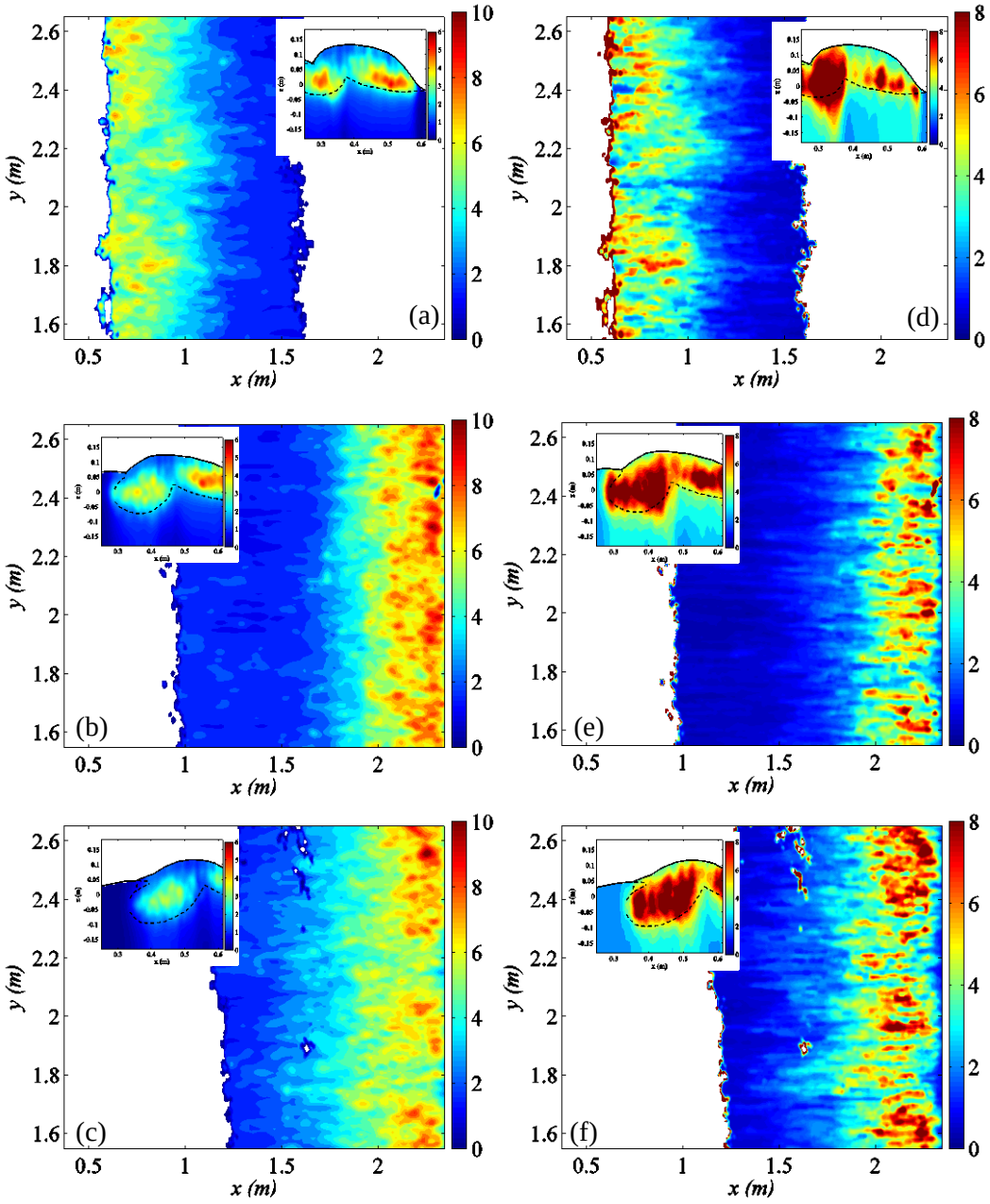

Fig. 4.8 The left column is the ensemble averaged LIMM and the right column is the corresponding normalized length scale (H / LS) at t/T = (a, d) 0.3, (b, e) 0.4, and (c, f) 0.5. The insets are the corresponding LIMM and LS on the x-z measurement plane taken from the small scale breakers in L15. The dotted lines in the insets indicate the boundaries of the aerated region obtained from the BIV images.

As the wave propagates, Fig. 4.8b and 4.8c show that H/LS becomes smaller ($H/LS \sim$ 1-3) at the surface near the impinging roller region ($x < 1.8$ m) in the present large scale results. In the small scale study shown in the insets, while H/LS in the impinging roller region ($0.28 \text{ m} < x < 0.48 \text{ m}$) are significantly larger ($H/LS \sim 5$), almost comparable to that in the splash-up region ahead, as shown in the insets of Fig. 4.8b and 8c. The difference in the horizontal and vertical eddy lengths could be caused by the fact that eddies at the surface are likely to stretch more (so a longer *LS*) in the streamwise and cross tank directions due to higher horizontal surface velocities (in comparison to the relatively lower vertical stretching caused by lower vertical velocities). The eddy anisotropic structures on the surface are similar to the anisotropic surface thermal structures observed by Huang and Hwang (2015). Turbulence generated by breaking waves are known to disrupt the skin layer at the surface and to transport warmer water from below to the surface, resulting in cool and warm temperature structure patches (Jessup et al., 1997a). Huang and Hwang (2015) used an infrared imagery technique to study these thermal structures in large scale breaking solitary waves, and observed that the thermal streaks stretched horizontally at the surface. This is consistent with the anisotropic structures observed in the present study.

Eddie length in the *y* direction was further investigated and compared to the corresponding length in the *x* direction. To do this, calculation of $LIMM(y) = \max\{LIM(s,y)\}$, and of the corresponding length scale in the lateral direction, was performed. To isolate the length scale of the turbulent eddies from the length scale of the mean flow, and to obtain the average size of these eddies, a threshold value of

LIMM is needed. The mean *LIMM* values within the aerated region are approximately 2-12, so a threshold value of 7 was selected to separate the turbulence-induced intermittent events from the surrounding mean flow. This threshold technique has been applied in past studies to quantify intermittency by identifying conditional vorticity (Cox and Kobayashi, 2000; Camussi, 2002; Huang et al., 2010). With the threshold technique applied, the length scales of eddies caused by the intermittent events were averaged to obtain the mean length scale.

In Fig. 4.9, the temporal evolution of the mean length scale of eddies in both the x direction (i.e., H/LS_h) and y direction (i.e., H/LS_l) are compared. The mean streamwise length scale H/LS_h varies between 4.1 and 5.4, while the mean lateral length scale H/LS_l almost stays constant at around 4.5. Note that the estimated length scales are about 40 times the spatial resolution of the velocity vectors (6.1×6.1 mm^2), so the errors caused by insufficient resolution are insignificant. Overall, the magnitudes of LS_h and LS_l are nearly identical, suggesting that energetic eddies at the surface of the large scale plunging breaking waves may be similar in length in x and y directions (or that the vertical energetic eddies are nearly circular). We are not aware of other studies featuring the length scale estimates of eddies on the surfaces of plunging breaking waves, so comparisons are unavailable.

The normalized length scale of the energetic vortical structures at the surface in the present large scale plunging breaking waves is comparable to that reported in L15, with the length scale of energetic eddies in their experiments (involving small scale plunging breakers) being approximately $H / LS = 3 - 20$. It may be worth pointing out that the

normalized length scales in small scale surf-zone spilling breakers are around $H/LS = 1-8$, as reported by Govender et al. (2009) and Huang et al. (2010).

Fig. 4.10a shows the spatial and temporal variation of the normalized horizontal mean kinetic energy, $K_h = 0.5U^2$, that is spatially averaged over the *y* direction. Fig. 4.10b shows the corresponding horizontal mean kinetic energy using data from the small scale experiment by L15. It is interesting to see that in both scales the mean kinetic energy is transported by a speed close to $2C$ until about $x/H \sim 2-3$, and not by the group velocity C_g, which is about $0.5C$ based on linear wave theory. The rapid decrease of K_h close to $x/H \sim 3$ coincides with the occurrence of the second impingement in both scales. This second impingement process is more like a weak continuous impingement in contrast to the first impingement of the overturning jet (L15). Overall, Fig. 4.10 shows that K_h evolves in a similar pattern at both scales when the streamwise propagation distance is normalized by the wave height, but not by the wavelength. Together with the length scale discussion above, this suggests that the proper characteristic length scale for the breaking waves is the wave height, and not the wavelength.

Similar to the mean kinetic energy in Fig. 4.10, Fig. 4.11 shows the spatial and temporal variation of the normalized turbulent kinetic energy in both the present large scale study and the small scale experiment by L15. Since the vertical velocity was not measured, the horizontal turbulent kinetic energy k_h is defined as

$$k_h = \frac{1}{2}\left(\langle u'^2 \rangle + \langle v'^2 \rangle\right) \tag{4.6}$$

In Fig. 4.11a, a distinct pattern of turbulence advection was observed, showing that a moderate level of turbulence is advected following close to the group velocity at the surface of the first impinging roller ($x/H < 1.2$). On the contrary, a high level of turbulence at the surface of the first splash-up roller is advected close to the maximum surface velocity ($U_{max} = 1.68C$). One common feature between both scales is the region of relatively low k_h between the two slopes of C and $2C$, occurring before the surface is affected by the second impingement and the second splash-up (i.e., between $x/H = 0.9$ and 2.8). However, the void fraction is expected to remain high in this region (to be discussed later), suggesting that the bubbles may not be effective in energizing the flow turbulence at the surface. In the vicinity of the second impingement, at approximately $x/H > 3$, k_h is dramatically increased and diffused in each of the two scales. Due to the continuous second impingement, turbulence is diffused over the entire bubbly flow region (both in time and space) and advected relatively slowly with C (which is unlike that in the first splash-up region). The rapid increase of k_h may be closely related with the increase of the small eddies (as shown in Fig. 4.8b,c,e,f) due to the significant energy transfer from larger eddies to smaller eddies.

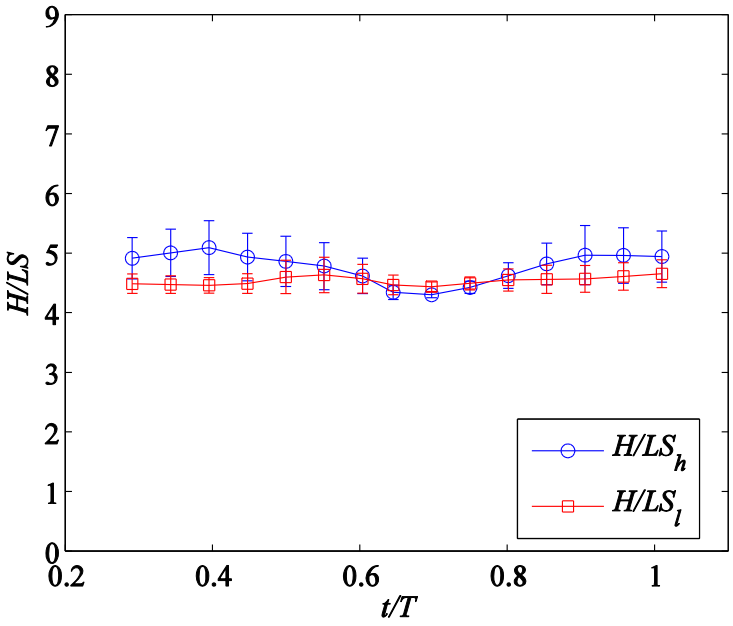

Fig. 4.9 Time series of the normalized mean length scales H/LS_h and H/LS_l of the energetic eddies in the x and y directions, respectively. The error bars represent standard deviations.

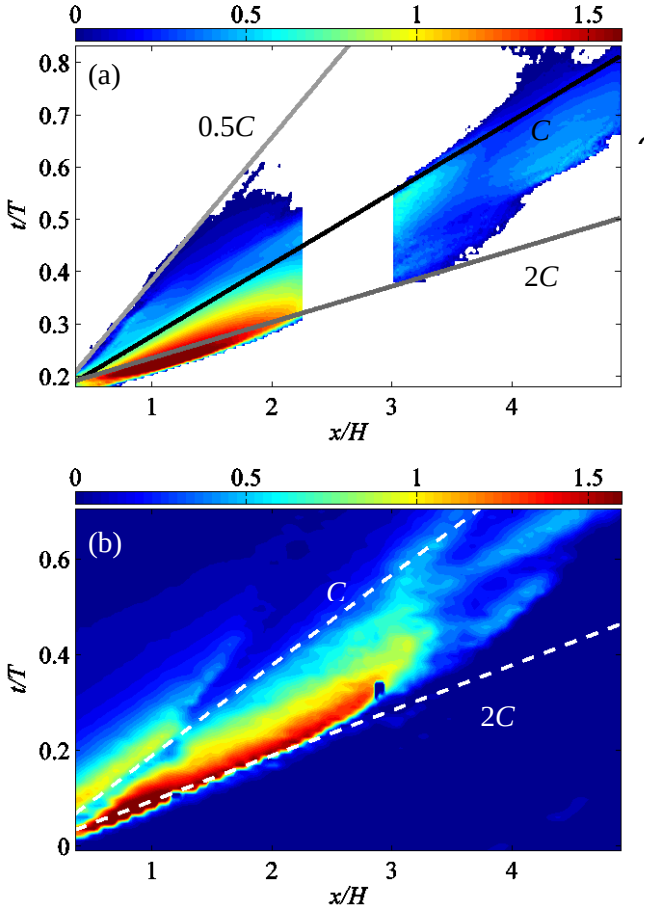

Fig. 4.10 Spatial and temporal evolution of horizontal mean kinetic energy K_h/C^2 in (a) the present large scale study, and (b) the small scale study by L15. The lines represent slopes of 0.5*C*, *C*, and 2*C* as indicated.

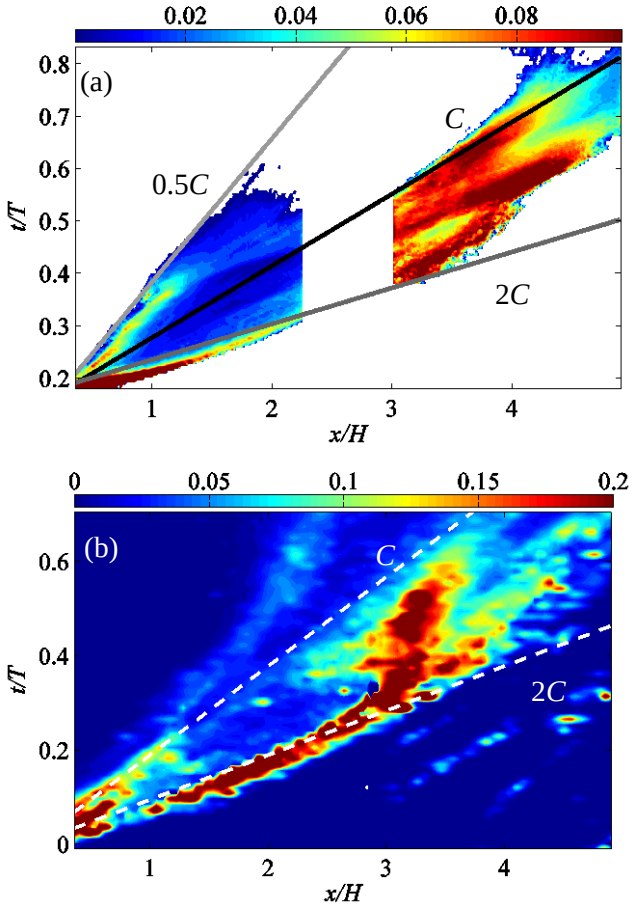

Fig. 4.11 Spatial and temporal evolution of horizontal turbulent kinetic energy k_h/C^2 in (a) the present large scale study, and (b) the small scale study by L15. The lines represent slopes of 0.5*C*, *C*, and 2*C* as indicated.

4.4 Void Fraction Measurements Using FOR

Fig. 4.12 shows the time series of the ensemble-averaged surface elevation and void fraction at x = 1.75 m. The FOR probes experienced a high concentration of air bubbles during the passage of the splash-up roller (at $0.2\ \text{s} < t < 0.4\ \text{s}$), and then they experienced a moderate concentration of bubbles causing a second peak, but with a relatively lower void fraction (at $0.5\ \text{s} < t < 0.7\ \text{s}$). Finally, for those probes below the still water level, they encountered almost pure water (at $0.7\ \text{s} < t < 0.9\ \text{s}$) before they were exposed to the air. This sequence of the signals has also been reported in small scale plunging breaking waves (e.g., Rojas and Loewen, 2010; L15). In Fig. 4.12b, void fraction stays close to zero at depth $z = -0.22$ m (until approximately $t < 1.3\ \text{s}$) during the passage of the breaking wave, indicating very weak air entrainment at and below that depth (i.e. the impinging jet did not penetrate much below $z/H = 0.21$). This supports the earlier discussion of a shallower penetration depth (relative to the wave height) in the present large scale experiment. Note that the overturning jet penetrated much deeper, to $z/H = 0.29$, in L15. Furthermore, at $z = -0.06\ \text{m}$, relatively high void fraction was found immediately after the first impingement ($t \le 0\ \text{s}$) which is likely due to the sprays and droplets arriving ahead of the first splash-up. Unfortunately, the FOR probes could not distinguish droplets from bubbles in the vicinity of the splash-up.

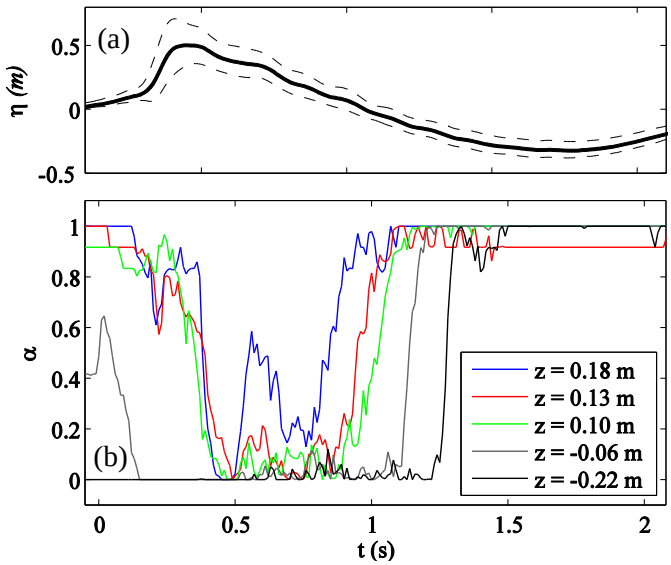

Fig. 4.12 Time series of (a) mean surface elevation, (b) emsemble-averaged void fraction at x = 1.75 m. The dotted lines in (a) represent standard deviations.

Fig. 4.13 compares the contour maps of the temporal evolution of the FOR measured void fraction in the present large scale study with those of the small scale results by L15. In both scales, the FOR probes encountered an intense concentration of air bubbles generated by the first splash-up roller, and the first impinging roller, at approximately $t/T < 0.3$. The magnitude of the maximum void fraction reached about 0.95 in the large scale breaker in Fig. 4.13a. This high level is comparable to the maximum void fraction in the small scale breaker (Fig. 4.13b), and to the maximum void fraction in other (previous) measurements during the first splash-up process (e.g., Blenkinsopp and Chaplin, 2007; Rojas and Loewen, 2010). However, it is considerably higher than the maximum void fraction (about 0.15 to 0.20) beneath the surf-zone breaking waves reported by Cox and Shin (2003). L15 further discussed that the smaller concentrated structure at $0.38 < t/T < 0.51$ (with maximum void fraction between 0.3 and 0.5; see Figure 13b)

occurred corresponding to the passage of the collapsed bubble cloud of the impinging roller. The same observation is also shown in the present large scale breaker in Fig. 4.13a. It should be noted that the front surface shapes are not quite the same between the two scales shown in Fig. 4.13. Two possible reasons associated with this discrepancy are as follows: Firstly, the vertical resolution of void fraction is coarser in the large scale measurements, leading to a less accurate estimation of the intermediate values. Secondly, the use of capacitance based wave gauges for free surface identification might lead to a milder front surface shape in the large scale measurements, because they cannot detect a very steep surface well (whereas images were used in the small scale measurements).

Fig. 4.14 shows the comparison of vertical profiles of the wave-averaged void fraction α_{wa} with the small scale results from L15. The maximum value of the measured void fraction in the current study is about α_{wa} = 0.42 at $z/H = 0.22$. This value is almost identical to that at the same relative depth in the small scale breaker. However, at the lower depth, particularly below the still water level, α_{wa} in the present large scale study is much lower, about 58% and 20% of the equivalent α_{wa} values of the small scale breaker at $z/H = -0.22$ and $z/H = -0.06$, respectively. Despite the similar patterns of the void fraction contours (in Fig. 4.13) and vertical profiles of α_{wa} (in Fig. 4.14) between the two scales, the entrapped air at the large scale tends to penetrate and stay at a relatively higher vertical location below the still water level.

Several researchers (e.g., Deane and Stokes, 2002; Blenkinsopp and Chaplin, 2007, 2011) have suggested that the total volume of entrained air due to wave breaking would scale geometrically, while the formation and break-up mechanisms of the entrained

bubbles (and the bubble size distributions) would be similar between the small laboratory scale and the prototype scale in open ocean. If the bubble sizes distributions are similar at both scales, the bubble rising velocity u_r will depend on the bubble size (e.g., Leifer et al., 2000), so the bubble rising time scale H/u_r will be proportional to the length scale (i.e., H), and not to the Froude time scale (i.e., $\sqrt{H}$). Therefore bubbles with similar size and density (i.e., void fraction) would persist longer before reaching, and bursting, at the free surface in the large scale breakers.

If the bubble sizes are assumed to be similar regardless of scale, this would mean that the number of bubbles detected in the large scale breakers by FOR will be 5 times greater than those detected in the small scale breakers. However, our FOR measurements show that the average number of bubbles detected by the FOR probes in the present large scale study is about 17 times greater than the number of bubbles detected in the small scale breaker (Na et al., 2016) during the first splash-up process. The discrepancy may have two implications. Firstly, the assumptions about a same size bubble distribution may not be always true. Secondly, there seems to be a larger number of smaller bubbles in the covered lower aerated region, while a lower number of larger bubbles in the uncovered upper region. The average bubble size in the large scale breakers (over the measurement range) is between 1/3 and 1/4 of that in the small scale breakers (over the equivalent range), based on the ratio of 17 over 5. This seems to be reasonable, based on the argument of bubble rising time presented above (since larger bubbles have more difficulty penetrating deep). But this argument fails to explain why there are 3 to 4 times more smaller bubbles in the lower half of the aerated region. More studies on bubble size measurements and

distributions are needed to clarify this.

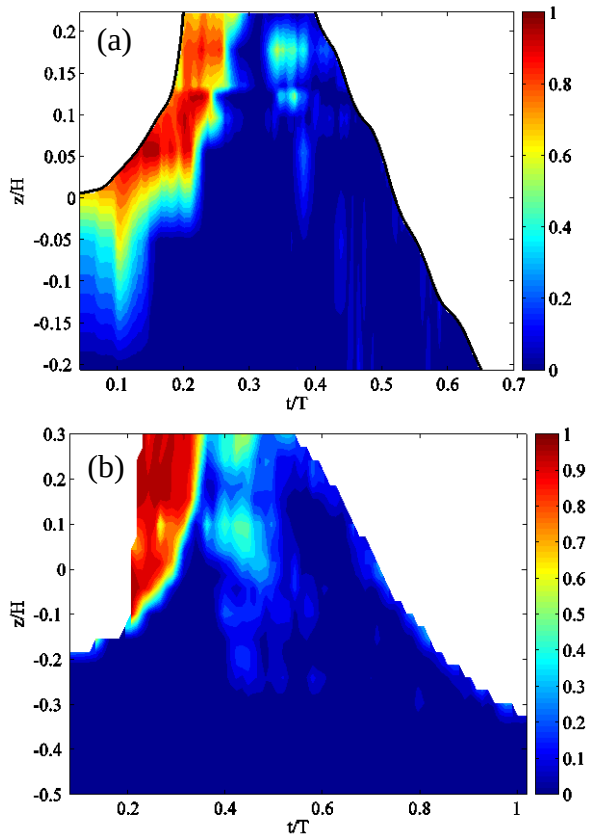

Fig. 4.13 Contour map of the FOR measured void fraction in (a) the present large scale study and (b) small scale study by L15 (redrawn after permission from L15, Figure 12a).

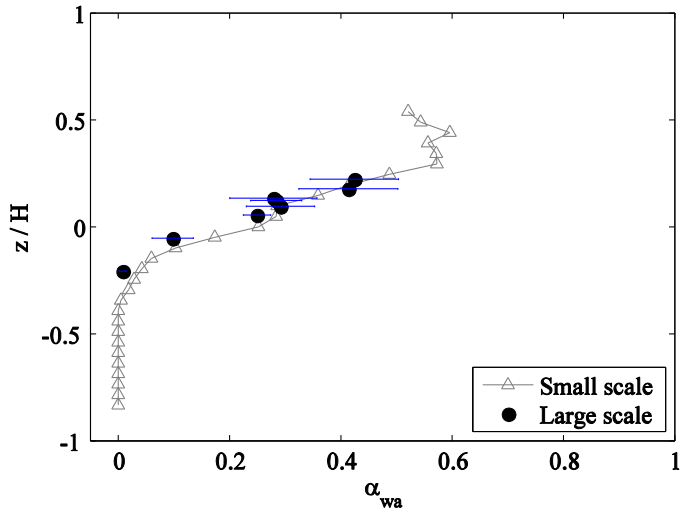

Fig. 4.14 Comparison of vertical profiles of wave-averaged void fraction in the present large scale breaking waves with that in the small scale breaking waves in L15. The horizontal lines indicate error bars calculated using bootstrapping.

4.5 Velocity Measurements Below Highly Aerated Region Using ADV

The ADV measured instantaneous velocity $\mathbf{u}$ is decomposed into the wave induced mean velocity $\mathbf{U}$ and the turbulence fluctuation $\mathbf{u}'$ as shown in Eq. 4.3. To estimate $\mathbf{U}$, ensemble-averaging and the differencing method proposed by Shaw and Trowbridge (2001) (hereafter referred as ST01) were used for comparison and verification. The ST01 method is a temporal filtering technique, assuming that the coherent signal between two adjacent ADVs is the wave motion whereas the incoherent signal is the turbulence. The ST01 method is particularly useful in extracting turbulence when two velocity time series are measured with insufficient repeats for ensemble averaging or for a non-stationary process. The ST01 method is based on the assumption that the distance between two measuring points is greater than the length scale of turbulence but shorter than the length scale of waves. In the present study, the ADVs were spaced by 0.20 m (~ *H*/5) which is

much smaller than the wave height and wavelength while the turbulence length scale is unclear. In surf-zone breakers, the length scale was found to vary from the wavelength to the breaker height (Longo, 2009), to less than one half of the water depth (Huang et al., 2010). In comparison, the length scale in the highly aerated region is lower than one half of the wave height in the deep water plunging breaking waves (Na et al., 2016).

ST01 defined the filtered velocity $\hat{u}_1$ due to the wave motion at ADV location 1 as a convolution product

$$\hat{u}_1(t) = \int_{-L_f/2}^{L_f/2} \hat{h}(t-\tau) u_2(t) d\tau \tag{4.7}$$

where u_2 is the measured velocity at ADV location 2, L_f is the selected filter length/period, and $\hat{h}$ is the filter weight. L_f is typically chosen as one half of the peak wave period (e.g., ST01; Yoon and Cox, 2010; Huang and Hwang, 2015). The filter weight vector $\hat{\mathbf{h}}$ is estimated by finding the ordinary least squares solution of a transversal filter model (e.g., Haykin, 1996) as

$$\hat{\mathbf{h}} = (\mathbf{A}^T\mathbf{A})^{-1}\mathbf{A}^T\mathbf{u_1} \tag{4.8}$$

where $\mathbf{A}$ is a windowed matrix with the size of M (the number of data points) by N (the number of filter weights) at ADV location 2 and $\mathbf{u_1}$ is the instantaneous velocity vector at

location 1. The wave-induced filtered velocity vector $\hat{\mathbf{u}}_1$ at location 1 is computed by convolving the measured windowed matrix $\mathbf{A}$ with $\hat{\mathbf{h}}$ as

$$\hat{\mathbf{u}}_1 = \mathbf{A}\hat{\mathbf{h}} \tag{4.9}$$

Accordingly, the turbulence velocity at location 1 is computed as

$$\mathbf{u}_1' = \mathbf{u}_1 - \hat{\mathbf{u}}_1 \tag{4.10}$$

Fig. 4.15 compares the ensemble-averaged velocity, over 33 repeated measurements, and the filtered velocity using the ST01 method. Moving average, which provides a simpler approach in extracting turbulence is also included for comparison. In measuring turbulence under breaking waves, ensemble-averaging is widely considered as a benchmark method (Ting and Kirby, 1996; Longo, 2003; Shin and Cox, 2006) if sufficient number of repeated measurements are available. Chang and Liu (1999) suggested that meaningful turbulence information can be obtained by ensemble-averaging over 16 repeats or more. Their argument was supported by Huang et al. (2009) who found that the relative errors of turbulent kinetic energy were less than 0.05 for $N \geq 20$ and L15 who showed that the error for turbulence intensity was less than $0.05C$ for $N \geq 20$. The turbulence velocities using the ST01 method show a similar pattern compared to that extracted using the ensemble-averaging method, indicating the chosen filter length of $H/5$

in the present large scale measurements is appropriate. On the contrary, moving averaging consistently and considerably underestimates the turbulence level.

Fig. 4.16 shows the power spectral densities (PSD) of instantaneous and turbulence velocites calculated based on ensemble-averaging. Note that the wave motion is clearly depicted by the local maxima near f = 0.43 Hz in the streamwise and vertical velocities in Fig. 4.16a and 16c. As expected, the wave motion is not clearly identified in the lateral velocity in Fig. 4.16b while the corresponding PSD between the instantaneous and turbulent velocities are nearly identical because of the vanishingly small mean velocity. The slopes of the PSDs, calculated on the ADV measurements taken below the aerated rollers, in Fig. 4.16 follow the Kolmogorov's -5/3 slope. It is worth pointing out that Na et al. (2016) showed that the PSD slope was milder than -5/3 in the aerated region in the small scale plunging breaking due to the injection of turbulence by bubbles.

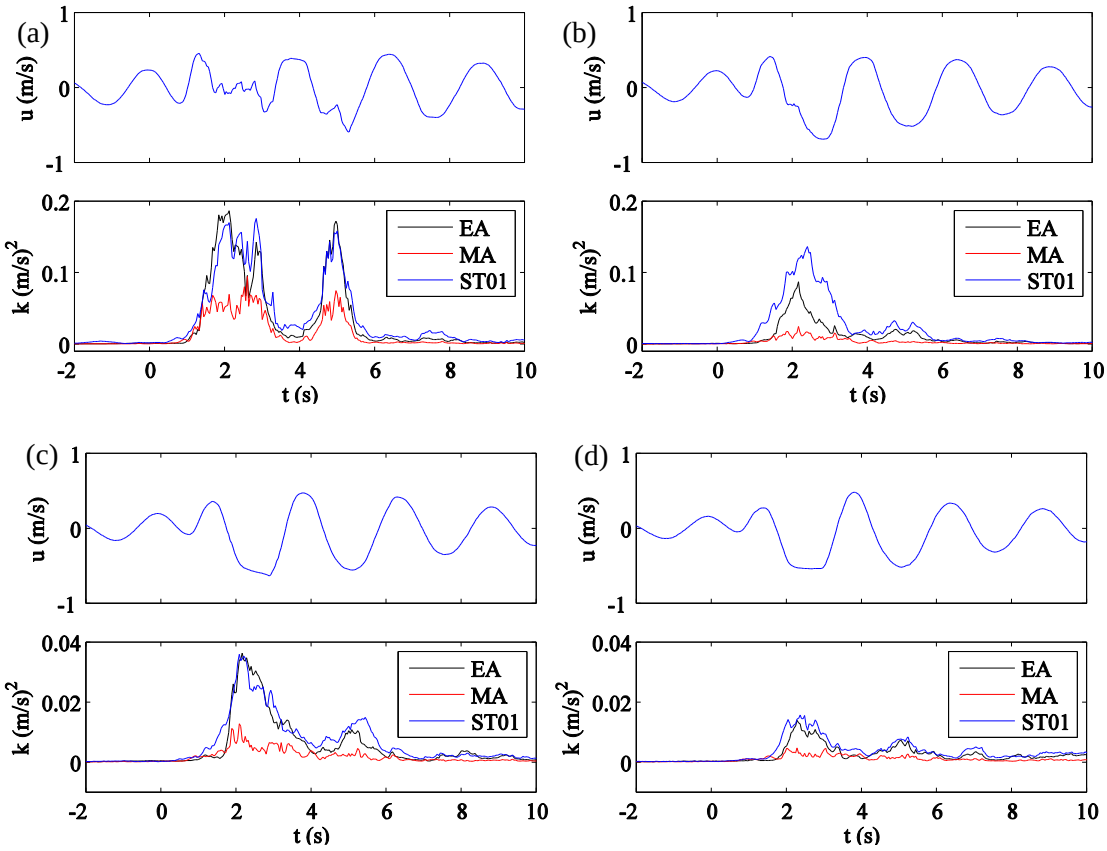

Fig. 4.15 The top panels show the ensemble-averaged horizontal velocity measured by ADV and the bottom panels show the comparison of corresponding turbulent kinetic energy extracted from ensemble averaging (EA), moving averaging (MA), and the ST01 method at *z* = (a) -0.34 m, (b) -0.55 m, (c) -0.72 m, and (d) -0.92 m.

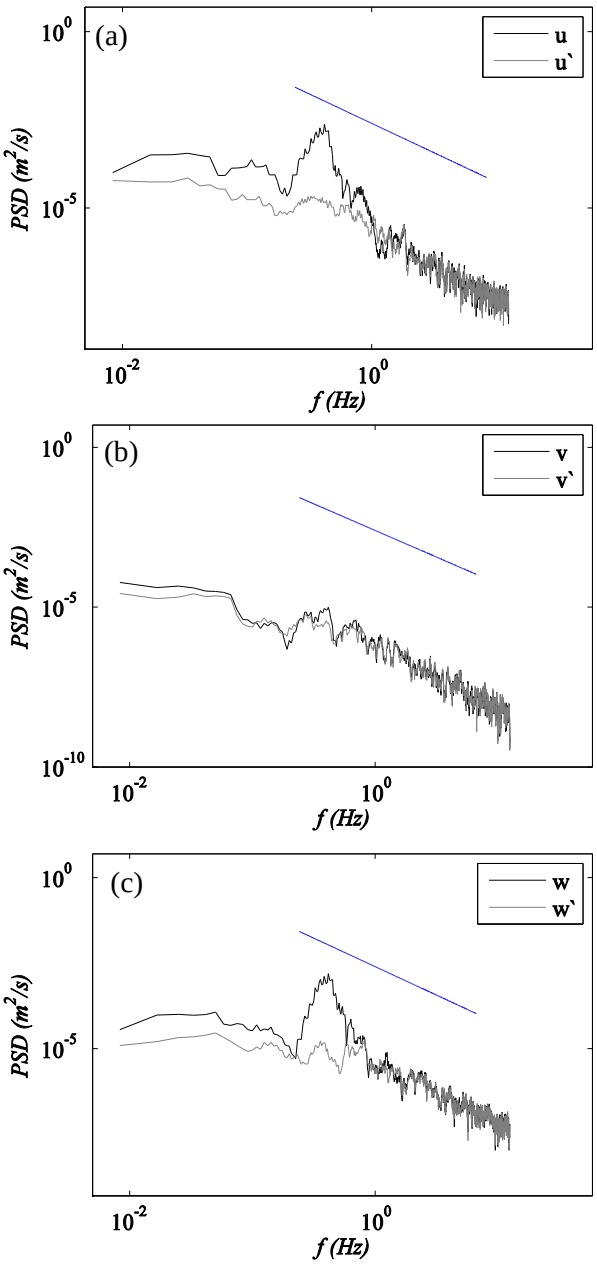

Fig. 4.16 Sample power spectral densities of instantaneous velocity and turbulent velocity at ADV2 for run 2: (a) the *x*-direction, (b) *y*-direction, and (c) *z*-direction velocity components. The Kolmogorov's -5/3 slope for the inertial subrange is also plotted for reference.

Fig. 4.17a shows the vertical profile of the wave-averaged mean velocity U_{wa} normalized by C measured using ADV in the present large scale study in comparison with the small scale results in L15. The wave-averaged velocity was calculated based on Eq. 4.3. The velocity profiles shows a sharp increase approximately at $z/H = -0.3$ in the small scale breakers. That indicates the splash-up and impinging rollers did not penetrate much below that depth (confirmed by the FOR void fraction measurements in L15). Similarly, U_{wa} in the large scale breakers shows a rapid increase between $z/H = -0.52$ and $z/H = -0.32$. The profiles between the two scales seem to be very close, although a noticeable discrepancy occurs at $0.52 < z/H < 0.88$.

Fig. 4.17b shows the vertical distribution of the square root of the wave-averaged turbulent kinetic energy $\sqrt{k_{wa}}$ normalized by C. Turbulent kinetic energy per unit mass k was calculated as

$$k = \frac{1}{2}\left(u'^2 + v'^2 + w'^2\right) \tag{4.11}$$

and k_{wa} was calculated using Eq. 4.2. Evidently, the profile of $\sqrt{k_{wa}}/C$ in the large scale breakers is consistent with that of the small scale results in L15. Based on the range of the measurement (below $z/H = -0.19$), $\sqrt{k_{wa}}/C$ decreases exponentially.

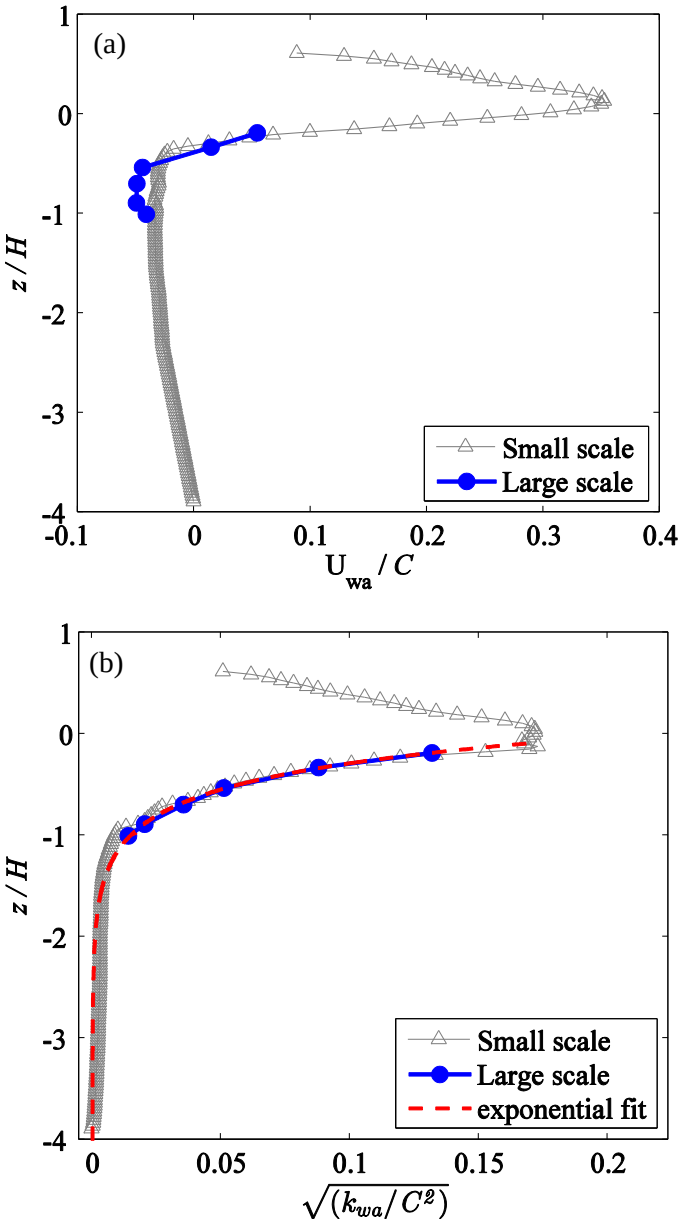

Fig. 4.17 Vertical distribution of (a) wave-averaged horizontal velocity U_{wa}/C. (b) Square root of wave-averaged turbulent kinetic energy $\sqrt{k_{wa}}/C$. Data below the still water level in (b) is fitted with an exponential curve $\sqrt{k_{wa}}/C = 0.043\exp(0.35z/H)$.

Accordingly, the vertical distribution of $\sqrt{k_{wa}}/C$ is fitted to an exponential curve (e.g., *Svendsen*, 1987; *Yoon and Cox*, 2010) as

$$\sqrt{k_{wa}}/C = a\exp(bz/H) \tag{4.12}$$

The two best fit coefficients are $a = 0.043$ and $b = 0.35$. From the close agreement between the two profiles, one may conclude that turbulent kinetic energy may be directly scaled, at least below the aerated region.

4.6 Conclusions

This paper presented the combined measurements of the surface velocity, the velocity below the region with intense air entrainment, void fraction, and free surface elevation in very large scale plunging breaking waves (of 1-m wave height). The results were compared with the study of small scale plunging breakers (of 0.2-m wave height) by L15. Some findings are summarized below.

The mechanism of the overturning jet impinging process between the two scales is similar; the impinging jet penetrates and pushes up the undisturbed water in front of it. The temporal evolution of the maximum surface horizontal velocity in the two scales is comparable, with a maximum difference of only about $0.2C$. In addition, the maximum surface velocity and the maximum of the mean kinetic energy in the streamwise direction near the center of the fully developed first splash-up roller are in close agreement.

The evolution of energetic eddies, and their length scales measured on the horizontal plane at the free surface, are revealed using a wavelet-based method. The energetic eddies are more localized at the surfaces of the first impinging roller and the first splash-up roller, but as the wave propagates, the eddies tend to spread across the entire aerated region beyond the second impingement. Furthermore, the second impingement and splash-up region is comprised of a wider range of eddy lengths (of $H / LS \sim 3-20$), compared to that in the first impingement and splash-up region (with lengths of $H / LS \sim 3-6$). The streamwise and lateral eddy lengths at the surface are nearly identical (0.2–0.25H) during the first and the second impingement/splash-up processes. If compared to the small scale breakers, the streamwise and vertical energetic eddy length scales at the surface of the impinging roller are found to be very close (at $LS \sim 0.1-0.2H$).

The temporal and spatial evolution of surface mean kinetic energy shared a common signature between the two scales when normalized by H (but not by L), which indicates that H is the characteristic length for normalizing breaking waves. The surface mean kinetic energy is transported following close to $2C$ until $x / H \sim 2-3$, indicating that the mean kinetic energy is transferred by the mean flow velocity (and not the wave group velocity).

The temporal contours of void fraction are similar between the two scales. The wave-averaged void fraction is almost identical in both scales at the measurement points above the still water level, but the void fraction is significantly lower below the still water level, indicating a shallower bubble penetration depth in the large scale breakers.

For the ADV measured velocities below the aerated region, the ensemble averaging

and the differencing method of ST01 provide reasonably close estimates of turbulence whereas the moving averaging constantly underestimates turbulence. All PSDs of the measured velocities below the aerated region follow the Kolmogorov -5/3 slope. The slope decreases in the aerated region above according to L15.

The vertical profiles of the wave-averaged horizontal velocities under the highly aerated region are in close agreement between the two scales. The measured vertical profile of the wave-averaged turbulent kinetic energy can be fitted to an exponential curve, consistent with the previous studies in surf zone breaking waves.

In summary, the kinematics and turbulence can be well represented among different physical scales if an appropriate scaling law is used. The dynamics, including void fraction and bubble number and size distributions, may be represented only to a certain extent. Cautions are needed when scaled model is used.

CHAPTER V

BUBBLE ENTRAINMENT IN LARGE SCALE PLUNGING BREAKING WAVES

5.1 Introduction

Wave breaking entrains large volumes of air bubbles into the water body to generate an air-water two phase flow. These breaking-induced bubbles interact intensely with the surrounding flows, producing a complex turbulent aerated flow that rapidly evolves both spatially and temporally as the breaking wave propagates. Bubbles plays a significant role in the physical, chemical, and biological processes occurring at the air-sea interface. The generated bubbles enhance transport of gases across the ocean surface, create aerosols that influence cloud and hurricane dynamics, and convey organic materials as they rise and burst at the surface.

The evolution of the bubble cloud relies on the air entrainment and associated bubbles. In plunging breaking waves, when the overturning jet impinges onto its front surface, the first splash-up roller is generated right in front of the jet and the first impinging roller is formed behind the jet. These two rollers form a lump of a large bubble cloud that evolves in intensity and shape as the breaking wave propagates. The evolution of the bubble cloud may be affected by the two factors – the wave field and the evolution of air entrainment (Anguelova and Huq, 2012). The evolution of the bubble cloud strongly influenced by the variations in the wave field including the scale (e.g., wave height H) and the intensity (e.g., plunging and spilling). The bubble cloud evolution may also depend on the change in the

air entrainment including the void fraction and the bubble size distribution. In addition, the saturation levels of dissolved nitrogen and oxygen in the surface layer of the ocean can affect the fate and the number of small bubbles (Stramska et al., 1990).

So far, despite the great advances, there exist only a small number of studies focusing on the bubble formation mechanisms, evolutions of the number of bubbles and their corresponding sizes during wave breaking. A pioneering study by Deane and Stokes (2002) proposed two bubble formation mechanisms associated with plunging breaking waves: firstly, smaller bubbles less than 1 – 2 mm in radius are generated by the impact and subsequent splashing of the overturning jet; secondly, larger bubbles greater than 2 mm in radius are generated by the fragmentation of the air cavity that is trapped and surrounded by the overturning jet and the undisturbed water below. Furthermore, Deane and Stokes observed both in laboratory and field breaking waves the two distinct power-law scaling relationships (a 3/2 slope for bubbles smaller than approximately 2 mm and a 10/3 slope for bubbles larger than 2 mm) in bubble size distributions. From their video recordings, Deane and Stokes also observed that the smallest bubbles fragmented were about 1 mm in radius and concluded the 1 mm bubble size as the Hinze scale.

This chapter discusses the preliminary results of the measured bubbles in the large scale plunging breaking waves. The experimental setup is identical to that described in Chapter III so is not repeated here.

5.2 Results

5.2.1 Length of the Bubble Cloud

The length of the bubble cloud in the large scale breaking wave was estimated by the

intensity level of the images that varied from 0 (black) to 255 (white) in the grey scale images (Fig. 5.1a). In the Figure, the length of the bubble cloud L_B is defined as the distance between the two lateral dotted lines (in the *y* direction) passing through the left and the right edges of the bubble cloud. The edges of the bubble cloud was easily distinguishable because of the high contrast between the bubble cloud (bright) and pure water (dark). However, one problem is associated with the sprays and droplets causing uneven edges along the *y* direction that creates ambiguity in identifying the bubble cloud. The occurrence of these sprays and droplets and their shapes were almost random among the repeated runs. In our approach, the mean intensities along the *y* direction were computed and an intensity threshold was set; the edges of the bubble clouds were defined as the first and the last points where the mean intensity exceeds the intensity threshold.

On the contrary, the BIV images in Lim et al. (2015) (hereafter referred as L15) showed that few droplets were observed in front of the splash-up roller of the small scale breaking waves. However, as the images in L15 are on the *x*-*z* plane (unlike the large scale images on the *x*-*y* plane), the edges of the bubble clouds are defined as the left and the right edges of the aerated region at the surface as shown in Fig. 5.1b. In the figure, the free surface and the inside of the aerated region were detected manually based on the ensemble-averaged BIV images. In addition, we step through each masking map, column by column, and use the upper boundary between the air-water mixture and the air to adjust each column up and down relative to the maximum upper boundary. As a result, it generates a new masking map with a horizontal upper boundary as shown in Fig. 5.1c. Based on that figure, the length of the aerated region was measured. Through this process, the plan view

length of the bubble cloud is obtained and compared to the length of the bubble cloud in the large scale experiment.

Figure 5.2 shows the time series of the normalized length of the bubble cloud in the current study and in L15. It is noted that the comparison of the cloud length was made until $t/T = 0.7$ when the two main bubble clouds generated by the first impingement and subsequent splash-ups became almost completely separated at the surface (see Figures 5h-5j in L15). Overall, the lengths of the normalized bubble clouds (by H) evolve following a very similar pattern within a difference within $L_B/H = 0.5$. The bubble cloud length reduces to about $L_B/H = 2.2$ at $t/T = 0.4$ when the first splash-up roller impinges on the free surface and forms the second splash-up roller. As the second splash-up continues to propagate downstream, the bubble cloud length continues to increase, reaching a maximum of about $L_B/H = 3.1$, until the near occurance of the complete separation of the first impinging roller and the subsequent splash-ups.

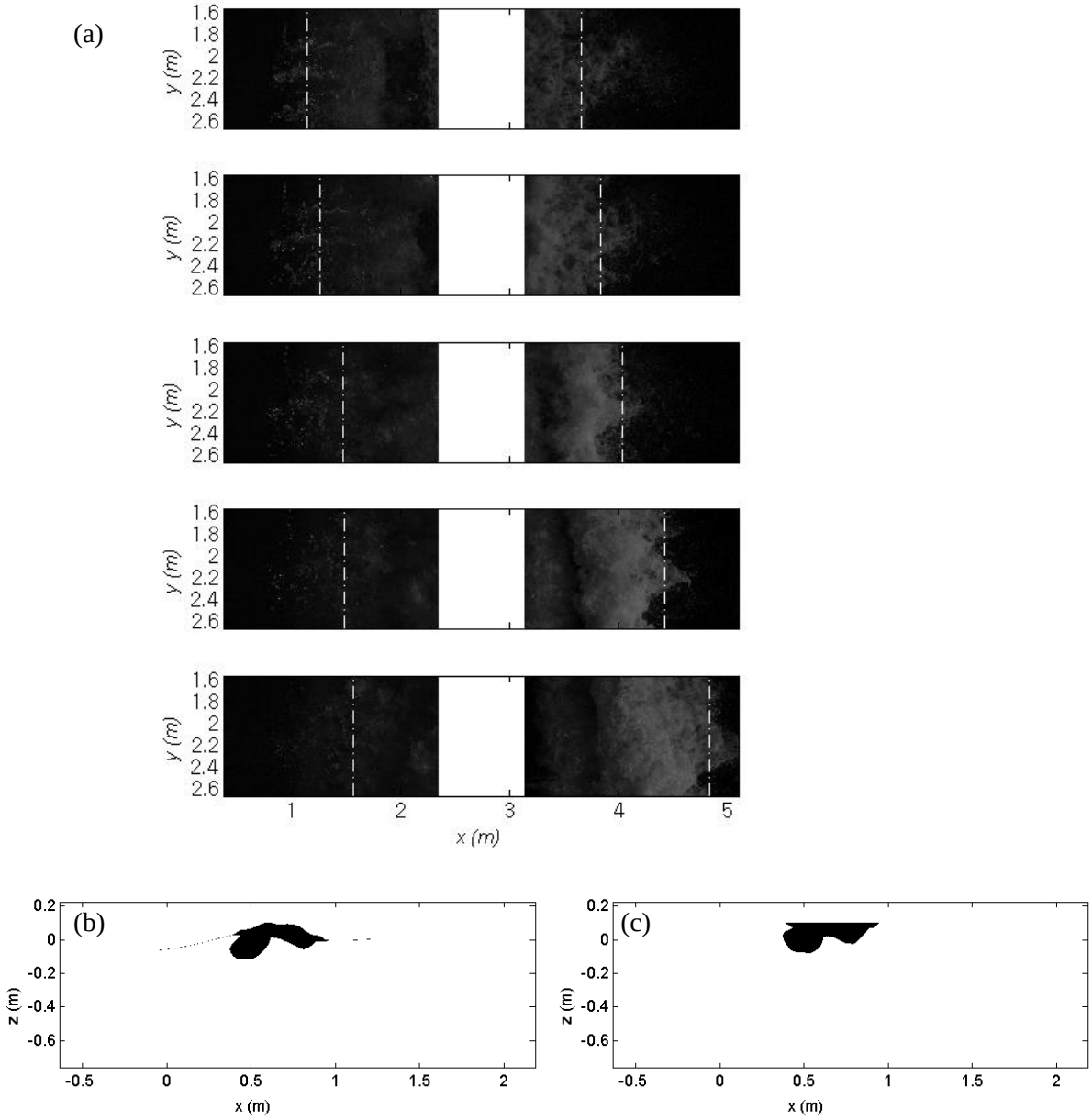

Fig. 5.1 Estimation of the bubble cloud length in (a) large scale experiment and (b, c) small scale experiments in L15. The vertical lines in (a) represents the start and the end boundaries of the bubble cloud. Each column in (b) was adjusted up and down relative to the maximum upper boundary resulting in (c) with a horizontal upper boundary.

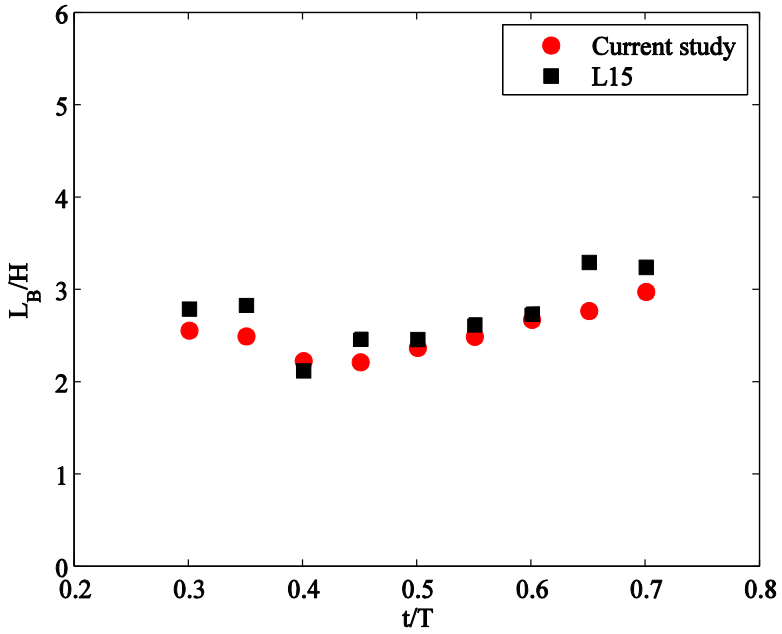

Fig. 5.2 Time series of the normalized length of the bubble cloud in the current study and in L15.

5.2.2 Average Number of Bubbles

The average number of bubbles N_B is defined as the number of bubbles detected at a point within one wave period averaged over the repeated runs

$$N_B = \frac{1}{N}\sum_{i=1}^{N} N_i \tag{5.1}$$

where N_i is the number of bubbles detected within one wave period in the ith repeated run and N is the number of repeats. To compare the amount of bubbles in the small and the large scale breaking waves with different total number of repeats, we computed the average number of bubbles. In the large scale experiment, the total number of repeats $N = 12$ was used for the bubble detection accounting only for the first wave of each run.

As mentioned in Chapter IV, the standard deviation of the impinging points of the first breaking wave in all the repeated runs was $0.2L$ in the large scale experiment despite the use of the identical input signals in wave generation. This means that some effects such as the possible imperfect control of the wavemaker and the wave instabilities that led to the variation of the impinging point cannot be neglected. This variation of the impinging point in the streamwise direction in turn affects the amount of sprays and droplets and their occurrence detected by the FOR probes mounted as a fixed location. Moreover, this discrepancy tends to accumulate in the second and the third breaking waves in each test run. For this reason, the bubble measurements were based on the FOR signals during the passage of the first wave only.

The total number of bubbles detected at the 8 FOR measurement points is greater than 6000. This number is about three times that detected in L15 and in Rojas and Loewen (2010), despite a smaller number of repeats of $N = 12$ in the large scale experiment, compared to $N = 20$ in L15. For a fair comparison, the ensemble averaged numbers of bubbles in the small and the large scale breaking waves were calculated.

Figure 5.3 shows the vertical profiles of the number of bubbles in the current large and in the small scale experiments. The maximum number of bubbles occurs close to $z / H = 0.1$ in both scales. That depth is in consistent with the occurrence of high shear caused by the differential motion between the high-speed rotation in the first splash-up roller and the low-speed wave motion under the trough level. The number of bubbles reduces as the depth increases below the high shear region. Since the void fraction becomes relatively low as the depth increases, it seems that only a few bubbles could

penetrate to that depth and reach the probes. Indeed, the decrease of bubble frequency below the high shear region is similar to the decrease of the wave-averaged void fraction as shown in Figure 4.14.

The number of bubbles in L15 is 6% of that in the present large scale experiment by averaging bubble numbers at each measured depth. Within one wave period, the first splash-up and the first impinging rollers (i.e., the bubble cloud) completely pass through the FOR probes in both scales as shown previously in Fig. 4.13. As mentioned earlier, the streamwise lengths (L_B) of the bubble cloud is strongly influenced by the wave height H. Assuming the bubble sizes and their distribution are similar in both scales, the number of the bubbles present at a certain depth within the bubble cloud of the large scale breaker would be about 5 times as many as that of the small scale breaker ($H_{large}/H_{small} = 5.1$).

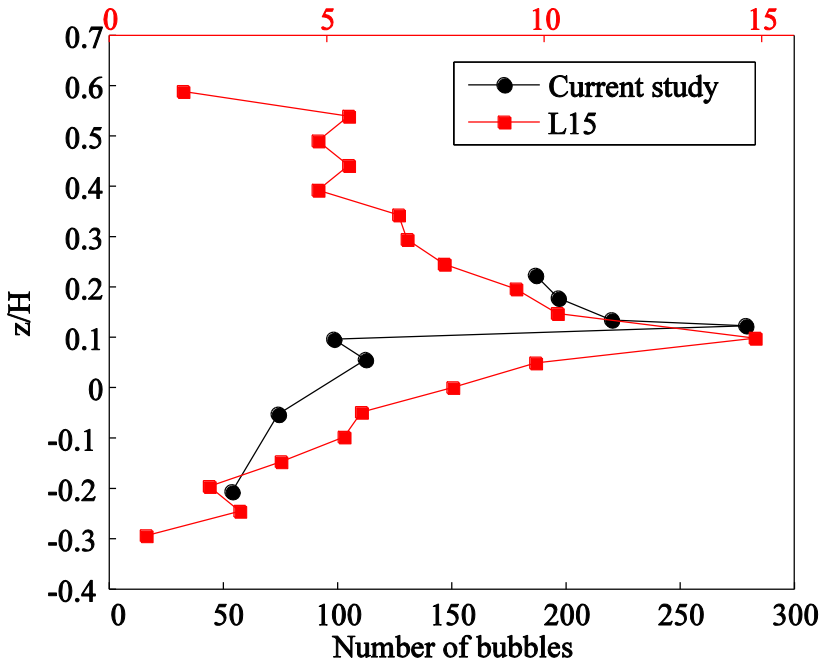

Fig. 5.3 Vertical profiles of the number of bubbles in the current large and in in L15.

However, the average number of bubbles in the large scale is about 17 times that of bubbles in the small scale breaker. This implies that the bubbles are more densely distributed resulting in a higher bubble frequency or bubble count rate in the large scale experiment. Althought the large scale results may have been affected by the presence of droplets, the results may indicate more frequent bubble break-up occurred in the large scale breaking waves. Further study is needed to clarify the observation and cause.

5.2.3 Bubble Size Distribution

FOR technique is capable of measuring the time interval when the fiber tip is inside a bubble. As discussed in Chapter IV, if this interval defined as the bubble residence time T_b as well as the velocity of the bubble are measured, the chord length of the bubble can be measured. However, the flow velocity inside the aerated region was not measured while

the surface velocity was measured in the large scale experiment. In contrast, since the flow velocity fields inside the aerated region were measured based on displacement of bubbles in L15 the flow velocitiy represent the speed of bubbles. Based on the close similarity of the kinematics such as the maximum horizontal velocities at the surface (Fig. 4.7) and the vertical profiles of the wave-averaged horizontal velocity (Fig. 4.17a) between the two scales, we postulate that the mean velocity fields within the aerated region are similar following the Froude scale. For this reason, we chose to use the mean flow velocity of L15 to estimate the mean speed of bubbles in the large scale experiments. The mean flow velocity in L15 may be scaled up based on the Froude scale such that

$$\frac{V(x/H,\ z/H,\ t/T)_{\text{large}}}{V(x/H,\ z/H,\ t/T)_{\text{small}}} = \sqrt{H_{\text{large}}/H_{\text{small}}} \sim 2.5 \qquad (5.2)$$

where V is the mean speed. It is noted that the wave height H is used for normalization because the evolutions of mean kinetic energy (Fig. 4.10) and turbulent kinetic energy (Fig. 4.11) showed a close agreement when x is normalized by H, but not L. Then the chord length s is defined as

$$s(x/H,\ z/H,\ t/T)_{\text{large}} = T_b(x/H,\ z/H,\ t/T)_{\text{large}} V(x/H,\ z/H,\ t/T)_{\text{large}} \qquad (5.3)$$

where T_b is the bubble residence time.

Fig. 5.4 shows the probability density function (PDF) of bubble size measured at x = 1.75 m in the large scale breaking waves based on Eq. 3.9. The visual identification of the

first impinging and the first spash-up rollers is ambiguous because the current setup uses the plan view images (*x*-*y* plane) unlike the side view (*x*-*z* plane) images used in the small scale experiment. Neverthelss, the distinct evolving patterns of void fraction as shown in Fig. 4.13a were used to identify the phases of the the first impinging and the first spash-up rollers. As a result, Fig. 5.4a and 5.4b show the bubble size distributions corresponding to the passage of the first impinging roller ($0.3 < t/T < 0.7$) and the first splash-up roller ($0 < t/T < 0.3$), respectively. The two distinct slopes are more evident in Fig. 5.4a than in Fig. 5.4b consistent with the results in the small scale (see Fig. 3.12). However, the slope change is not as significant as in Fig. 3.12 mainly due to the relatively large number of larger bubbles causing a flatter slope of Φ_{2f} = -1.6. On the other hand, this value is close to Φ_2 = -1.7 reported under large scale experiments in Mori et al., (2007). Further study is needed to clarify the results by increasing the vertical resolution of FOR measurements.

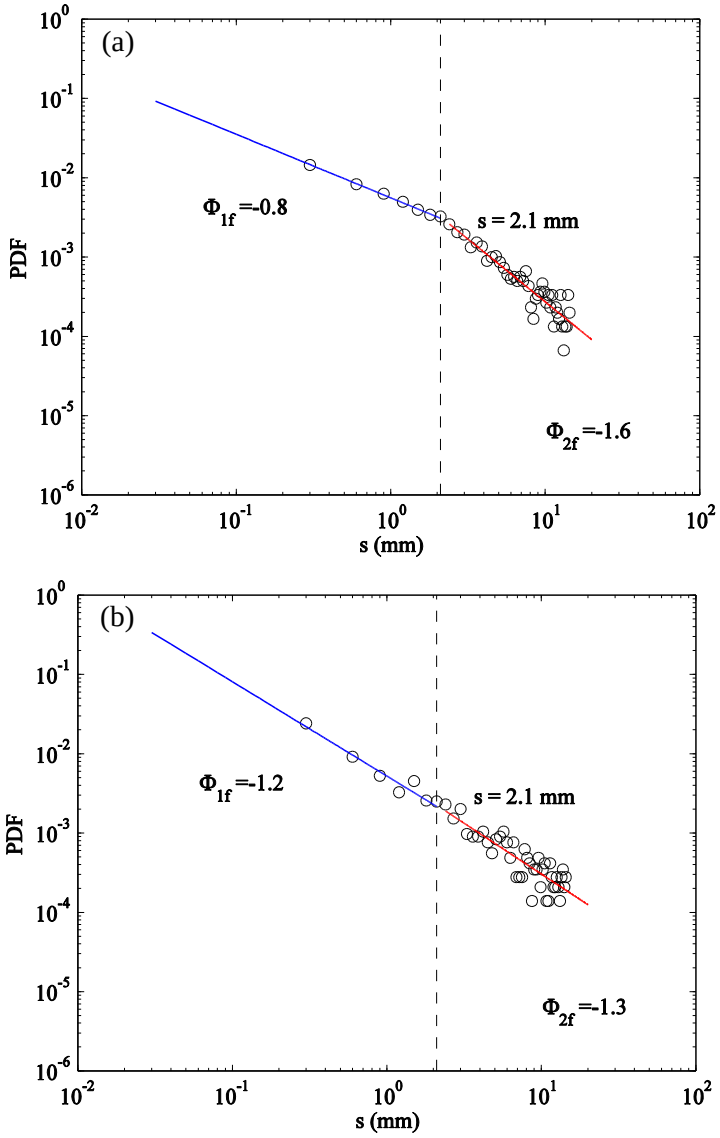

Fig. 5.4 The bubble size distributions at x = 1.75 m during the passage of (a) the impinging roller ($0.3 < t/T < 0.7$), and (b) the splash-up roller ($0 < t/T < 0.3$). The lines in (a) and (b) are least-square fits (with exponents of Φ_{1f} and Φ_{2f}). The Hinze scale was defined at a point where the slope change is the most significant in Fig 5.4a and plotted as a vertical dotted line in both 5.4a and 5.4b for a clear comparison.

CHAPTER VI

CONCLUSIONS AND FUTURE WORK

6.1 Conclusion

Section 6.1.1 summarizes the findings from the small scale plunging breaking waves with a 0.2 m wave height, mainly presented in Chapters II and III. Section 6.1.2 summarizes the findings from the large scale plunging breaking waves with a 1 m wave height, presented in Chapters IV and V.

6.1.1 Small-Scale Breaking Waves

Combined measurements of velocities and void fraction as well as free surface under an unsteady deep-water plunging breaking wave in a laboratory were presented. The plunging breaking waves were generated mechanically using a wave focusing method. The flow velocities were measured by the modified PIV technique in the entire flow region, the void fraction at the three splash-up regions were measured using the FOR technique, and the free surface was measured using both images and wave gauges. These techniques were combined to study the flow structure in the aerated rollers and splash-ups and investigate the effect of void fraction on kinematic and dynamic properties of the flow. A special focus was given to the relation between turbulent flow fields and bubbles generated by wave breaking. The wavelet-based technique was employed to extract the vortical structures and estimate their length scales in the impinging and the splash-up rollers. Evolution of bubble sizes and numbers at the three splash-up rollers were investigated in

conjunction with the swirling strength of the highly aerated flow fields. The turbulent dissipation rates were estimated based on mixture theory considering void fraction, and then compared with the total energy dissipation rates. This section summarizes some important findings of experimental results under the small scale deep-water plunging breakers with a breaking wave height of 0.2 m.

The maximum velocity in the plunging breaker reaches $1.68C$ at the first impingement and reaches much higher $2.14C$ at the beginning of the first splash-up process (at $t = 0.06T$). Multiple coherent vortical structures were found in the rolling foamy clouds of impingements and splash-ups. Clockwise vortices were observed at each impinging and splash-up roller, while counterclockwise backward impingement occurs in between the impinging and splash-up roller pair.

Combining the void fraction measurements with the velocity measurements allows us to examine the relation between flow kinematics and fluid density under the breaking wave. Time contours of void fraction signatures reveal distinct evolving patterns of entrained bubbles under the plunging breaker, such as the splash-up and the impinging roller. The maximum void fraction at the middle of the first splash-up roller is about 0.98. The averaged void fraction can be modeled as a linear growth followed by an exponential decay. In addition, the root-squared vorticity of the mean flow and turbulent intensity in the foamy turbulent flow are strongly correlated to the entrained bubbles and void fraction level. In the violent foamy splashing stage, the vorticity and turbulent intensity are strongly correlated to and possibly enhanced by the void fraction in the relatively low void fraction region (void fraction ~ 0 to 0.6 in the lower part of the roller); these quantities

then start to decrease as the void fraction varying within a narrow range after reaching the maximum (void fraction ~ 0.6 to 0.8 in the upper part of the roller). The turbulent intensity in the collapsed bubble cloud of impinging roller and wake region is comparable to that in the splashing stage even though the void fraction in the this stage is much lower. The possible cause could be that the passing air bubbles inject and transfer energy into the flow and cause the residue turbulence to remain energetic and maintain a similar level of flow fluctuations, although other mechanisms such as turbulent production and advection may also play a role in the process.

The mass flux, momentum flux, kinetic energy, potential energy, and total energy fluxes were computed and compared with and without void fraction being accounted for. If void fraction is not considered, all the mean and turbulence properties in the highly aerated breaker are significantly overestimated - the total kinetic energy shows a 100% overestimation and the image-based potential energy shows a 50% overestimation in the first splash-up region. A less significant overestimation is observed at the second and third splash-ups, reducing to about 20% to 30%. When accounting for the density variation, about 54% and 85% of the total energy are dissipated within one and two wavelengths beyond the wave impingement point, respectively. The results showed that void fraction measurements are essential for investigating certain flow properties that involve the fluid density, such as the mean and turbulent kinetic energy budget and the potential energy of the flow.

The vortical structures and the corresponding length scales in the highly aerated flow fields were successfully extracted using the wavelet-based technique by identifying the

local maximum intermittency measure (*LIMM*). The distributions of *LIMM* coincide well with classical measures of turbulence, such as swirling strength and vorticity. The estimated length scales of the vortical structures range from $0.05H$ to $0.15H$ during the initial impinging and the splash-up roller stages and are comparable to the integral length determined from auto-correlation.

The distributions of number of bubbles, separated as small and large bubbles by an estimated Hinze scale of approximately 2 mm in chord length (or 3 mm in diameter), were correlated with the swirling strength. During the passage of the first impinging roller, the results show that the number of smaller bubbles (s < 2 mm) is well correlated, but the number of larger bubbles is poorly correlated with the swirling strength of the flow. The results suggests that the local swirling motion of the energetic eddies enhances the breakup of larger bubbles into smaller bubbles in the impinging roller. On the contrary, during the passage of the first splash-up roller the swirling strength does not show clear correlation with the number of bubbles generated. This indicates that the mechanism of shearing the larger bubbles off, and splitting them into smaller bubbles, is relatively infrequent in the splash-up roller.

The PDF of bubble size versus bubble number was presented to examine the power scaling and Hinze scale of bubbles. Two distinct slopes and a Hinze scale were observed in the first impinging roller, the second impinging/splash-up roller, and the third impinging/splash-up roller. On the contrary, in the first splash-up roller the power law scaling for the larger bubble is flatter, implying that the bubble break-up events were not as frequent as those in the other rollers. The Hinze scale is also not evident in the first

splash-up roller. The reason is not clear, but the very high void fraction in the roller is likely involved.

The turbulent dissipation rate was estimated based on the mixture viscosity model with and without considering void fraction. If void fraction is not accounted for, the turbulent dissipation rate is significantly underestimated. This underestimation becomes greater for higher void fraction, reaching 70% in the initial impinging and the splash-up roller region. This implies that bubbles play a prominent role in enhancing the turbulent dissipation rate. With void fraction accounted for, the turbulent dissipation rate was found to be significantly lower than the rate of total energy dissipation. The ratio of the turbulent dissipation rate to the total energy dissipation rate is 57%, 19%, and 6% at FOR stations 1, 2 and 3, respectively, with an average ratio of 33% integrated from the breaking point to two wavelengths. This imbalance is consistent with observations previously reported on surf zone breakers. The 67% excess energy dissipation is likely caused by the presence of bubbles. The integrated bubble-induced dissipation is found to be 23%. Note that the bubble break-up process is not considered in the current analysis, but it may be responsible for the remaining imbalance.

6.1.2 Large-Scale Breaking Waves

To investigate the kinematics and air entrainment in large scale plunging breaking waves of 1 m wave height, combined measurements of the surface velocity, void fraction, velocity below the region with intense air entrainment, and surface elevation were presented using a suite of measurement techniques. The surface velocity fields were measured by the BIV technique in the air-water mixture, void fraction was measured by

the FOR technique during the violent splash-up processes. Time series of velocity was measured by a vertical array of acoustic Doppler velocimeters below the intense aerated region. The combined results were used to investigate the scale effects associated with the kinematics and air entrainments under the large scale plunging breaking waves by the comparisons to the results of the small scale plunging breaking waves as presented in Chapters II and III.

The mechanism of the overturning jet impinging process between the two scales is similar; the impinging jet penetrates and pushes up the undisturbed water in front of it. The temporal evolution of the maximum surface horizontal velocity in the two scales is comparable, with a maximum difference only about $0.2C$. Moreover, the maximum surface velocity and the maximum of the mean kinetic energy in the streamwise direction near the center of the fully developed first splash-up roller are in close agreement.

Wavelet analysis was employed to reveal the evolution of the energetic eddies and their length scales on the horizontal plane at the free surface. The energetic eddies are more localized at the surface of the first impinging roller and the first splash-up roller, while as the wave propagates, the eddies spread across the entire aerated region beyond the second impingement. Furthermore, the second impingingement and splash-up region comprises of a wider range of eddy length of $H/LS \sim 3-20$, compared to that in the first impingement and splash-up region of $H/LS \sim 3-6$. The streamwise and lateral length eddy lengths at the surface are nearly identical ($H/LS \sim 4.1-5.4$) during the first and the second impingement/splash-up processes.

The temporal and spatial evolution of surface mean kinetic energy shared a common

signature between the two scales when normalized by H (but not by L), indicating that the H is the charactertistic length in normalizing breaking waves. The surface mean kinetic energy is transported following close to $2C$ until $x/H \sim 2-3$, indicating the mean kinetic energy is transferred by the mean flow velocity, not the wave group velocity.

The temporal contours of void fraction are similar between the two scales. The wave-averaged void fraction is almost identical between both scales at the measurement points above the still water level, but void fraction is significantly lower below the still water level, indicating a shallower bubble penetration depth in the large scale breakers.

For the ADV measured velcoities below the aerated region, the ensemble averaging and the differencing method of ST01 provide a reasonably close estimates of turbulence, whereas the moving averaging constantly underestimate turbulence. All PSDs of the measured velocities below the aerated region follow the Kolmogorov -5/3 slope. The slope decreases in the aerated region above as discussed in Chapter III.

The vertical profiles of the wave-averaged horizontal velocity under the highly aerated region are in close agreement between the two scales. The measured vertical profile of the wave-averaged turbulent kinetic energy can be fitted to an exponential curve, consistent with the previous studies in surf zone breaking waves.

6.2 Future Work and Suggestions

In Chapter II and III, we have presented the significant overestimation of energy and underestimation of turbulent dissipation rate when void fraction was not considered. Unlike spilling breakers, plunging breakers entrain a large amount of air bubbles causing intense interactions between air and water. The evolution of this air-water mixture varies

in time and space. Although FOR technique is capable of measuring void fraction/ bubbles accurately in high temporal resolution, it is a point measurement and the measurements are limted in space. This may lead to some missing physics related to the horizontal variation of the air-water mixture under wave breaking. FOR probes can be deployed horizontally with a higher spatial resolution at least in some degrees to interpolate the intermediate values.

The velocity fields and void fraction were measured under spilling breaking waves in both the small scale and the large scale experiments. The measured data will be analysed to compare the spilling breaker to the plunging breaker and the small scale spilling breaker to the large scale spilling breaker.

The surface velocity fields, time series of velocity, and void fraction were measured under the large scale surf zone plunging breakers. Many field and laboratory studies (e.g. Scott et al., 2009) reported that breaking-induced turbulence can approach seabed and cause significant sediment suspension in the shallow water. Nadaoka et al., (1989) demonstrated that the mechanisms of this advection of turbulence to the seabed are through the evolution of the aerated roller into 3D obliquely descending eddies. On the other hand, few experimental studies measured the evolution of turbulent eddies quantitatively due to the difficulties in measuring velocity fields within the aerated roller. The effects of void fraction on the evolution of turbulent eddies also remain unknown. The plan view size of the obliquely descending eddies will be estimated by the measured surface velocity fields using BIV, the advection of turbulence will be estimated by the measured velocity using a set of ADVs, and the effect of void fraction will be considered

based on the measurements using FOR.

In Chapter III, the contributions of bubble-induced dissipation to total energy dissipation were obtained by measuring velocity fields and void fraction in the highly aerated region of plunging breaking waves. However, validating this result was difficult because few studies from other researchers exist – they are mostly based on numerical simulations (e.g. Ma et al., 2011; Derakhti and Kirby, 2014) unlike the current study. Moreover, the bubble break-up energy was not quantified. A new breaking wave experiment using different surfactants to adjust the number of breaking-induced bubbles will be conducted to estimate the variation of energy dissipation.

The bubble frequency as well as the bubble size distribution in the large scale breaking waves were obtained as presented in Chapter V. However, the number of visible droplets near the splash-up region appeared to be significantly more than that in the small scale based on the BIV images. Until now, FOR technique is not capable of distinguishing droplets and bubbles that may have contaminated some results such as the bubble size distribution under the large scale breaker. Nevertheless, the high speed camera used to estimate the impinging point indeed captured some sparays and droplets in front of the splash-up roller. With the images, the sizes of the splays and droplets can be estimated.

REFERENCES

Adrian, R. J., Christensen, K. T. and Liu, Z. C. (2000), Analysis and interpretation of instantaneous turbulent velocity fields. *Exp. Fluids* **29**, 275.

Anguelova, M. D., and Huq, P. (2012), Characteristics of bubble clouds at various wind speeds, *J. Geophys. Res.*, *117*, C03036.

Baldy, S. (1988), Bubbles in the close vicinity of breaking waves. *J. Geophys. Res.* **93**, 8239–8249.

Baldy, S. (1993), A generation-dispersion model of ambient and transient bubbles in the close vicinity of breaking waves, *J. Geophys. Res.*, **98**(C10), 18277–18293.

Banner, M. L., and Peregrine, D. H. (1993), Wave breaking in deep-water, *Annu. Rev. Fluid Mech.*, *25*, 373-397.

Basco, D. (1985), A Qualitative Description of Wave Breaking, *J. Waterway, Port, Coastal, Ocean Eng.*, **10**.1061/(ASCE)0733-950X(1985)111:2(171), 171-188.

Battjes, J. A. (1988), Surf-zone dynamics, *Annu. Rev. Fluid Mech.*, *20*, 257-293.

Blenkinsopp, C. E., and Chaplin, J. R. (2007), Void fraction measurements in breaking waves, *Proc. R. Soc. A-Math. Phys. Eng. Sci.*, *463*(2088), 3151-3170.

Blenkinsopp, C.E., Chaplin, J.R., (2010), Bubble Size Measurements in Breaking Waves Using Optical Fiber Phase Detection Probes. *IEEE Journal of Oceanic Engineering*, **35(2)**, 388-401.

Blenkinsopp, C. E. and Chaplin, J. R. (2011), Void fraction measurements and scale effects in breaking waves in freshwater and seawater, *Coast. Eng.*, **58**, 417-428.

Bonmarin, P. (1989), Geometric properties of deep-water breaking waves, *J. Fluid Mech.*, *209*, 405-433.

Bonnet, J.P., Delville, J., (2001), Review of coherent structures in turbulent free shear flows and their possible influence on computational methods. *Flow Turbul. Combust.* **66** (4), 333–353.

Bullock, G. N., Crawford, A. R., Hewson, P. J., Walkden, M. J. A., Bird, P. A. D. (2001), The influence of air and scale on wave impact pressures, *Coast. Eng.*, **42**, 4, 291-312.

Camussi, R. (2002), Coherent structure identification from wavelet analysis of particle image velocimetry data. *Exp. Fluids* **32**, 76–86

Camussi, R. and Felice, F. D. (2006), Statistical properties of vortical structures with spanwise vorticity in zero pressure gradient turbulent boundary layers. *Phys. Fluids* **18**, 035108

Chang, K.A., Ariyarathne, K., and Mercier, R. (2011), Three-dimensional green water velocity on a model structure. *Exp. in Fluids*, *51*, 327-345.

Chang, K. A., Lim, H. J., and Su, C. B. (2002), A fibre optic Fresnel ratio meter for measurements of solute concentration and refractive index change in fluids, *Meas. Sci. Technol.*, *13*(12), 1962-1965.

Chang, K. A., Lim, H. J., and Su, C. B. (2003), Fiber optic reflectometer for velocity and fraction ratio measurements in multiphase flows, *Rev. Sci. Instrum.*, *74*(7), 3559-3565.

Chang, K. A., and Liu, P. L. F. (1998), Velocity, acceleration and vorticity under a breaking wave, *Phys. of Fluids*, *10*(1), 327-329.

Chang, K. A., and Liu, P. L. F. (1999), Experimental investigation of turbulence generated by breaking waves in water of intermediate depth, *Phys. of Fluids*, *11*(11), 3390-3400.

Chang, K. A., and Liu, P. L. F. (2000), Pseudo Turbulence in PIV Breaking-wave Measurements, *Exp. in Fluids, 29*, pp 331-338.

Chanson, H. (2002), Air–water flow measurements with intrusive phase-detection probes: Can we improve their interpretation? *J. Hyd. Eng. ASCE* **128(3)**, 252–255.

Cheng, J. and Wang, P. (2015), Extracting Turbulence under Breaking Waves in the Surf Zone, *J. Waterway, Port, Coastal, Ocean Eng.*, 10.1061/(ASCE)WW.1943-5460.0000307, 06015003.

Christensen, E. D. (2006), Large eddy simulation of spilling and plunging breakers, *Coastal Eng.*, *53*, 463-485.

Christensen, E. D., Walstra, D. J., and Emerat, N. (2002), Vertical variation of the flow across the surf zone, *Coastal Eng.*, *45*(1), 165-198.

Chuang, W. –L, Chang , K.-A., Mercier, R. (2015), Green water velocity due to breaking wave impingement on a tension leg platform, *Exp. Fluids*, **56**:139.

Clark, N. N. and Turton, R. (1998), Chord length distributions related to bubble size distributions in multiphase flows. *Int. J. Multiphase Flow*, **14(4)**, 413–424.

Cowen, E. A., I. M. Sou, P. L.-F. Liu, and B. Raubenheimer (2003), PIV measurements within a laboratory generated swash zone, J. Eng. Mech., 129, 1119–2003.

Cox, D. T. and Kobayashi, N., (2000), Identification of intense, intermittent coherent motions under shoaling and breaking waves. *J. Geophys. Res.* **105** (6), 223–236.

Cox, D. T., and Shin, S. W. (2003), Laboratory measurements of void fraction and turbulence in the bore region of surf zone waves, *J. Eng. Mech.*, *129*(10), 1197-1205.

Deane, G. B. (1997), Sound generation and air entrainment by breaking waves in the surf zone, *J. Acoust. Soc. Am.*, *102*(5), 2671-2689.

Deane, G. B., and Stokes, M. D. (2002), Scale dependence of bubble creation mechanisms in breaking waves, *Nature, 418*(6900), 839-844.

Derakhti, M. and Kirby, J. T. (2014), Bubble entrainment and liquid–bubble interaction under unsteady breaking waves. *J. Fluid Mech.* **761**, 464-506.

Doron, P., Bertuccioli, L., Katz, J. and Osborn, T. R. (2001), Turbulence characteristics and dissipation estimates in the coastal ocean bottom boundary layer from PIV data. *J. Phys. Oceanogr.* **31**, 2108–2134

Drazen, D. A., Melville, W. K., and Lenain, L. (2008), Inertial scaling of dissipation in unsteady breaking waves, *J. Fluid Mech.*, *611*, 307-332.

Drazen, D. A., and Melville, W. K. (2009), Turbulence and mixing in unsteady breaking surface waves, *J. Fluid Mech.*, 628, 85-119.

Elgar, S., R. T. Guza, B. Raubenheimer, T. H. C. Herbers, and E. L. Gallagher (1997), Spectral evolution of shoaling and breaking waves on a barred beach, *J. Geophys. Res.*, 102(C7), 15,797–15,805, doi:10.1029/97JC01010.

Farge, M. (1992), Wavelet transform and their applications to turbulence. *Annu. Rev. Fluid Mech.* **24**, 395–457

Farmer, D. M., McNeil, C. L., and Johnson, B. D. (1993), Evidence for the importance of bubbles in increasing air sea gas flux, *Nature, 361*(6413), 620-623.

Garrett C., Li M., and Farmer D., (2000), The connection between bubble size spectra and energy dissipation rates in the upper ocean, *J. Phys. Oceanogr.*, 30, 2163-2171.

George, R., Flick, R. E., and Guza, R. T. (1994), Observations of turbulence in the surf zone, *J. Geophys. Res.*, 99, 801–810.

George, W. K., and H. J. Hussein (1991), Locally axisymmetric turbulence, *J. Fluid Mech.*, 233, 1–23.

Govender, K., Mocke, G. P., and Alport, M. J. (2002), Video-imaged surf zone and roller structures and flow fields, *J. Geophys. Res.*, *107*, C73072.

Govender, K., Mocke, G. P., and Alport, M. J. (2004), Dissipation of isotropic turbulence and length-scale measurements through the wave roller in laboratory spilling waves, *J. Geophys. Res.*, *109*(C08018), 5115-5124.

Hinze, J. O. (1955), Fundamentals of the hydrodynamic mechanism of splitting in dispersion processes, *AIChE J.*, 1, 289–295.

Hoque, A. (2002), Air bubble entrainment by breaking waves and associated energy dissipation. PhD thesis, Department of Architecture and Civil Engineering. Toyohashi University of Technology, Toyohashi, pp. 151.

Hoque, A., and Aoki, S. I. (2005), Distributions of void fraction under breaking waves in the surf zone, *Ocean Eng.*, *32*, 1829-1840.

Huang, Z. C., Hsiao, S. C., Hwung, H. H., and Chang, K. A. (2009), Turbulence and energy dissipations of surf-zone spilling breakers, *Coastal Eng.*, 56, 733-746.

Huang, Z. C., Hwang, K., -S. (2015), Measurements of surface thermal structure, kinematics, and turbulence of a large-scale solitary breaking wave using infrared imaging techniques, *Coast. Eng.*, 96, 132-147.

Huang, Z. C., Hwung, H. H. and Chang, K. A. (2010), Wavelet-based vortical structure detection and length scale estimate for laboratory spilling waves. *Coast. Eng.* 57(9) , 795–811

Huang, Z. C., Lenain, L., Melville, W. K., Middleton, J. H., Reineman, B. D., Statom, N., and McCabe, R. M. (2012a), Dissipation of wave energy and turbulence in a barrier-reef lagoon, *Journal of J. Geophys. Res.*, *117*, C03015.

Huang, Z. C., Reineman, B. D., Lenain, L., Melville, W. K., and Middleton, J. H. (2012b), Airborne LIDAR measurements of wave energy dissipation in a coral reef lagoon system, *Journal of J. Geophys. Res.*, *117*, C03016.

Hwung, H. H., Chiang, W. S., and Hsiao, S. C. (2007), Observations on the evolution of wave modulation, *Proc. R. Soc. A-Math. Phys. Eng. Sci.*, *463*(2077), 85-112.

Ishii, M. and K. Mishima (1984), Two-fluid model and hydrodynamic constitutive relations, *Nucl. Eng. Des.*, 82, 107–126.

Ishii, M. and N. Zuber (1979), Drag Coefficient and Relative Velocity in Bubbly, Droplet or Particulate Flows, *AIChE J.*, 25, 843–855.

Kiger, K. T., and Duncan, J. H. (2012), Air-entrainment mechanisms in plunging jets and breaking Waves, in *Annu. Rev. Fluid Mech., Vol 44*, edited by S. H. Davis and P. Moin, pp. 563-596, Annual Reviews, Palo Alto.

Kimmoun, O., and Branger, H. (2007), A particle images velocimetry investigation on laboratory surf-zone breaking waves over a sloping beach, *J. Fluid Mech.*, *588*, 353-397.

Lamarre, E., and Melville, W. K. (1991), Air entrainment and dissipation in breaking waves, *Nature*, *351*(6326), 469-472.

Lamarre, E., and Melville, W. K. (1992), Instrumentation for the measurement of void-fraction in breaking waves - labratory and field results, *IEEE J. Ocean. Eng.*, *17*(2), 204-215.

Lance, M., and Bataille, J. (1991), Turbulence in the liquid-phase of a uniform bubbly air-water-flow, *J. Fluid Mech.*, *222*, 95-118.

Leifer, I., R. K. Patro, and P. Bowyer (2000), A study on the temperature variation of rise velocity for large clean bubbles, *J. Atmos. Oceanic Technol.*, **17**, 1392 – 1402.

Leifer, I., Caulliez, G., and de Leeuw, G. (2006), Bubbles generated from wind-steepened breaking waves: 2. Bubble plumes, bubbles, and wave characteristics, *J. Geophys. Res.*, *111*(C6), C06021.

Leifer, I., and de Leeuw, G. (2006), Bubbles generated from wind-steepened breaking waves: 1. Bubble plume bubbles, *J. Geophys. Res. Oceans.*, *111*(C6), C06020.

Lim, H. J., Chang, K. A., Su, C. B., and Chen, C. Y. (2008), Bubble velocity, diameter, and void fraction measurements in a multiphase flow using fiber optic reflectometer, *Rev. Sci. Instrum.*, *79*(12), 125105.

Lim, H. J., K. A. Chang, Z. C. Huang, and B. Na (2015), Experimental study on plunging breaking waves in deep water, *J. Geophys. Res. Oceans*, 120, 2007–2049, doi:10.1002/2014JC010269.

Lin, C., Hsieh, S. C., Lin, I. J., Chang, K. A., and Raikar., R. V. (2012), Flow property and self-similarity in steady hydraulic jumps, *Exp. in Fluids.*, *53*, 1591–1616.

Lin, P., and Liu, P. L. F. (1998), A numerical study of breaking waves in the surf zone, *J. Fluid Mech.*, *359*, 239-264.

Liu, W. and Clark, N. N. (1995), Relationships between distributions of chordlengths and distributions of bubble sizes including their statistical parameters. *Int. J. Multiphase Flow*, **21**, 6, 1073–1089

Liu, W., Clark, N. N., and Karamavruc, A. I. (1996), General method for the transformation of chord-length data to a local bubble-size distribution. *AIChE J.*, **42**, 10, 2713–2720

Loewen, M. R., Odor, M. A., and Skafel, M. G. (1996), Bubbles entrained by mechanically generated breaking waves, *J. Geophys. Res.*, *101*(C9), 20759-20769.

Longo, S., Petti, M., and Losada, I. J. (2002), Turbulence in the swash and surf zones: a review, *Coastal Eng.*, *45*, 129-147.

Longo, S. (2003), Turbulence under spilling breakers using discrete wavelets. *Exp. Fluids* **34**, 181–191.

Longo, S. (2009), Vorticity and intermittency within the pre-breaking region of spilling breakers. *Coast. Eng.* **56 (3)**, 285–296

Ma, G. (2012), Multiscale numerical study of turbulent flow and bubble entrainment in the surf zone. PhD thesis, University of Delaware, Newark DE.

Ma, G., F. Shi, and J. T. Kirby (2011), A polydisperse two-fluid model for surf zone bubble simulation, *J. Geophys. Res.*, **116**, C05010.

Manninen, M., V. Taivassalo, S. Kallio (1996), On the Mixture Model for Multiphase Flow, VIT Publications, Technical Research Center of Finland, 288, 1–65.

Martinez-Bazan, C., Rodriguez-Rodriguez, J., Deane, G. B., Montanes J. L., and Lasheras J. C. (1999), On the breakup of an air bubble injected into a fully developed turbulent flow. Part 1. Breakup frequency. *J. Fluid Mech.*, **401**, 157-182.

Melville, W. K. (1983), Wave modulation and breakdown, *J. Fluid Mech.*, *128*, 489-506.

Melville, W. K. (1996), The role of surface-wave breaking in air-sea interaction, *Annu. Rev. Fluid Mech.*, *28*, 279-&.

Melville, W. K., and Matusov, P. (2002), Distribution of breaking waves at the ocean surface, *Nature*, *417*, 58-63.

Melville, W. K., Veron, F., and White, C. J. (2002), The velocity field under breaking waves: coherent structures and turbulence, *J. Fluid Mech.*, 454, 203-233.

Miller, R. (1976), Role of vortices in surf zone prediction: sedimentation and wave forces, in Beach and Nearshore sedimentation, edited by R. A. Davis and R. L. Ethington, pp. 92-114, *Soc. Econ. Paleontol. Mineral.*

Mori, N., and Kakuno, S. (2008), Aeration and bubble measurements of coastal breaking waves, *Fluid Dynamics Res., 40*, 616-626.

Mori, N., Kakuno, S., and Cox, D., (2009), Aeration and Bubbles in the Surf Zone, *Handbook of Coastal and Ocean Engineering*, Y.C. Kim (ed.), 115 - 130.

Mori, N., T. Suzuki, and S. Kakuno (2007a), Experimental study of air bubbles and turbulence characteristics in the surf zone, *J. Geophys. Res., 112*, C05014, doi:10.1029/2006JC003647.

Mori, N., T. Suzuki, and S. Kakuno (2007b), Noise of acoustic Doppler velocimeter data in bubbly flows, *J. Eng. Mech.*, **133**, 122–125.

Na, B., K.-A. Chang, Z.-C. Huang, and H.-J. Lim (2016), Turbulent flow field and air entrainment in laboratory plunging breaking waves, *J. Geophys. Res. Oceans*, 121, doi:10.1002/2015JC011377.

Nadaoka, K., Hino, M., and Koyano, Y. (1989), Structure of the turbulent flow field under breaking waves in the surf zone, *J. Fluid Mech., 204*, 359-387.

Nimmo Smith, W. A. M., Katz, J., and Osborn, T. R. (2005), On the structure of turbulence in the bottom boundary layer of the coastal ocean. *J. Phys. Oceanogr.*, **35**, 72–93.

Oh, S.-H., Mizutani, N. and Suh, K.-D. (2008), Laboratory observation of coherent structures beneath microscale and large-scale breaking waves under wind action. *Exp. Therm. Fluid.* **32**, 1232–1247.

Peregrine, D. H. (1983), Breaking waves on beaches, *Annu. Rev. Fluid Mech., 15*, 149-178.

Perlin, M., He, J. H., and Bernal, L. P. (1996), An experimental study of deep water plunging breakers, *Phys. of Fluids*, *8*(9), 2365-2374.

Perlin, M., Choi, W., and Tian, Z. (2013), Breaking waves in deep and intermediate waters, *Annu. Rev. Fluid Mech.*, *45*, 115-145.

Qiao, H., and Duncan, J. H. (2001), Gentle spilling breakers: crest flow-field evolution, *J. Fluid Mech.*, *439*, 57-85.

Rapp, R. J., and Melville, W. K. (1990), Laboratory measurements of deep-water breaking waves, *Philos. Trans. R. Soc. Lond. Ser. A-Math. Phys. Eng. Sci.*, *331*(1622), 735-800.

Rensen, J., Luther, S., and Lohse, D. (2005), The effect of bubbles on developed turbulence. *J. Fluid Mech.*, **538**, 153-187.

Rodríguez-Rodríguez, J., Marugán-Cruz, C., Aliseda, A., Lasheras, J., C. (2011), Dynamics of large turbulent structures in a steady breaker, *Exp. Therm. Fluid*, **35**, 2, 301-310.

Rojas, G., and Loewen, M. R. (2007), Fiber-optic probe measurements of void fraction and bubble size distributions beneath breaking waves, *Exp. in Fluids*, *43*(6), 895-906.

Rojas, G., and Loewen, M. R. (2010), Void fraction measurements beneath plunging and spilling breaking waves, *J. Geophys. Res.*, *115*, C08001.

Ruppert-Felsot, J., Farge, M. and Petitjeans, P. (2009), Wavelet tools to study intermittency: application to vortex bursting. *J. Fluid Mech.* **636**, 427–453

Ryu, Y., Chang, K. A., and Lim, H. J. (2005), Use of bubble image velocimetry for measurement of plunging wave impinging on structure and associated greenwater, *Meas. Sci. Technol.*, *16*, 1945-1953.

Ryu, Y., and Chang, K. A. (2008), Green water void fraction due to breaking wave impinging and overtopping, *Exp. in Fluids*, *45*(5), 883-898.

Ryu, Y. G., Chang, K. A., and Mercier, R. (2007), Runup and green water velocities due to breaking wave impinging and overtopping, *Exp. in Fluids*, *43*(4), 555-567.

Saberi S., Shakourzadeh K., Bastoul D., and Militzer J. (1995), Bubble size and velocity measurements in gas liquid systems: application of fiber-optic technique to pilot plant scale. *Can. J. Chem. Eng.*, **73**, 253–257.

Scott, C. P., D. T. Cox, T. B. Maddux, and J. W. Long (2005), Large-scale laboratory observations of turbulence on a fixed barred beach, Meas. Sci. Technol., 16, 1903–1912.

Serdula, C. D. and Loewen, M. R. (1998), Experiments investigating the use of fiber-optic probes for measuring bubble-size distributions. *IEEE J. Ocean. Eng.*, **23(4)**, 385–399

Serizawa, A., and Kataoka, I. (1990), Turbulence suppression in bubbly two-phase flow, *Nucl. Eng. Des.*, **122**, 1–16.

Shaw, W. J., and J. Trowbridge (2001), The direct estimation of near bottom turbulent fluxes in the presence of energetic wave motions, J. Atmos. Ocean. Tech., 18, 1540–1557.

Shi, F., Kirby, J. T., Ma, G. (2010), Modeling quiescent phase transport of air bubbles induced by breaking waves, *Ocean Modelling*, 35, 1–2, 105-117.

Skyner, D. (1996), A comparison of numerical predictions and experimental measurements of the internal kinematics of a deep-water plunging wave. *J. Fluid Mech.* **315**, 51

Skyner, D. J., Gray, C., and Greated, C. A. (1990), A comparison of the time-stepping numerical predictions with whole-field flow measurement in breaking waves, in *Water Wave Kinematics*, edited by A. Torum and O. T. Gudmestad, pp. 491-508, Kluwer Academic Publishers, Boston.

Stansby, P. K., and Feng, T. (2005), Kinematics and depth-integrated terms in surf zone waves from laboratory measurement, *J. Fluid Mech., 529*, 279-310.

Sutherland, P., and Melville, W. K. (2013), Field measurements and scaling of ocean surface wave-breaking statistics, *Geophys. Res. Lett.*, **40**, 3074–3079 doi:10.1002/grl.50584.

Svendsen, I. A. (1987), Analysis of surf zone turbulence, *J. Geophys. Res.*, *92*(C5), 5115-5124.

Tennekes, L. and Lumley, J. L. (1972), *A First Course in Turbulence*. MIT Press.

Thornton, E. B., R. A. Dalrymple, T. Drake, E. Gallagher, R. T. Guza, A. Hay, R. A. Holman, J. Kaihatu, T. C. Lippmann, and T. Ö zkan-Haller (2000), State of nearshore processes research: II, *Technical Report NPS-OC-00-001,* 37 pp., Naval Postgraduate School, Monterey, Calif.

Tian, Z. G., Perlin, M., and Choi, W. (2008), Evaluation of a deep-water wave breaking criterion, *Phys. of Fluids, 20*(6), 066604.

Tian, Z. G., Perlin, M., and Choi, W. (2010), Energy dissipation in two-dimensional unsteady plunging breakers and an eddy viscosity model, *J. Fluid Mech.*, *655*, 217-257.

Ting, F. C. K., and Kirby, J. T. (1995), Dynamics of surf zone turbulence in a strong plunging breaker, *Coastal Eng.*, *24*, 177-204.

Ting, F.C.K., Kirby, J.T. (1996), Dynamics of surf-zone turbulence in a spilling breaker. *Coast. Eng.* **27**, 131–160.

Troshko, A. A., and Y. A. Hassan (2001), A two-equation turbulence model of turbulent bubbly flows, *Int. J. Multiphase Flow*, **27**, 1965–2000.

Vagle, S., and Farmer, D. M. (1998), A comparison of four methods for bubble size and void fraction measurements, *IEEE J. Ocean. Eng.*, *23*(3), 211-222.

Wang, S. K., Lee, S. J., Jones, O. C. and Lahey, R. T. (1987), 3-D turbulence structure and phase distribution measurements in bubbly two-phase flows, *Int. J. Multiphase Flow*, **13**, 327–343.

Watanabe, Y., Saeki, H. S., and Hosking, R. J. (2005), Three-dimensional vortex structures under breaking waves, *J. Fluid Mech.*, *545*, 291-328.

Yoon, H.-D., and D. T. Cox (2010), Large-scale laboratory observations of wave breaking turbulence over an evolving beach, *J. Geophys. Res.*, **115**, C10007, doi:10.1029/2009JC005748.

Zhou, J., Adrian, R. J., Balachandar, S., and Kendall, T. M. (1999), Mechanisms for generating coherent packets of hairpin vortices in channel flow. *J. Fluid Mech.*, **387**, 353-396.

APPENDIX A

The density variation in the air-water mixture of the plunging breaker is needed to estimate dynamic quantities, such as the mean kinetic energy and turbulent kinetic energy. Since void fraction measurements were taken at only three vertical cross sections in the experiment, the effect of density variation could not be included for plotting the entire flow map. However, these quantities may still be useful to researchers since they are still relevant, if not highly valuable, to the complex physical process.

Fig. A1 shows evolution of the mean kinetic energy per unit mass of the plunging breaker by assuming a uniform fluid density (i.e., water). It is clearly seen that high mean kinetic energy is transported and dissipated in mainly the aerated region. Mean kinetic energy in the impinging jet is transported to the first splash-up. Maximum mean kinetic energy during the first impingement is about $1.64C^2$, occurring at t = 0.01 s (close to Fig. A1a), whereas the maximum mean kinetic energy during the first splash-up (and also in the entire breaking process) is about $2.31C^2$ that occurs at the beginning of the first splash-up at t = 0.05 s (close to Fig. A1b) after converting potential energy to kinetic energy from the first impingement. The maximum mean kinetic energy in the first impingement and splash-up and second impingement (Fig. A1a-e) occurs close to the front face of the impinging jet or roller. As mentioned earlier, the second splash-up is not as pronounced but only barely visible; the maximum mean kinetic energy also appears near the front face of the roller as shown in Fig. A1f. As the breaking process continues, the mean kinetic energy diffuses and dissipates. The maximum mean kinetic energy reduces to about C^2 around t = 0.37 s (close to Fig. A1f) from the maximum value of $2.31C^2$ at t = 0.05 s in

merely 0.32 s (or about 0.4*T*). In the breaking process the first splash-up roller appears to be the main source of kinetic energy. Fig. A1f-h shows the mean kinetic energy of the second splash-up, and Fig. A1i, j shows the mean kinetic energy of the third splash-up; both rollers are not as distinguishable as the first impinging roller and the first splash-up roller.

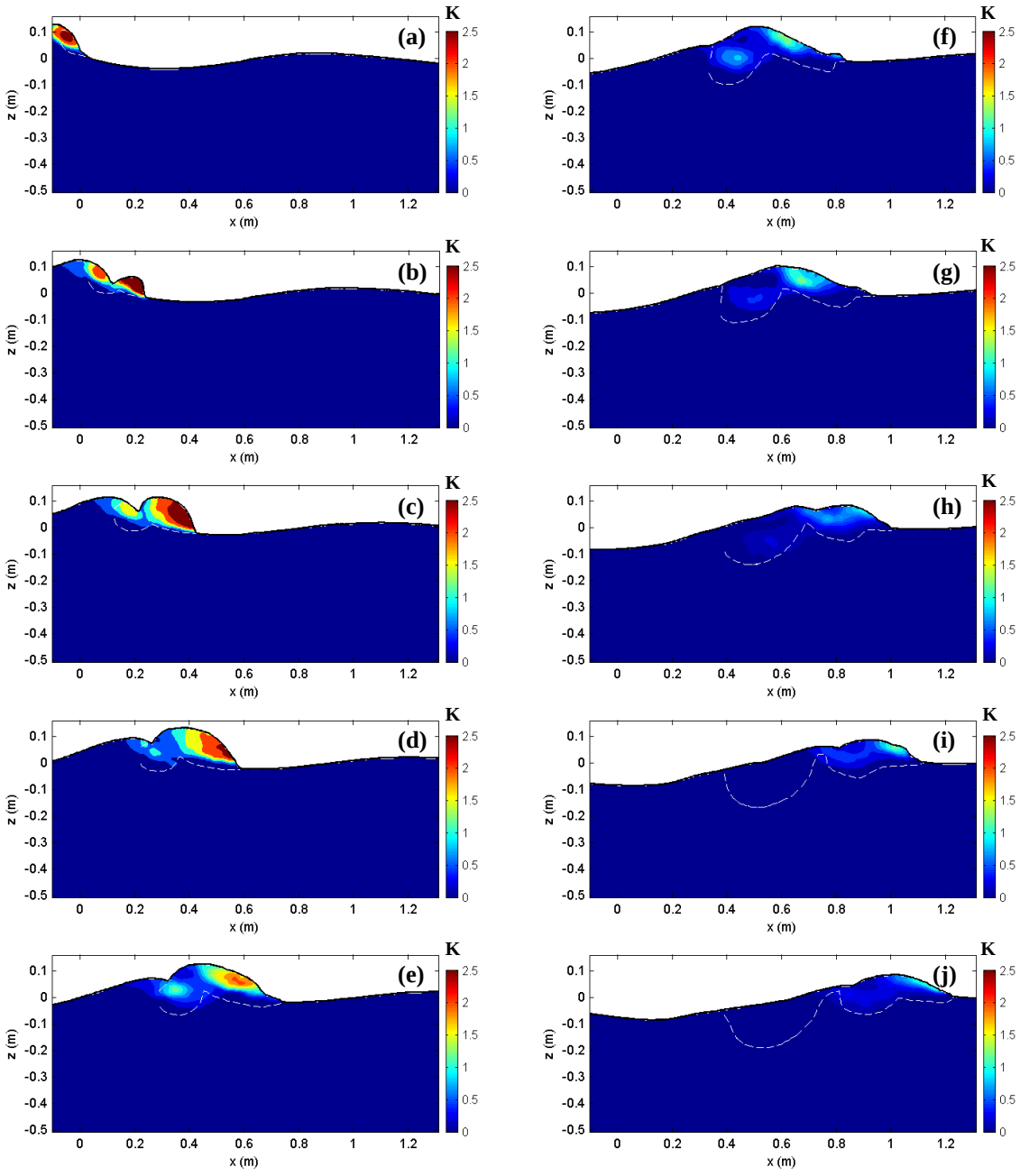

Fig. A1 Mean kinetic energy per unit mass (units: m^2/s^2) in the plunging breaker at *t* = (a) 0.00 s, (b) 0.08 s, (c) 0.16 s, (d) 0.24 s, (e) 0.32 s, (f) 0.40 s, (g) 0.48 s, (h) 0.56 s, (i) 0.64 s, (j) 0.72 s by assuming a constant density (ρ_w).

APPENDIX B

Turbulent kinetic energy per unit mass in the breaking process without considering the density variation is shown in Fig. B1. In the beginning of the first splash-up, significant turbulent kinetic energy is generated as shown in Fig. B1a. High turbulence develops near the lower boundary of the aerated region (i.e., the lower boundary of the impinging roller and the first splash-up roller as shown in Fig. B1b-e) in which turbulence is continuously generated due to the high shear between the high-velocity aerated region and the low-velocity non-aerated region, and the region formed by the penetration of the first impinging jet. High turbulence kinetic energy is especially generated near the toe of the first splash-up roller. After the first splash-up roller developed by significantly gaining energy from the impingement and shear, turbulence kinetic energy is gradually diffused and dissipated in the first impinging roller, as seen in Fig. B1a-e.

Fig. B1f, g shows the dominant turbulent kinetic energy moved upward from the toe to the middle of the first splash-up roller, probably due to the decrease in turbulent generation of the shear layer at the lower boundary of the roller, and advection of the energy due to the clockwise, upward moving mean flow in the roller. At the same moment, the mean kinetic energy continuously decreases as shown in Fig. B1e, f. Fig. B1g shows the turbulent kinetic energy at the moment of the second impingement. It generates neither a prominent roller nor high turbulent kinetic energy. After this stage, the turbulent kinetic energy gradually decreases (except for a very small peak during the third impingement which is not shown in the figure), as shown in Fig. B1h-j.

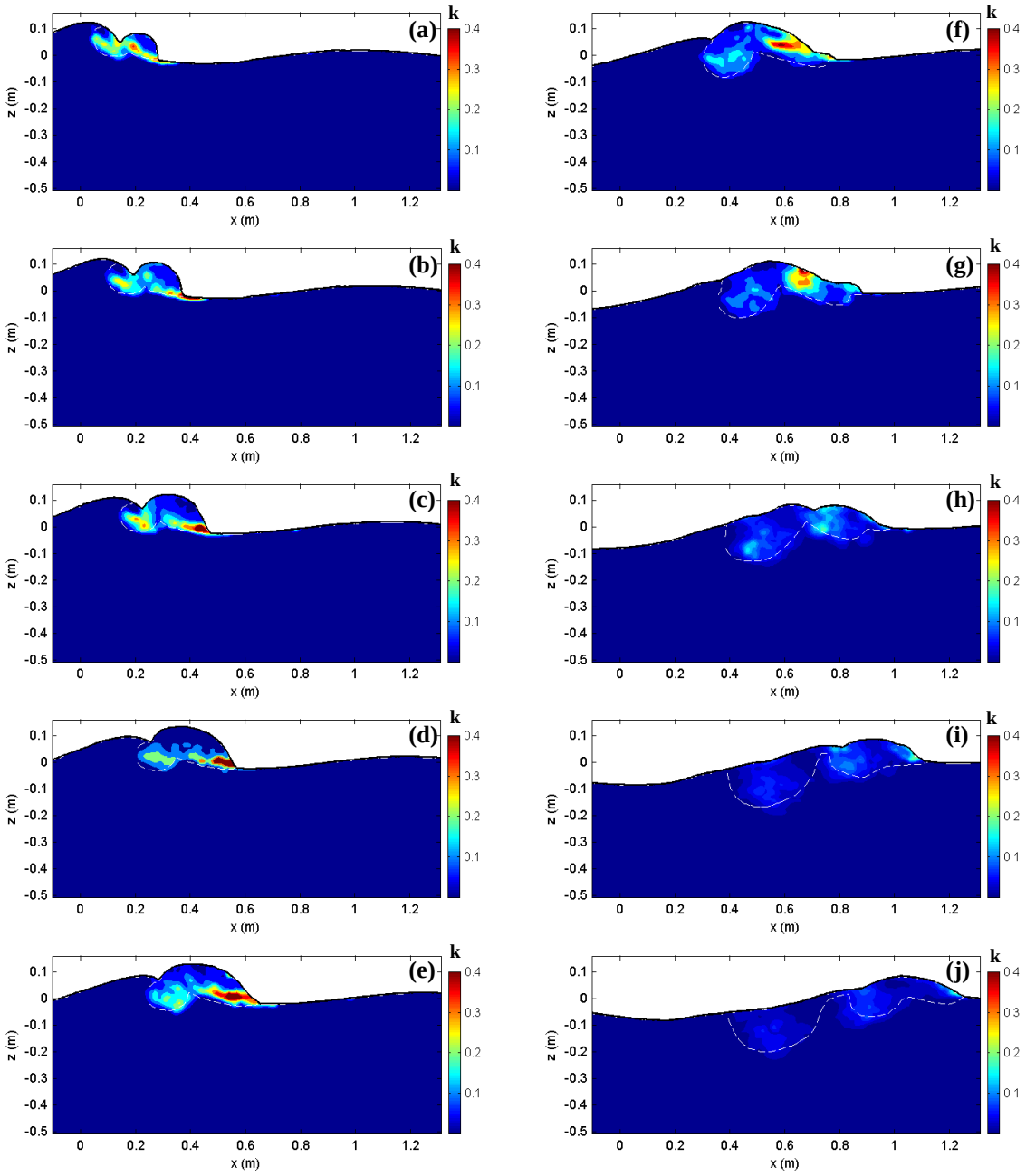

Fig. B1 Turbulent kinetic energy per unit mass (units: m^2/s^2) in the plunging breaker at *t* = (a) 0.10 s, (b) 0.14 s, (c) 0.18 s, (d) 0.23 s, (e) 0.27 s, (f) 0.35 s, (g) 0.44 s, (h) 0.54 s, (i) 0.64 s, (j) 0.75 s by assuming a constant density (ρ_w).

APPENDIX C

The depth averaged void fraction may be obtained based on the difference between wave gauge measurements and PIV video images. Let η_1 be the elevation measured by a resistant-type wave gauge and η_2 be the surface elevation (with an aerated region below) measured based on the PIV images. If we simply assume that the elevation difference (η_2 - η_1) is caused by air entrainment, the depth-averaged void fraction can be computed as (η_2 - η_1)/H with H being the wave height. Note that H = 0.20 m is close to the "height" (vertical spreading) of the bubble cloud based on the measurements at FOR station 1. Hence, H is used as the length scale in the void-fraction depth averaging process for the deep water condition here.

The depth-averaged void fraction profiles computed using the wave gauge-image method is compared with that measured using FOR; the results at the FOR station 1 are shown in Fig. C1. Even though the gauge-image method is very simple, good agreement is obtained, especially at the front of the foamy splash-up roller. On the other hand, the wave gauge-image method results in consistently higher void fraction behind the peak in the figure. We do not know the exact cause, but suspect that it might be attributed to the video images that may have a slight lag-effect on the glass walls due to the solid boundary. As a result, the wave gauge-image method gives a slightly higher reading on the rear face of the wave crest. Similar results were also obtained at FOR stations 2 and 3 (not shown here).

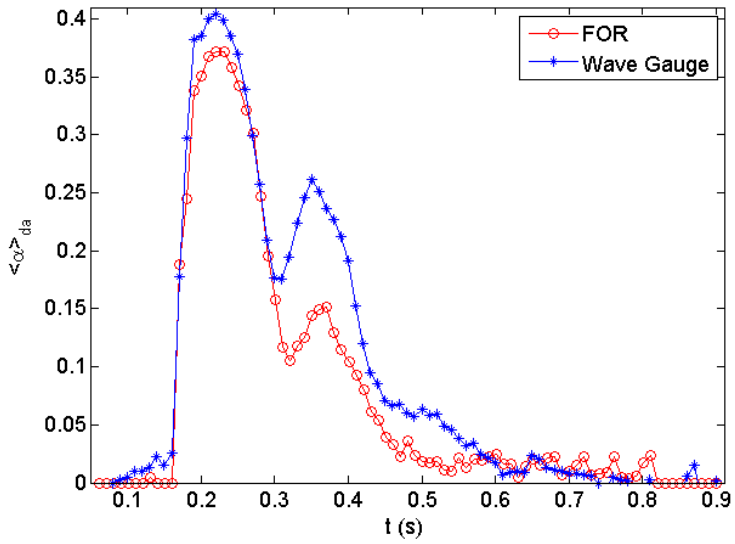

Fig. C1 Comparison of depth averaged void fraction using the wave gauge-image method and the FOR method in the aerated region at FOR station 1.

APPENDIX D

We revisit here that the maximum horizontal velocity reaches 2.14*C* at the beginning of the first splash-up (Fig. 2.6d) and verify it by examining mass conservation in a control volume. Note that applying momentum conservation is not available because the force or the pressure are not measured in the current study. A moving control volume that follows the phase speed (*C* = 1.3 m/s) of the plunging breaker was defined at each of the three phases in FOV1 (during the first splash-up) as shown in Fig. D1. The resolution of velocity vectors is $\Delta x = \Delta y = 5.8 \text{ mm}$. Conservation of mass in the finite control volume can be written as

$$\frac{\partial}{\partial t}\int_{CV} \rho dV + \int_{CS} \rho \vec{V} \cdot \hat{n} dA = 0 \qquad \text{(A2.1)}$$

in which $\vec{V}$ is the relative velocity to the moving control volume. We further assumed unit width in the analysis so $dV = \Delta x \Delta y = (\Delta x)^2$ and $dA = \Delta x$. The fluid density was estimated as $\rho = (1-\alpha)\rho_w$ where ρ_w is the density of water. Using central differences (Δt = 0.07 s) from the three time instances, we can obtain the first term in the mass conservation equation as

$$\frac{\partial}{\partial t}\int_{CV} \rho dV \approx \frac{1}{2\Delta t}\left[\sum_{CV(t=t_3)} \rho(\Delta x)^2 - \sum_{CV(t=t_1)} \rho(\Delta x)^2\right] \qquad \text{(A2.2)}$$

Similarly, we can obtain the second term in the mass conservation equation by integrating

over the four straight lines that form the control surface at the central time instance as

$$\int_{CS} \rho\vec{V}\cdot\hat{n}dA \approx \sum_{CS1\ (t=t_2)} \rho\vec{V}\cdot\hat{n}\Delta x + \sum_{CS2\ (t=t_2)} \rho\vec{V}\cdot\hat{n}\Delta x + \sum_{CS3\ (t=t_2)} \rho\vec{V}\cdot\hat{n}\Delta x + \sum_{CS4\ (t=t_2)} \rho\vec{V}\cdot\hat{n}\Delta x \tag{A2.3}$$

in which the measured mean velocities (*U*-*C*) and *W* were used in the calculation of $\vec{V}\cdot\hat{n}$.

The analysis was performed by assuming a uniform void fraction inside the aerated region; we then compared the calculated uniform void fraction with the measured void fraction at FOR station 1. To satisfy the conservation equation above, the uniform void fraction was found as 0.54. This value is very close to the measured mean void fraction of 0.58 in Fig. 2.14a, averaged over the penetration depth from *z* = -0.02 m (the lowest point of the aerated region in Fig. D1b, c) to the free surface at *z* = 0.12 m (the highest point of the aerated region in Fig. D1b, c).

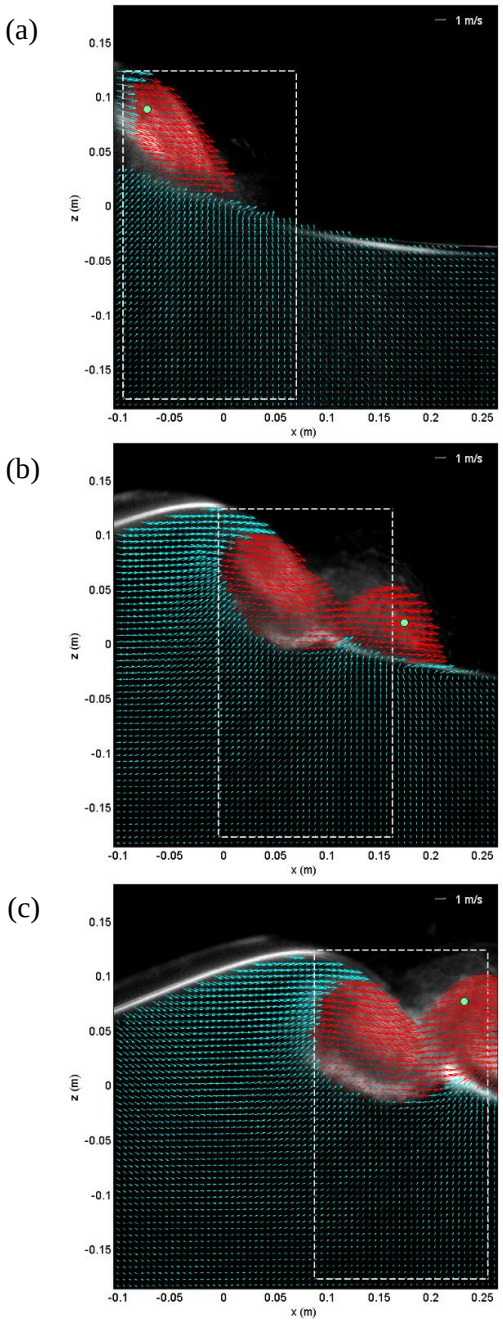

Fig. D1 Velocity maps and moving control volume (with phase speed *C*) at t = (a) -0.01 s (pre-breaking), (b) 0.06 s, (c) 0.13 s.

APPENDIX E

For a Newtonian fluid, the rate of dissipation of turbulent kinetic energy ε is defined as (Tennekes and Lumley, 1972):

$$\varepsilon = 2\nu s_{ij} s_{ij} = \nu \left\langle \frac{\partial u'_i}{\partial x_j} \left(\frac{\partial u'_i}{\partial x_j} + \frac{\partial u'_j}{\partial x_i} \right) \right\rangle \tag{E.1}$$

Where ν is the kinematic viscosity. The equation can be expanded and rewritten as:

$$\begin{aligned} \varepsilon = \nu \Bigg[& 2\left\langle \left(\frac{\partial u'}{\partial x} \right)^2 \right\rangle + \left\langle \left(\frac{\partial u'}{\partial z} \right)^2 \right\rangle + \left\langle \left(\frac{\partial w'}{\partial x} \right)^2 \right\rangle + 2\left\langle \left(\frac{\partial w'}{\partial z} \right)^2 \right\rangle + 2\left\langle \frac{\partial u'}{\partial z} \frac{\partial w'}{\partial x} \right\rangle \\ & + \left\langle \left(\frac{\partial u'}{\partial y} \right)^2 \right\rangle + \left\langle \left(\frac{\partial v'}{\partial x} \right)^2 \right\rangle + 2\left\langle \left(\frac{\partial v'}{\partial y} \right)^2 \right\rangle + 2\left\langle \frac{\partial u'}{\partial y} \frac{\partial v'}{\partial x} \right\rangle \\ & + \left\langle \left(\frac{\partial v'}{\partial z} \right)^2 \right\rangle + \left\langle \left(\frac{\partial w'}{\partial y} \right)^2 \right\rangle + 2\left\langle \frac{\partial v'}{\partial z} \frac{\partial w'}{\partial y} \right\rangle \Bigg] \end{aligned} \tag{E.2}$$

In order to estimate ε using the measured 2D velocity field, the lateral velocity v and the gradient terms with respect to y were estimated based on various assumptions. George and Hussein (1991) proposed a locally axisymmetric turbulence approach, assuming that turbulence is invariant to rotations around an axis, and derived the turbulent energy dissipation rate ε_A as:

$$\varepsilon_A = \nu\left[-\left\langle\left(\frac{\partial u'}{\partial x}\right)^2\right\rangle + 2\left\langle\left(\frac{\partial u'}{\partial z}\right)^2\right\rangle + 2\left\langle\left(\frac{\partial w'}{\partial x}\right)^2\right\rangle + 8\left\langle\left(\frac{\partial w'}{\partial z}\right)\right\rangle + 6\left\langle\frac{\partial u'}{\partial z}\frac{\partial w'}{\partial x}\right\rangle\right] \quad \text{(E.3)}$$

Kimmoun and Branger (2007) assumed that $\left\langle(\partial u'/\partial y)^2\right\rangle$, $\left\langle(\partial v'/\partial y)^2\right\rangle$, $\left\langle(\partial v'/\partial x)(\partial v'/\partial z)\right\rangle$, and $\left\langle(\partial w'/\partial y)^2\right\rangle$ can be neglected when compared with the other terms, and that $\left\langle(\partial v'/\partial x)^2\right\rangle$ and $\left\langle(\partial v'/\partial z)^2\right\rangle$ can be approximated as $\left[\left\langle(\partial u'/\partial x)^2\right\rangle + \left\langle(\partial w'/\partial x)^2\right\rangle\right]/3$ and $\left[\left\langle(\partial u'/\partial z)^2\right\rangle + \left\langle(\partial w'/\partial z)^2\right\rangle\right]/3$, respectively. Accordingly the turbulent energy dissipation rate, ε_C , is estimated as:

$$\varepsilon_C = \nu\left[\frac{7}{3}\left\langle\left(\frac{\partial u'}{\partial x}\right)^2\right\rangle + \frac{4}{3}\left\langle\left(\frac{\partial u'}{\partial z}\right)^2\right\rangle + \frac{4}{3}\left\langle\left(\frac{\partial w'}{\partial x}\right)^2\right\rangle + \frac{7}{3}\left\langle\left(\frac{\partial w'}{\partial z}\right)^2\right\rangle + 2\left\langle\frac{\partial u'}{\partial z}\frac{\partial w'}{\partial x}\right\rangle\right] \quad \text{(E.4)}$$

Doron et al. (2001) proposed a “direct method” assuming that all lateral fluctuations have similar average magnitudes: the non-product terms $\left\langle(\partial u'/\partial y)^2\right\rangle$, $\left\langle(\partial v'/\partial y)^2\right\rangle$, $\left\langle(\partial v'/\partial x)^2\right\rangle$, and $\left\langle(\partial v'/\partial z)^2\right\rangle$ are approximated as $\left[\left\langle(\partial u'/\partial z)^2\right\rangle + \left\langle(\partial w'/\partial x)^2\right\rangle\right]/2$; and the product terms $\left\langle(\partial u'/\partial y)(\partial v'/\partial x)\right\rangle$ and $\left\langle(\partial w'/\partial y)(\partial v'/\partial z)\right\rangle$ are approximated as $\left\langle(\partial u'/\partial z)(\partial w'/\partial x)\right\rangle$. Accordingly, the estimated turbulent energy dissipation rate ε_D becomes:

$$\varepsilon_D = \nu\left[3\left\langle\left(\frac{\partial u'}{\partial x}\right)^2\right\rangle + 3\left\langle\left(\frac{\partial u'}{\partial z}\right)^2\right\rangle + 3\left\langle\left(\frac{\partial w'}{\partial x}\right)^2\right\rangle + 3\left\langle\left(\frac{\partial w'}{\partial z}\right)\right\rangle + 6\left\langle\frac{\partial u'}{\partial z}\frac{\partial w'}{\partial x}\right\rangle + 2\left(\left\langle\frac{\partial u'}{\partial x}\frac{\partial w'}{\partial z}\right\rangle\right)^2\right] \tag{E.5}$$

Cowen et al. (2003) applied a central difference technique to the product of fluctuating strain rate and used an empirical coefficient to estimate the turbulent energy dissipation rate ε_E as:

$$\varepsilon_E = 2\nu c_1\left[\left\langle\left(\frac{\partial u'}{\partial x}\right)^2\right\rangle + \frac{1}{2}\left\langle\left(\frac{\partial u'}{\partial z}\right)^2\right\rangle + \frac{1}{2}\left\langle\left(\frac{\partial w'}{\partial x}\right)^2\right\rangle + \left\langle\left(\frac{\partial w'}{\partial z}\right)\right\rangle + \left\langle\frac{\partial u'}{\partial z}\frac{\partial w'}{\partial x}\right\rangle\right] \tag{E.6}$$

where the empirical coefficient $c_1 = 1.4$.

APPENDIX F

Additional figures obtained from the wavelet analysis in the small scale plunging breaking waves are provided in this Appendix F. The time difference between figures is 0.05 s.

Table F.1
Description of figures

Figure Number	Description
Fig. F.1	LIMM
Fig. F.2	Normalized Length Scale (H / LS)
Fig. F.3	Swirl Strength (ψ)
Fig. F.4	Root-squared Vorticity (ω^*)

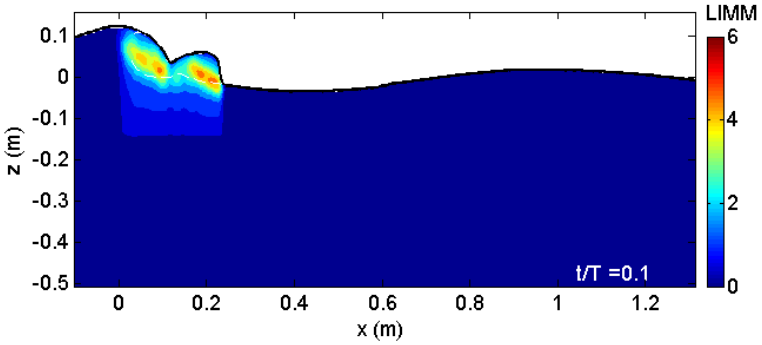

(a) $t/T = 0.10$

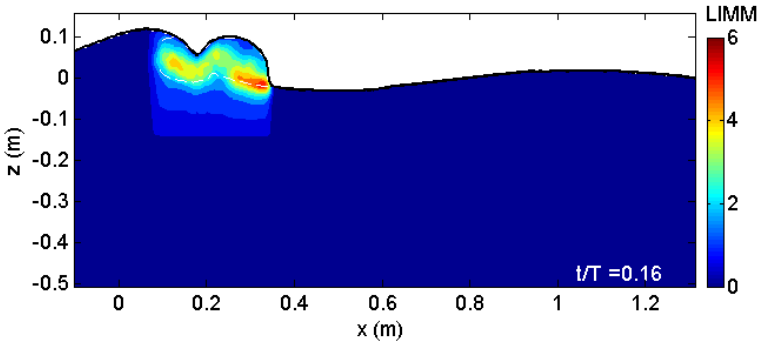

(b) $t/T = 0.16$

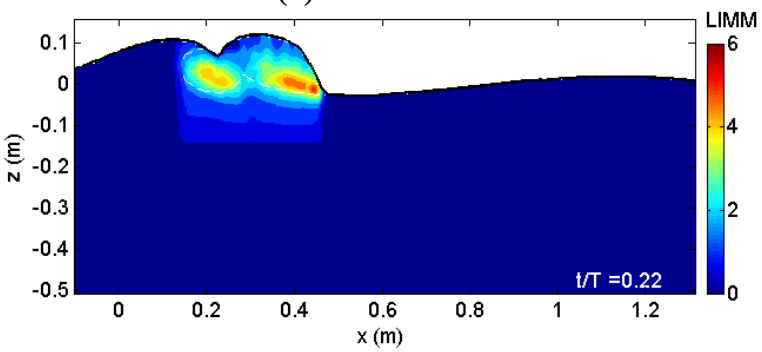

(c) $t/T = 0.22$

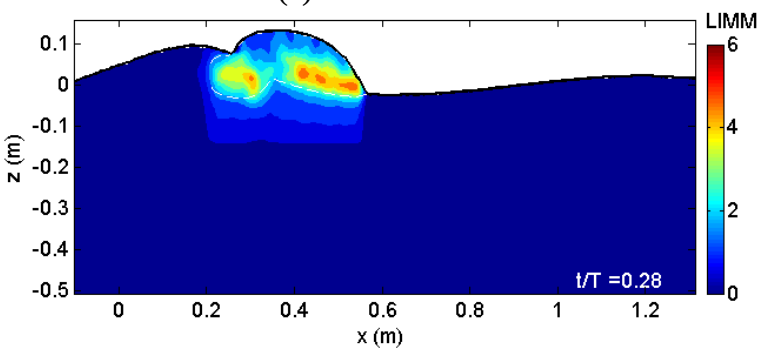

(d) $t/T = 0.28$

Fig. F.1 LIMM.

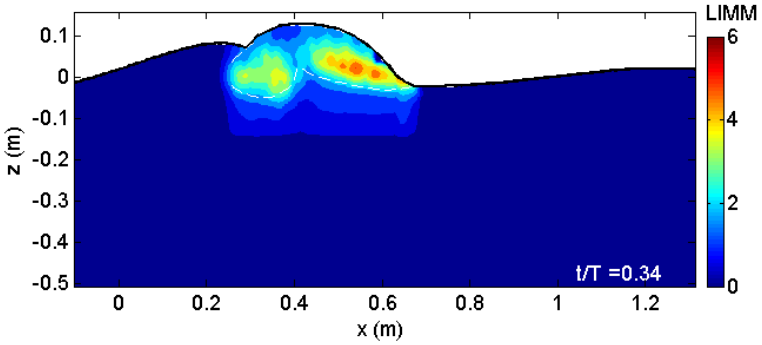

(e) t/T = 0.34

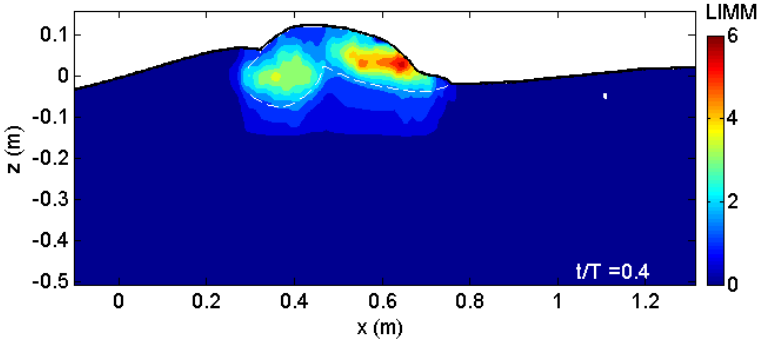

(f) t/T = 0.40

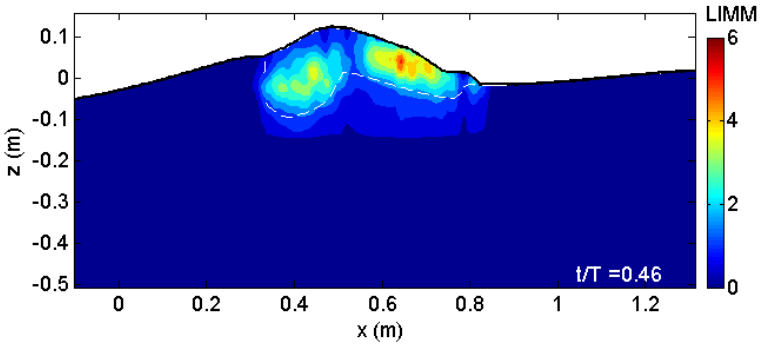

(g) t/T = 0.46

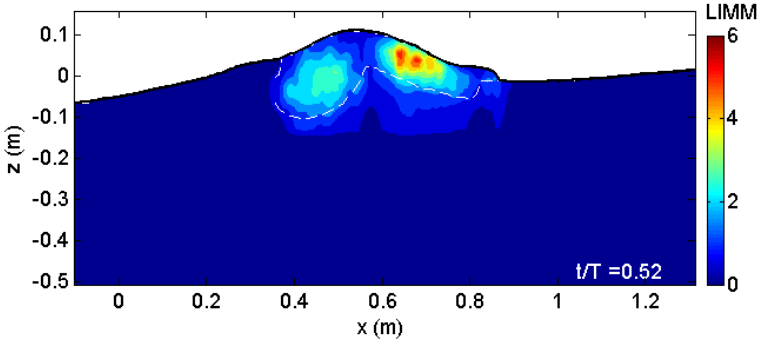

(h) t/T = 0.52

Fig. F.1 (Continued).

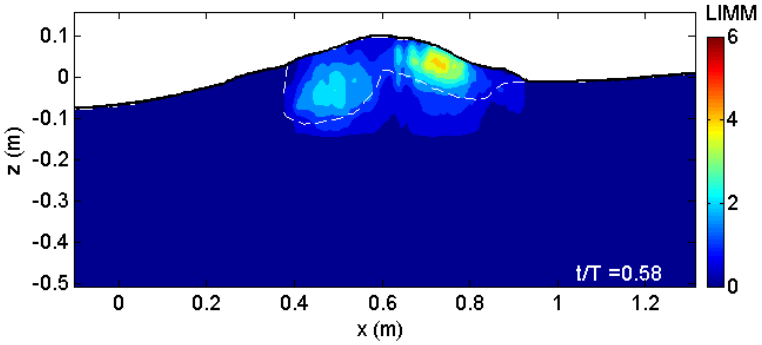

(i) t/T = 0.58

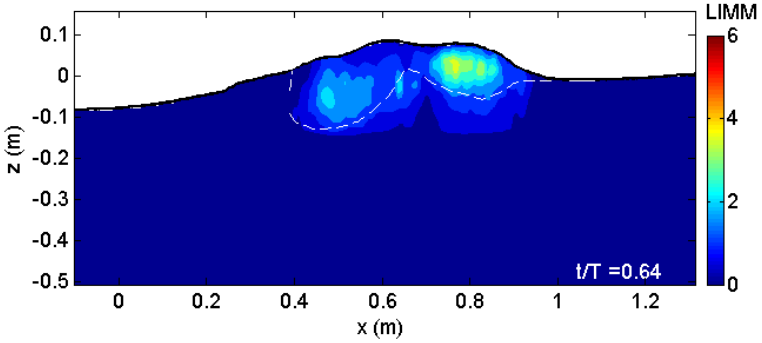

(j) t/T = 0.64

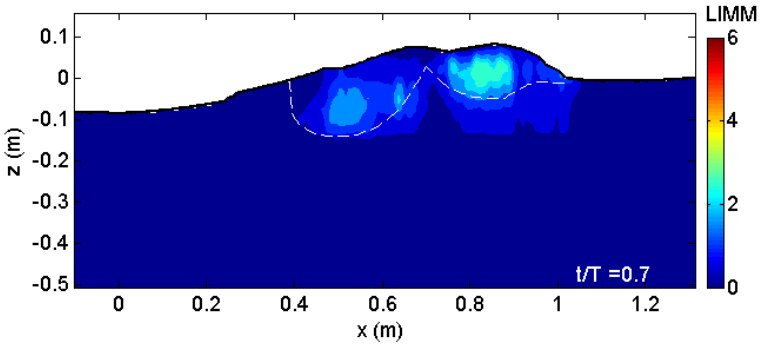

(k) t/T = 0.70

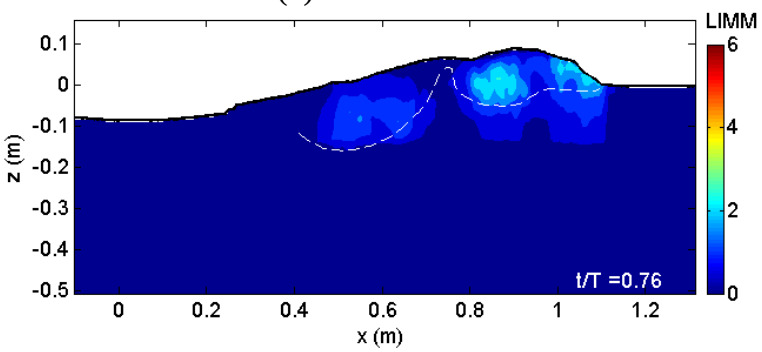

(l) t/T = 0.76

Fig. F.1 (Continued).

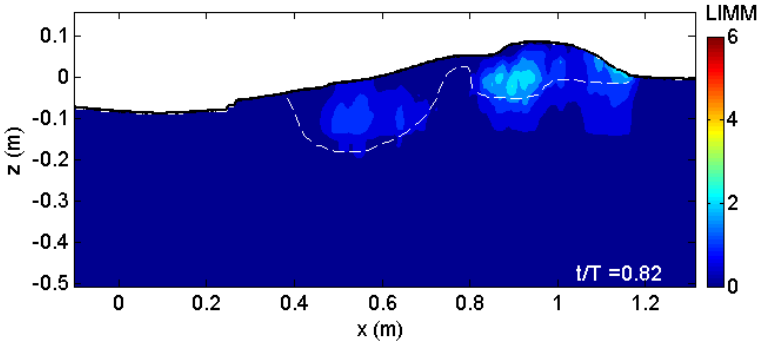

(m) $t/T = 0.82$

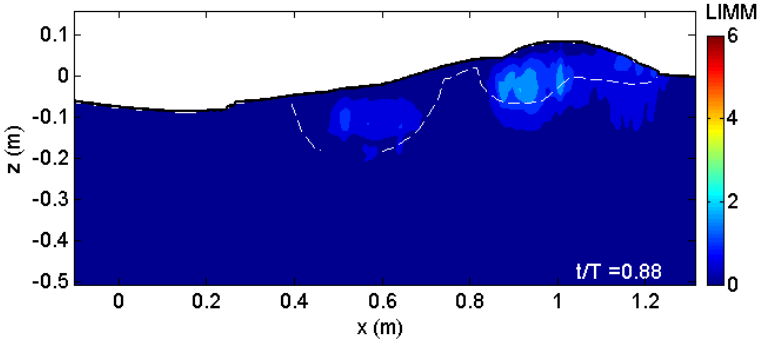

(n) $t/T = 0.88$

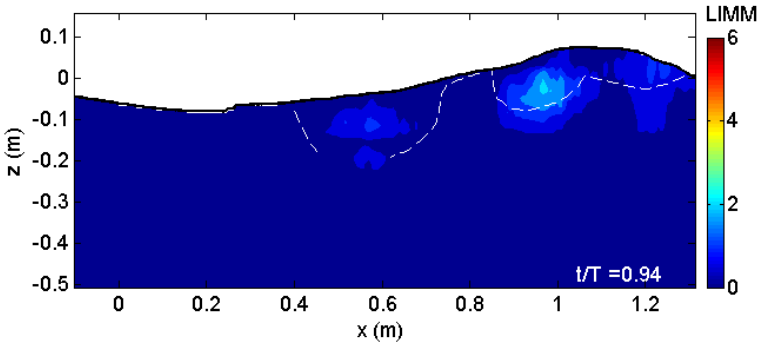

(o) $t/T = 0.94$

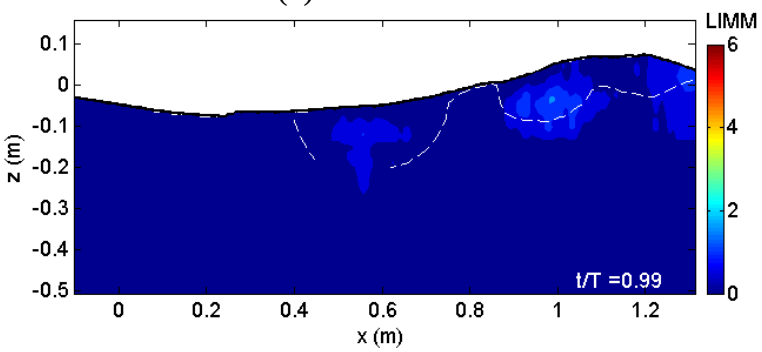

(p) $t/T = 0.99$

Fig. F.1 (Continued).

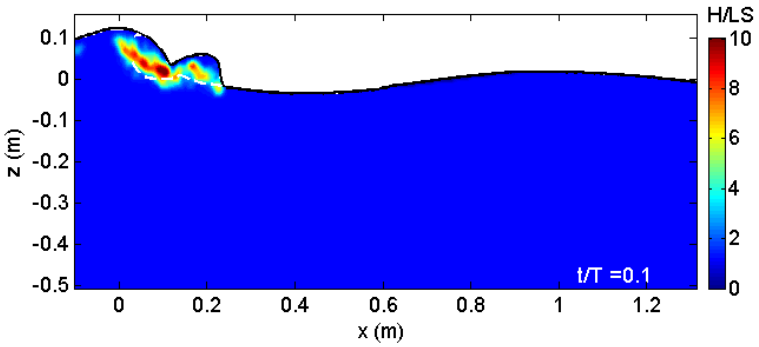

(a) t/T = 0.10

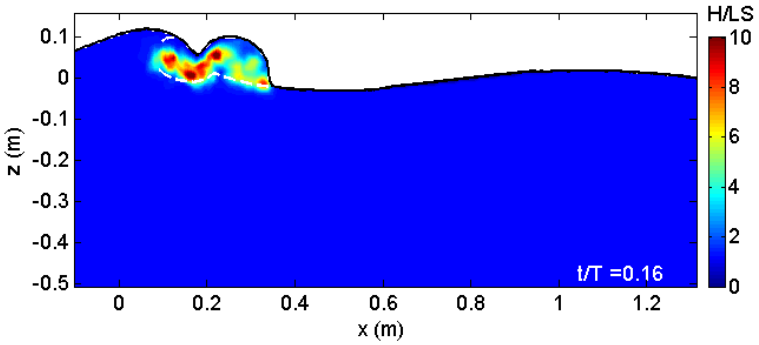

(b) t/T = 0.16

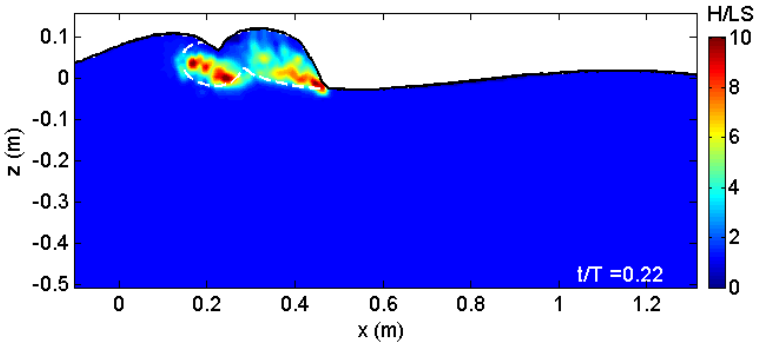

(c) t/T = 0.22

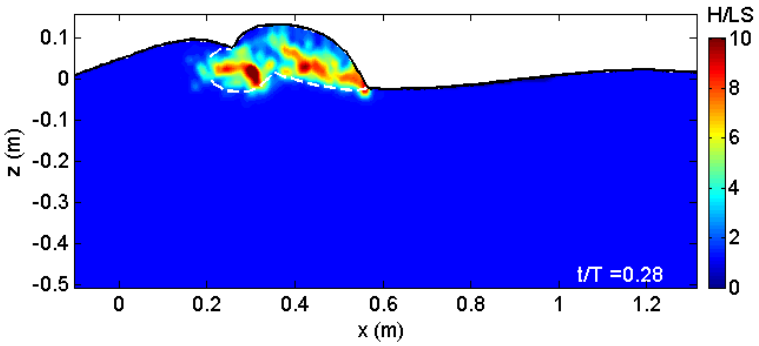

(d) t/T = 0.28

Fig. F.2 Normalized Length Scale (*H*/*LS*).

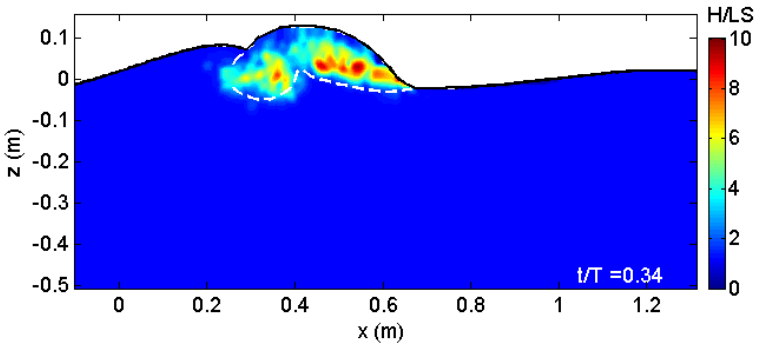

(e) t/T = 0.34

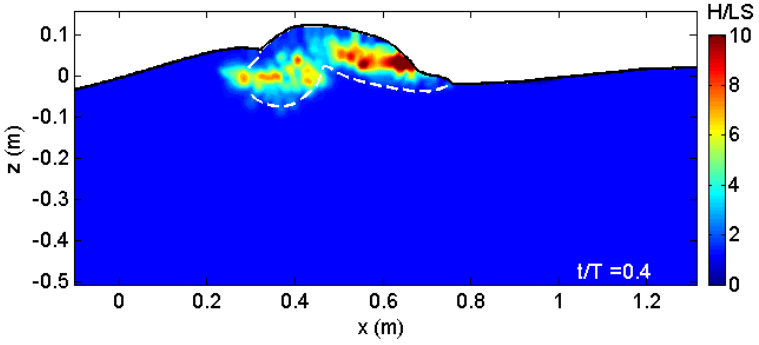

(f) t/T = 0.40

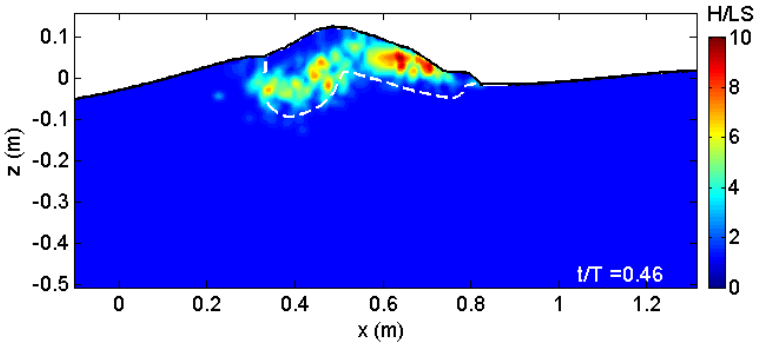

(g) t/T = 0.46

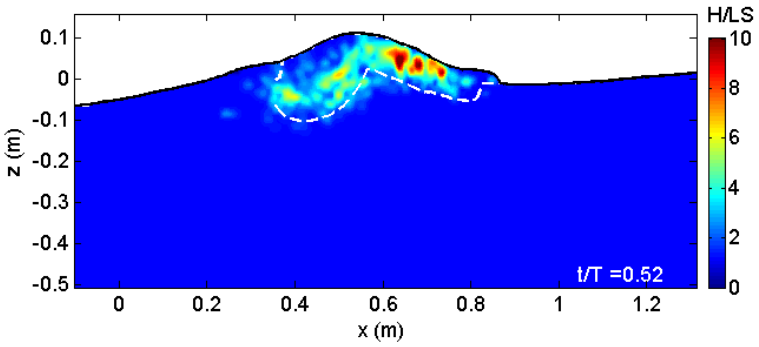

(h) t/T = 0.52

Fig. F.2 (Continued).

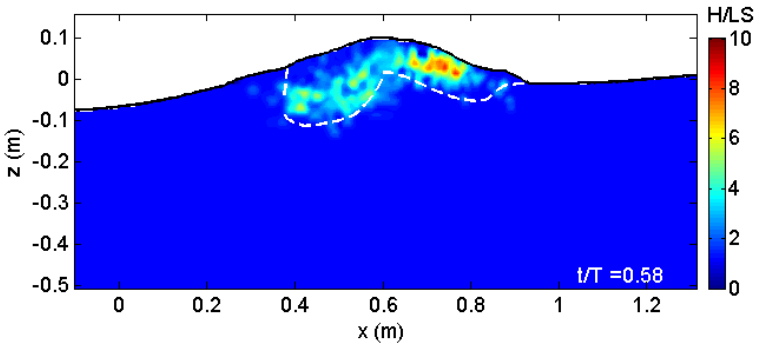

(q) t/T = 0.58

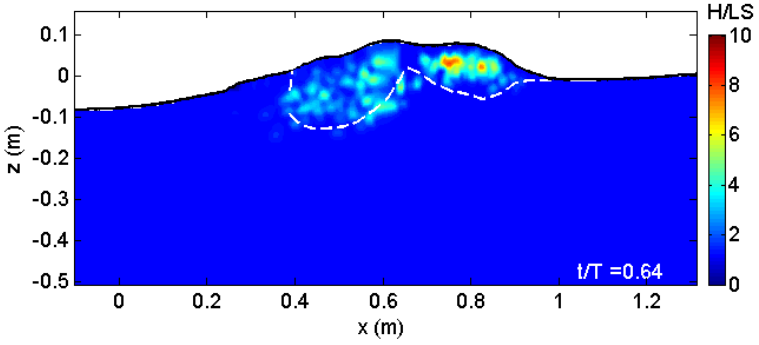

(r) t/T = 0.64

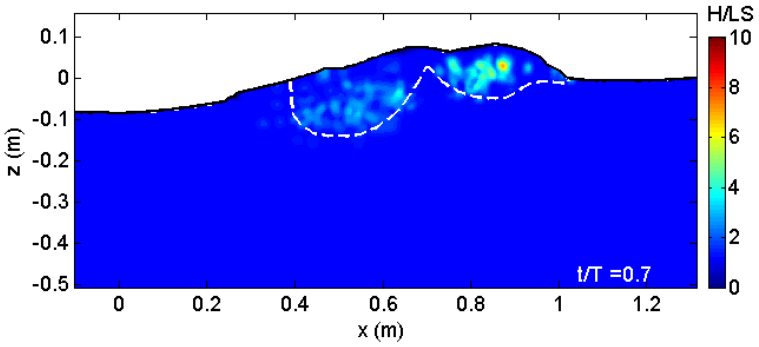

(s) t/T = 0.70

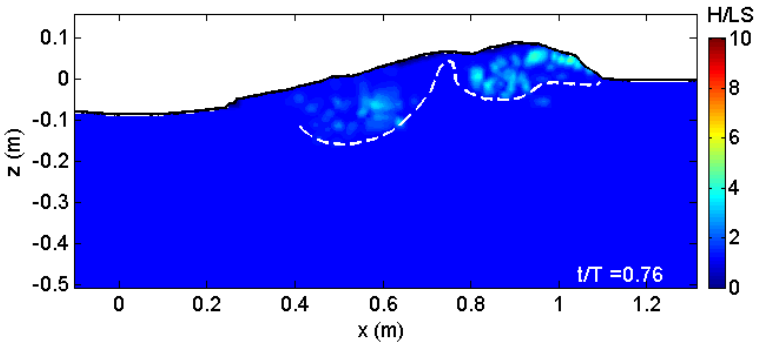

(t) t/T = 0.76

Fig. F.2 (Continued).

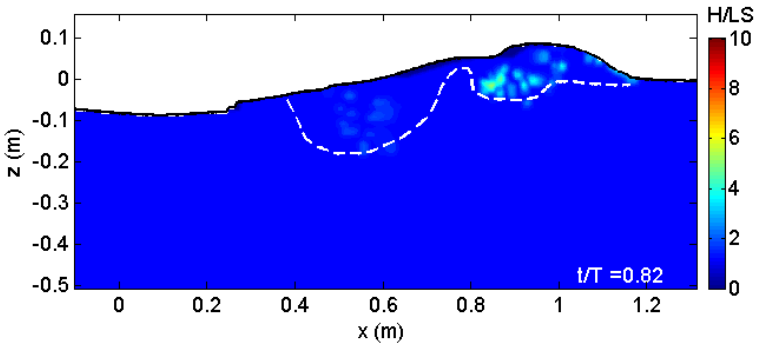

(q) t/T = 0.82

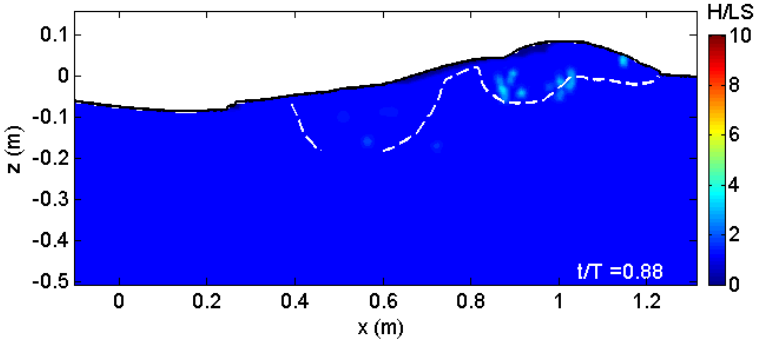

(r) t/T = 0.88

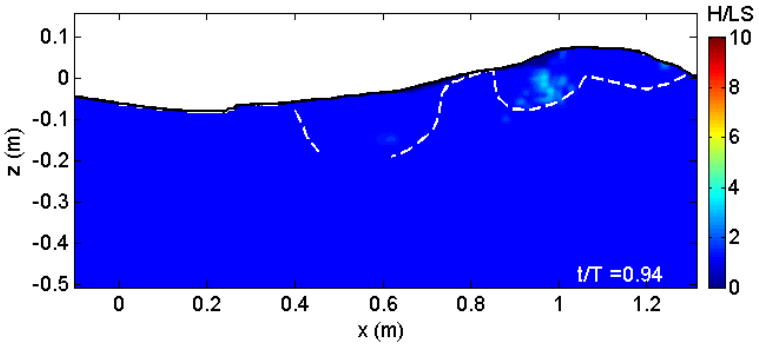

(s) t/T = 0.94

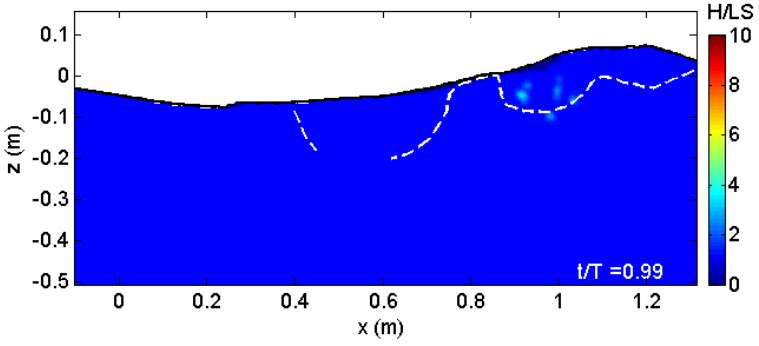

(t) t/T = 0.99

Fig. F.2 (Continued).

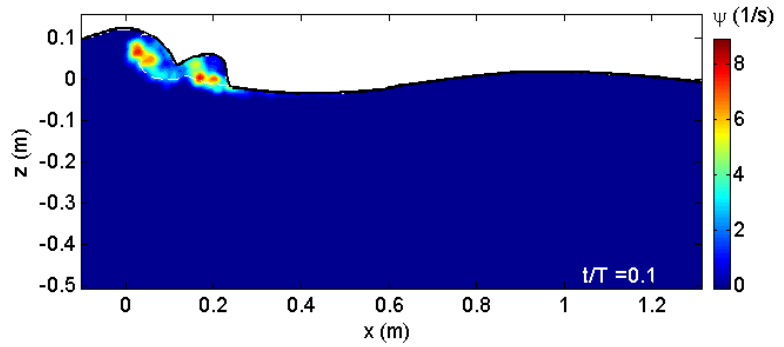

(a) t/T = 0.10

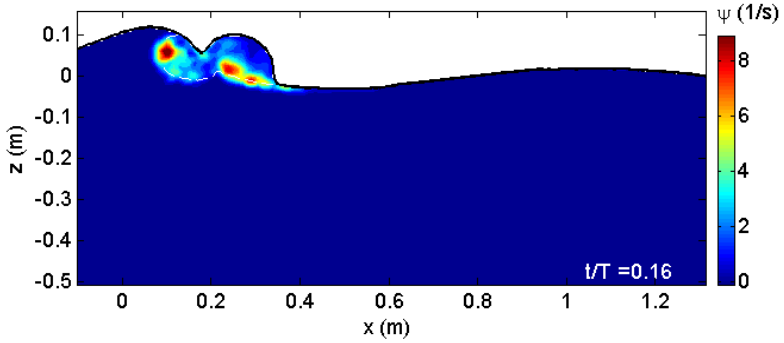

(b) t/T = 0.16

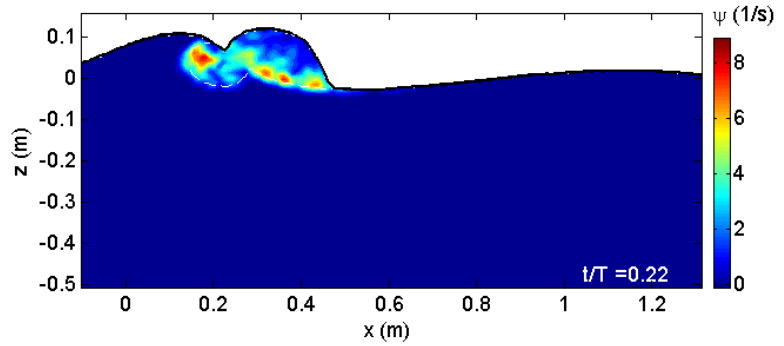

(c) t/T = 0.22

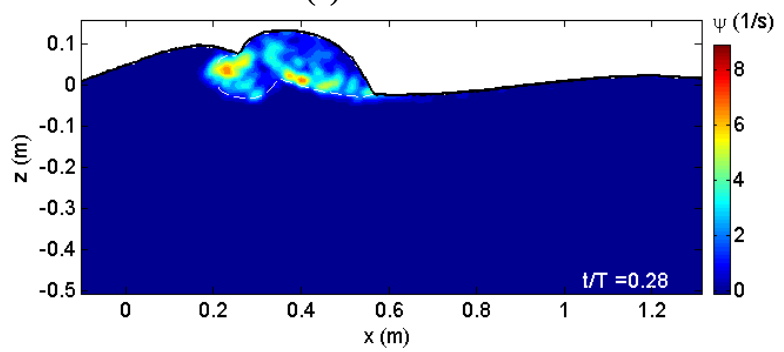

(d) t/T = 0.28

Fig. F.3 Swirl strength (ψ).

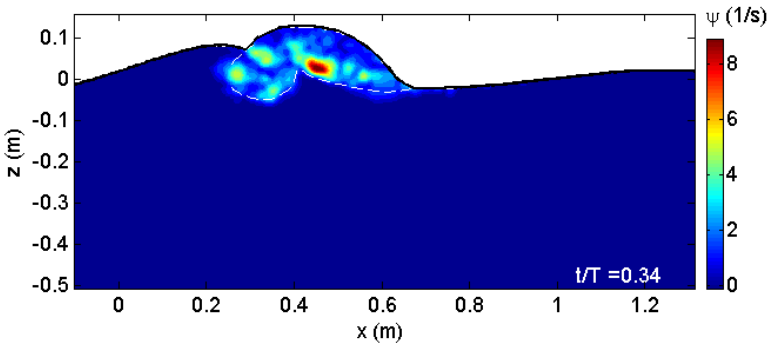

(e) t/T = 0.34

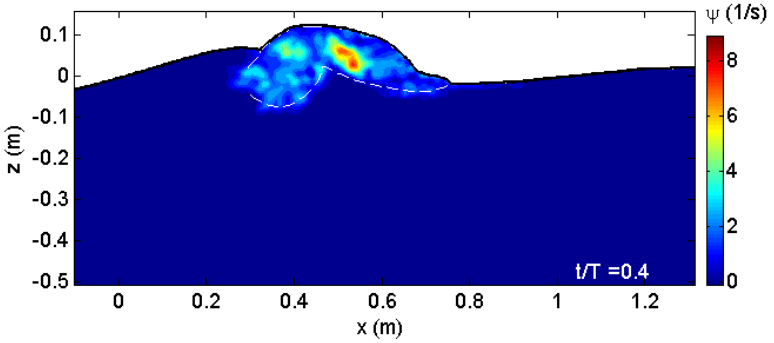

(f) t/T = 0.40

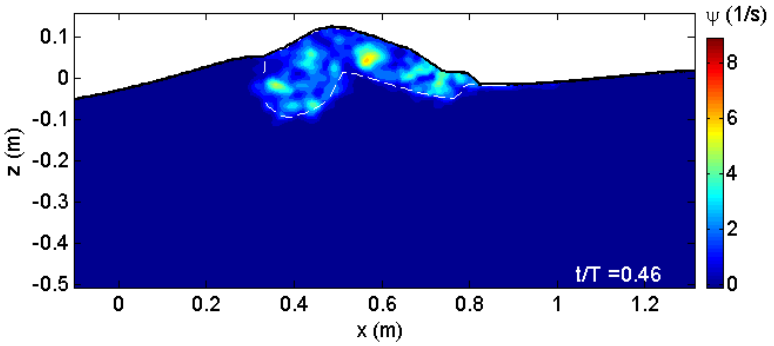

(g) t/T = 0.46

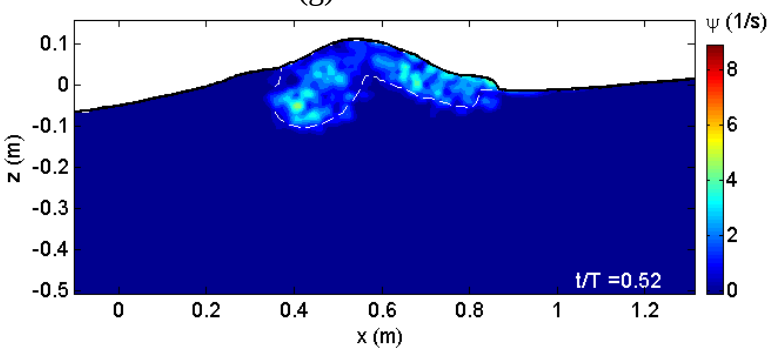

(h) t/T = 0.52

Fig. F.3 (Continued).

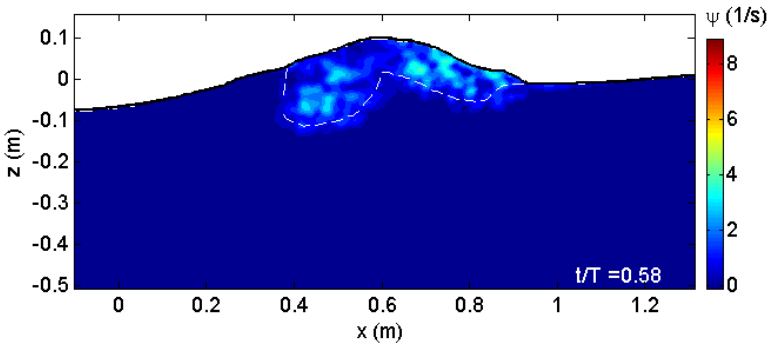

(q) t/T = 0.58

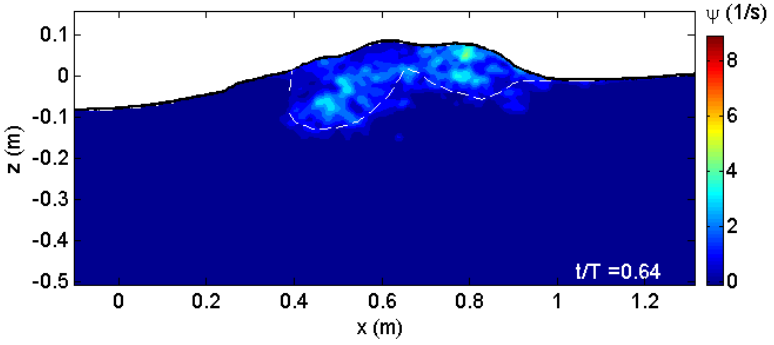

(r) t/T = 0.64

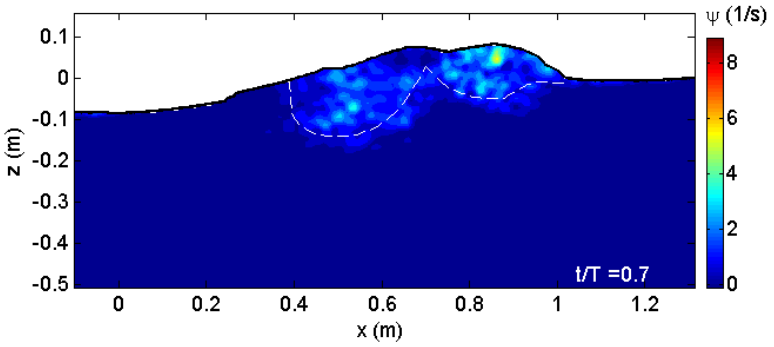

(s) t/T = 0.70

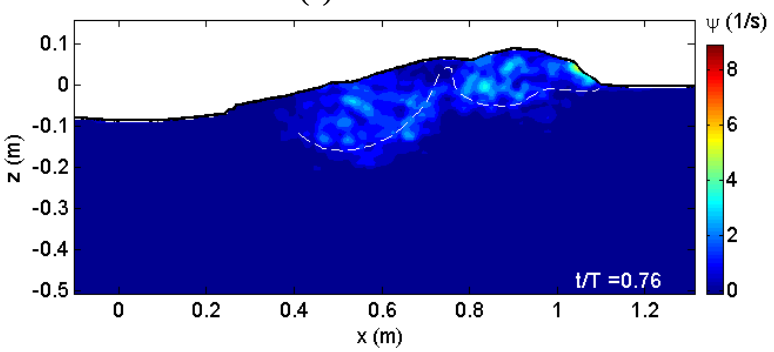

(t) t/T = 0.76

Fig. F.3 (Continued).

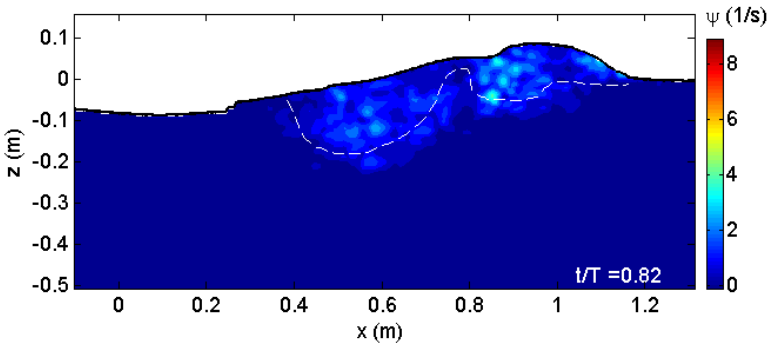

(q) t/T = 0.82

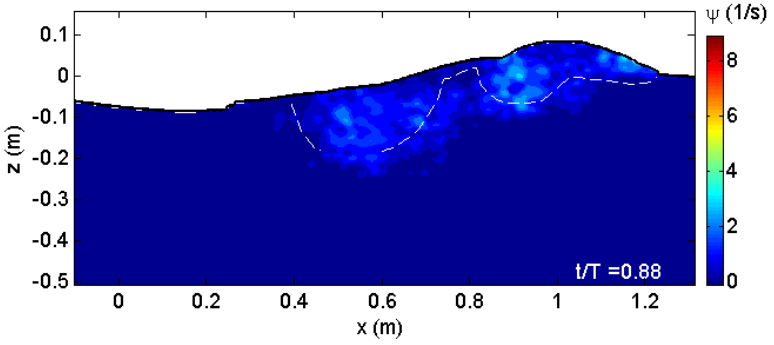

(r) t/T = 0.88

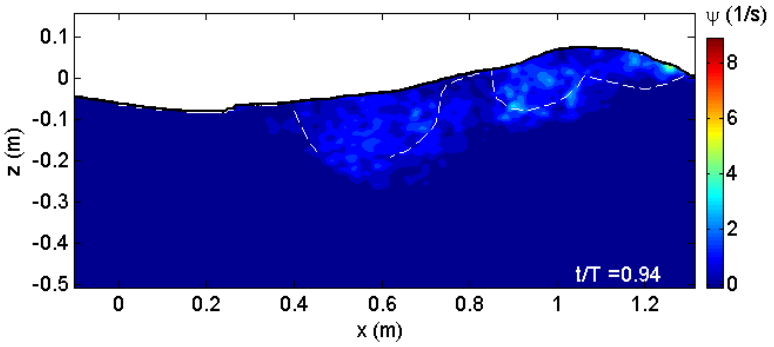

(s) t/T = 0.94

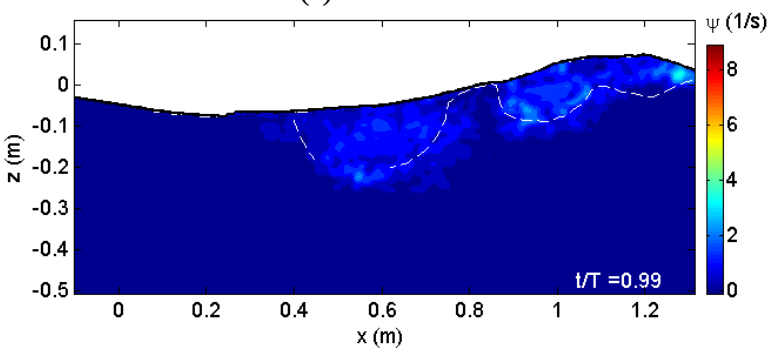

(t) t/T = 0.99

Fig. F.3 (Continued).

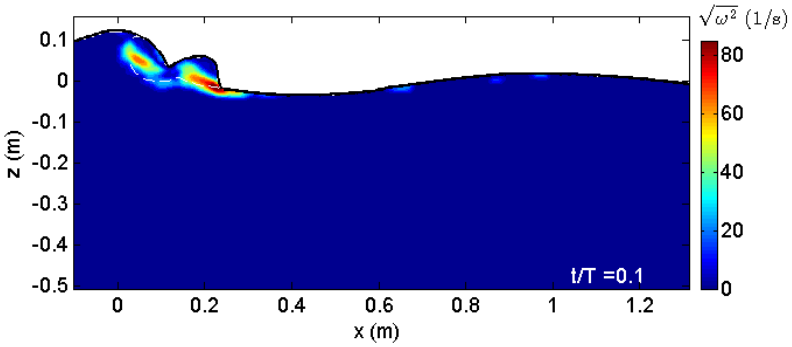

(a) t/T = 0.10

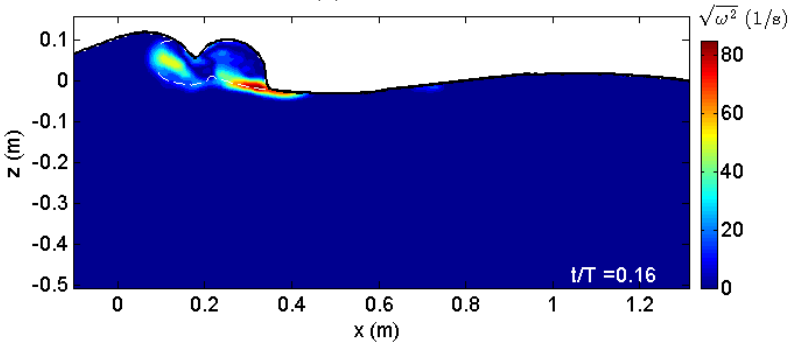

(b) t/T = 0.16

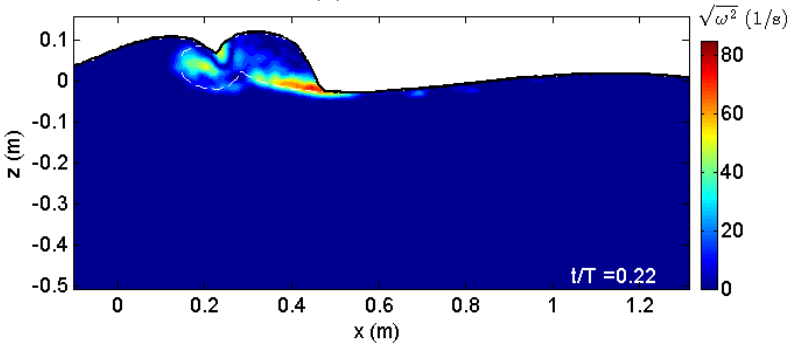

(c) t/T = 0.22

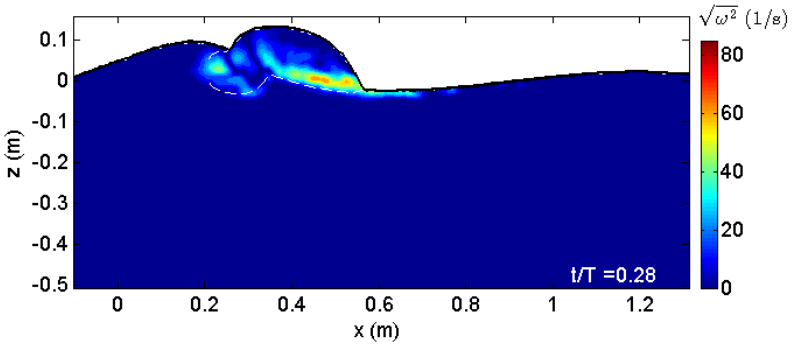

(d) t/T = 0.28

Fig. F.4 Root-squared Vorticity (ω^*).

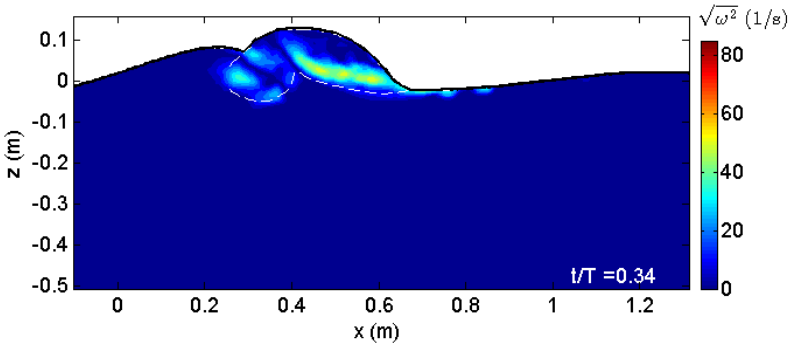

(e) t/T = 0.34

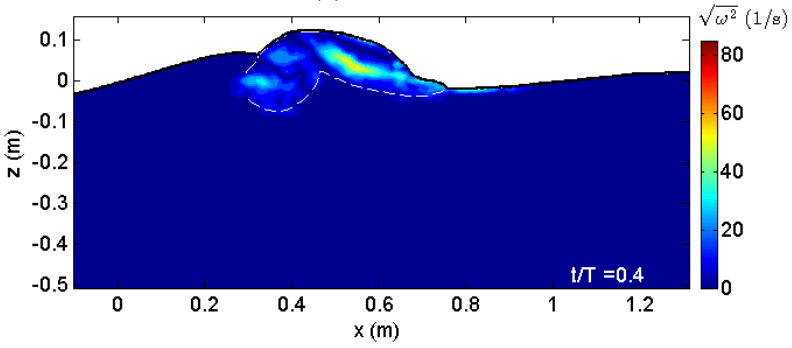

(f) t/T = 0.40

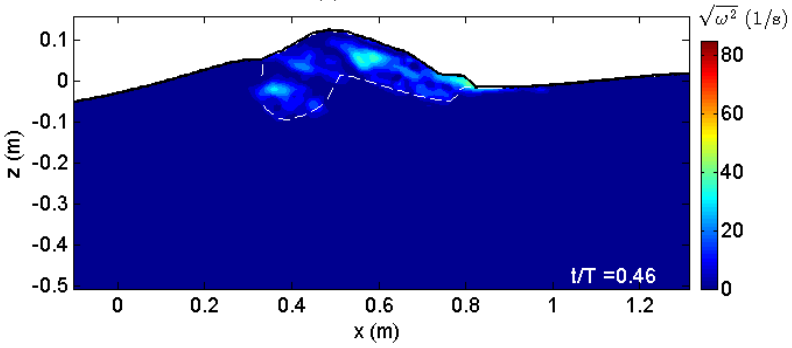

(g) t/T = 0.46

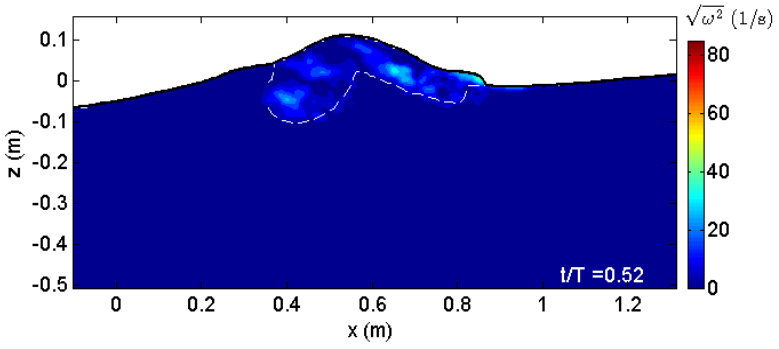

(h) t/T = 0.52

Fig. F.4 (Continued).

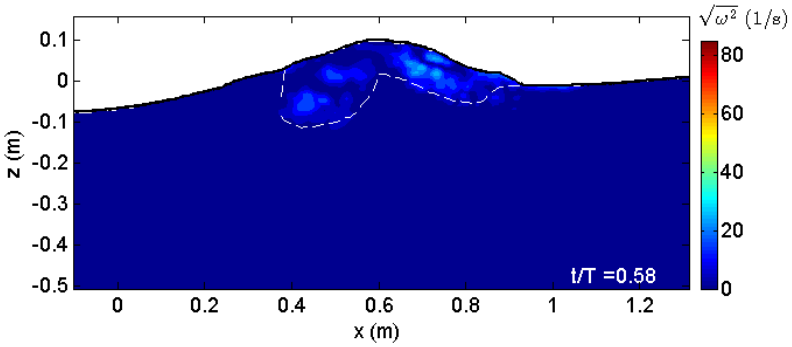

(q) t/T = 0.58

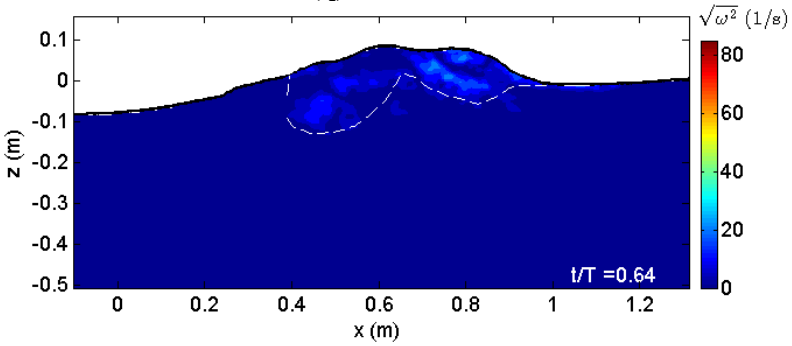

(r) t/T = 0.64

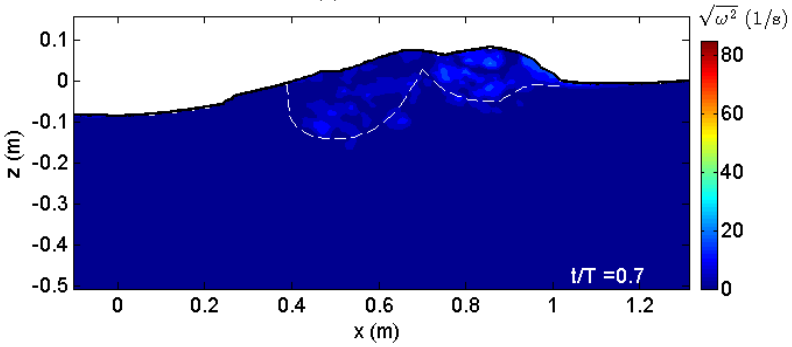

(s) t/T = 0.70

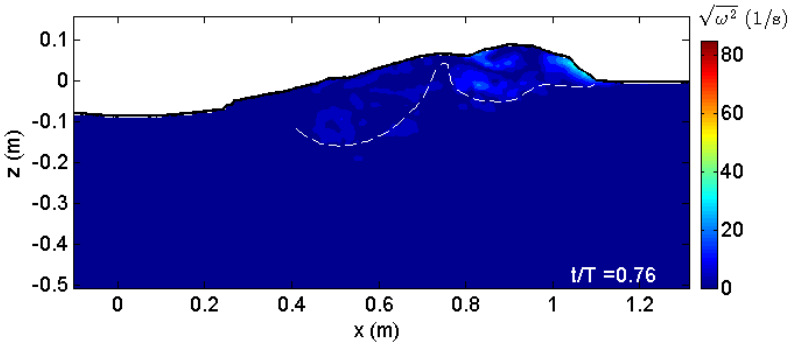

(t) t/T = 0.76

Fig. F.4 (Continued).

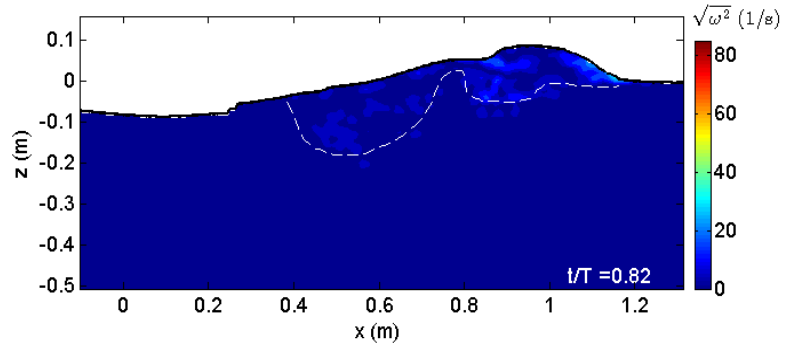

(q) t/T = 0.82

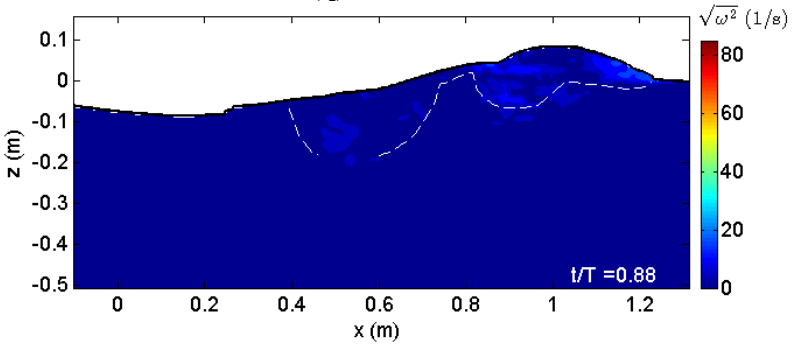

(r) t/T = 0.88

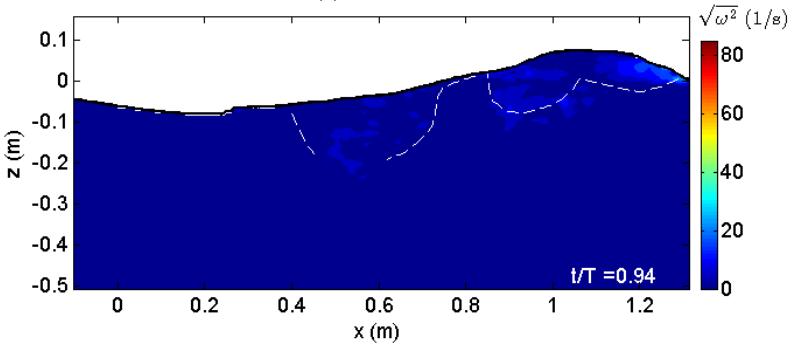

(s) t/T = 0.94

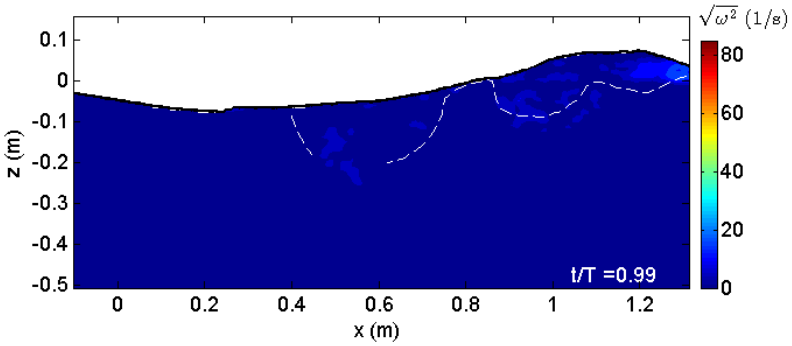

(t) t/T = 0.99

Fig. F.4 (Continued).